Neutron and Muon Studies of the Vortex Lattice in Anisotropic Superconductors

by

Cameron Ager

September 1999.

A thesis submitted for the degree of Doctor of Philosophy.

Abstract

A study of extreme type II superconductors has been carried out using primarily tranverse field μSR and small-angle neutron scattering (SANS). This study has encompassed a range of systems from the moderately anisotropic $YBa_2Cu_3O_{7-\delta}$(YBCO), through the highly anisotropic $Bi_{2.15}Sr_{1.85}Ca_1Cu_2O_{8+\delta}$ (BSCCO) and κ-(BEDT-TTF)$_2$Cu(SCN)$_2$ [ET-Cu] systems to the extremely anisotropic α-(BEDT-TTF)$_2$NH$_4$Hg(SCN)$_4$ [ET-NH4].

Characterisation of the anisotropy of an untwinned sample of YBCO indicate that microscopic measurements of the in and out-of-plane anisotropies are in reasonable agreement with those obtained from other microscopic measurements, but the out-of-plane anisotropy exhibits a discrepancy with torque measurements.

Measurements on the phase diagram of the layered organic systems ET-Cu and ET-NH4 indicate that these exhibit vortex behaviour similar to that of BSSCO, that can be viewed as generic amongst the highly layered superconductors. Primarily, these measurements indicate that although Josephson coupling is assumed to dictate the coupling landscape between pancake-vortices in these systems, electromagnetic coupling cannot be ignored, as this certainly plays a role and may even dominate vortex dynamics. Further, measurements of the behaviour of thermal disorder in optimally doped BSSCO add weight to the consensus that electromagnetic coupling must play a role.

In addition, samples of BSCCO have been irradiated to produce columnar defects. The introduction of defects, which act as strong pinning centres, was found to strongly influence both static and dynamic order and thereby introduce a number of interesting features into the phase diagram of BSSCO.

I would like to dedicate this work to Elizabeth Margaret Fleming and Gordon Cameron

&

Pete.

Contents

Acknowledgements

In common with much of this thesis I drafted out these acknowledgements yesterday morning, but have come here today to find that I'm dis-satisfied with what I have, so here goes! In the last three years as a Ph.D student I have made the aquaintance of many distinguished people and it is with great pleasure that I acknowledge them here. First and foremost I would like to thank my supervisor Dr S.L.Lee. Working with Steve has been excellent and I can honestly say that dull moments have been few and far between. His unwavering enthusiasm and keen sense of fun have been an inspiration.

Thanks also go to Feodore, Natasha and Tanya for putting up with the endless stream of questions about Russia, Russian and Russians, and the excellent atmosphere in the office.

Special thanks also go to Sion Lloyd, Christof Aegerter, Bob Cubitt and Steve Blundell for helping to make central facility experiments, which are a test of both mental and physical tenacity at the best of times, fulfilling and enjoyable. I would also like to thank other members of the collaboration... Paul Kealey, Ted Forgan, Francis Pratt, Stuart Johnson, Micheal Hunt, Hugo Keller, Sara Romer and the list goes... apologies to those I've missed. I would also like to thank members of the magnetism group, both old and new, for making my time in St. Andrews pleasant and enjoyable: Mark Telling, Rob Bewley, Ross Stewart, Alfie Rustom,

Shannon Brown, Colin Oates, Judith Dann, Naiara Elejalde, Sue Kilcoyne and Bob Cywinski.

A very special thanks goes to Steve White for many interesting discussions and shared passion in martial arts. I can see a scenario where I return to St. Andrews in ten years time just to train on the beach... can't you?!

I would like to take this opportunity to thank the EPSRC for my studentship, the Physics Trust, the Department of Physics and Astronomy and the Assistant Hebdomadar, Alan Douglas, for the financial assistance I received from them this summer.

I would also like to thank those people who have extended their hospitality to me over the last two weeks when I have been effectively homeless AND A.G.Barr plc should get a mentions for producing a drink which is ten times as potent as Coke (No royalties please!!).

Last, but certainly not least, are my parents, Gordon and Elizabeth, You have my deepest thanks.

Chapter 1

Superconductivity

1.1 Introduction

It was a student of *H.Kamerlingh Onnes, Von Holst* in 1911 [1], who first noted that the resistance of mercury (and other metals) became immeasurably small at liquid helium temperatures. This phenomenon, which is now known as superconductivity, escaped advance by workers in the field until *W Meissner and R Ochsenfeld(1933)* [2] discovered that upon cooling in an external field H_{ext} (smaller than a critical value H_c) the superconductor expelled the magnetic field completely. This was called the Meissner effect and proved that superconductivity was a true thermodynamic phase (see Fig. 1.1). In 1935, 24 years after the first observations of superconductivity, *F and H.London* [3] proposed the first theory of superconductivity. They postulated that the superconductivity could be described by a macroscopic wavefunction or order parameter based on an analogy with electron orbitals which *flow* without dissipation. This theory was superceded by the theory of *Ginzburg and Landau (1950)* [4], based on the phenomelogical theory of second and higher order phase transitions of *Landau (1937)* [5]. G-L

theory incorporated spatial variations of the order parameter which were unaccounted for in the model of the London brothers. The first microscopic theory of superconductivity was developed by *Bardeen, Cooper and Schrieffer (1957)* [6] (BCS theory). BCS theory proposed that electrons in the superconducting state are paired together into what is known as a *Cooper pair*. This *exotic* coupling of electrons was proposed to be mediated by the exchange of a phonon between the pair. These superconducting pairs behave much like bosons in that they form a condensate, rather like a Bose condensate.

It is now known that the phenomenon occurs in about half of the elemental metals in the periodic table. The critical temperatures for these are all low with niobium having the highest T_c of 9.25 K. Certain alloys were also known to superconduct and by the late 1970's the highest transition temperature belonged to Nb_3Ge ($T_c \sim 23$ K).

Research in the superconducting field was revitalised when *Bednorz and Muller (1986)* [7] discovered superconductivity in a compound at 30 K. This was $La_{2-x}Ba_xCuO_{4-y}$ and the huge research effort which followed yielded $YBa_2Cu_3O_{7-\delta}$ (YBCO) with a $T_c \approx 92$ K [8]. The continued research effort has led to the discovery of many other compounds with higher T_cs and the highest to date is >150 K when the mercury based compound $HgBa_2Ca_2Cu_3O_{8+\delta}$ [9] is cooled under high pressure. The most recent discoveries noted here are all of what are known as *high temperature cuprate superconductors* (HTSC) and these all exhibit type II superconductivity. The early elemental superconductors were almost all type I materials. These exhibit the Meissner effect up to a critical field $H_c(T)$ (see Fig. 1.2). Type II materials exhibit the Meissner effect up to a lower critical field $H_{c1}(T)$, above which flux begins to penetrate in the form of fluxons. These fluxons

are composed of a quanta of magnetic flux maintained by the flow of supercurrent. In isotropic type II superconductors in the mixed state the fluxons form a well ordered flux-line lattice which has triangular symmetry [10]. Upon increasing the external magnetic field the density of fluxons increases up until the upper critical field $H_{c2}(T)$ is reached, when the cores of the flux-lines overlap and the sample goes normal (see Fig. 1.3). In the mixed state of *anisotropic* type II superconductors, like HTSC, the simple picture of a flux-line lattice does not hold throughout the mixed-state and much interest has been generated by the novel flux structures that exist in these compounds. This thesis is concerned with the nature of the vortex structures in anisotropic extreme type II superconductors, primarily focusing on the dominant coupling mechanism controlling the behaviour of flux-lines in these anisotropic systems. This investigation uses principally the muon spin rotation (μSR) technique, but also makes use of the techniques of small angle neutron scattering (SANS) and torque magnetometry.

The remainder of this chapter deals with the basic fundamentals of the theories of superconductivity. A more comprehensive treatment may be found in *Tilley & Tilley (1990)*[11] or *Waldram (1996)* [12].

1.2 London Theory

In 1935 *F and H.London* [3] proposed that electrons in the superconducting state were described by a macroscopic quantum mechanical wavefunction. This was analogous to the resistanceless currents in atomic orbits and had the form

$$\Psi(r,t) = \Psi_o exp(iS(r,t)) \tag{1.1}$$

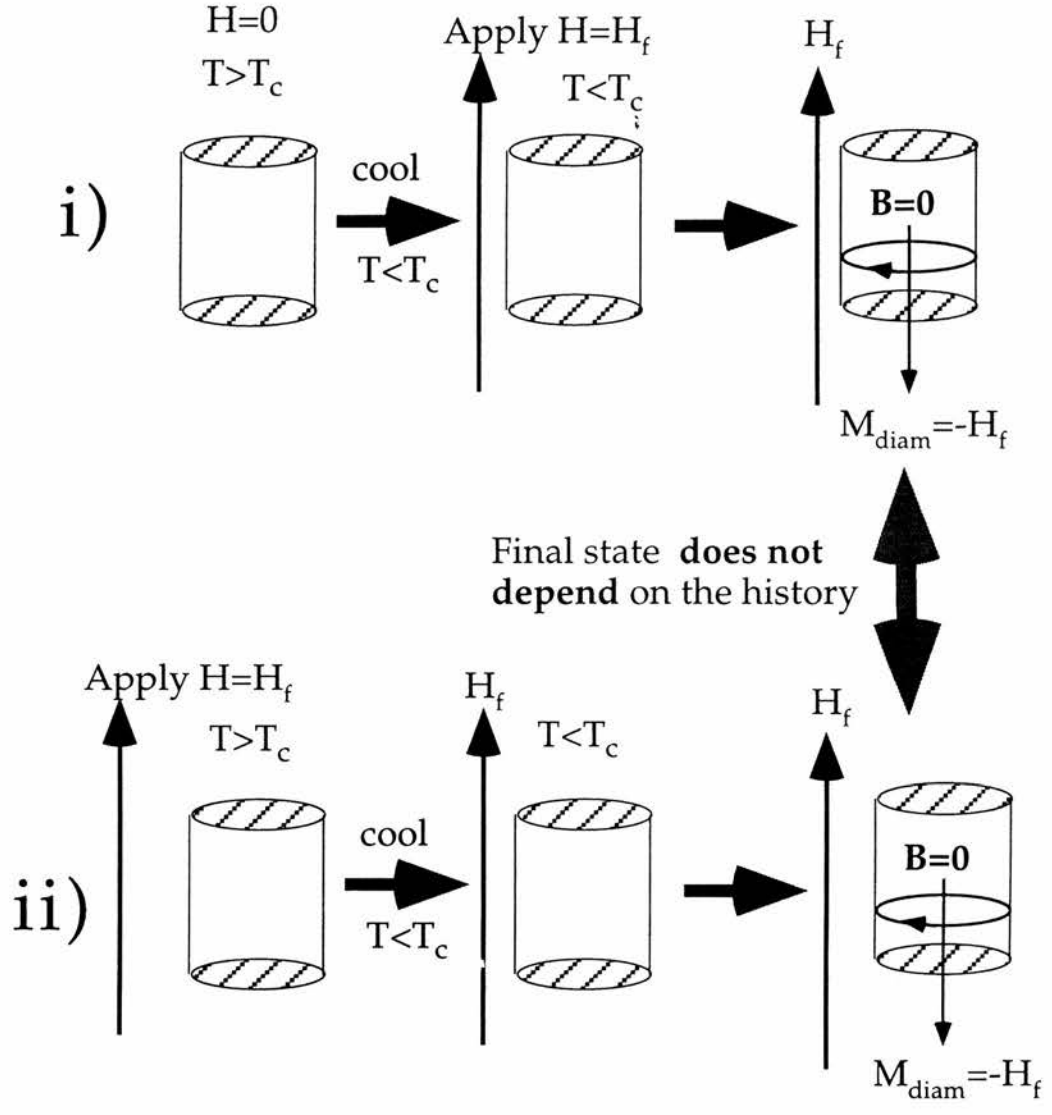

Figure 1.1: If a superconductor was just a perfect conductor one would obtain a different state when one cools to $T<T_c$ if the field is applied above or below T_c. For the case of a superconductor one obtains the same *state* regardless of how the final conditions of temperature and field are reached. i) and ii) depict the possible paths to the superconducting state, indicating that superconductivity is indeed a true thermodynamic phase.

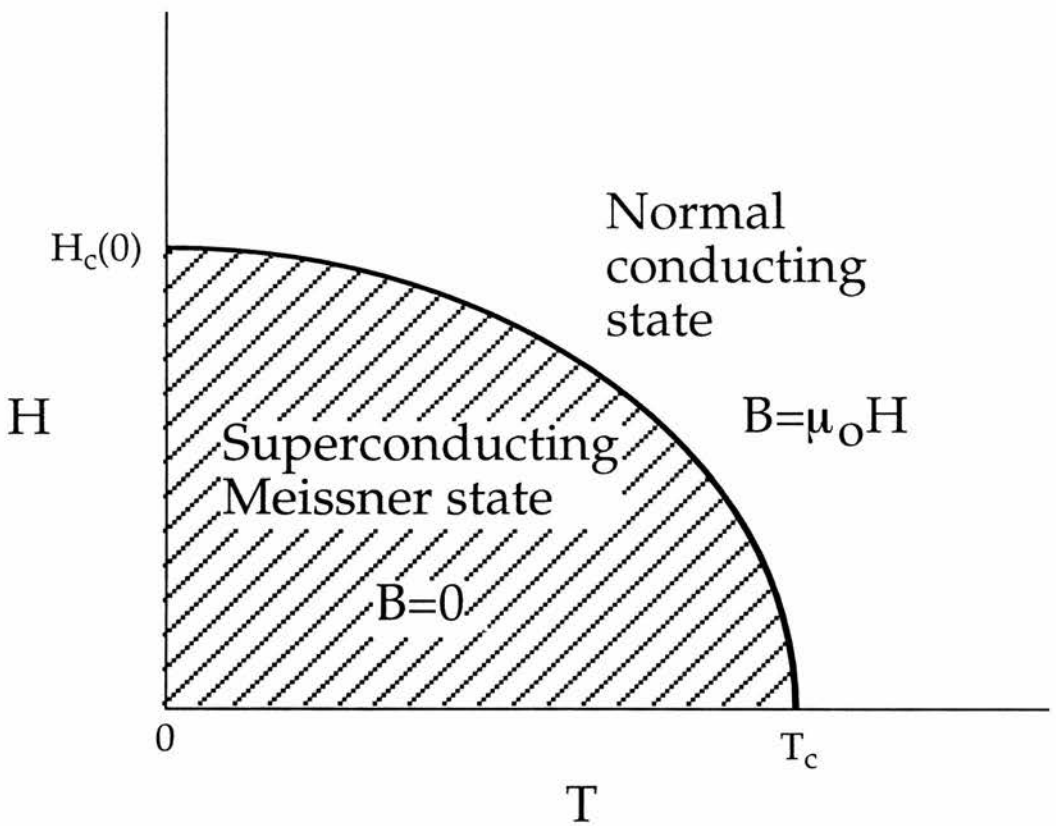

Figure 1.2: The magnetic phase diagram of a type I superconductor.

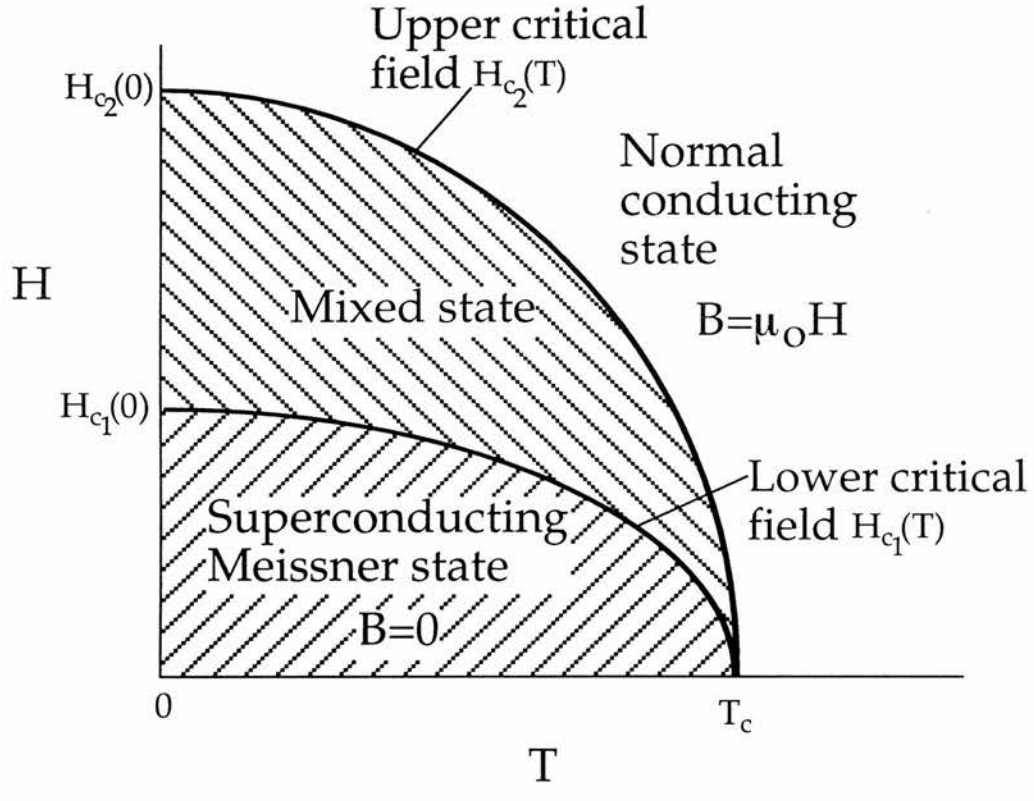

Figure 1.3: The magnetic phase diagram of a type II superconductor. The region of the phase diagram in which the fluxons begin to enter the bulk is called the mixed state.

where S is the phase of the wavefunction and $|\Psi_o|^2$ is the number density of superconducting carriers. Using the probability current density from Schrödingers equation and the quantum mechanical form of the ∇ operator (cf Eq. 1.2) to allow for the influence of a magnetic field

$$\nabla \rightarrow \nabla \pm \frac{iqA}{\hbar} \tag{1.2}$$

with the + sign acting on Ψ^* and the - sign acting on the Ψ, yields the most general form of the London equation

$$\mathbf{J}_e = \frac{e\hbar|\Psi_o|^2\nabla S}{m_s} - \frac{2e^2|\Psi_o|^2\mathbf{A}}{m_s} \tag{1.3}$$

where the first term describes the current due to changes in phase and the second is that due to the vector potential. In this equation the electron mass has been replaced by m_s=2m_e and the charge q by 2e to account for the paired electrons. Setting $|\Psi_o|^2 = n_s$ and taking the curl of both sides of Eq. 1.3 yields

$$\nabla \times \mathbf{J}_e = \frac{-e_s^2}{m_s} n_s \mathbf{B}. \tag{1.4}$$

Combining this with Maxwell's equations $\nabla \times \mathbf{B} = \mu_o \mathbf{J}$ and $\nabla.B$=0 yields what is known as the *second* London equation

$$\nabla^2 \mathbf{B} = \frac{\mathbf{B}}{\lambda_L^2} \tag{1.5}$$

where $\lambda_L = \sqrt{\frac{m_s}{\mu_o e_s^2 n_s}}$ is called the London penetration depth, m_s, the mass ,e_s, the charge and n_s, the density of superconducting carriers. Equation 1.5 has a physical solution $\mathbf{B} = B_o exp(-x/\lambda)$. This equation describes the Meissner effect, implying that the magnetic field is excluded from the bulk but manages to penetrate a distance λ into the bulk of the superconductor from the surface (see Fig. 1.4).

The *first* London equation is given by

$$\frac{\partial \mathbf{J}_e}{\partial t} = \frac{1}{\mu_o \lambda_L^2} \mathbf{E} \tag{1.6}$$

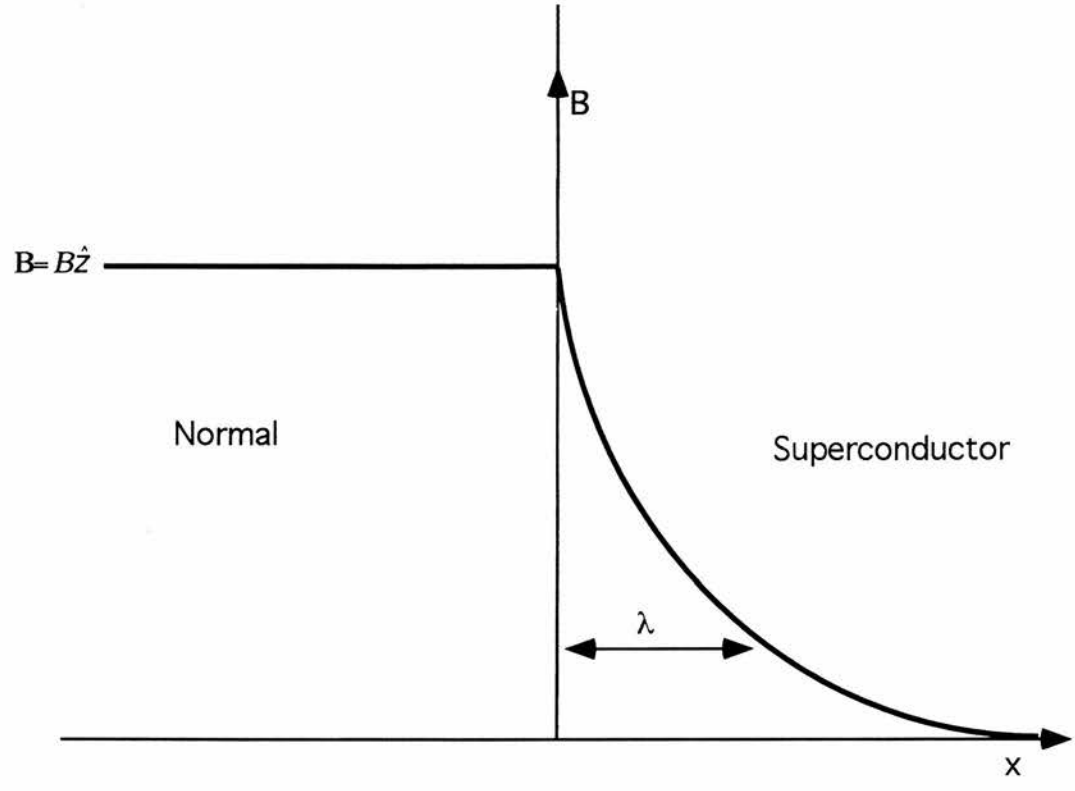

Figure 1.4: The penetration of a magnetic field into the bulk of the superconductor in the Meissner state in one dimension. Supercurrents flow and shield the field from the bulk. The field is not immediately excluded at the surface however, and penetrates some distance, governed by the penetration depth, λ, into the bulk of the superconductor.

This equation does not predict superconductivity itself, but is useful in describing the acceleration of superelectrons in the presence of an electric field, such as a short pulse of electric field. This would result in a supercurrent which would not decay, precisely one of the properties of superconductivity.

1.3 The Two-Fluid model

The two-fluid model was the first successful *description* of superconductors, specifically proposed in order to explain experimental results in the superfluid ^4He by *Gorter and Casimir (1934)* [13]. According to this model a superconductor behaves as if it contains *normal electrons* (e_n) and *superelectrons* (e_s). Both e_n and e_s can carry current, the latter without resistance and the former with resistance. The superfluid of e_s are perfectly ordered, have no entropy and can carry no heat, while the e_n can carry heat. As one passes below the critical temperature, T_c, the density of superfluid rises from zero (cf Eq. 1.7), while the density of e_n decreases.

$$n_s(T) = n_s(0)\frac{1}{\sqrt{1-(T/T_c)^4}} \tag{1.7}$$

Combining Eq. 1.7 with results of the London model, the temperature dependence of the penetration depth may be obtained,

$$\lambda(T) = \lambda(0)\frac{1}{\sqrt{1-(T/T_c)^4}} \tag{1.8}$$

This kind of temperature dependence has been observed in low T_c superconductors such as lead by *Gasparovic (1970)* [14]. It is also interesting to note that Eq. 1.8 can be recovered from G-L theory (see section 1.5).

1.4 BCS Theory

The first theory offering a complete microscopic desciption of superconductivity was provided by *Bardeen, Cooper and Schrieffer (1957)* [6] (BCS theory). This theory proposed that electrons in the superconducting state pair up and behave much like bosons. These are called *Cooper pairs* following from *Cooper's(1956)* [15] demonstration that even a weak interaction can bind pairs of electrons. This weak interaction was proposed by *Fröhlich (1950)* [16] as being mediated by vibrations of the positive ions of the metal lattice . Fröhlich's suggestion was afforded firmer footing when the T_c of mercury was observed to depend upon the particular isotope of the metal involved. This is the so called isotope effect (cf Eq. 1.9) . Mercury follows Eq. 1.9 setting a to the order of 0.5.

$$T_c \propto M^{-a} \tag{1.9}$$

It is not the authors desire to provide a comprehensive discussion of BCS theory, but it is worthwhile to exemplify a few key points here. In its simplest form the seed of BCS theory is realised upon visualisation of the journey of an electron through a charged lattice. This electron will leave a positive history in the form of phonons. A second electron sees this positive 'wave' and is consequently bound to the first (see Fig. 1.5). Such a phonon mediated interaction occurs between electrons within $\hbar\omega_{Debye}$ of the Fermi surface and is most effective between electrons of opposite momenta and spin. BCS theory proposes that Cooper pairs have less energy than normal electrons, with a temperature dependent energy gap Δ vanishing at the transition temperature. This energy gap is related to T_c according to the simple relation

$$\Delta(0) = 1.76 k_B T_c. \tag{1.10}$$

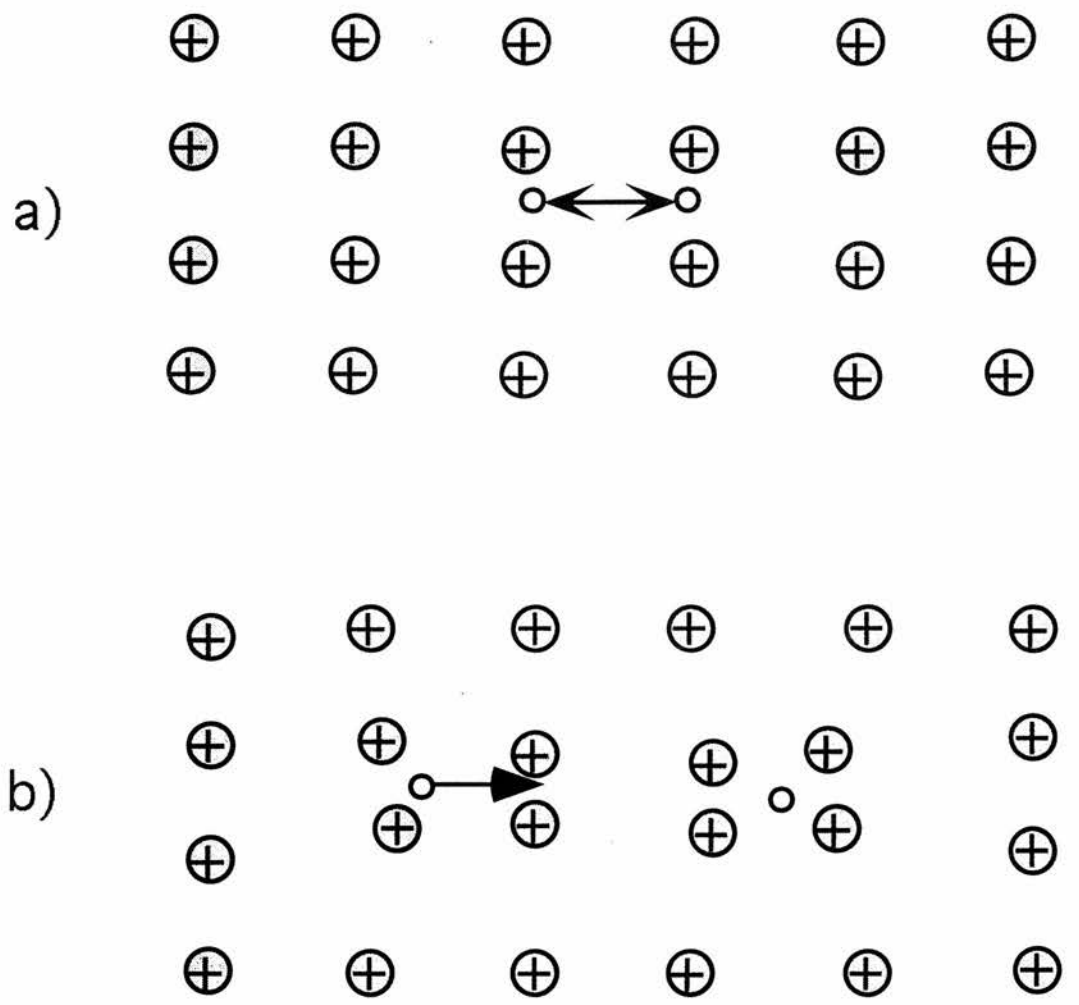

Figure 1.5: A schematic of the Cooper pair. a) In the simple picture two electrons will always repel one another due to the mutual electrostatic repulsion. b) In Fröhlich's scheme the first electron distorts the lattice by attracting the ions and this acts to 'shield' the following electron from the simple electrostatic repulsion between the electrons.

Figure 1.6 [17] shows this variation of this energy gap with temperature for various elements. The agreement with BCS theory is excellent. The density of states within Δ either side of the Fermi energy is zero with an increased density at the edges of the gap described by

$$N_s(E) = N(0)\left(\frac{E}{E^2 - \Delta^2}\right)^{\frac{1}{2}} \tag{1.11}$$

with the added provision that $k_B T_c \ll \hbar\omega_{Debye}$. One limit that is imposed on superconductivity by BCS theory is that too strong a phonon interaction results in an unstable crystal lattice. This limits the transition temperature predicted by BCS to approximately 30 K, well below those seen in the high temperature superconductors. Strong-coupled BCS (as opposed to the weak coupling in conventional BCS) has been considered [18] but is limited by the fact that if the electron-phonon coupling is strong then the quasi-particles have a finite lifetime. Evidence for this electron-phonon-electron coupling regime has been demonstrated by *C.E.Gough et al* (1987)[19] in high temperature superconductor $YBa_2Cu_3O_{7-\delta}$ (YBCO) where it was shown that electrons are paired. The *Cooper pairs* that have been discussed in the BCS theory have opposite spin, but no angular momentum. These electrons are in a symmetric s-state. High temperature superconductors (HTSC) , such as YBCO and $Bi_{2.15}Sr_{1.85}Ca_1Cu_2O_{8+\delta}$ (BSCCO), as well as breaking through predictions made by BCS theory (see section 2.1) have been speculated to exist with superconducting electrons in the d-state. This would result in an anisotropic energy gap, zero in certain symmetry directions. These nodes in the energy gap allow excitations at low temperatures, resulting in an increase in the penetration depth and deviations from the two fluid model (cf Eq. 1.8) if applicable. A number of phenomena produce a similar effect and as a consequence this is extremely difficult to verify experimentally.

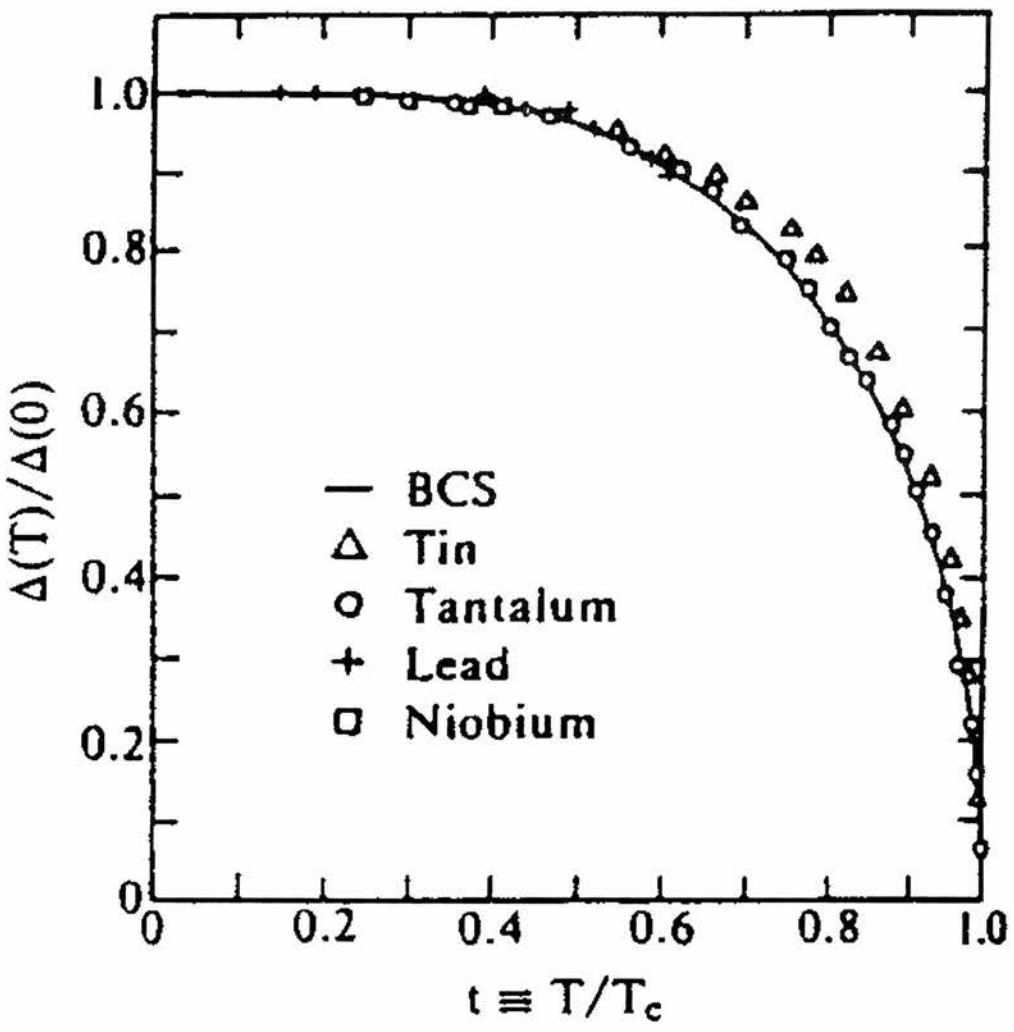

Figure 1.6: Reduced energy gap as a function of reduced temperature. The line is the BCS prediction and the points are experimental values (From *Townsend and Sutton (1962)*). Δ_o is the value of the energy gap at T=0.

1.5 Ginzburg-Landau Theory

In 1950, seven years before BCS theory, *V.L.Ginzburg and L.D.Landau* published in Russian [4] a description of the superconducting state. This theory was *phenomenological* in that it was based on generally observed features of superconductivity. G-L theory was built on an earlier theory of *Landau's* [5] which was based on a theory of phase transitions and described the free energy of a superconductor in the uniform state. G-L theory allowed for the fact that the density of superconducting carriers can vary from point to point in the superconductor. Following from the success of the London equations which seemed to show that the behaviour of the superconductor was governed by an effective wavefunction they identified the superconducting electron density as being related to a *complex order parameter* via

$$n = |\Psi(r)|^2 \tag{1.12}$$

Following Landau's approach, a second order phase transition can be characterised by such an order parameter and the free energy can be written as a function of this parameter provided that Ψ is small and varies slowly in space. G-L theory is therefore applicable close to T_c where Ψ is small, but not so close to the transition temperate that fluctuations become important. To allow for the possibility that the free energy may depend upon the spatial derivatives of Ψ as well as Ψ itself the resultant power series describing the free energy density is therefore

$$f_s = f_n + \alpha|\Psi(r)|^2 + \frac{1}{2}\beta|\Psi(r)|^4 + \frac{\hbar^2}{2m}|\nabla\Psi(r)|^2 \tag{1.13}$$

where f_n is the Helmholtz free energy density in the normal state. The fourth term in this equation is a 'kinetic-energy' contribution as a consequence of Ψ being a function of position. The coefficient of the gradient term, following the

usual convention of G-L theory, is $\hbar^2/2m$, where m is the mass of the electron. Further to this equation it is necessary to include explicitly the coupling of the supercurrent to the magnetic field and the magnetic energy. This results in a free energy density of the form

$$f_s = f_n + \alpha|\Psi(r)|^2 + \frac{1}{2}\beta|\Psi(r)|^4 + \frac{1}{2m}|(-i\hbar\nabla - 2e\mathbf{A})\Psi|^2. \qquad (1.14)$$

In a uniform external magnetic field, **H**, the Gibbs free energy function, G_s is given by

$$G_s = \int (f_s - \mathbf{H}.\mathbf{M})d^3r. \qquad (1.15)$$

The G_s must be stationary with respect to variations in the order parameter and the vector potential **A**. Minimising G_s with respect to a small variation in Ψ^* gives

$$\alpha\Psi + \beta|\Psi|^2\Psi + \frac{|(-i\hbar\nabla - 2eA)|^2}{2m}\Psi = 0. \qquad (1.16)$$

This is the *first* G-L differential equation and describes the behaviour of Ψ, given the vector potential **A** and an appropriate set of boundary conditions. The G-L coefficients can be obtained by examining the free energy in the absence of external fields or field gradients. Examining Eq. 1.14 gives

$$f_s - f_n = \alpha|\Psi|^2 + \frac{1}{2}\beta|\Psi|^4. \qquad (1.17)$$

This is the condensation energy of the superconducting state. By inspection it can be seen that as $|\Psi|^2$ tends to zero the condensation energy also tends to zero as expected as T_c is approached. In order to obtain a minimum in the condensation energy β must be positive, with α being positive or negative. If α is positive then a minimum occurs at $|\Psi|^2$=0 corresponding to T>T_c. If however, α is negative a minima occurs for non-zero $|\Psi|^2$ and this corresponds to T<T_c. From Landau

theory the order parameter is related to the G-L coefficients according to

$$|\Psi|^2 = |\Psi|^2_\infty = \frac{-\alpha}{\beta} \tag{1.18}$$

where the temperature dependence of α and β remain that of Landau theory (cf Eq. 1.19)

$$\begin{aligned} \alpha &= constant_1(T - T_c) \ \ and \\ \beta &= constant_2 \end{aligned} \tag{1.19}$$

and Ψ_∞ is the value of the wavefunction well within the bulk of the superconductor. It is clearly seen from Eq. 1.18 that if α is positive the superconducting density is rendered negative, and therefore meaningless.

The *second* G-L equation is given by minimising with respect to **A**, which eventually gives

$$\mathbf{J}_e = -\frac{ie\hbar}{m}(\Psi^*\nabla\Psi - \Psi\nabla\Psi^*) - \frac{4e^2}{m}\Psi^*\Psi\mathbf{A} \tag{1.20}$$

It is instructive to view some of the fundamental results which are born out of the G-L equations. If the Meissner state is considered for a bulk type I superconductor and the dimensions of the specimen is large in comparison to the penetration depth, then **B**=0 inside the specimen. As $\nabla\Psi$=0 the second G-L equation reduces to

$$\mathbf{J}_e = -\frac{4e^2}{m}\frac{|\alpha|}{\beta}\mathbf{A}. \tag{1.21}$$

Similarly to London theory this yields a penetration depth of

$$\lambda = \left(\frac{m\beta}{4e^2\mu_o|\alpha|}\right)^{1/2} \tag{1.22}$$

which leads , incorporating Eq. 1.19, to an explicit form of the temperature dependence of λ:

$$\lambda \propto (1-t)^{-1/2} \tag{1.23}$$

where t=$\frac{T}{T_c}$ is the reduced temperature. Expanding the two-fluid model

$$(1-t^4)^{-1/2} = (1+t^2)^{-1/2}(1+t)^{-1/2}(1-t)^{-1/2} \tag{1.24}$$

it can be seen that near to T_c where Landau theory holds and t$\sim$1 the first two terms in Eq. 1.24 vary slowly so that the dependence on t is dominated by the singularity given by the last term.

In the absence of fields (**A**=0) with the wavefunction normalised, such that P$\equiv \Psi/\Psi_\infty$, the first G-L equation (cf Eq. 1.16) can be written in one dimension as

$$\frac{\hbar^2}{2m|\alpha|}\frac{d^2P}{dx^2} + P - P^3 = 0 \tag{1.25}$$

where a characteristic length ξ(T) can be defined below T_c as

$$\xi^2 = \frac{\hbar^2}{2m_e|\alpha|}. \tag{1.26}$$

ξ(T) is a characteristic distance over which spatial changes in Ψ occur and this is demonstrated by setting P=1+p (p <<1) and investigating the behaviour of Eq. 1.25. To first order in p

$$\begin{aligned} \xi^2\frac{d^2p}{dx^2} + (1+p) - (1+3p+....) &= 0 \\ \xi^2\frac{d^2p}{dx^2} &= 2p \\ \frac{d^2p}{dx^2} &= (2/\xi^2)p \\ p(x) &\sim exp\left[\frac{\sqrt{2}x}{\xi(T)}\right] \end{aligned} \tag{1.27}$$

A small disturbance in Ψ will therefore decay to Ψ_∞ with a characteristic length ξ(T). At this stage it is possible to define an important quantity:

$$\kappa = \frac{\lambda(T)}{\xi(T)} = \sqrt{\frac{m^2\beta}{2\mu_o\hbar^2e^2}}. \tag{1.28}$$

It is evident from this that κ is temperature independent in G-L theory as it only depends upon the G-L coefficient β. In G-L theory the value of κ for a compound defines the nature of superconductivity in this compound. For $\kappa < 1/\sqrt{2}$ the compound is a type I superconductor and for $\kappa > 1/\sqrt{2}$ it is a type II superconductor. Type II superconductivity was discovered in a remarkably significant piece of work by *Abrikosov(1957)* [20]. Abrikosov, a student of Landau, solved the G-L equations for $\kappa \gg 1$. From his solution, which indicated a periodic order parameter, he deduced that this indicated the presence of a regular array of flux tubes each carrying a quantum of flux, $\Phi_o = h/2e$. He initially predicted a square lattice , but after a numerical error was corrected, a stable triangular lattice, with lower free energy was predicted. *Abrikosov's* work highlighted the distinction between type-I and type-II superconductivity. This distinction hinges on the sign of the surface energy of the normal/superconducting interface which was first pointed out by *Pippard (1951)* [21] to depend upon the relative magnitudes of λ and ξ. For $\lambda >> \xi$ the magnetic field will penetrate some distance into the superconducting region where Ψ will not be greatly depressed (see Fig. 1.7). The reduction in the field self energy due to the penetration will therefore be much larger than the increase in the internal free energy associated with a decrease in Ψ, so a negative boundary energy should be expected. To minimise the free energy this unstable system will attempt to maximise the boundary, in this case by the introduction of normal domains in the form of flux-lines each carrying a quanta of flux and stabilised by supercurrents. For $\xi >> \lambda$, the opposite is true and the increase in free energy associated with a reduction in Ψ will greatly outweigh the small reduction in field self energy associated with a shorter λ (see Fig. 1.8).

Using the G-L equation it is possible to derive an expression for H_{c2}, the upper

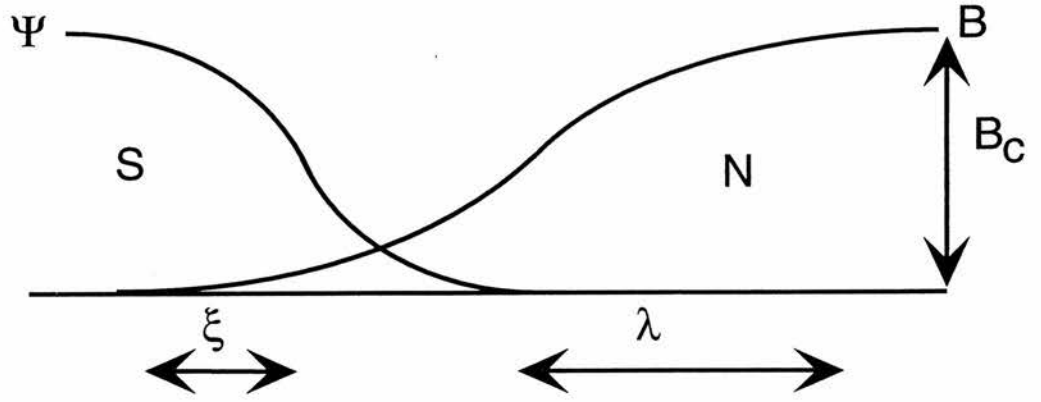

Figure 1.7: A cross-section through a NS boundary for a type II superconductor ($\kappa > 1/\sqrt{2}$).

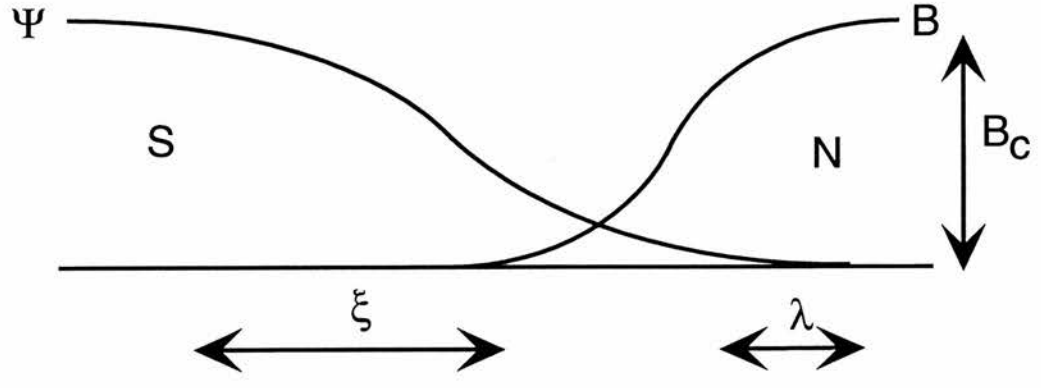

Figure 1.8: A cross-section through a NS boundary for a type I superconductor ($\kappa < 1/\sqrt{2}$).

critical field

$$H_{c2} = \frac{\Phi_o}{2\pi\mu_o\xi^2} \tag{1.29}$$

where the normal cores of the fluxons effectively overlap and drive the sample normal. From G-L theory it can also be shown that the lower critical field is given by

$$\mu_o H_{c1} = \frac{\Phi_o}{4\pi\lambda^2}(ln(\kappa) + \eta) \tag{1.30}$$

where η is a constant of order 0.5.

1.6 Flux Quantisation

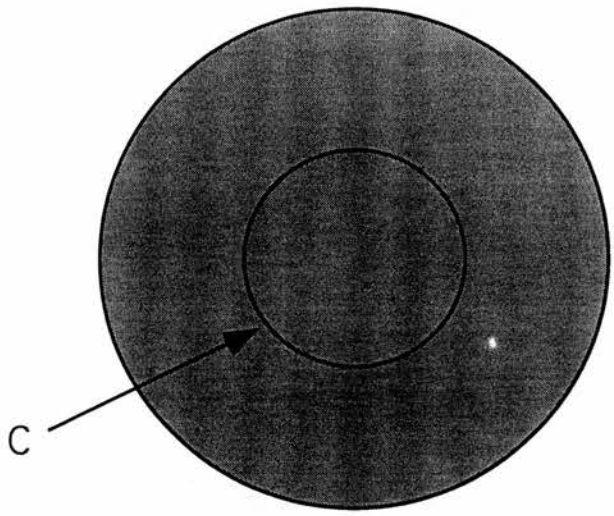

Figure 1.9: A simply connected bulk superconductor.

The quantisation of penetrative flux in type II superconductors is a consequence of the quantum mechanical nature of superconductivity. If a simply connected superconductor is considered (see Fig. 1.9), then integrating round path C is single valued giving

$$\Delta S = \oint_C \nabla S.dl = 0. \tag{1.31}$$

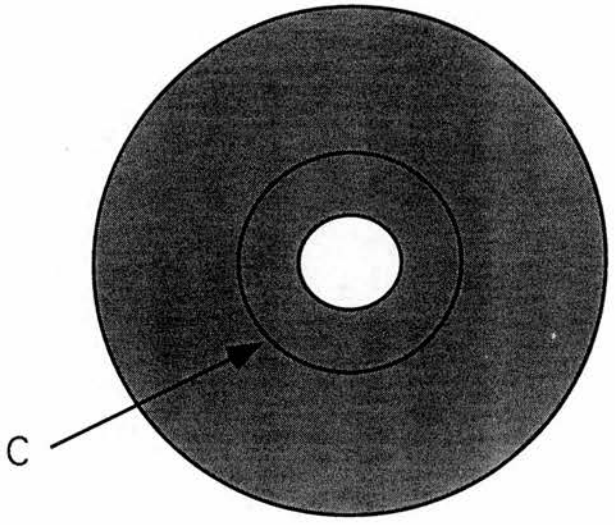

Figure 1.10: A multiply connected superconductor.

If a superconductor with a hole in is now considered (see Fig. 1.10), such as a superconducting ring, then the superconductor is multiply connected and integrating round a path C in the bulk of the superconductor where $\mathbf{J}_e$ is zero, then applying Eq. 1.3 gives

$$\hbar \oint_C \nabla S.dl = 2e \oint_C A dl. \tag{1.32}$$

Using Stokes' theorem viz.

$$\oint_C A.dl = \oint_\sigma (\nabla \times A).d\sigma = \oint_\sigma B.d\sigma = \Phi \tag{1.33}$$

gives

$$\oint_C \nabla S.dl = \frac{2e\Phi}{\hbar}. \tag{1.34}$$

As a consequence of the wavefunction being single valued, going round the path C once must result in the phase of the wavefunction changing by integer multiples of 2π viz.

$$\Delta S = \oint_C \nabla S.dl = 2\pi n \tag{1.35}$$

Combining Eqs. 1.34 and 1.35 leads to the remarkable result that the flux in the ring is quantized,

$$\Phi = n\frac{h}{2e} \tag{1.36}$$

where the flux quantum Φ_o=2.068$\times 10^{-15}$ Weber.

1.7 Shape effects and Demagnetisation factors

Consider a type I superconductor in the Meissner state. Due to the finite extent of the superconductor perpendicular to the field, the lines of **H** are bunched together. This results in an effective field at the surface which is higher than the actual applied field. This effect is most pronounced for samples with their longest dimension perpendicular to the applied field (see Fig 1.11) and is quantified by N, known as the demagnetisation factor. N is the factor by which the maximum field at the surface is larger than the applied field (cf Eq. 1.37).

$$H_{effective} = \frac{H_{applied}}{1-N} \tag{1.37}$$

Thus the demagnetisation factor for a long thin sample aligned with the applied field is very close to zero, for a plate-like sample perpendicular to the applied field N is close to one (see Fig 1.11) and for a sample shaped like a sphere it has been analytically derived to be 1/3.

With a finite N, the magnetisation as a function of applied field has a gradient greater than one as the Meissner currents respond to the effective field (see Fg. 1.12). When the surface field reaches the critical field H_c the sample will enter what is known as the *intermediate state* when flux enters the sample resulting in interweaved regions of normal and superconducting material.

The same principle applies to type II superconductors where flux-lines may begin to enter the sample when the surface field reaches the lower critical field H_{c1}.

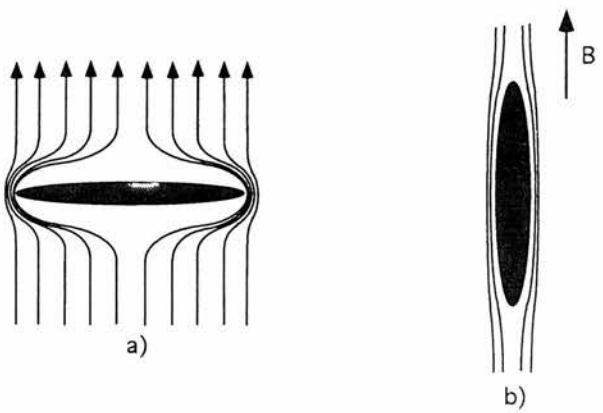

Figure 1.11: The effect of the demagnetisation factor on a type I superconductor. The extreme cases for a plate-like sample are shown. a) The effective surface field is many times that of the applied field and N$\sim$1. b) Here there is negligible field distortion and N$\sim$0.

1.8 Ginzburg-Landau theory applied to layered systems: The Lawrence-Doniach model

In the *Lawrence-Doniach* model [22] layered superconductors, such as the HTSC, are modeled as a stack of two-dimensional superconductors coupled together by Josephson tunneling between adjacent layers. As with G-L theory the free energy is defined in terms of a free energy expression for the stack of layers. Generalizing

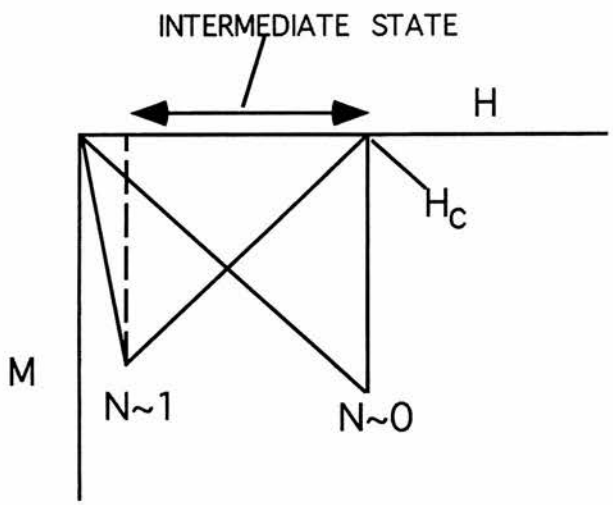

Figure 1.12: A schematic of the magnetisation of a type I superconductor as a function of the applied field. For a sample of finite N the effective field at the surface will reach H_c well below an applied field of H_c. At this point, flux enters the sample in the form of interweaved regions of normal and superconducting material known as the intermediate state.

Eq. 1.13 gives

$$F = \int f d^2r = \sum \int \alpha|\psi_n|^2 + \frac{1}{2}\beta|\psi_n|^4 + \frac{\hbar^2}{2m_{ab}}\left(\left|\frac{\delta\psi_n}{\delta x}\right|^2 + \left|\frac{\delta\psi_n}{\delta y}\right|^2\right) + \frac{\hbar^2}{2m_c s^2}|\psi_n - \psi_{n-1}|^2 \tag{1.38}$$

where the crystallographic axes a and b define the layers and the c axis is normal to them. The z direction is along c and the x and y coordinates are in the planes. s is the interplanar distance, the sum runs over the layers and the integral is over the area of each layer. Different effective masses m_{ab} and m_c have also been introduced to reflect the different modes of charge transport in the two principal directions. The z derivative has also been replaced by a finite difference form that is appropriate to a discrete system. If ψ_n is written $\psi_n = |\psi_n| e^{i\phi_n}$ and assuming that all $|\psi_n|$ are equal, then the last term in Eq. 1.38 becomes

$$\left(\frac{\hbar^2}{m_c s^2}\right)|\psi_n|^2[1 - cos(\phi_n - \phi_{n-1})]. \tag{1.39}$$

This term is $\propto \frac{1}{m_c}$ making clear the equivalence of this term to a Josephson coupling energy between layers. Minimising Eq. 1.38 with respect to a small variation in ψ_n^* gives the L-D model for ψ_n

$$\alpha\psi_n + \beta|\psi_n|^2\psi_n - \frac{\hbar}{2m_{ab}}\left(\frac{\delta}{\delta x^2} + \frac{\delta}{\delta y^2}\right)\psi_n - \frac{\hbar^2}{2m_c s^2}(\psi_{n+1} - 2\psi_n + \psi_{n-1}) = 0 \tag{1.40}$$

where the last term in this equation is the discrete form of the second derivative. Inserting the vector potential term, Eq. 1.40 can be generalised to the full form of the LD equation,

$$\begin{aligned} \alpha\psi_n + \beta|\psi_n|^2\psi_n - \frac{\hbar}{2m_{ab}}\left(\nabla - i\frac{2e}{\hbar}\mathbf{A}\right)^2\psi_n \quad & - \\ \frac{\hbar^2}{2m_c s^2}(\psi_{n+1}e^{2ieA_z s/\hbar} - 2\psi_n - \psi_{n-1}e^{2ieA_z s/\hbar}) \quad & = \quad 0 \end{aligned} \tag{1.41}$$

where the m_{ab} term, ∇ and $\mathbf{A}$ are two-dimensional vectors in the xy plane. From the structure of Eq. 1.38 it is clear that the free energy reduces to a G-L form with

ellipsoidal anisotropy in the long-wavelength limit with variations along z being smooth enough so that $(\psi_n - \psi_{n+1})/s$ can be replaced by $\delta\psi/\delta z$. In this limit Eq. 1.41 reduces to

$$\alpha\psi + \beta|\psi|^2\psi - \frac{\hbar^2}{2}\left(\nabla - i\frac{2e}{\hbar}\mathbf{A}\right).\left(\frac{1}{m}\right).\left(\nabla - i\frac{2e}{\hbar}\mathbf{A}\right)\psi = 0 \qquad (1.42)$$

where ∇ and $\mathbf{A}$ are now 3-D quantities, and (1/m) is the reciprocal mass tensor with principal values $1/m_{ab}$, $1/m_{ab}$ and $1/m_c$. This mass anisotropy causes the coherence length to be anisotropic. In a similar way to Eq. 1.26, in the anisotropic case the coherence length is given by

$$\xi_i^2 = \frac{\hbar^2}{2m_i|\alpha(T)|} \qquad (1.43)$$

where the subscript i identifies a particular principal axis. As before, sufficiently close to T_c as α is isotropic and proportional to $(T\text{-}T_c)$, ψ will vary sufficiently slowly to justify this continuum G-L approximation.

1.9 Type II superconductors and the Irreversibility Line(IL)

As has been noted, HTSC are all extreme type II materials. As a consequence of this they exhibit a very low value of H_{c1} and a very high value of H_{c2} and over much of the phase diagram are in the mixed state. Upon application of an external current to a superconductor in the mixed state, the flux-lines feel a Lorentz force per unit length given by

$$\mathbf{F}_L = \mathbf{J} \times \Phi_o \qquad (1.44)$$

where $\mathbf{J}$ is the transport current and Φ_o is the flux quantum. Unless the flux-lines are held in place they will move under the action of this force. Such movement

causes the dissipation of energy in the system, which appears as resistance in the sample. The sample will therefore be unable to sustain supercurrent even though it is below the transition temperature. The onset of resistivity, and the reversible magnetic behaviour associated with the free movement of flux-lines, is known as the irreversibility line (IL). Above the IL, upon application of **J** the superconductor will be unable to sustain a supercurrent, rendering it useless for technical applications. Generally, HTSC exhibit an IL which is well below the superconducting transition. In order to increase the IL in HTSC the flux-lines must be strongly pinned. Intrinsic defects in HTSC, such as grain boundaries, twin boundaries, exhibited in YBCO (see section 2.1) and inclusions of normal material act as pinning centres. In the superconducting state the *order parameter* is suppressed at these sites making it energetically favourable for the normal core of flux-lines in the mixed state to sit at these sites. The effect of a pinning site depends upon the field, temperature and applied current (see chapter 7).

Chapter 2

Novel Superconductors

2.1 High Temperature Superconductivity

The area of superconductivity was revitalised after the discovery by *Bednorz and Muller* in 1986[7] of a compound $La_{2-x}Ba_xCuO_{4-y}$, reported to have a transition temperature, T_c, of 30 K. This discovery, after the slow increase in reported $T_c's$ of the previous decades was surprising and exciting, not only in itself, but in the unsuspected class of superconductors which these oxides presented (this broke through BCS theory's upper limit and prompted ideas of strongly coupled BCS). Rapid progress was made with groups in the United States, Japan and China claiming to have synthesised materials with transition temperatures in the region of 90 K. This material was $YBa_2Cu_3O_{7-\delta}$ (YBCO) ($T_c \approx$92 K) which was attributed to *Wu et al (1987)* [8]. (The yttrium in this structure can be replaced with other rare earths to form compounds with similarly high T_c). Further work lead to the discovery of the bismuth based, $Bi_{2.15}Sr_{1.85}Ca_1Cu_2O_{8+\delta}$ (BSCCO), and the thallium based, $Tl_2Ba_2Ca_{\delta-1}Cu_\delta O_{3+2\delta}$ (TBCCO), HTSC with the highest transition temperature to date discovered by *Schilling et al (1993)* [9] in the

mercury based compound $HgBa_2Ca_2Cu_3O_{8+\delta}$ (T_c >150 K under high pressure). A common structural component of HTSC is the copper oxide layers and these are thought to dominate the phenomenon. Putting the HTSC under structural scrutiny (see Figs. 2.1 and 2.3) it can be seen that the copper oxide layers are separated by layers of metal oxide which act as a charge reservoirs, removing electrons from the copper oxide planes (Neodymium based HTSC, e.g. $Nd_{2-\delta}Ce_\delta CuO_4$, are electron doped). The holes that are left are the charge carriers for superconductivity. The metal oxide can be separated by more than one copper oxide layer and in general the highest transition temperatures are afforded when stochiometry allows 2 or 3 copper oxide planes within the crystallographic unit cell. Further increase in the number of these layers results in a decrease from the optimal T_c, indicating qualitatively at least that the optimal T_c may depend upon an optimal plane separation for the CuO_2 layers or may be restricted by the difficulty in doping many layers. Figure 2.1 [23] shows the structure of YBCO. YBCO is formed by heating the tetragonal structured non-superconducting compound $YBa_2Cu_3O_6$ to 973 K in an oxygen rich atmosphere. Under these conditions it undergoes a phase transition to the orthorhombic structure which is superconducting when $0.03 > \delta > 0.5$. The unit cell is composed of two buckled CuO_2 planes, separated by Y atoms and CuO chains (cf Fig. 2.1). During the fabrication process twin-planes are formed as a result of internal stresses experienced when the crystal undergoes the transition from a tetragonal to an orthorhombic structure. Twin-planes occur where the a-b axes of neighbouring unit cells do not match up. This is shown in Fig. 2.2. The crystals can be detwinned by applying a uniaxial pressure of ~50 MPa along the a-b axes at 823 K in air for 20 minutes [24]. The crystals will subsequently need to be re-annealed in flowing O_2 at 773 K.

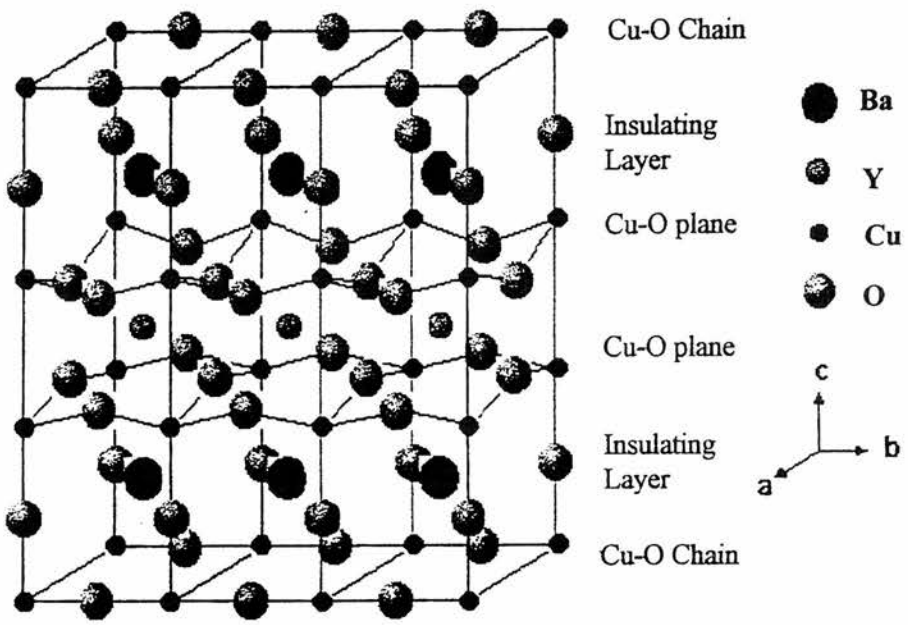

Figure 2.1: Diagram of the structure of YBCO showing 3 unit cells. The copper oxide planes in this structure are shown in the centre of the diagram. These planes are separated by a layer of yttrium atoms and are separated from the next set by an insulating *Ba-O* layer. *Cu-O* chains are shown at the top and bottom of the diagram. (Taken from *McDevitt et al (1997)* [23]).

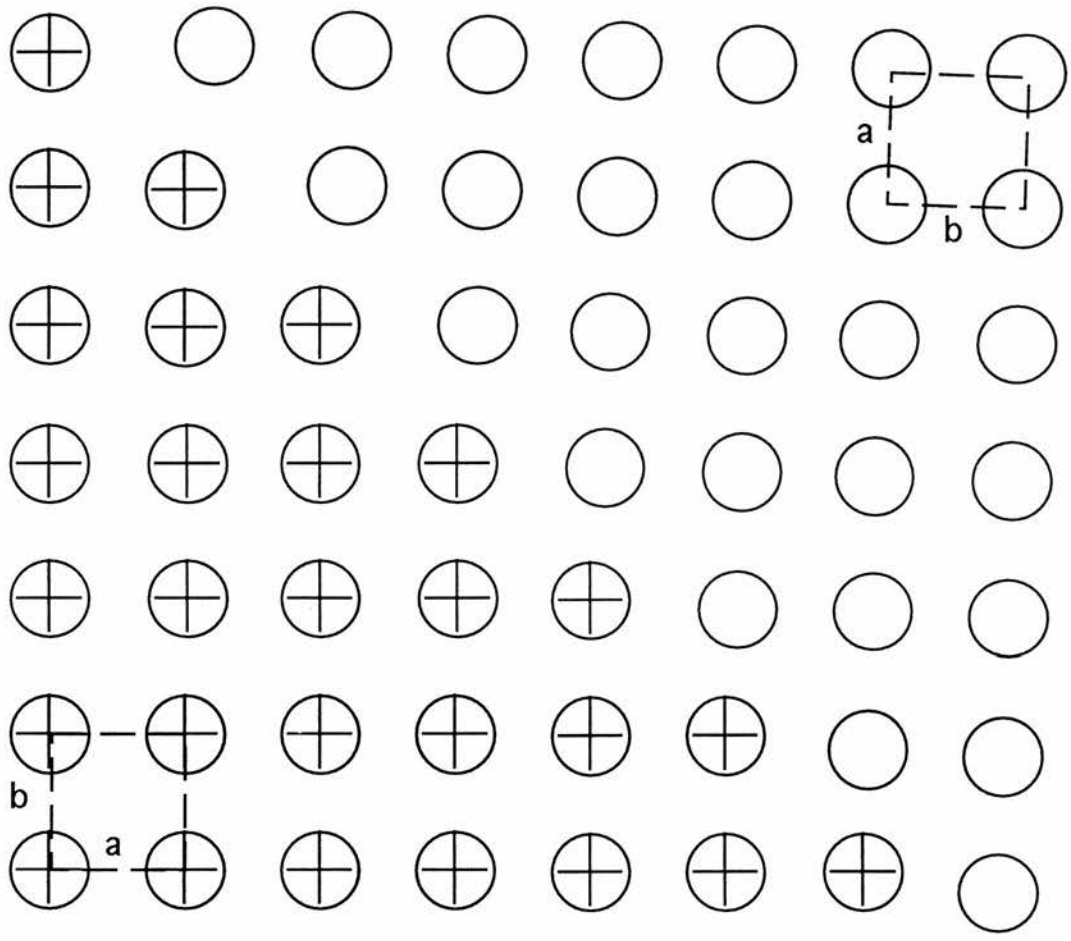

Figure 2.2: A diagrammatic representation of a twin-plane defect. The circles correspond to the Cu sites at the base of each unit cell, with the different types of circle representing the orthogonal orientations of the unit cells, with the a and b directions depicted in both regions. *Bell (1988)*[25] reports that a=3.859 Å and b=3.920 Å and also that c=11.843 Å.

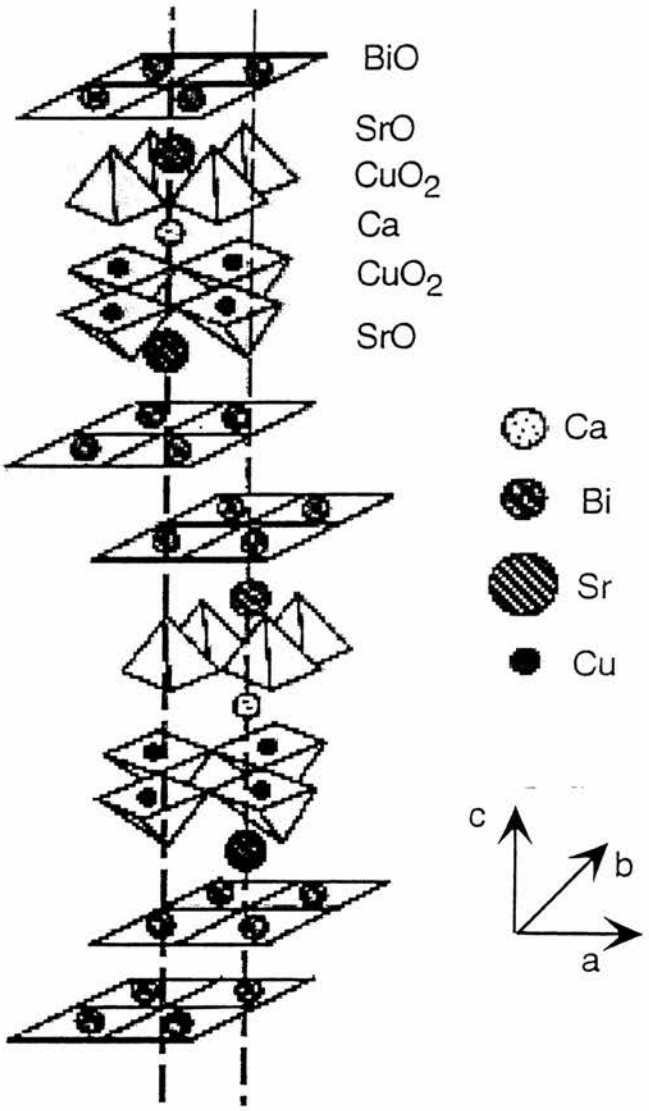

Figure 2.3: Diagram of the structure of $Bi_{2.15}Sr_{1.85}Ca_1Cu_2O_{8+\delta}$. A representation with polyhedrons has been used to denote the relationship of the oxygen atoms to the metal atoms. In BSCCO (2212) the double copper oxide layer is separated by a layer of *Ca*. On either side of the copper oxide layers are SrO layers and on either side of these are BiO layers. The O atoms form an octahedron around the Bi atoms. Courtesy of *S. Romer* [26].

Figure 2.3 shows the structure of BSCCO. This structure was discovered by *Chu et al (1988)* [27] and has a $T_c \approx 108$ K. BSCCO has a very similar structure to YBCO, with two CuO_2 layers per unit cell. The charge reservoirs are the $Bi-O$ layers and the material can be doped by altering the oxygen content or by replacing the calcium with yttrium. Important differences are the larger separation of sets of CuO_2 planes which result in a more anisotropic structure and the absence of chains of CuO.

2.2 Organic Superconductivity

The history of organic conductors and superconductors dates back to the year 1954 when *Akamatu et al.* reported a resistivity of about 10 Ωcm for an organic material. This was a bromine salt of perylene [28]. Further investigation into this research field remained meagre until a suggestion by *W.A.Little (1964)* [29, 30] that the correct construction of synthetic materials could show superconductivity with transition temperatures as high as room temperature. This model, an extension of the BCS theory [6], discusses the pairing of electrons within an organic polymer mediated via their coupling to highly polarisable side molecules. This expectation came from the fact that the characteristic energy of this excitation $\hbar\omega_{exc}$ exceeds that for the lattice vibrations by about two orders of magnitude resulting in an enormous increase in the superconducting transition temperature compared to the phonon coupled regime. The search for superconductivity in these materials concentrated on quasi-1D systems. This was rewarded by the discovery of superconductivity in the quasi-1D Bechgaard salt (TMTSF-*tetramethyltetraselenafulvalene*)$_2$PF$_6$ (T_c=0.9 K under pressure) by *Jerome et al* in 1979 [31]. The substitution by other monovalent anions such as AsF_6 and ClO_4

created a whole series of $(TMTSF)_2X$ organic superconductors. These superconductors have transition temperatures which are limited to around 3 K and it was soon clear that Bechgaard salts did not exhibit the *"Little mechanism"* of superconductivity. A substantial improvement in T_c was obtained by the synthesis of the organic building block BEDT-TTF(*bisethylenedithiotetrathiafulvalene*) [32, 33] which was a modification of the TTF donor molecule. Unlike the 1D electronic structure of the $(TMTSF)_2X$ salts the extended π-electron system in the BEDT-TTF(ET) molecules tends to form materials of higher dimensionality, in particular the quasi-2D systems. The ET based superconductors have yielded the largest number of organic superconductors and of particular interest are the $(ET)_2X$ salts with complex anions $X=Cu(NCS)_2$, $Cu[N(CN)_2]Br$ and $Cu[N(CN)_2]Cl$ with the highest-T_c values to date of 9.4 K, 11.4 K and 12.8 K (at 0.3 kbar) respectively [34, 35, 36]. The quasi-2D electronic structure of these systems are extremely reminiscent of the layered high-T_c cuprate superconductors and this is the root of a number of novel vortex phenomena in these structures; the marked difference from the well known Abrikosov vortex lattice and phenomena such as the melting of the vortex lattice. Given the layered nature of the organic superconductors they form excellent low temperature models for the high-T_cs and lend themselves to an investigation of the pairing mechanism and intrinsic vortex structures in a regime of greatly reduced thermal energy. Figure 2.4 shows a diagram of the electron-donor molecule BEDT-TTF. Superconduction originates at the central $C = C$ double bindings of the organic structure which forms a layered system from alternating conducting and non-conducting planes. Figure 2.5 [34] shows the κ-type packing that is exhibited in the organic superconductor $(ET)_2Cu(NCS)_2$ (ET-Cu) with only the ET molecules depicted. There are two independent ET molecules

in an asymmetric unit and these form a dimer, connected to one another by short S–S contacts, forming a ET sheet in the *bc* plane. Experiments in this thesis where also carried on the organic superconductor α-(BEDT-TTF)$_2$NH$_4$Hg(SCN)$_4$ (ET-NH4). Figure 2.6 indicates α type packing. The α-type structure consists of ordered stacks arranged in a herring-bone pattern. These stacks are connected by S-S contacts and this weak interstack interaction enhances the dimensionality.

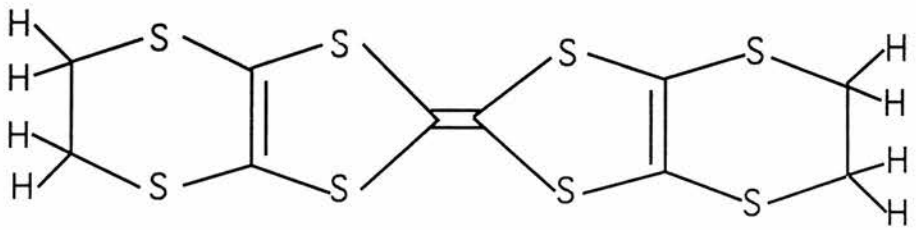

Figure 2.4: A schematic of the electron-donor molecule BEDT-TTF (ET)

2.3 Anisotropy

The High-T_cs and the organics, as have already been seen, have extremely anisotropic structures. This leads to very anisotropic superconducting properties. The effective mass for superelectrons flowing perpendicular to the superconducting planes may be many orders of magnitude larger than those flowing within. This approximate uniaxial behaviour can be quantified therefore as

$$\gamma = \sqrt{\frac{m_\perp}{m_{||}}} \tag{2.1}$$

where $m_\perp$ and $m_{||}$ are the effective masses of superelectrons flowing perpendicular and parallel to the superconducting planes respectively (cf Fig. 2.7) (YBCO$\approx$5 [38, 39, 40, 41] BSCCO$\sim$150 [42, 43] ET-Cu$\geq$100 [44, 45, 46, 47, 48, 49] ET-

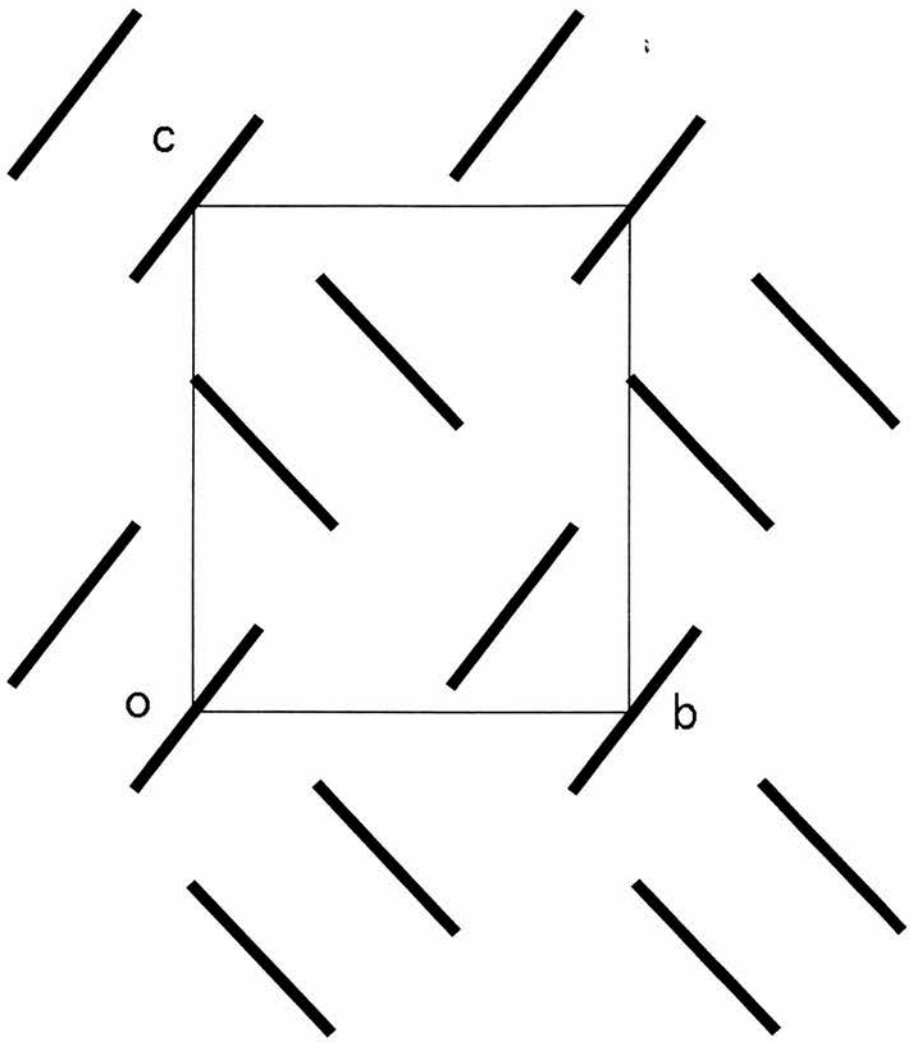

Figure 2.5: The κ-type packing that is exhibited by $(ET)_2Cu(NCS)_2$. The κ-type packing is unique in that it does not consist of interacting stacks but rather of interacting dimers, i.e. face-to-face aligned ET molecules. Adjacent dimers are arranged in almost orthogonal order so that the intra dimer interaction becomes nearly equal to the interdimer interaction. Reproduced from [34].

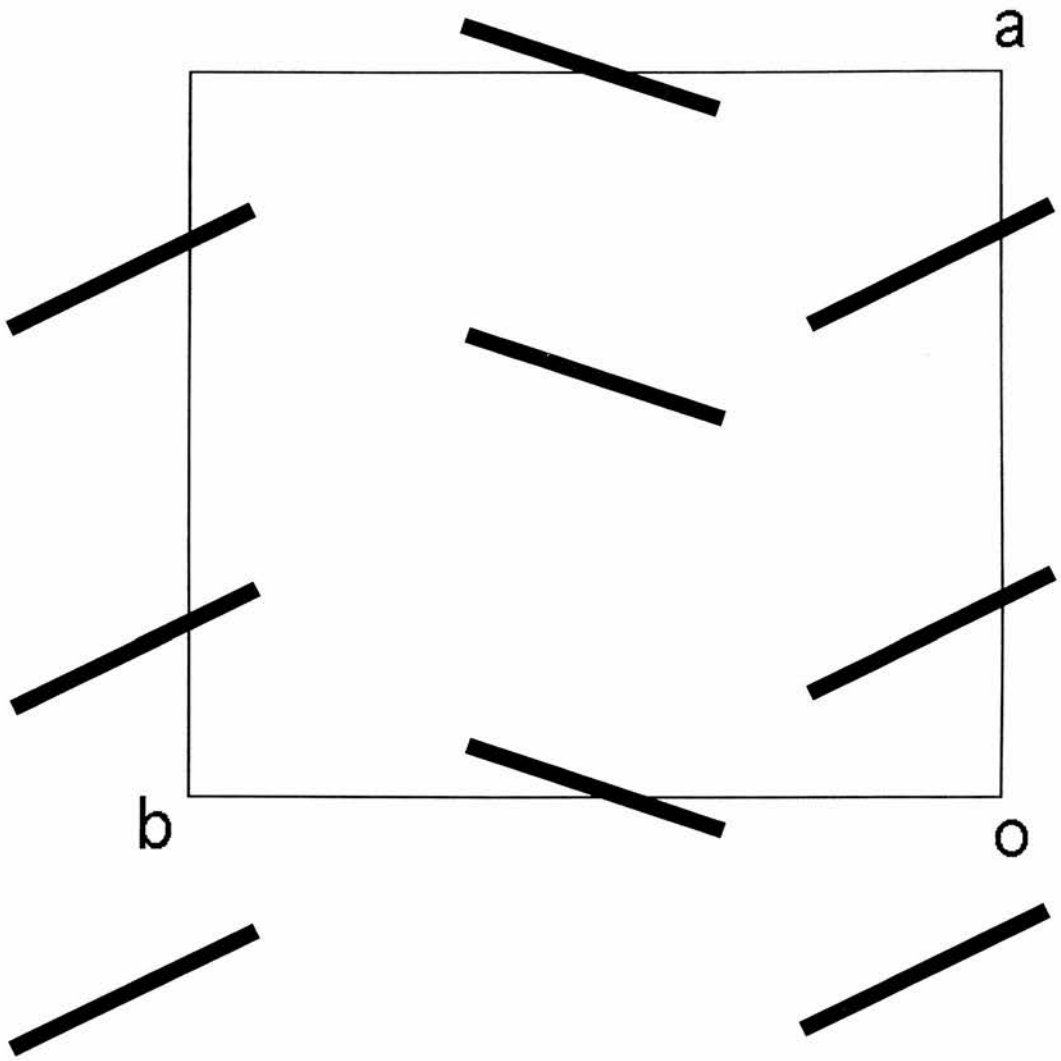

Figure 2.6: The α-type packing that is exhibited by α-(BEDT-TTF)$_2$NH$_4$Hg(SCN)$_4$. Unlike the κ-type packing, the α-type packing consists of interacting stacks. Reproduced from [37].

NH4$\sim$1000 [50]). As was seen in the first chapter, G-L theory can be extended to encompass moderately anisotropic systems by replacing these effective masses with an appropriate effective mass tensor and is quantitatively applicable to YBCO down to 80 K [10] .

The penetration depth is related to the effective mass according to Eqs. 2.2.

$$\lambda_{\|} = \frac{1}{m_{\|}^{\frac{1}{2}}}, \quad \lambda_{\perp} = \frac{1}{m_{\perp}^{\frac{1}{2}}} \tag{2.2}$$

As a consequence of the anisotropy in these superconducting materials, such as

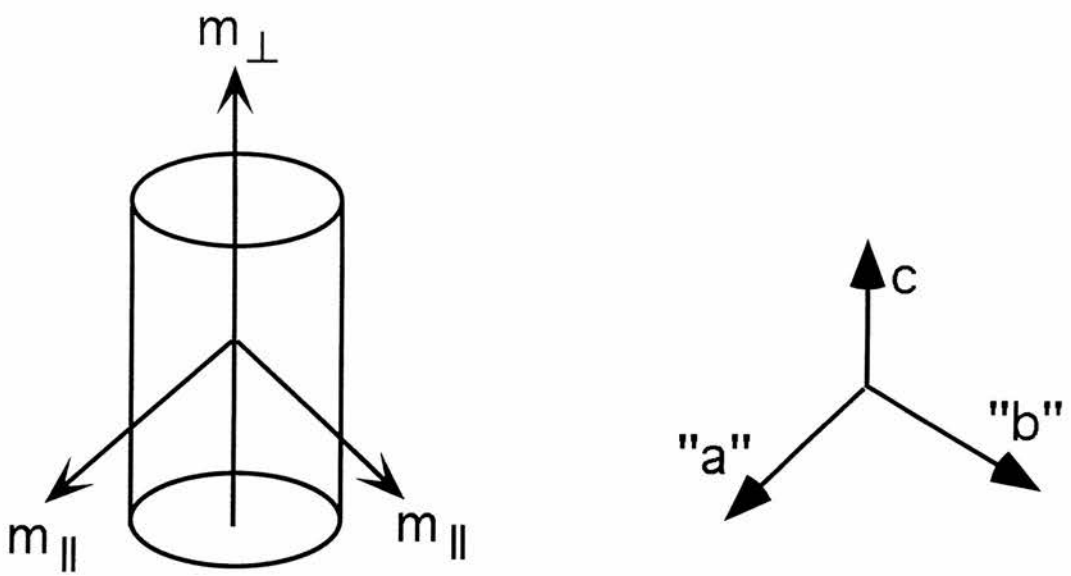

Figure 2.7: A schematic off the effective masses for superelectrons in a HTSC. $m_{\perp}$ is the effective mass for a superelectron flowing perpendicular to the superconducting planes or in the crystallographic c-direction. $m_{\|}$ is the effective mass for electrons flowing parallel to the superconducting planes, either in the crystallographic a or b-directions.

the HTSC, it is more appropriate, therefore, to describe a vortex line as a string of two-dimensional *pancake* vortices confined to the superconducting planes, but

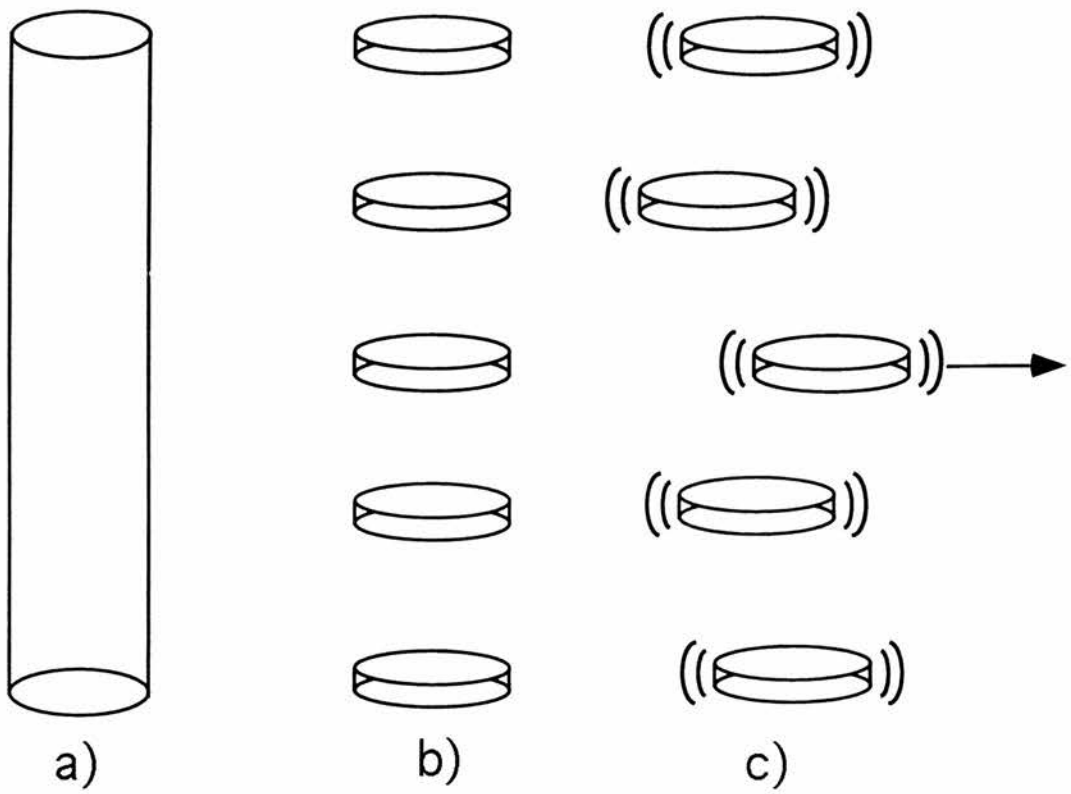

Figure 2.8: Schematic representation of flux vortices in anisotropic superconductors. a) In a system approaching the isotropic limit, the conventional view of a vortex line is valid. b) For highly layered systems such as the HTSC, a more appropriate picture is one consisting of two-dimensional pancake vortices , each confined to the conduction planes. If the inter-layer coupling between pancakes is sufficiently strong the pancakes will line up and form a fluxline. Distortions in this picture occur when intra-layer interactions overcome inter-layer interactions. c) Disorder, such as thermal disorder, which will cause the pancakes to vibrate, will also affect the straightness of the flux-line.

weakly connected via interlayer interactions [22] (cf Fig. 2.8). This weak coupling ensures that the flux structure of these anisotropic systems are not solely confined to the simple Abrikosov case and possibly exhibit many exotic flux structures . The nature of this coupling interaction is normally assumed to arise from Josephson tunnelling of current between the layers [11, 10] (Details of this herein) . *Lee et al (1997)* [51] has recently demonstrated that in BSCCO electromagnetic coupling plays a dominant role in this interaction over much of the *low* field phase diagram.

2.4 Pinning & the Flux Lattice

Abrikosov's perfect hexagonal lattice only exists in samples in which there are no pinning mechanisms. In practise, perfectly homogenous, clean superconductors are extremely difficult to fabricate and flux lines will always be affected by pinning sites such as point disorders, grain boundaries and oxygen vacancies. *Larkin & Ovchinnikov*(1979) [52] showed that even arbitrarily weak pinning destroys the infinite long range order of the lattice, the flux line positions tending to coincide with the pinning sites. They proposed that the length scale over which the lattice is ordered to be the *Larkin-Ovchinnikov* correlation length, determined by the elastic properties of the flux lines. This argument was extended to HTSC by *Fisher et al (1991)* [53]. From this work a vortex solid phase known as the vortex glass phase was proposed. This phase exists in the presence of point pins and corresponds to a state where all of the flux lines will undergo the minimum amount of elastic deformation to take advantage of the maximum local pinning potential. As a consequence of this, there is a breakdown in any long range order with all flux line positions determined by the sample dependent distribution of point pins. At higher temperatures and/or fields the vortex glass state undergoes a transition into

the vortex liquid phase, where the flux pancakes are free to move at all applied currents. This transition or melt in HTSC is dictated by the elastic moduli of the flux-lattice. The elastic energy for a 3D isotropic superconductor was calculated by *Brandt et al (1977)* [54] and a generalization to the anisotropic case was made, e.g., in ref.[55]. The associated elastic moduli have the form [56, 57, 58, 59],

$$Compression : c_{11}(\mathbf{k}) = \frac{B^2}{\mu_o}\left[\frac{1+k^2\lambda_c^2}{(1+k^2\lambda_{ab}^2)(1+k_{ab}^2\lambda_c^2+k_c^2\lambda_{ab}^2)}\right] \tag{2.3}$$

$$Shear : c_{66} = \frac{\phi_o B}{16\pi\mu_o\lambda_{ab}^2} \tag{2.4}$$

The low-field form of c_{66} is

$$c_{66} \propto \frac{B^{1/4}\lambda^{1/2}}{\phi_o^{7/8}} c^{-\frac{1}{\lambda}\sqrt{\frac{\sqrt{3}\phi_o}{2B}}} \tag{2.5}$$

The tilt moduli $c_{44}(\mathbf{k})$ consists of a bulk term, $c_{44}^o(\mathbf{k})$, and a single vortex contribution, $c_{44}^c(k_c)$, with

$$c_{44}^o(\mathbf{k}) = \frac{B^2}{\mu_o(1+k_{ab}^2\lambda_c^2+k_c^2\lambda_{ab}^2)} \tag{2.6}$$

and

$$\begin{aligned} c_{44}^c(k_c) &= \frac{B\phi_o}{4\pi\mu_o\lambda_c^2} ln\left(\frac{\frac{\gamma^2\lambda_{ab}^2}{\xi_{ab}}}{1+(\lambda_{ab}\gamma^2)K_{BZ}^2+\lambda^2k_c^2}\right) + \\ &\quad \frac{B\phi_o}{4\pi\mu_o\lambda_c^3k_c^2} ln\left(1+\frac{\lambda^2k_c^2}{1+\lambda^2K_{BZ}^2}\right) \end{aligned} \tag{2.7}$$

where $K_{BZ} = \sqrt{4\pi}/a_o$ (=radius of the circularised Brillouin zone of the vortex lattice [58]). The second term in the single vortex tilt c_{44}^c is due to the electromagnetic coupling between the layers. Both tilt and the compression moduli (cf Eq. 2.3) are dispersive. For a uniform tilt or compression the compression and tilt moduli are both large. However, for small displacements (k large), the compression and tilt moduli both become small, resulting in a flux-lattice that is soft and easily distorted by small wavelength displacements and the energetic cost

of distorting the lattice is small. This simple fact shows that the flux-lattice is very susceptible to pinning and thermal fluctuations. The latter is quantified by the Lindemann criterion which states that the flux-lattice will melt when thermal fluctuations exceed a fraction, $c_L \sim 0.1 - 0.4$, of the lattice spacing, a_o,

$$\langle u^2(T_m)\rangle_{th} \approx c_L^2 a_o^2 \tag{2.8}$$

where $\langle u^2\rangle_{th}$ is the mean squared thermal displacement. A number of authors have calculated the melting line using the elastic moduli to calculate the amplitude of thermal fluctuations as a function of field and temperature, invoking the Lindemann criterion to calculate the melting line in the BT phase diagram (see e.g.[58, 57]). *Houghton et al*(1989) [55] has shown that for a 3D flux-lattice the melting line is given by

$$B_{3D}(T_m) \approx \frac{1}{[(4(\sqrt{2}-1)+1)^2\pi\mu_o^2]}[\frac{\phi_o^5 c_L^4}{(\gamma k_B T_c \lambda_{ab}^2(0))^2}][\frac{1-(T_m/T_c)^n}{(T_m/T_c)}]^2 \tag{2.9}$$

where T_m is the lattice melting temperature and n is the temperature dependence of the penetration depth (it has already been seen that $n = 4$ if the penetration depth follows the two-fluid model). Equation 2.9 successfully describes the melting of a 3D flux-lattice and is valid for a system of low anisotropy such as YBCO. Equation 2.9 is not particularly applicable to compounds such as BSCCO and the superconducting organic salts of form $(ET)_2X$, as this calculation ignores the single vortex term due to electromagnetic coupling. This term is important in these compounds as it may dictate the vortex dynamics over much of the phase diagram in these systems (see section 2.6). *Blatter et al (1996)* [59] has discussed the low-field phase diagram of very anisotropic superconductors. In this sense, the role of electromagnetic coupling has been discussed and may dominate in the low temperature regime [51, 60] (see section 2.6) where the associated melting line

was found to be independent of γ and has the form [51]

$$B_m^{em} = \frac{\phi_o^3 c_L^2 s}{4\pi\mu_o 2k_B\beta}\frac{1}{\lambda_{ab}^4 T} \tag{2.10}$$

where $\beta = [ln(1 + 4\lambda_{ab}^2/c_L^2 a_o^2)]^{-1}$. It was also predicted that when the additional coupling of Josephson coupling becomes relevant ($\lambda_{ab} \geq \gamma s$) above a characteristic temperature T^{em} (see section 2.6) the melting line will have the form

$$B_m^{em,J}(T) = \frac{\phi_o^3 \pi c_L^2}{8\pi\mu_o 2k_B\sqrt{\beta}}\gamma\frac{1}{\lambda_{ab}^3 T}. \tag{2.11}$$

Blatter et al (1996) [59] has also computed the shape of the melting line for decoupling of the vortices. Decoupling of the vortices occurs when there is a loss of interlayer coherence due to strong thermal fluctuations of the pancakes within the individual layers. According to ref.[59], in the appropriate region of low fields and large anisotropy, below a characteristic temperature, T^{em}, this takes the form [51]

$$B_{dc}^{em}(T) = \frac{\phi_o^3 c_D}{4\pi\mu_o k_B}\frac{1}{\lambda_{ab}^4 T} \tag{2.12}$$

where c_D $\sim$0.1 and plays a similar role to the Lindemann number and allows the decoupling line to be estimated [59, 57]. For $T>T^{em}$ this dependence ($\propto (1/\lambda_{ab}^4(T)T)$) crosses over to

$$B_{dc}^{J}(T) = \frac{\phi_o^3 c_D}{4\pi\mu_o k_B s\gamma}\frac{1}{\lambda_{ab}^2 T}. \tag{2.13}$$

Lee et al (1997) [51] has carried out experiments in the low field phase diagram of BSCCO which indicate that T^{em} $\sim$70 K and that above T^{em}, the melting line $B_m^{em,J}(T)$, which is predicted to behave according to $B_m^{em,J}(T) \propto 1/\lambda^3 T$ (cf Eq. 2.11) actually has a weaker dependence, $B_m^{em,J}(T) \propto 1/\lambda^2 T$ (cf Eq. 2.13). The authors of ref.[51] indicate that in this phase region the *decoupling* and *melting* of the lattice are very closely separated or may even occur simultaneously.

2.5 Josephson Coupling

Before the next section which will discuss generic phase diagrams in materials of low and high-anisotropy it is instructive to review Josephson vortices (JV). An example in considering one of these structures is to consider the effect if pancakes from a pancake stack move from the equilibrium flux-*line* positions (see Fig. 2.9). According to to Eq. 1.3 currents will flow as a result of the phase-difference, ΔS, of the order parameter in adjoining layers. Figure 2.10 shows a schematic of the Josephson vortex (JV) which would be "set-up" in this situation. Some important points should be highlighted about a JV. The JV has a magnetic extent which spreads out a distance of $\lambda_\perp$ perpendicular to the superconducting planes and a distance $\lambda_{||} = \gamma\lambda_\perp$ parallel to the superconducting planes. The corrugated effect seen in Fig. 2.10 is a consequence of the Josephson currents flowing through several superconducting layers and the differing effective masses for electrons flowing in the $||$ and $\perp$ directions. The most significant part of a JV structure is the phase core. The phase core defines a region of the JV which is unable to screen phase fluctuations and is therefore a length scale which defines the effectiveness of Josephson coupling between pancake vortices in different superconducting layers and between adjacent flux-lines. The dimensions of the phase core are s perpendicular to the superconducting planes and γs parallel to the planes. γs is defined as the Josephson screening length λ_J.

2.6 Phase diagrams: generic trends

In this section some of the basic similarities that may be exhibited by systems of high and low-anisotropy are discussed in as clear and concise a manner as possible.

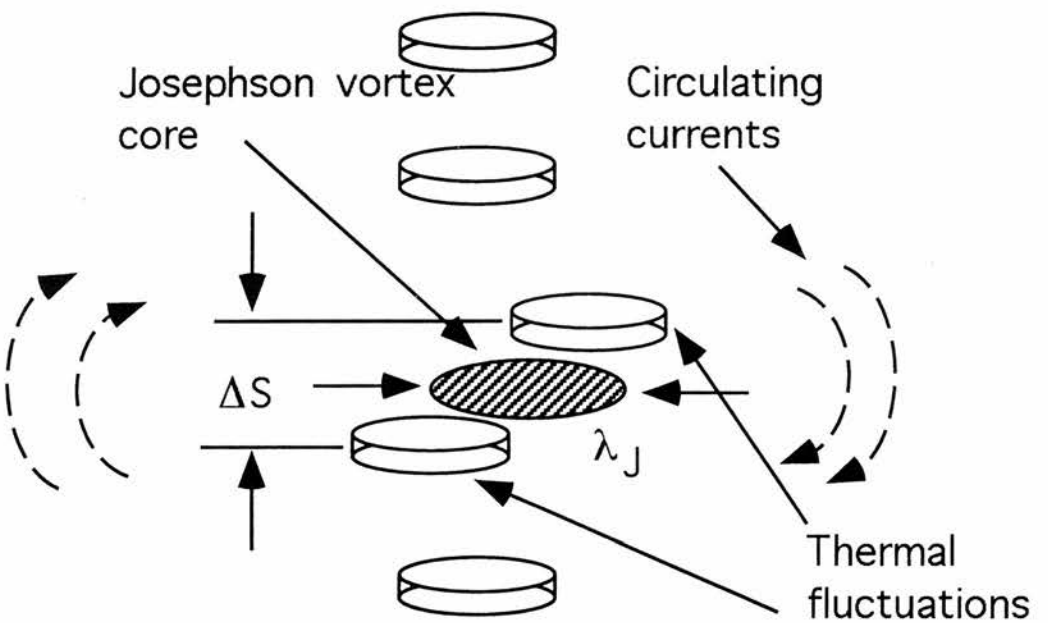

Figure 2.9: A schematic representation of the effect if pancakes from a pancake stack move from their equilibrium flux-*line* positions. Pancakes may move from their equilibrium positions as a result of thermal fluctuations or as a result of point disorder. As a result of this movement there will be a phase fluctuation, ΔS, of the order parameter in adjoining layers. This 'sets-up' a Josephson vortex whose properties are discussed in the text and depicted in Fig. 2.10.

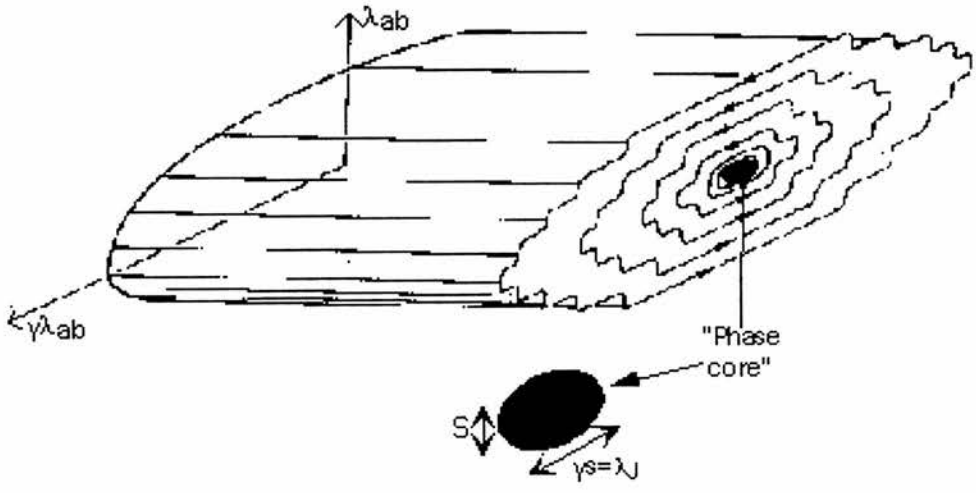

Figure 2.10: A schematic of a Josephson vortex (JV) in a layered superconductor. The JV has a magnetic extent which spreads out a distance of $\lambda_\perp$ perpendicular to the superconducting planes and a distance $\lambda_{||} = \gamma\lambda_\perp$ parallel to the superconducting planes. The phase core of the JV is also indicated and this has dimensions of s perpendicular to the superconducting planes and γs parallel to the planes. Reproduced from [58].

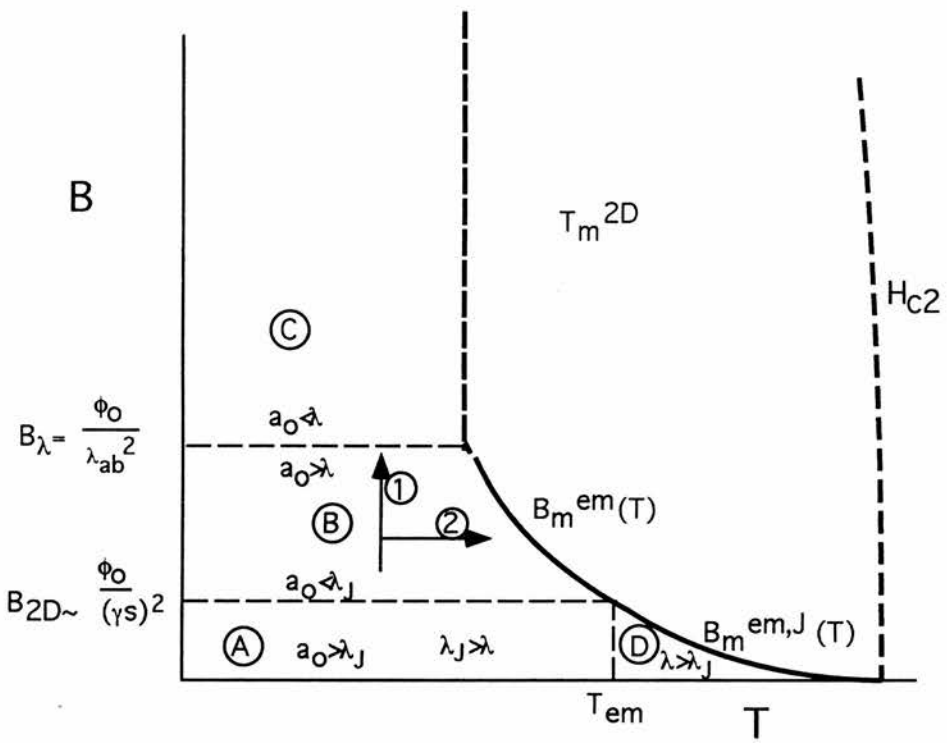

Figure 2.11: A schematic representation of a generic phase diagram expected for a system with high-anisotropy such as BSSCO. Here a_o is average intervortex distance and H_{c2} is the upper critical field. The different regions are discussed in the text.

Further detail may be found in the review by *Blatter et al (1994)* [58] and in ref.[59]. Figure 2.11 shows a schematic of the phase diagram for system of high anisotropy such as BSSCO. In region **A** the flux-lines are dilute (see Fig. 2.12). Appealing to the behaviour of the elastic moduli in this region, the shear modulus will be extremely small (cf Eq. 2.5). The fluxlines will therefore move past each other without interaction. The tilt modulus (cf Eqs. 2.6 and 2.8) will also be small with only contributions from the single vortex terms of the elastic moduli. In this region flux-pancakes will form fluxlines.

B_{2D} in Fig. 2.11 marks the point at which a_o falls below λ_J. It is worth noting that the significance of this field would be much greater in a strongly Josephson coupled superconductor, as it would occur when the fluxlines were already close together, i.e. $a_o \ll \lambda$. In that case the strong in-plane interactions would cause a disordering of the vortices along their length when the influence of the Josephson interaction is reduced above B_{2D}. In a highly anisotropic system as described here, however, B_{2D} does not have great significance, as the vortex-line stiffness is already controlled by the single-vortex electromagnetic line tension (cf Eq. 2.8) as the density of fluxlines is still small ($a_o > \lambda$) (see Fig. 2.13).

In region **B** the magnetic extents of the fluxlines have started to overlap more, although the condition $a_o > \lambda$ still holds. Again, appealing to the elastic moduli, in the lower part of region **B** the shear modulus will be small as the overlap of fluxlines will still be small and they will therefore move easily past each other. Tilt deformation will remain energetically unfavourable here. As one increases the applied field and traces through region **B** along direction **1** (see Fig. 2.11) towards the phase-line B_λ, the shear modulus, c_{66}, increases and it becomes increasingly difficult for fluxlines to bypass each other and more energetically favourable for the

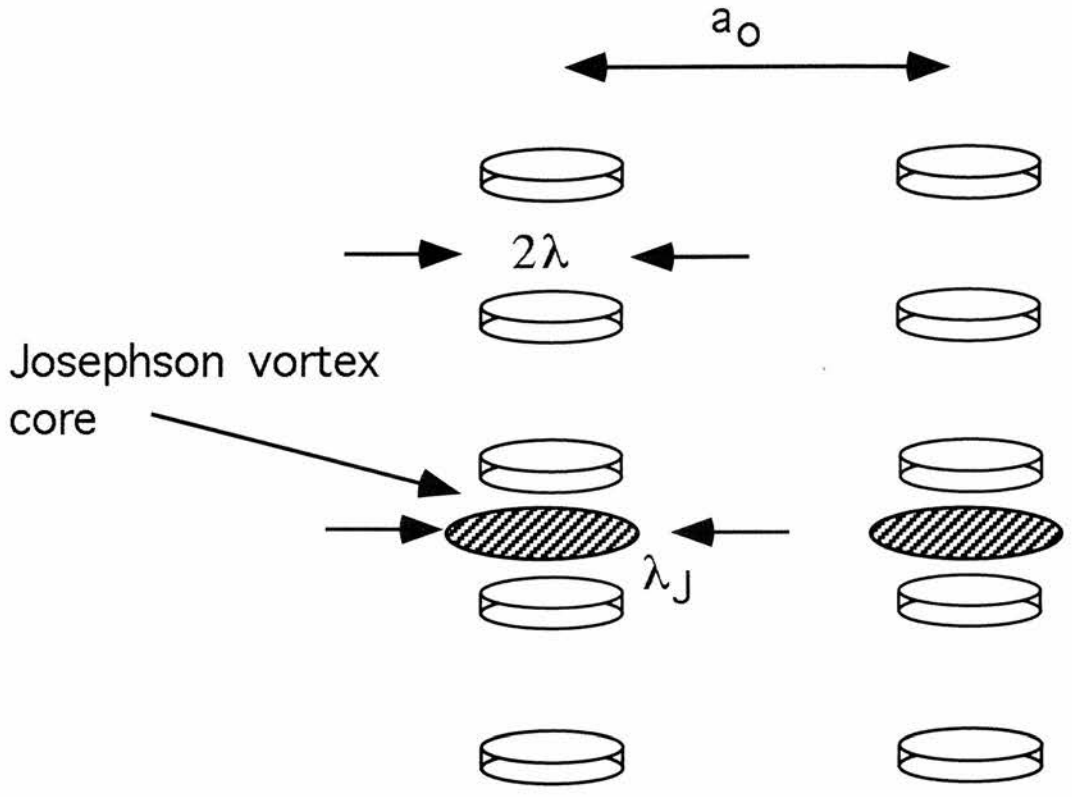

Figure 2.12: A schematic of the interaction between fluxlines in region **A** of the phase diagram with high-anisotropy. Indicated in the figure are pancake-vortices in different superconducting layers. The magnetic extent of the pancakes is indicated as 2λ and the distance between adjacent flux-pancakes is also indicated, a_o. The flux-pancakes are seen here to line-up, forming fluxlines. In this *dilute* limit the pancake vortices in-plane would be expected to have only a weak influence on each other. Also indicated is the extent of the in-plane phase core of a Josephson vortex. Although $\lambda_J > \lambda$ in this region and one would expect electromagnetic coupling to dominate over Josephson, the fluxlines are only weakly aware of each other as $a_o > \lambda_J > \lambda$.

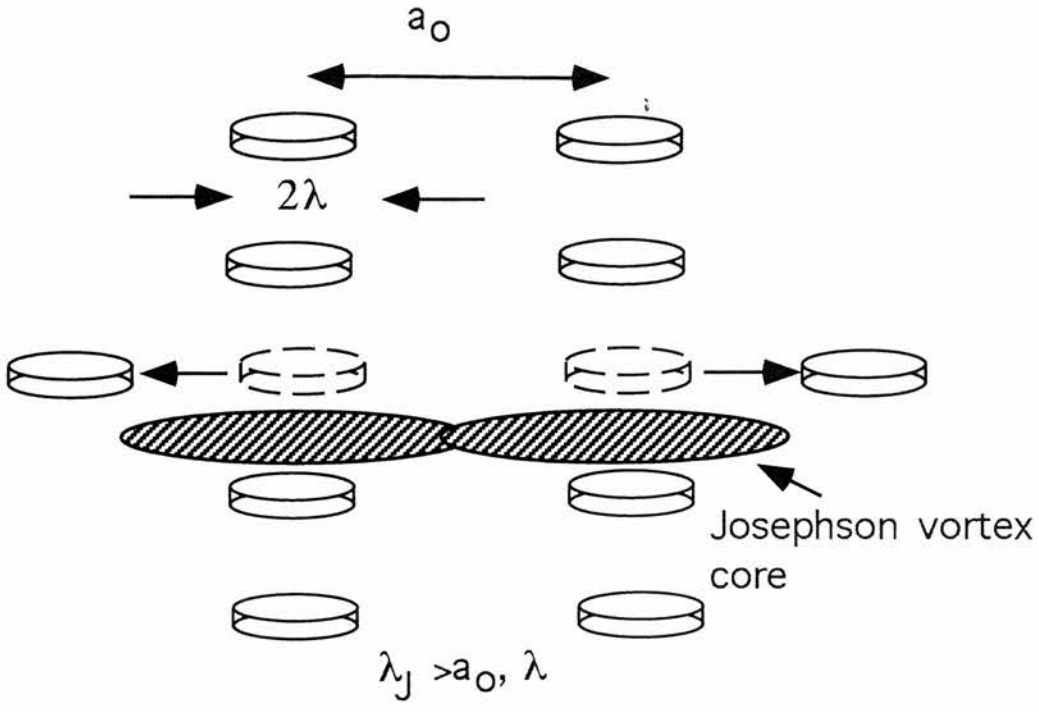

Figure 2.13: A schematic of the behaviour of Josephson coupling at B_{2D} in Fig. 2.11. Indicated in the figure are pancake-vortices in different superconducting layers. The in-plane magnetic extent of each pancake is indicated as 2λ and the distance between adjacent flux-pancakes is also indicated, a_o. Also shown in this figure are the extent of Josephson vortex cores should phase fluctuations have existed in this system for a JV to be generated (the vortex-pancake displacements required for this are indicated by arrows here). The primary point of this diagram is to indicate that at point B_{2D} in Fig. 2.11 the fluxlines remain straight. This straightness is afforded by the fact that in this regime single-vortex electromagnetic terms dominate the coupling interaction between pancakes ($a_o > \lambda$). Conversely, in this region, if Josephson vortices were generated, it is evident from the size of the JV cores that the JV generated would be ineffective in coupling the pancake-vortices i.e. $\lambda_J > a_o, \lambda$.

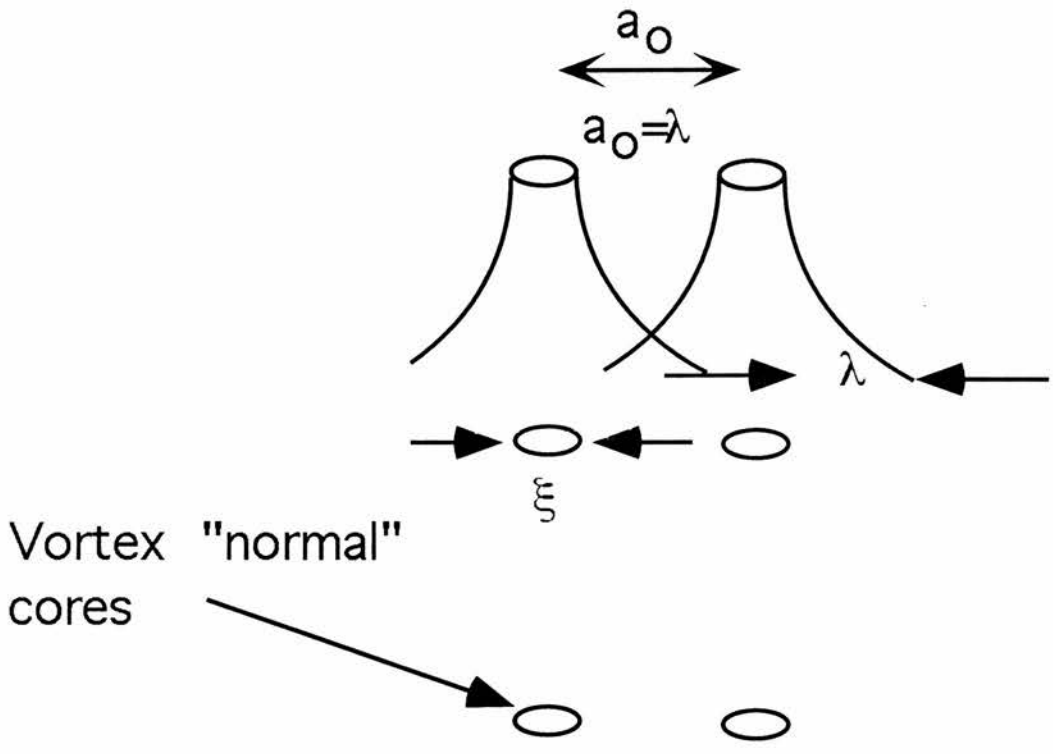

Figure 2.14: A schematic of the fluxline behaviour at the phaseline B_λ. This diagram shows the cores of pancakes vortices in the superconducting layers and the extent of λ. Here, $a_o=\lambda$, and as a consequence, the magnetic extents of the fluxlines have started to overlap strongly. As the dominant coupling mechanism between pancakes in adjacent layers is electromagnetic coupling it is more likely that the point at which the vortex system undergoes a *dimensional crossover* in these extremely anisotropic systems is given by $B_\lambda=\phi_o/\lambda_{||}^2$.

fluxlines to undergo tilt deformation. B_λ marks a phaseline where the magnetic extents of the fluxlines start to overlap strongly (see Fig. 2.14) and may mark a length-scale at which these systems start to behave in a more '2D' manner. Following direction **2** in region **B** of Fig. 2.11, as the temperature is increased the penetration depth will increase and the melting line, $B_m^{em}(T)$, will be controlled by electromagnetic coupling. As was seen in section 2.4, this was studied theoretically by *Blatter et al (1996)* [59] who computed that the melting line should have the form $B_m^{em}(T) \propto 1/\lambda_{ab}^4 T$. This was observed in BSCCO by *Lee et al (1997)* [51].

Region **C** marks a part of the phase diagram where tilt deformation will be energetically favourable over shear (see Fig. 2.15) and as a consequence of this the fluxlines will become *softer* and the system will behave in a more '2D' manner. *Glazman & Koshelev (1991)* [57] have computed that at high field this '2D' phase will melt according to

$$k_B T_m^{2D} = \frac{s\Phi_o^2}{8\pi\sqrt{3}\mu_o 4\pi\lambda_{ab}^2} \tag{2.14}$$

which is field independent and where s is the inter-layer spacing.

Region **D** marks a region in the phase diagram where the penetration depth exceeds λ_J and Josephson coupling becomes more effective in coupling the pancake vortices. *Blatter et al (1996)* has computed the melting line in this region of the phase diagram and this indicates that it has the form $B_m^{em,J}(T) \propto 1/\lambda_{ab}^3 T$ [59]. Recent experimental work on BSCCO by *Lee et al (1997)* [51] have indicated that the melting line in this part of the phase diagram may have a *weaker* dependence of the form $B_m^{em}(T) \propto 1/\lambda_{ab}^2$ (see section 2.4).

Figure 2.16 shows a schematic of the phase diagram for a system of low anisotropy such as YBCO. In such a system B_λ occurs very low in the phase diagram. As a consequence of this the collective vortex term in the tilt modulus

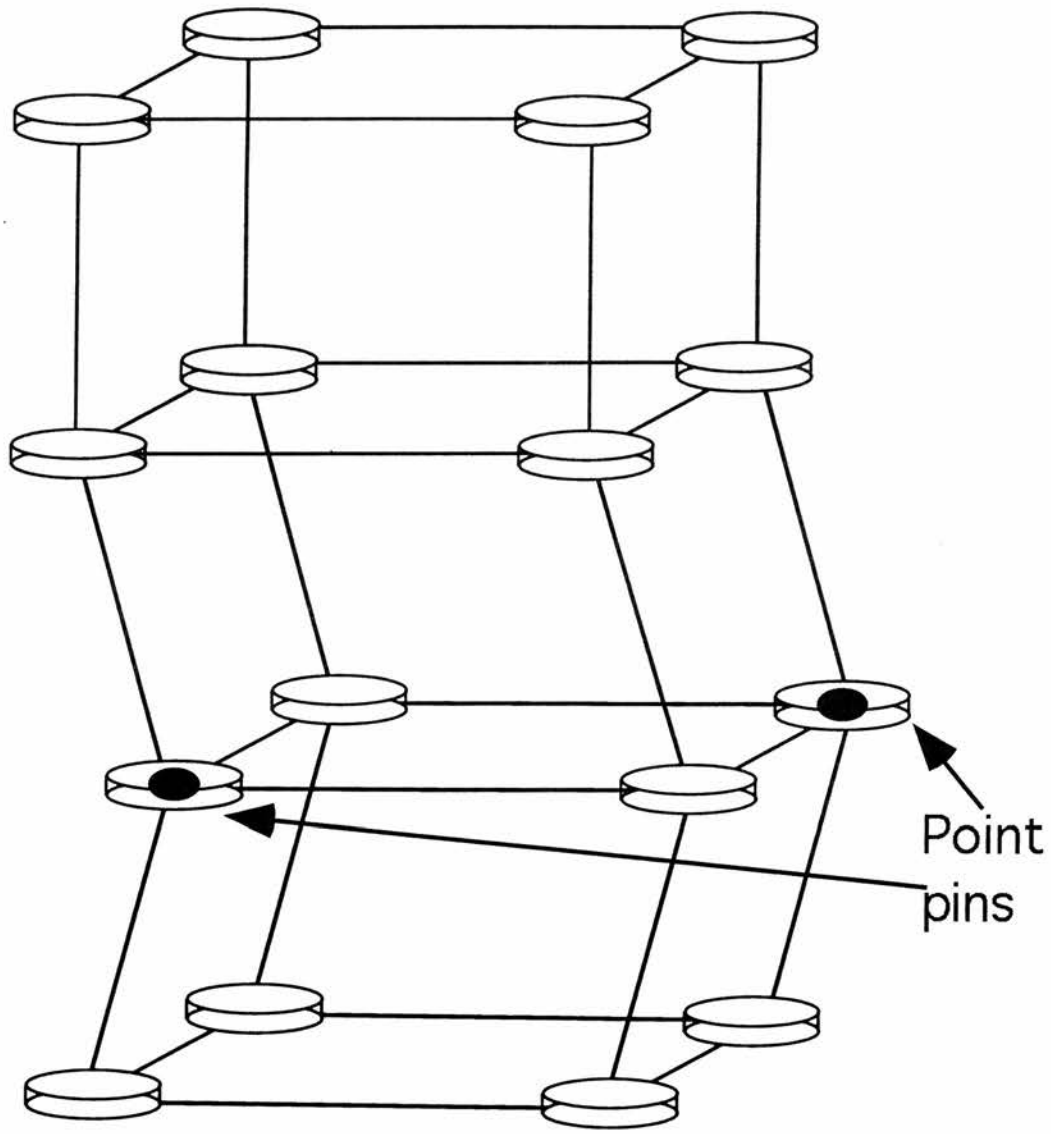

Figure 2.15: A schematic of the flux-lattice in region C of Fig. 2.11. Indicated in the figure are the vortex cores, ξ. In this region tilt deformation of the fluxlines will be more energetically favourable than shear deformation. This diagram depicts flux-pancakes and the effect of disorder, such as point pins, on these flux-pancakes. Instead of the whole fluxline *shearing* to accommodate the disorder, the fluxline simply *tilts*. As a result of tilt being more favourable the fluxlines in region C of the phase diagram are softer and behave in a more '2D' manner.

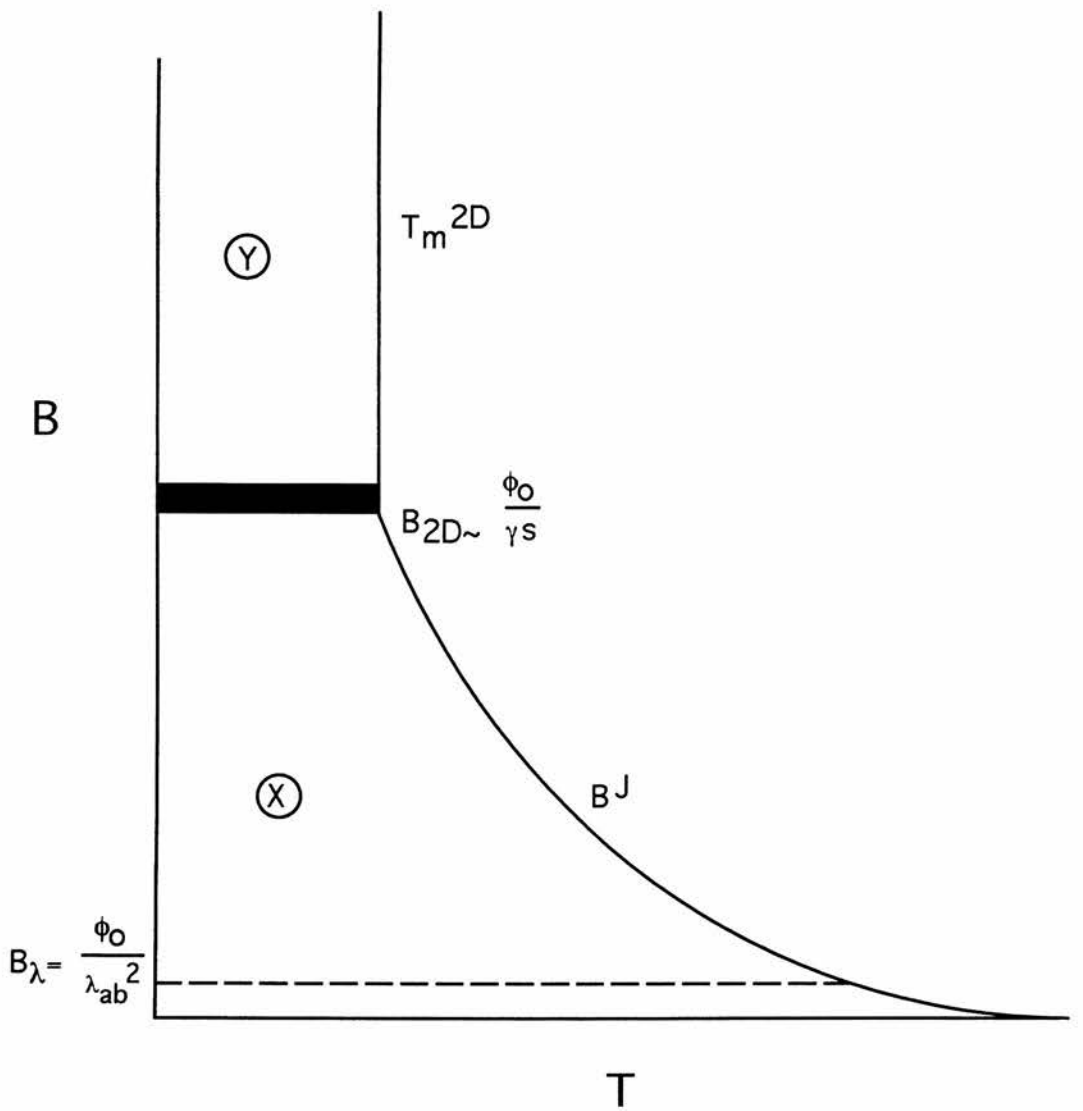

Figure 2.16: A schematic representation of the generic phase diagram for a system with low-anisotropy such as YBCO. The different regions are discussed in the text.

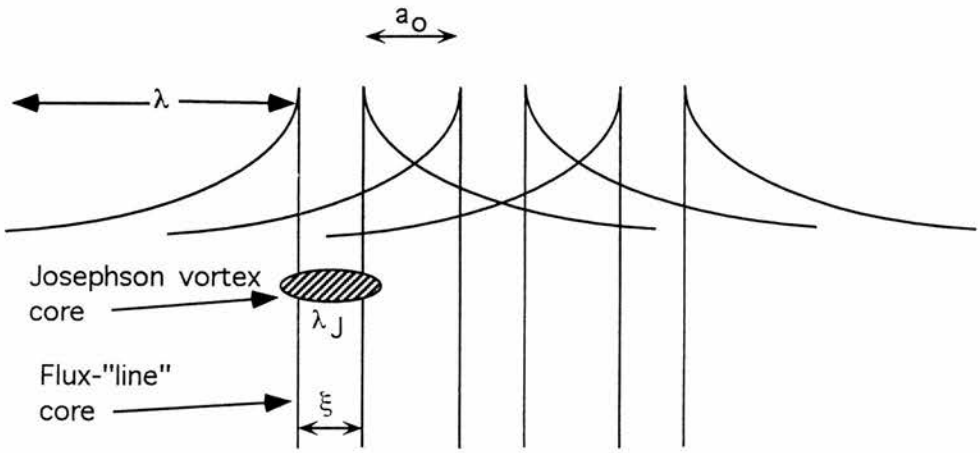

Figure 2.17: A schematic of region **X** of Fig. 2.16. As the anisotropy is low, pancake vortices have not been depicted and the fluxlines have been drawn as *lines*. The fluxline core has been depicted as has their magnetic extent and the extent of a Josephson vortex core. In this region of the phase diagram non-local elasticity effects dominate in controlling the stability of the lattice as a whole and this is achieved by a strong overlap of the magnetic penetration depth, λ, over a distance of several a_o. Local stiffness of the fluxlines is achieved by Josephson coupling ($\lambda > \lambda_J$) and this is maintained until the fluxlines overlap to such an extent that the Josephson cores overlap. At this point the system will undergo a *dimensional crossover* and this occurs at the crossover field, $\sim B_{2D}$.

(cf Eq. 2.6) becomes more important in defining the stability of the flux-lattice above this line. In order to alter the long-range order associated with this stable configuration the system has to be provided with enough energy to disrupt whole regions of the flux-lattice. As a consequence of this, in region **X**, both the shear and tilt moduli are large. It is difficult therefore, as suggested before, for fluxlines to move past each other, or shear, and also for flux-lines to tilt (see Fig. 2.17). Region **X** of the phase diagram has been computed to have a melting line which is dictated by the behaviour of Josephson coupling and is of the form $B_m^J(T) \propto 1/\lambda_{ab}^4 T^2$ [59] (cf Eq. 2.9). In region **Y** the fluxlines are very close together and Josephson vortices can no longer screen phase fluctuations between the *order parameter* in adjacent layers, while intra-layer interaction between pancakes ensures that the long-range fluxline order is broken as in region **C** of Fig. 2.11. This occurs above a field $\sim B_{2D}$. Region **Y** of the phase diagram has been computed to melt according to Eq. 2.14.

The above discussion has highlighted the fact that the parameters of the superconducting state, such as λ, γ and ξ have a profound influence on the behaviour of the vortex lattice and the details of the magnetic phase diagram. Much of the work in this thesis involves characterising these lengthscales and relating them to the details of the vortex behaviour on a microscopic scale.

Chapter 3

Experimental Techniques

3.1 Introduction

The measurements in this thesis were carried out primarily using three techniques; μSR; SANS; and torque magnetometry. As applied to superconductivity , and the vortex lattice, these techniques are in many ways highly complementary. μSR gives information on the local microscopic fields inside a superconductor; SANS gives microscopic information on the long range spatial coherence of the vortex lattice; torque magnetometry measures the bulk magnetisation of the material.

3.2 Transverse Muon Spin Rotation (μSR)

3.2.1 Introduction

The muon spin rotation technique is an established tool in the field of condensed matter and extremely powerful in the investigation of the mixed state of Type II superconductors. This power comes from the fact that muons can be used to probe

the microscopic field distribution in the bulk of the sample. Randomly introduced into the sample the muons effectively probe the probability distribution of the magnetic field within the superconductor. This probability distribution contains important information yielding the penetration depth and information concerning flux lattice melting and other lattice dynamics [61]. This probability distribution will be discussed in following sections.

3.2.2 μSR Theory

The muon has a rest mass 207 times that of the electron, and, like the electron, manifests itself either as a positive or negative particle. For the purposes of μSR, positive muons are produced by striking a suitable target (Be or C) with a high energy proton beam (cf Eq. 3.1)

$$p + p \rightarrow \pi^+ + p + n, \quad and \qquad p + n \rightarrow \pi^+ + n + n \tag{3.1}$$

which in turn decay into a muon and a muonic neutrino (cf Eq. 3.2).

$$\pi^+ \rightarrow \mu^+ + \nu_\mu. \tag{3.2}$$

As the neutrino's spin is anti-parallel to its momentum, and noting that the pion has zero spin, the muon's spin is also anti-parallel to its momentum. As a consequence of this the muons produced are highly spin polarised. For the purposes of transverse field μSR, muons are implanted into the sample with this spin polarisation perpendicular to the applied field. During a short thermalisation process, the positive muons come to rest at interstitial sites without losing their polarisation. *Brewer et al (1990)* [62] has reported that the muons become chemically bonded to oxygen atoms in the unit cell. These muons, however, can still be considered as being implanted randomly on the length scales of interest in superconductivity

as flux line spacings are typically of the order of hundreds of Angstroms. This fixed oxygen site prevents muon diffusion and hence motional narrowing. The next stage in the muons life is their Larmor precession at a rate determined by the local magnetic field (cf Eq. 3.3).

$$\omega_\mu = \frac{e}{m_\mu} B \tag{3.3}$$

After a brief lifetime (2.2 μs) the muon decays via the weak interaction into a positron, neutrino and antineutrino(cf Eq. 3.4).

$$\mu^+ \rightarrow e^+ + \nu_e + \bar{\nu_\mu} \tag{3.4}$$

As a consequence of parity violation in muon decay the angular distribution $P(\theta)$ of the positron is strongly anisotropic with respect to the muon spin. This anisotropy has a maximum when the emitted positron attains its maximal energy E_{max}. This occurs when the positron is emitted in exactly the opposite direction to the two neutrinos (see Fig. 3.1). Ones reasoning here follows from the fact that since the muon has positive helicity and the spins of the neutrinos add to zero, the positron must be emitted predominantly in the direction of the muon spin. Integrating

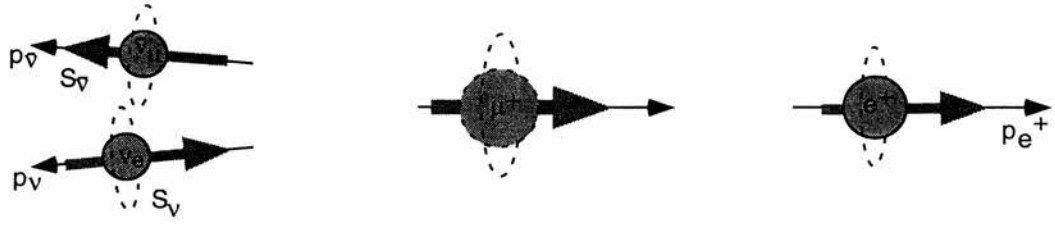

Figure 3.1: The decay of the muon. This picture graphs the decay of a muon with energy close to the maximum E_{max}. Conservation of angular and linear momentum dictate that in this case the two neutrinos are emitted in approximately the same direction.

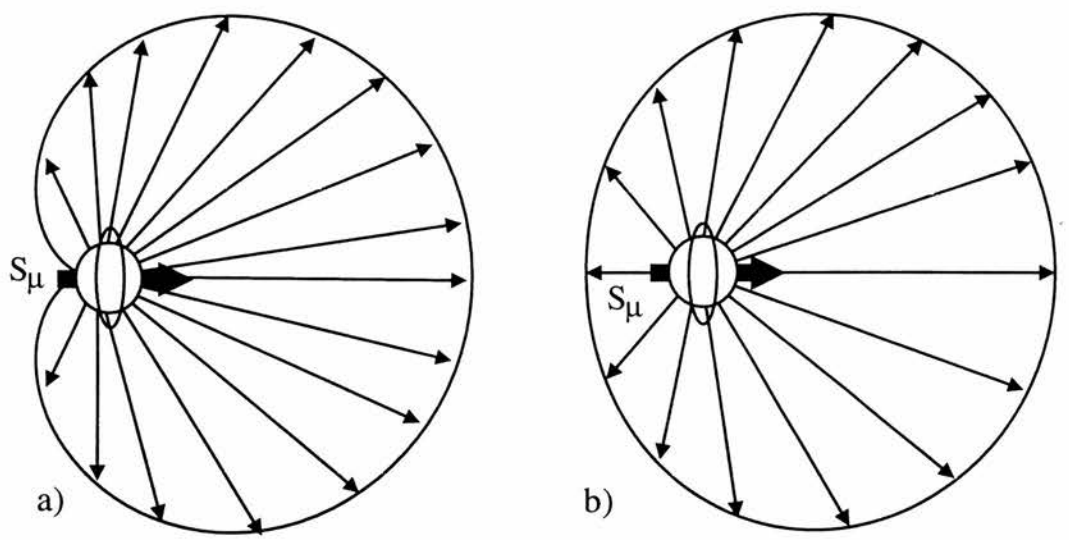

Figure 3.2: Probability distribution for emission of a positron with respect to the muon spin for *a)* positrons of maximal energy E_{max} and *b)* integrated over positron energy.

over all positron energies reduces this asymmetry, the angular distribution of the emitted positron with respect to the muon spin being given by

$$P(\theta) = \frac{1}{2\pi}(1 + a_o cos\theta) \tag{3.5}$$

where a_o is the asymmetry. The theoretical value of a_o is 1/3. Figure 3.2 shows the angular distributions when only maximum energy positrons are detected and when all energies of positrons are detected. These positrons are recorded by a detector bank and recorded in a time histogram. In transverse μSR the observed positron counts, N(t), at a detector in a given direction as a function of time is given according to *H.Keller (1989)* [63] as

$$N(t) = N(0)exp(-t/\tau)[1 + AR(t)cos(\omega_\mu + \phi)] + b \tag{3.6}$$

where τ is the muon lifetime, N(0), the initial counts, A, the observed fractional amplitude, R(t), the relaxation function of the polarisation, ω_μ, the mean angular frequency, ϕ, a phase offset for a given detector and b the time independent background. After the muon pulse has arrived the muons will precess at different rates depending on the field they experience in the sample. This dephasing of the muon spins reduces the coherence of the muon spin directions with time. As the muons decay into positrons it is possible to monitor this dephasing as a decaying amplitude of observation, faster dephasing occurring for a larger range of internal fields. The detector bank therefore records an oscillating component of frequency, ω_μ, starting with an initial amplitude, A, superimposed upon the exponential decay due to the muon lifetime. This is clearly seen in Fig. 3.3. R(t) describes the damping of the muon signal. If we assume that the field distribution in the sample is Gaussian, then the relaxation function has the form

$$R(t) = exp[\frac{-\sigma^2 t^2}{2}] \tag{3.7}$$

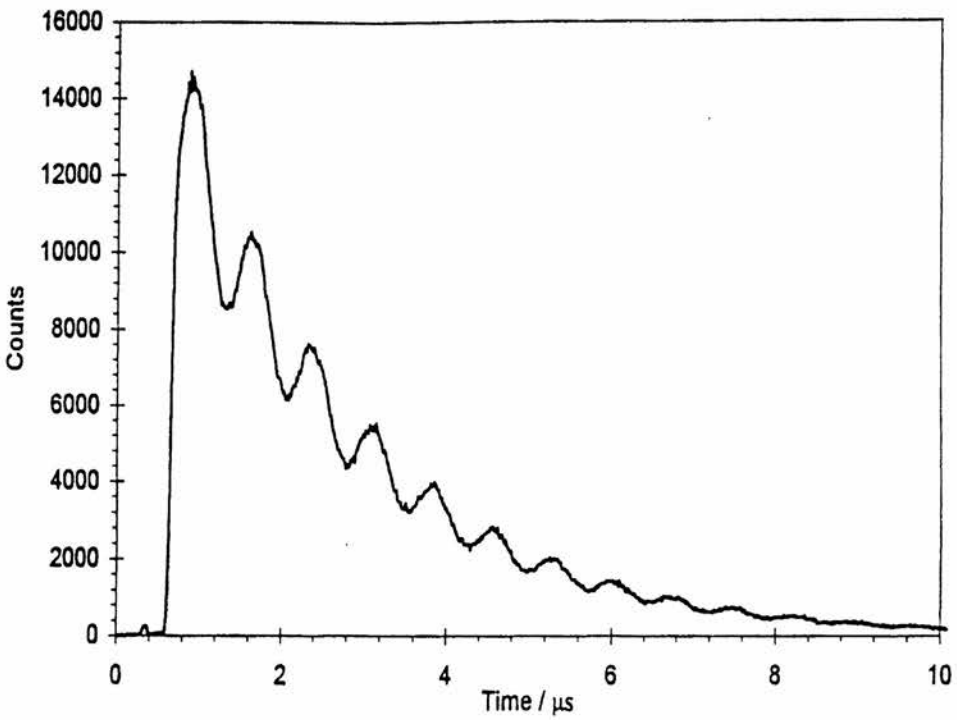

Figure 3.3: Data from a group of 4 detectors at RAL for a sample of BSCCO at 0.01 T and 95 K when the sample is in the *normal state.* The detector bank in this case has clearly recorded an oscillating component of frequency, ω_μ, starting with an initial amplitude, A, superimposed upon the exponential decay due to the muon lifetime. The damping seen here is low as the field variation within the sample is small.

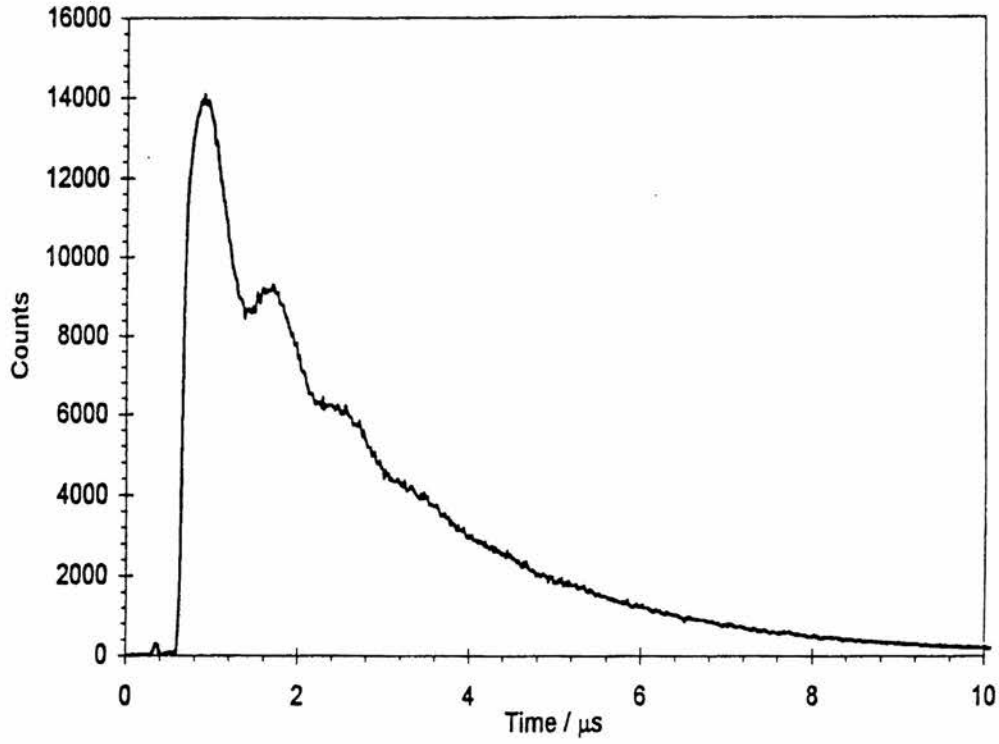

Figure 3.4: Data from a group of 4 detectors at RAL for a sample of BSCCO at 0.01 T and 5 K when the sample is in the *superconducting state*. Much larger damping occurs here due to the larger internal field variation.

where the spin relaxation rate, σ, is related to the variance of the internal field via

$$\langle \Delta B^2 \rangle = \sigma^2 (\frac{e}{m_\mu})^2. \tag{3.8}$$

It should be noted here that the nuclear dipole fields within the sample can make a considerable contribution to the internal field variation so that in the superconducting state the observed relaxation rate is given by

$$\sigma_{observed} = \sqrt{\sigma^2_{superconducting} + \sigma^2_{nuclear}}. \tag{3.9}$$

The value of this dipole component can be estimated by measuring the damping above T_c, assuming that they are static and assumed to be independent of temperature and applied field. *Barford and Gunn (1988)* [64] showed that for $H_{c1} \ll H \ll H_{c2}$, in an extreme type II superconductor (i.e large κ) the penetration depth can be estimated according to

$$\langle \Delta B^2 \rangle = \frac{0.003706 \Phi_o^2}{\lambda^4} \tag{3.10}$$

where $\Phi_o = h/2e$ is the elementary flux quantum. In the case of anisotropic superconductors one has to consider this penetration depth as an effective penetration depth comprising of an appropriate combination of λ_c and λ_{ab} depending upon the orientation of the applied field. The angular dependence of the second moment has been obtained within the London approximation via the introduction of an anisotropic effective-mass tensor [65, 66] resulting in

$$\langle \Delta B^2 \rangle^{1/2}(T)(\vartheta) = \langle \Delta B^2 \rangle^{1/2}(0)(cos^2\vartheta + 1/\gamma_{ij}^2 sin^2\vartheta)^{1/2} \tag{3.11}$$

where, for example, the second moment for the field applied parallel to the c-axis is

$$\langle \Delta B^2 \rangle = \frac{0.003706 \Phi_o^2}{\lambda_{ab}^4}. \tag{3.12}$$

Equation 3.11 together with Eq. 3.8 yields

$$\sigma(\vartheta) = \sigma(\vartheta = 0)(cos^2\vartheta + 1/\gamma_{ij}^2 sin^2\vartheta)^{1/2}. \tag{3.13}$$

This equation is only valid for a static flux lattice of rigid rods, aligned parallel to the applied field. Equations 3.10 and 3.13 give a clear indication that useful information such as the temperature dependence of the penetration depth and the superconducting anisotropy can be gathered by performing μSR measurements.

3.2.3 μSR Lineshapes

The field distribution for an ideal triangular lattice has been theoretically calculated and the associated probability distribution has been found to follow the form shown in Fig. 3.5. This figure shows a low field cut-off (B_{min}) which is non-zero if the flux line's magnetic extent overlaps, a peak which reflects the most common field occurring at the saddle point between flux lines (B_{sad}) and a high field cut-off (B_{core}) representative of those fields near the flux-line cores. This lineshape is characteristic of a perfect 3D flux lattice. In the preceding section (section 3.2.2) it was seen that in order to extract information about this 3D flux lattice it is necessary to make assumptions about the shape of the internal field of the superconductor. If this characteristic shape is lost, in order to infer lattice transitions it is necessary to remove these assumptions. This is overcome by transforming the data into the frequency domain by performing a Fast Fourier Transform(FFT) where qualitative changes in the shape of the distribution can be measured. The analysis carried out in this thesis requires the μSR lineshape, which is the Fourier transform of the positron decay spectrum, in order to obtain the probability distribution of the internal field values of the superconductor, p(B). Conventional Fourier methods may be used, but in order to suppress noise due to Poisson counting statistics and

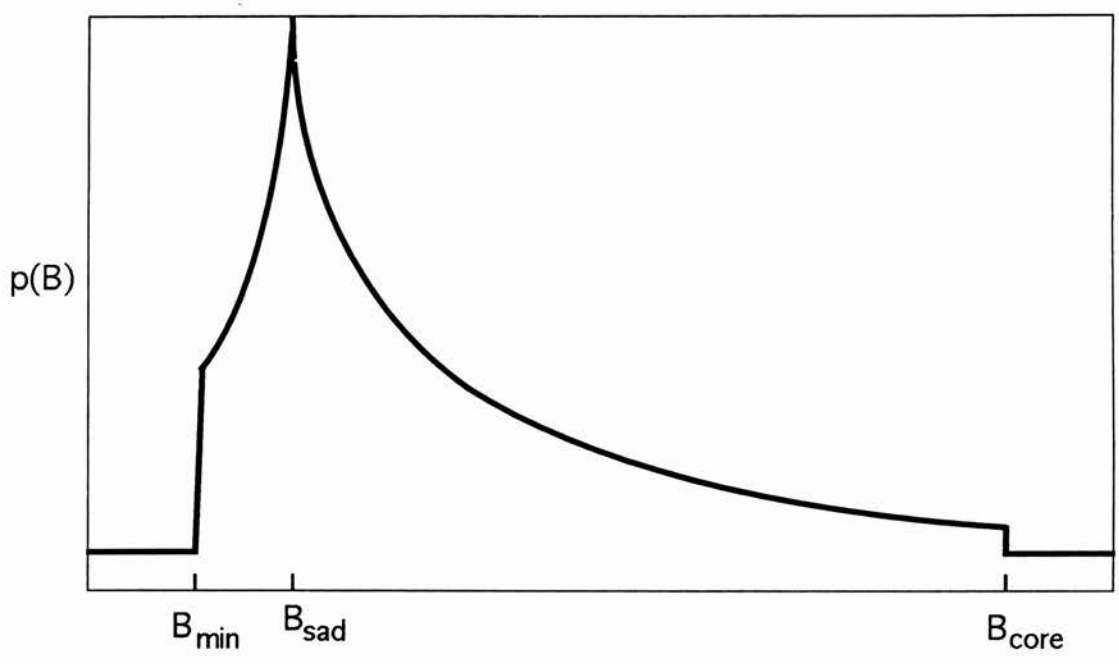

Figure 3.5: A schematic of the probability distribution for an ideal triangular lattice. This figure shows a low field cut-off, B_{min}, non-zero if the penetration depth associated with each flux line overlaps, B_{sad}, the most common field, occurring at the saddle point between flux-lines, and B_{core}, a high-field cut off associated with the field near the flux-line cores.

produce cleaner lineshapes for qualitative analysis it has proved essential to utilise a maximum entropy method [67]. Such an approach is particularly useful if one desires to perform a systematic investigation of the moments of p(B) , which are extremely sensitive to the presence of random noise. The main analysis program to carry out this procedure was written by *B.D. Rainford* and *G.J.Daniel* [67] and modified into its present form by *R.Cubitt* and *E.M.Forgan* [68].

Without any constraints, a uniformly flat probability distribution will maximise the entropy

$$S = \sum p(B_i) ln(p(B_i))/d_i \tag{3.14}$$

where d_i represent default values, which in the analysis are assumed to constitute a flat distribution. In order to obtain the desired field distribution, maximising the entropy has to be constrained by the data. This is achieved by introducing the usual quantity $\chi = \sum(n_i - y_i)^2/\sigma_i^2$, where n_i are the time domain data, after correction for the exponential decay of the muon, σ_i^2 are the associated experimental errors, and y_i constitute the Fourier transform of the calculated field distribution. The desired field distribution is then obtained by minimising the quantity

$$L = S - \lambda\chi^2 \tag{3.15}$$

where λ is a Lagrange multiplier. In this way the maximum entropy algorithm results in the most uniform distribution consistent with the data. Some degree of freedom in weighting the χ^2 argument with respect to the entropy argument can now be gained by artificially increasing χ^2 through scaling the errors σ_i^2 by a small fraction. One can thus optimise the agreement between the data and the calculated field distribution by increasing the weight of χ^2. The best criteria to use is to choose that scaling factor which is closest to unity, but which will not increase the noise in the distribution such that the moments can no longer be calculated

with confidence, the aim being to produce a spectrum which is flat outside the region of interest. Once this has been achieved, this scaling factor must remain constant throughout the investigation.

To expedite an investigation of changes in vortex studies it has proved fruitful to define the dimensionless parameter α, a measure of the skewness of the lineshape (cf Eq. 3.16).

$$\alpha = \frac{\sqrt[3]{\Delta B^3}}{\sqrt[2]{\Delta B^2}} \tag{3.16}$$

where

$$\sqrt[3]{\Delta B^3} = \sqrt[3]{\frac{\sum_i p_i(B_i)(B_i - B)^3}{\sum_i p_i(B_i)}} \tag{3.17}$$

$$\sqrt[2]{\Delta B^2} = \sqrt[2]{\frac{\sum_i p_i(B_i)(B_i - B)^2}{\sum_i p_i(B_i)}}. \tag{3.18}$$

and the mean field is given by

$$B = \sqrt{\frac{\sum_i p_i(B_i) B_i}{\sum_i p_i(B_i)}}. \tag{3.19}$$

μSR lineshapes for a perfect 3D lattice vary markedly from that of a symmetric distribution (α=0). In practice the value of α observed in a real experiment is 1.5 [61]. This positive value reflects the weighting towards higher fields in the field distribution. The highest fields, however, are under sampled with finite statistics. This under sampling is effectively due to the fact that a significant enough amount of information is not gathered about the very highest fields encountered in the flux line cores for the maximum entropy technique to distinguish this information from the background signal. Experimentally this results in a shorter high field tail and an underestimate of the true width of lineshapes. Theoretical estimates of α rise to values as high as 2.2. The *power* of the parameter α comes from its relative independence of run characteristics, and as a consequence of this, its

sensitivity to very subtle changes in the vortex lattice. *Lee et al (1993)* [61] noted a sudden change in the sign of the α parameter in BSCCO and attributed this to the melting of the flux lattice. Other changes in the flux structure, such as the decomposition into decorrelated 2D flux lattices from the 3D lattice may also be inferred from changes in α. In quantifying the lineshapes it has also been fruitful to utilise another dimensionless skewness parameter β (cf Eq. 3.20). The β parameter has been used successfully by *Lee et al (1997)* [69] in the characterisation of the organic superconductor κ-(BEDT-TTF)$_2$Cu(NCS)$_2$. It is more sensitive to the subtle changes in the probability distribution, which, for a narrow lineshape , due to finite binwidth (i.e. finite time window) in the p(B), may only be formed from relatively few points. Here, as with the α parameter, a value of β=0 indicates a symmetric lineshape. A positive value reflects that for a lineshape arising from a vortex line lattice.

$$\beta = (\langle B \rangle - B_{sad})/(\langle B^2 \rangle - \langle B \rangle^2)^{1/2} \tag{3.20}$$

3.2.4 Experimental facilities

The muon spin rotation experiments described in this thesis were undertaken at two international facilities. The μSR beam line, ISIS, Rutherford Appleton Laboratory (RAL), Oxfordshire and on the πM3 beam line, Paul Scherrrer Institute (PSI) Villigen, Switzerland.

MUSR Instrument, RAL

The ISIS facility at RAL provides a pulsed muon source. A pulsed proton beam strikes a graphite target and muons of 29 MeV/c are selected by bending magnets in the beamline. These muons stop within a fraction of a millimetre upon entering

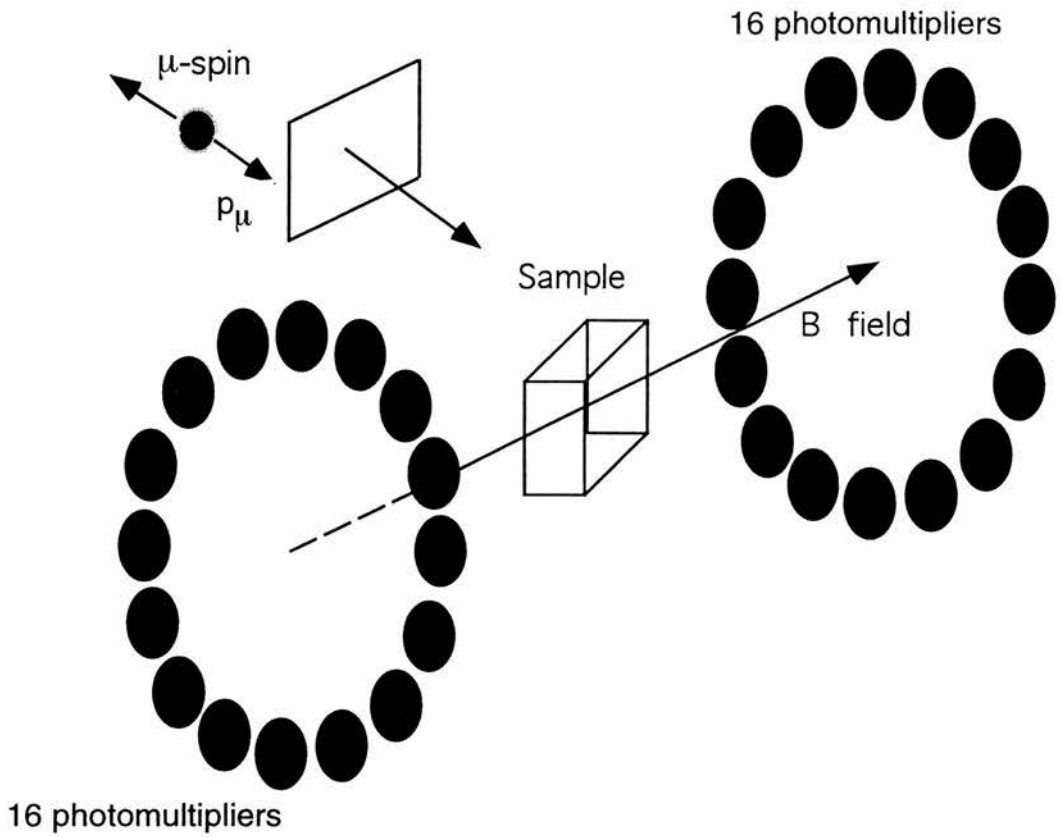

Figure 3.6: Schematic diagram of the MUSR spectrometer at RAL. The arrival of the muon pulse is indicated by a Cherenkov counter which starts a timer. The positrons emitted by decaying muons are detected by 32 photomultiplier tubes arranged around the sample.

the sample. Pulses lasting 90 ns arrive in the sample area every 20 ms. One drawback of a pulsed source is the restriction that is put on the applied field. Muons arriving first at the sample will begin to precess before those at the tail of the pulse. If the applied field is too high the phase coherence between muons will be lost resulting in an increasingly smaller signal as the field is increased. This limits the applied field to about 60 mT in the transverse field geometry. A Cherenkov counter starts a clock when the pulse arrives and all subsequent decays are timed relative to this. 32 photomultiplier tubes mounted around the sample record the positron decays in time histograms with 1024 bins of 16 ns width (see Fig. 3.6). In order to simplify the analysis, output from the detectors are usually grouped in groups of 4. The early part of the signal is discarded as, in this initial stage, just after the muon pulse has arrived, saturation of the detectors will occur due to deadtimes effects. The magnetic field is applied at right angles to the incoming beam, and also, the muons magnetic moment. The MUSR instrument presents a slight problem for crystals formed as plates with the superconducting planes parallel to the crystal faces. If one were to align these crystals with the applied field perpendicular to the superconducting planes, as is usually desired in such an experiment, a very small cross-sectional area would be presented to the incoming beam. Alternatively to present the maximum crystal x-sectional area would result in the field applied parallel to the planes. For an investigation which involves applying the field at large angles to the planes, the MUSR instrument is ideal, as larger crystal cross-sectional areas will be presented to the beam the higher the angle attained (see Fig. 3.7).

The sample environment used for the high temperature experiments described in this thesis were a close cycle refrigerator (CCR). The CCR allowed temperatures

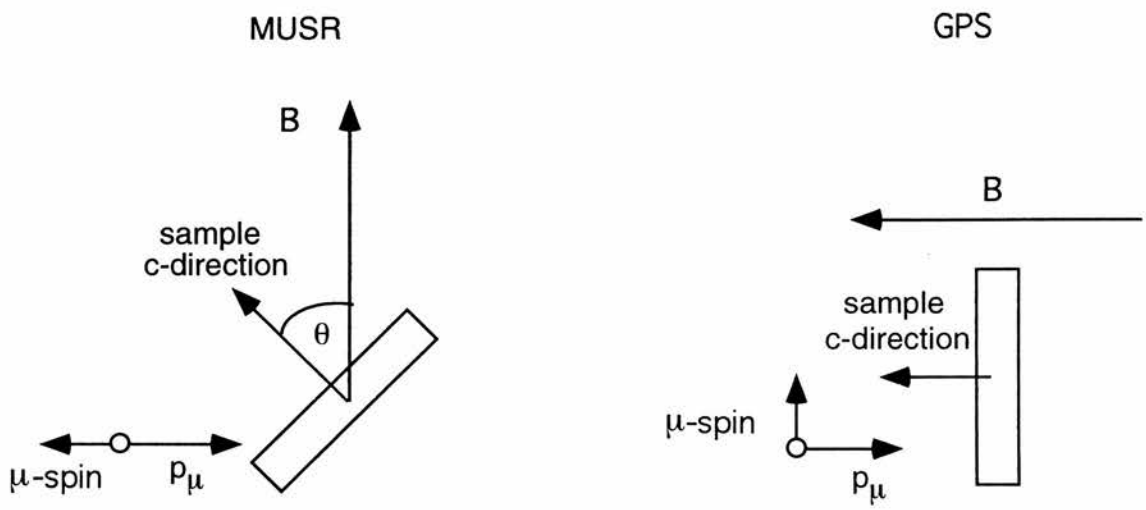

Figure 3.7: A plan view of the experimental geometry on the MUSR spectrometer RAL and at the GPS on the πM3 beamline (PSI). Transverse μSR requires the muon spin to have a component perpendicular to the field. For MUSR it can be seen that the plate-like crystal shape, coupled with the longitudinal spin-polarisation of the beam, favours larger angles θ between the field and the crystallographic c-direction, such that a larger cross-section of the sample is presented to the beam. MUSR is thus ideal for measurements with angles of c to the applied field of $45^o < \theta \leq 90^o$. Conversely the transverse polarisation of the πM3 beam is ideal for covering the range $0^o \leq \theta < 45^o$.

between 10 K and 300 K to be attained. For the experiments at lower temperatures an A.S. Scientific orange cryostat and dilution fridge were used, allowing temperatures as low as 40 mK to be attained. One of the most important considerations in experiments, such as those carried out at RAL, is the destiny of those muons which do not land in the sample. Muons landing in the metal sample holder will precess according to the applied field, producing a second peak in the field distribution and masking important sample behaviour. In order to reduce this, exposed surfaces of the sample holder are covered in anhydrous haematite. Muons landing in this haematite are rapidly depolarised. These muons do not contribute to the oscillating μSR signal, but they do contribute to the overall counts recorded by the detector, reducing the signal to noise ratio. To reduce this, a flypast holder has been implemented for use with the CCR. This holder, which holds the sample in place with two thin, haematite covered, arms, allows the majority of the muons which do not stop in the sample to bypass. These muons leave the CCR via mylar exit windows and decay in the air some distance away, contributing few positrons to the overall signal.

Paul Scherrer Institute(PSI)

This facility differs from that of ISIS in that it provides a quasi continuous source, requiring a different method of data aquasition to that above. A counter detects the arrival of a muon in the sample area, starting a timer. Ideally, this muon lands in the sample, precesses, and is detected by one of three detectors (see Fig. 3.8). The electronics will record a valid data point if another muon has not arrived in the sample area within 10 μs of the first. This procedure ensures that any positron detected comes from the original muon and not from one which entered

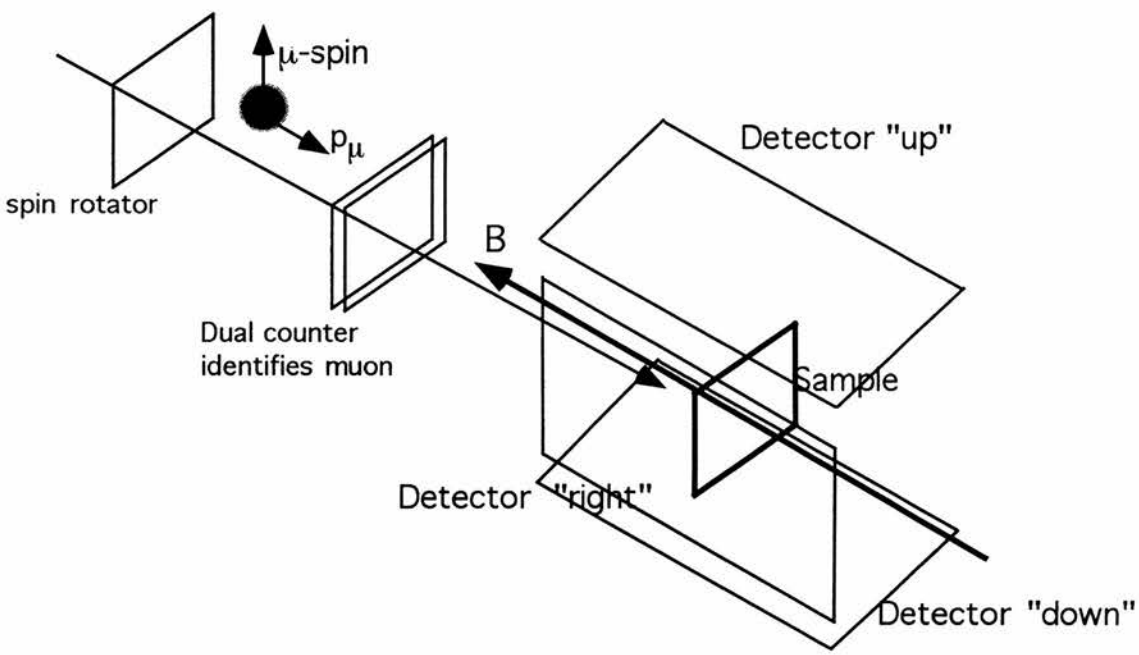

Figure 3.8: A schematic of the GPS (General purpose Spectrometer) on the πM3 beamline PSI.

the sample later. This technique is not perfect however, and spurious decays produce a constant background of about 1%. As the muons arrive individually in the sample, useful data can be obtained very soon after this arrival. This allows samples with high damping rates to be investigated. The time window is shorter, however than the MUSR time window($\sim$16 μs). In comparison to MUSR, this short time-window reduces the amount of useful information that can be collected for systems with long dephasing times such as κ-(BEDT-TTF)$_2$Cu(NCS)$_2$. On the GPS the applied magnetic field is parallel to the incoming beam. Transverse μSR at this facility would be impossible if it was not for a spin rotator contained in the beamline. This device uses crossed electric and magnetic fields to rotate the muon spin 90^o with respect to its momentum (see Fig. 3.7). The sample environment on GPS is a Quantum Technology continuous flow cryostat which can attain a temperature of 1.5 K. An Oxford instruments Dilution Fridge was also used for experiments on the organic superconductor α-(BEDT)$_2$NH$_4$Hg(SCN)$_4$, and this could attain temperatures as low as 100 mK. As at RAL, the sample holder was covered in haematite to ensure that muons that miss the sample depolarise too rapidly to contribute to the measured damping.

3.3 Small Angle Neutron Scattering (SANS)

3.3.1 Introduction

The technique of neutron scattering is a well established tool for the investigation of the structure of condensed matter. The basis for this lies in the fact that the neutron, with no electric charge, can penetrate deeply into the bulk of most materials. This, combined with the fact that the wavelength of thermal neutrons are

comparable to interatomic spacings lends them to interference effects which can yield valuable information about the internal structure of many materials. Due to the magnetic moment of the neutron, magnetic structures may also be studied. In this sense the neutron is an excellent tool for studying flux lattices in type II superconductors where coherent Bragg scattering will occur if the flux lines form a regular array. Such a study yields spatial information, the shape and intensity of the diffraction spots as a function of temperature providing a wealth of information about the arrangement of the flux lines. This has obvious advantages over techniques, such as Bitter decoration, which are restricted to an investigation of flux structures at the surface of crystals. In a typical experiment, as the separation, d, of planes of vortex-lines in a lattice is typically of the order of thousands of Angstroms at the fields of interest, the scattering angle 2θ, given by Bragg's law $n\lambda_n = 2dsin\theta$, is typically $\sim 1^o$ or less (larger scattering angles may be achieved with neutrons of longer wavelength, but this results in a reduction of neutron flux (see Fig. 3.9)). The technique employed, therefore, is usually referred to as small-angle neutron scattering (SANS). The remainder of this chapter outlines the basics of SANS. A more comprehensive treatment can be found in e.g. refs [70, 71].

3.3.2 Theory

The neutron has a magnetic moment $\mu_\mathbf{n}$

$$\mu_\mathbf{n} = -\gamma|\mu_n|\hat{s} \tag{3.21}$$

where μ_n is the nuclear magneton and γ a positive constant of value 1.913. As has been mentioned, this moment allows the neutron to interact with a magnetic

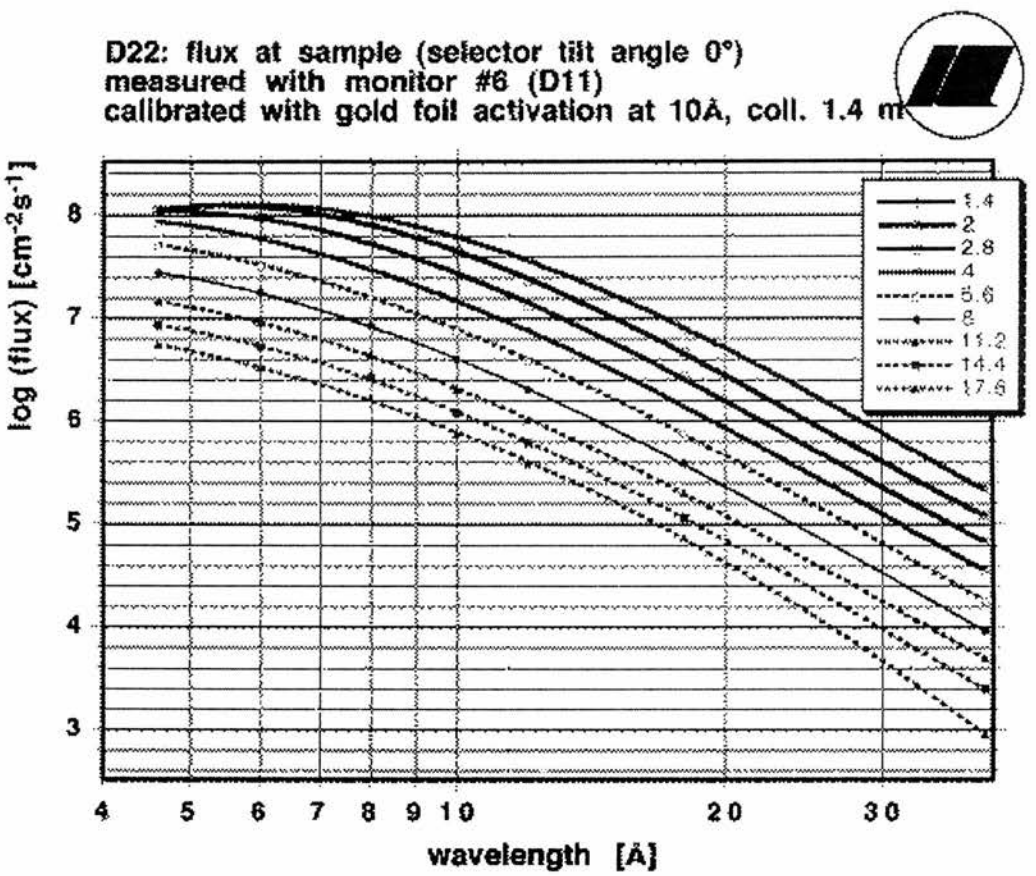

Figure 3.9: A graph of the neutron flux against wavelength for the D22 instrument, ILL, at different detector distances. Using a longer neutron wavelength results in better resolution of the diffraction pattern, but this has to be traded against a decrease in the neutron flux. Courtesy of *C. Dewhurst* [72].

field , its potential in this field, $\mathbf{B}$, being given by

$$U = -\mu_{\mathbf{n}}.\mathbf{B} \tag{3.22}$$

Magnetic field variations in the magnetic field inside the sample lead to scattering of the incident neutrons. In an analogous way to the planes of atoms in a crystal lattice coherent scattering will be realised if the magnetic field variation form a regular pattern, as in the case of a flux lattice. Neutrons scatter from these "planes" of magnetic flux, the familiar form of Bragg's law describing the phenomenon. In such a diffraction experiment, coherent scattering will occur if incident neutrons with wavelength λ_n and of incident angle satisfy the Bragg condition (cf Eq. 3.23) for a set of magnetic "planes", defined by Miller Indices hk, if

$$\lambda_n = 2d_{hk}sin\theta \tag{3.23}$$

where d_{hk} is the spacing between the hk planes. According to *Laue* [73] (a more rigorous form of Braggs law expressed in terms reciprocal lattice vectors), since the scattering is elastic the incident and scattering wavevectors are of the same magnitude, that is

$$|\mathbf{k_{in}}| = |\mathbf{k_{out}}| = \frac{2\pi}{\lambda_n}. \tag{3.24}$$

For coherent scattering $\mathbf{k}_{in}$ and $\mathbf{k}_{out}$ must satisfy

$$\mathbf{k_{out}} - \mathbf{k_{in}} = \mathbf{q_{hk}} \tag{3.25}$$

where $\mathbf{q}_{hk}$ is the reciprocal lattice vector for a set of planes hk. $\mathbf{q}_{hk}$ is directed perpendicular to the hk planes with a magnitude given by

$$|\mathbf{q_{hk}}| = \frac{2\pi}{|\mathbf{d_{hk}}|} \tag{3.26}$$

where, as before, $|\mathbf{d}_{hk}|$ is the spacing of the hk planes in real space. In a type II superconductor the spacing of the flux lines, and hence the magnetic planes is

determined by the magnetic field **B**. This spacing is related to the applied field **B** according to the type of lattice the planes form. This is most commonly a hexagonal lattice, but square flux-line lattices have been observed, e.g. in Strontium Ruthenate (Sr_2RuO_4) [74, 75] and YNi_2B_2C [76]. The spacing is given below for triangular and square lattices respectively

$$|\mathbf{d_{hk}}| = \sqrt{\frac{\sqrt{3}\Phi_o}{2B}} \tag{3.27}$$

$$|\mathbf{d_{hk}}| = \sqrt{\frac{\Phi_o}{B}} \tag{3.28}$$

All of the possible orientations of planes in real space correspond to lattice points in reciprocal space.

Laue's diffraction condition is therefore equivalent to stating that the origin of the reciprocal lattice and a point on the reciprocal lattice must lie on the surface of the sphere of radius $\mathbf{k_{out}}$, known as the Ewald sphere (see Fig. 3.10).

The total amount of scattering produced by a set of planes *hk* is referred to as the integrated intensity. In general, as the planes are not perfectly aligned along the beam direction, it is necessary to rotate the sample about an axis perpendicular to the neutron beam in order to observe all of this scattering from the planes. This 'rocking curve', which is the intensity from the *hk* planes as a function of the angle of the sample rotation allows the integrated intensity to be determined. The integrated intensity from a Bragg peak for a particular set of planes *hk* is given by *Christen et al(1977)* [77] as

$$|I_{hk}| = 2\pi\varphi(\frac{\mu_n}{4})^2 \frac{V\lambda_n^2}{\Phi_o^2|\mathbf{q_{hk}}|}|F_{hk}^2| \tag{3.29}$$

where φ is the incoming neutron flux, μ_n is the magnetic moment of the neutron in nuclear magnetons, V is the irradiated volume of the sample, and F_{hk} the

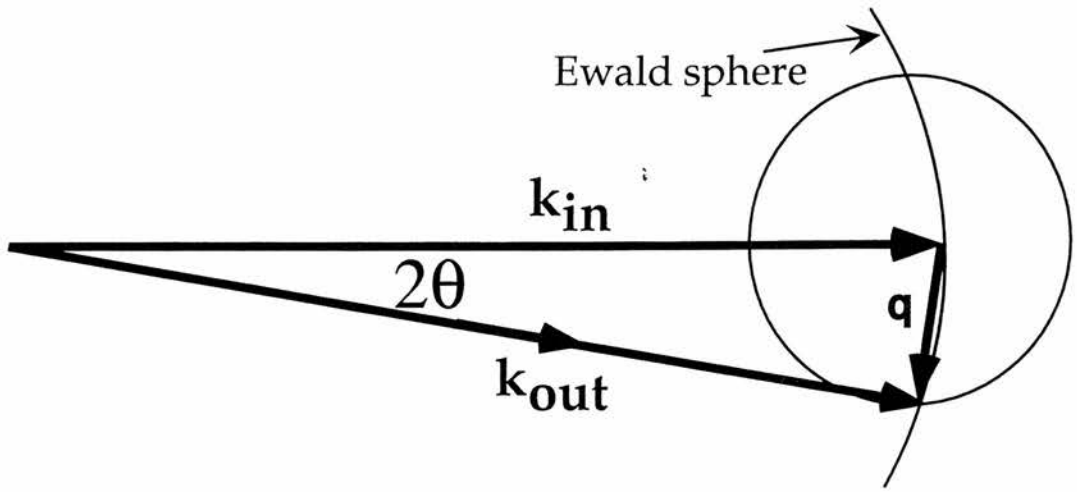

Figure 3.10: The vector representation of Bragg's law, where $\mathbf{k}_{out}$ and $\mathbf{k}_{in}$ are the final and initial neutron wavevectors.

'form factor' for the set of planes *hk*. This form factor is the normalised Fourier transform of the two dimensional field distribution *h(***r***)* viz.

$$AF_{hk} = \int h(\mathbf{r}) exp(i\mathbf{q_{hk}}.\mathbf{r}) d^2\mathbf{r} \tag{3.30}$$

where A is the normalisation factor. Bragg diffraction effectively picks out spatial frequencies of the magnetic field variation inside the sample. Significant Bragg scattering will therefore occur when the flux lattice is well ordered. The larger the amplitude of variations of the internal magnetic field, the greater the contrast and therefore stronger the diffracted intensity. For large κ superconductors, such as HTSC, the form factor can be written explicitly as

$$F_{hk} = \frac{B}{1 + (q_{hk}\lambda_{ab})^2}. \tag{3.31}$$

For all fields larger than H_{c1}, the second term in the denominator of Eq. 3.31 is dominant, so the intensity given by Eq. 3.29 varies with wavevector as $(q_{hk})^{-5}$. The consequence of this is that higher order reflections are much weaker than low

order ones, because the flux lines are finite objects with a field extending over a distance λ. It is worth noting that through the form factor that experiments on materials with long penetration depths are significantly more difficult than in many conventional superconducting materials (cf Eq. 3.32).

$$I_{hk} \propto \frac{1}{\lambda^4} \tag{3.32}$$

Under the ideal conditions above the observed diffraction spots would be delta functions. Experimentally however, there are several reasons for a deviation from this ideal situation and the Bragg spots will be of finite extent in reciprocal space due to the mosaic spread of the vortex lattice. The possible origin of the width due to the mosaic spread are twofold. The correlation length of the vortex crystal along the field direction may be finite due to vortex pinning and this will destroy the long range order. Secondly, mosaic spread may also come from a bending of the vortex lines, indistinguishable from finite correlation effects. It should also be stressed here that the width of the Bragg spots is also dependent upon the instrumental resolution parameters [78]. These include the wavelength spread $\Delta\lambda/\lambda \sim 9\%$ [79] and the angular beam divergence, which is determined by the input collimation. The spread of the vortex lattice parameters could in principle be determined by the size of the Bragg spots, but unless this is large, it is the instrumental factors which determine the measured spot size. (see e.g. ref. [78]).

Together with the above spread of the scattered intensity, this may also be further reduced by the presence of thermal vibrations as is the case in atomic systems [80]. Thermal fluctuations have been found to reduce the form factor F_{hk} for scattering by a Debye Waller factor

$$exp(-\frac{1}{2}\mathbf{q_{hk}^2}\cdot\langle\mathbf{u}\rangle^2) \tag{3.33}$$

where $\mathbf{q_{hk}}$ is the reciprocal lattice vector for the Bragg peak and $\langle \mathbf{u^2} \rangle$ the displacement produced by disorder, which can either be static or dynamic. Static disorder can be produced in a flux-lattice by the presence of pinning, while dynamic disorder will become increasingly important at higher temperatures. The effect of thermal fluctuations are of particular importance as they drastically alter the temperature dependance of the scattered intensity. By the nature of the scattering only displacements perpendicular to the field will affect the scattered intensity and as the amplitude of thermal fluctuations, $\langle u_{th}^2 \rangle$, increase with temperature, this Debye Waller factor leads to a stronger temperature dependance than given by the two-fluid model. Higher order scattering is strongly affected due to the factor of $\mathbf{q_{hk}^2}$ in the Debye Waller factor.

3.3.3 Experimental

Observing the flux lattice in the high temperature and organic superconductors such as $Bi_{2.15}Sr_{1.85}Ca_1Cu_2O_{8+\delta}$ (BSSCO) and κ-(BEDT-TTF)$_2$Cu(NCS)$_2$ (ET-Cu) respectively, is not trivial. This is primarily due to the long penetration depths that these materials exhibit. As an example, BSSCO has a penetration depth which is 4.5 times as long as niobium. This results in a huge decrease in the scattered intensity in accordance with Eq. 3.32.

Figure 3.11a shows a very basic schematic of a typical SANS experiment. Some further information should be provided. A rotating "chopper" acts as a velocity/wavelength selector for the incoming neutrons. The beam then passes through a monitor, which allows the number of neutrons incident on the sample to be recorded. After passing through a source slit the beam travels along an evacuated tube and is incident on the sample. The collimation length is variable to

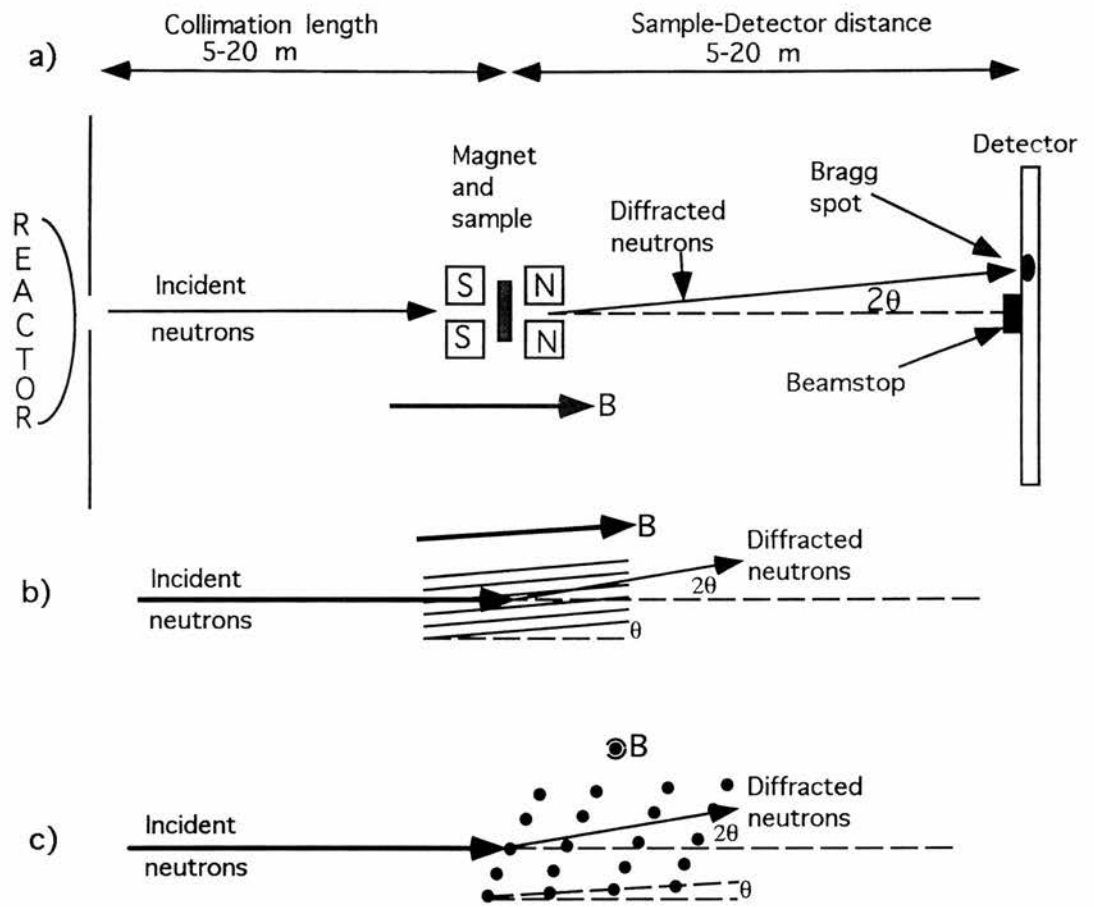

Figure 3.11: a) A Schematic representation of the experimental arrangement for a SANS experiment. b) The geometry is usually chosen with the field approximately parallel to the incident neutrons. In this configuration the planes of the vortex lattice may easily be brought into the scattering condition. c) The alternative geometry with the field perpendicular to the beam.

allow the optimum trade-off between resolution and intensity to be obtained. The incident beam is also produced by using a "cold" moderator which produces neutrons of longer wavelength which increase the angles of diffraction. In Fig. 3.11a the neutrons are Bragg scattered by the vortex lattice and are detected using a two-dimensional multi-detector. In order to allow good angular resolution this detector is usually a large distance from the sample (5-20 m). In order to prevent damage to the detector due to the straight-through beam a beamstop is employed. The geometry which is normally chosen is one with the applied field parallel to the incoming beam, shown in Fig. 3.11b. In this geometry any of the planes of the vortex lattice may easily be brought into the scattering condition by rotating the sample through a small angle about an appropriate axis. In the alternative geometry (cf Fig. 3.11c) in which the field is applied perpendicular to the incident beam, large sample rotations would be required to bring successive equivalent planes of a triangular lattice into the Bragg condition [71]. Initial alignment of the magnetic field with respect to the beam may be achieved by observing a single crystal niobium sample. Niobium, apart from the considerable increase in diffracted intensity mentioned earlier, is isotropic and therefore any flux-lattice grown in this system follows the field more closely than HTSC [81, 82]. This allows the tilt and rotation of the magnet to be adjusted for a symmetrical diffraction pattern very quickly. Scattering from the flux-lattice is far weaker than the background due to the cryostat and the crystal and crystallographic defects. In order to observe scattering from the flux-lattice a background measurement is taken, either above T_c or, more appropriately, at the desired measurement temperature with the field off. By subtracting this background form the foreground (field-on), only the scattering from the lattice will remain. The data is analysed using a program called

SANSAN that was written at Birmingham University by *R. Cubitt & E.M.Forgan & S.L.Lee* [68]. This program performs the background subtractions. In order to produce a good subtraction the background may be shifted slightly by a small amount ($\sim$ pixel) with respect to the foreground. The intensities of diffracted spots can be analysed by summing up the counts in a box that includes the spot or by fitting the data to a Gaussian profile.

3.3.4 Experimental Facilities

The experiments in this thesis were performed at the Institut Laue-Langevin(ILL) in Grenoble, France. The ILL is the world's most powerful reactor neutron source, with a peak flux of 57 MW, producing neutrons for a wide range of instruments. The reactor is equipped with a "cold source" that allows the use of long wavelength neutrons. This is a tank of liquid deuterium held at 25 K in the neutron beamline. As the neutrons pass through it they are thermalised and leave the tank with wavelengths $\sim$ 4-25 Å which are invaluable in SANS measurements. The experiments in this thesis were performed on the D22 small angle diffraction instrument whose specifications are given in Table 3.1. Further details of the experiments are given in chapters 5 and 6.

Diffractometer Specifications					
Instrument	Sample detector distance	Collimation distance	Wavelength	Detector Array	Pixel Size
ILL D22	1.3-18m	2.5-18m	4-25Å	128×128	7.5×7.5mm^2

Table 3.1: The specifications [79] of the diffractometer D22, ILL used during investigations carried out in this thesis.

3.4 Magnetization of layered superconductors and Torque Magnetometry

3.4.1 Introduction and theory

It was originally thought that the torque on a superconductor in a magnetic field H was dominated by trapped flux or sample shape effects. It is now a well known phenomenom that anisotropic HTSC experience intrinsic torque for $H_{c1} << H < H_{c2}$ [82, 83]. The physical reason for this is the fact that the current loops around the vortex core have a tendency to lie in the copper oxide planes (ab-planes). When the field is applied at an arbitrary angle to the c-direction a magnetisation which is not parallel to the applied magnetic field develops. This is depicted in Fig. 3.12.

The torque per unit volume of a superconductor is the vector product of the magnetization and the applied field (cf Eq. 3.34).

$$\tau = \mu_o \mathbf{M} \times \mathbf{H} = \mu_o M_\perp H. \tag{3.34}$$

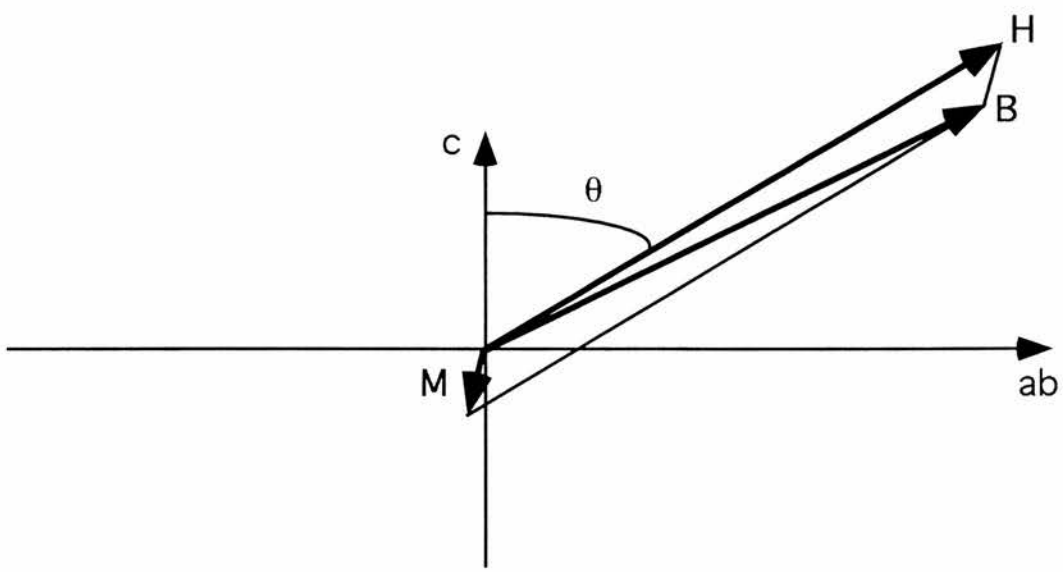

Figure 3.12: A schematic diagram illustrating the fact that **M** is not collinear with **B** unless **B** lies along a principle axis. (i.e. the torque on the sample will be zero when the applied field is directed along directions a,b or c in HTSC). Also depicted is the fact that $|\mathbf{M}| \ll |\mathbf{B}|$ so that $\mathbf{B} \approx \mathbf{H}$. This was shown to be the case in HTSC for the field range $H_{c1} \ll H < H_{c2}$ by *Kogan et al (1988)* [82] and greatly simplifies torque experiments by allowing demagnetizing fields to be negelected.

In a layered superconductor the reversible torque has been evaluated in the London limit as depending on angle θ_{cl} according to [82, 83]

$$\tau(\theta_{cl})_{rev} = \frac{\phi_o HV}{16\pi\lambda_{ab}^2} \frac{\gamma_{cl}^2 - 1}{\gamma_{cl}^{1/3}} \frac{sin2\theta_{cl}}{\epsilon(\theta_{cl})} ln\left(\frac{\gamma_{cl}\eta H_{c2}^{\perp}}{H\eta(\theta_{cl})}\right) \tag{3.35}$$

where $\varepsilon(\theta_{cl}) = (sin^2\theta_{cl} + \gamma_{cl}^2 cos^2\theta_{cl})^{1/2}$, θ_{cl} is the angle between the applied field and the c axis, $\gamma_{cl} = \lambda_c/\lambda_l$ (l denotes either a or b), $H_{c2}^{\perp}$ is the upper critical field perpendicular to the ab plane, η depends on the structure of the flux-line lattice, λ_{ab} is the effective in-plane penetration depth and V is the sample volume. There is no reliable theoretical estimate for η at present [82] but it is thought to be of the order of unity. It is evident from Eq. 3.35 that the measurement of torque in a layered superconductor may yield such interesting information as the superconducting anisotropy, γ and the the upper critical field perpendicular to the superconducting planes, $H_{c2}^{\perp}$.

3.4.2 Experimental apparatus

The torque magnetometry carried out in this thesis was carried out on a home-built torque magnetometer at the University of St.Andrews, Scotland. The facility was initially developed for the routine characterisation of nanoparticles utilising a torque sensor based on a commercial piezoresistive cantilever (see e.g. [84]). For the characterisation of the large single crystal detailed in this work (see Chapter 4) a capacitance detection system was employed. A basic schematic of the capacitance-cantilever rig is shown in Fig. 3.13. The cantilever was constructed from phosphor bronze and is depicted as it rests in its equilibrium position. In the presence of a homogenous applied field, a transverse component of field in the experimental sample will cause the cantilever to deviate from this equilibrium position. This deviation results in a variation in the capacitance between the cantilever and the

fixed capacitance plates. This deviation was measured using the set-up shown in Fig. 3.14. At the start of an experimental scan the voltage across the detector was balanced using the variable capacitor. During a measurement, deviation of the sensor from the balanced position would result in the flow of current through the detector (Det.). This capacitance-cantilever rig has a torque sensitivity of $\Delta\tau \approx 10^{-8}$N m. In an applied field of 1 T this makes it possible to measure magnetic moments of $\Delta m \approx 10^{-8}$ A m^2. The sample environment was an Orange Cryostat supplied by A.S Scientific products ltd, Abingdon, Oxon. This cryostat was mounted on a rotation rig which allowed the cantilever to be rotated around a fixed field direction through scan angles of over 360°. The field could also be swept through a range of 1 Tesla and temperatures as low as 1.4 K could be attained. Further details of the torque experiments are given in Chapter 4.

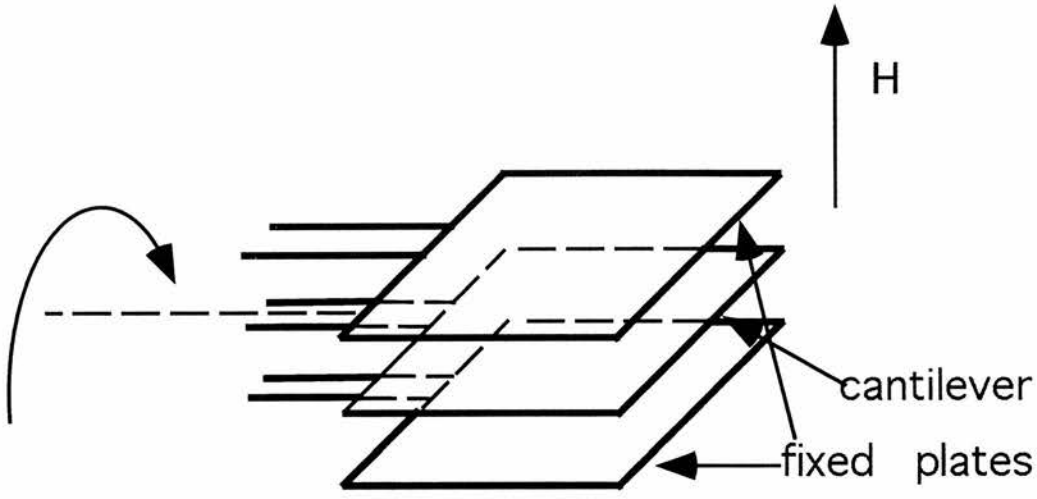

Figure 3.13: A basic schematic of the capacitance-cantilever rig. The cantilever and fixed plates were made from phosphor bronze and may be rotated round the fixed field direction as shown. Samples can be attached to the cantilever via a mixture of Bostik glue and acetone.

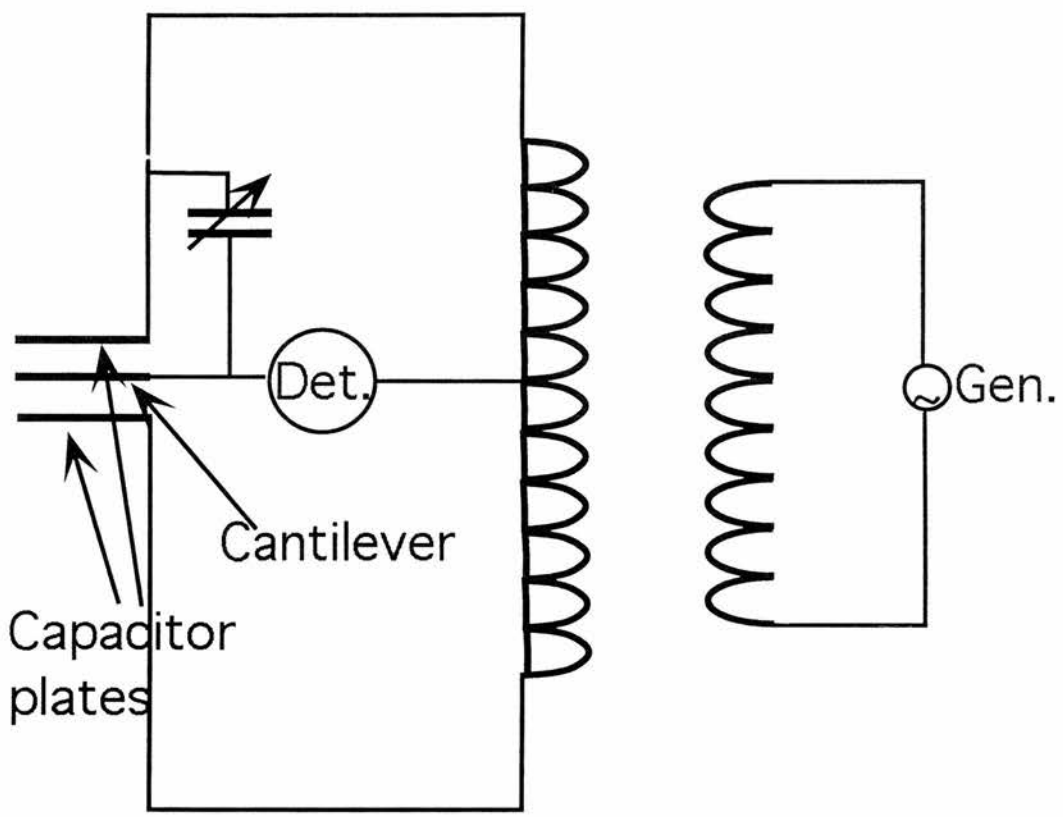

Figure 3.14: A schematic of the basic setup for the measurement of deviations of the cantilever. Shown in the diagram are the cantilever with capacitance plates on either side. Before a measurement was undertaken the potential across the detector (Det.) was balanced. When the cantilever deviated from the balanced position a signal could be measured.

Chapter 4

Flux lattice melting and Anisotropic Flux Lattice in $YBa_2Cu_3O_{7-\delta}$ (YBCO)

4.1 Introduction

The flux lattice in the high-Tc superconductors (HTSC) is a subject area which has grown rapidly over the last decade. This interest has mainly been driven by the extremely exotic vortex behaviour that they appear to exhibit and their obvious technological potential. The key feature in the high-Tc materials that governs the structure of the flux lattice is the superconducting anisotropy [53]. As has been seen, this anisotropy is reflected in the ability of the superconducting charge carriers to screen magnetic fields, and is normally quantified as $\gamma = \lambda_c/\lambda_{ab}$, where λ_c and λ_{ab} are the penetration depths for currents flowing perpendicular ($\lambda_\perp$) and parallel ($\lambda_\parallel$) to the superconducting copper oxide planes respectively. In the HTSC $YBa_2Cu_3O_{7-\delta}$ (YBCO123) previous studies of this anisotropy have been

masked by the presence of twin-plane defects which run parallel to the c direction and cause the a and b directions in different parts of the crystal to coincide (see section 2.1). These twin-plane defects also mask the intrinsic anisotropy between the a and b directions. This latter anisotropy is not of significance in systems such as $Bi_{2.15}Sr_{1.85}Ca_1Cu_2O_{8+\delta}$ (BSCCO) (which is tetragonal) or $HgBa_2Ca_3Cu_4O_{10}$ (HBCCO), but for a system of such moderate out-of-plane anisotropy such as YBCO123 [85, 86, 87, 39, 40, 88, 83, 89, 90] this anisotropy cannot be overlooked. A large *untwinned* YBCO123 crystal has been the subject of an extensive study. This study includes both the out-of plane anisotropy, $\gamma = \lambda_c/\lambda_{ab}$, and the in-plane anisotropy, $\gamma_{ab} = \lambda_b/\lambda_a$, the determination of the penetration depths, and evidence for melting of the flux-line lattice (FLL) in YBCO123.

4.2 Previous work

The anisotropy of YBCO123 has previously been extensively studied. In comparison to other HTSC, e.g. BSCCO, $\gamma = 150$ [43] and HBCCO, $\gamma = 52$ [84] the out-of-plane anisotropy of YBCO123 is very modest, making it the prime candidate amongst HTSC for technological development. Previous estimates of the anisotropy in YBCO are summarized in Table 4.1. The majority of these previous studies have been carried out on twinned crystals. As has been already mentioned, twin-planes are extended defects which run parallel to the crystalographic c direction and cause the a and b crystalographic axes to interchange in different parts of the crystal [38]. In the presence of these twin-plane defects, determining the importance of the 'in' and 'out'-of-plane anisotropies can be particularly difficult. Studies have also been carried out on detwinned crystals [24] . Detwinned crystals are fabricated by applying uniaxial pressure along the a direction ($b > a$)

of optimally doped flux grown crystals at moderately high temperatures. Large detwinned crystals are difficult to fabricate and μSR studies require either a large mosaic of well-aligned detwinned crystals or a large untwinned crystal.

A large amount of research effort has concentrated on the melting transition in the HTSC. It has been argued that twinned YBCO exhibits a second order transition as a result of the effect of the extremely strong pinning afforded by the twin-plane defects which mask an intrinsically first order transition [53]. This is further supported by the fact that the transition observed (for instance by μSR [61] and SANS [91]) in BSCCO were generally sharp and not inconsistent with a first order transition [92], while twinned YBCO samples gave a more gradual transition. The low anisotropy exhibited by YBCO ensures that the vortex lattice melts at sufficiently high fields to be studied using thermal measurements such as differential thermal analysis (DTA) [93, 94] and specific heat [95]. DTA measurements on untwinned samples have clearly shown the existence of a first order transition [93, 94]. Specific heat measurements have also shown a first order transition even though the sample was heavily twinned [95]. The order of the transition is in general much more complicated than the untwinned case in that the order of the transition may also depend on the applied field [95]. The order of the melting transition may also influenced by the the degree of defects (both impurities and twin planes), where an excess of pinning sites of any kind drives the transition to second order. Further interest has included the dependence of the melting transition on the angle of the field with respect to the c-axis [94] with detailed predictions on the field dependence of the melting temperature (melting line) on angle from anisotropic London theory [96].

YBCO123, anisotropy			
Method(Sample)	$\gamma = \lambda_c/\lambda_{ab}$	$\gamma = \lambda_b/\lambda_a$	References
μ SR(S/OP)	5(1)	...	[85]
μ SR(SC)	>5	...	[86]
Bitter Decoration(SC)	5.5(1.0)	1.13	[87, 39]
Josephson tunnel junctions	...	$\geq \sqrt{2}$	[41]
Polarized reflectivity	...	1.2-1.7	[40, 88]
SANS(SC)	$\approx$ 4.5	...	[97, 98]
SANS(USC)	...	1.18(2)	[38]
Magnetic torque(SC)	5.1	...	[83]
Magnetic torque(SC*)	12.3	...	[89]
Magnetic torque(USC)	7.55(63)-8.95(76)	1.18(14)	[90]

Table 4.1: Values of the 'in' and 'out'-of-plane anisotropies for a sintered sample(S), c-axis orientated polycrystals(OP), single crystals(SC) and untwinned single crystals(USC). SC* refers to work carried out on a crystal of YBCO124. This compound has double CuO chains along the b axis which prevents the formation of twin-plane defects [89].

YBCO123, penetration depths			
Method(Sample)	$\lambda_{ab}(0)$(Å)	$\lambda_c(0)$(Å)	References
μ SR(S/OP)	1300(100)	500-800	[85]
μ SR(SC)	1415(30)	>700	[86]
Josephson tunnel junctions	$\lambda_a \approx 1600 - 4000$ $\lambda_b \approx 900 - 1800$	...	[41]
Polarized reflectivity	$\lambda_a \approx 1600$ $\lambda_b \approx 1000 - 1200$	...	[40, 88]
SANS(USC)	$\lambda_a = 1500(60)$ $\lambda_b = 1270(60)$	...	[38]
Magnetic torque(SC*)	1430	...	[89]

Table 4.2: Values of the penetration depths for samples. The abbreviations used here are as for Table 4.1.

4.3 Sample Characterisation

The sample used in this study consisted of a large (1.125 g) YBCO123 single crystal supplied by *A. I. Rykov* SRL-ISTEC, Koto-ku, Toykyo 135, Japan. This was grown untwinned by the application of uniaxial stress during the cooling from melt [99]. For the oxygenation process, the sample was treated in flowing O_2 at 490^oC. Magnetisation measurements using a vibrating sample magnetometer (VSM) on a small piece of the sample indicate a T_c of 93.5 K with a transition of $\sim$0.5 K [100].

4.4 Muon Spin Rotation Measurements

4.4.1 Experimental Setup

Muon spin rotation measurements were performed to characterise the sample using the MUSR spectrometer at the Rutherford Appleton Laboratory(RAL) and the GPS spectrometer on the πM3 beamline at PSI. The sample environment on MUSR was a close cycle refrigerator (CCR). In the CCR the sample was mounted on a flypast sample holder. This holder, which holds the sample in place with two thin, haematite covered arms, allows the majority of the muons which do not stop in the sample to bypass. These muons leave the CCR via thin mylar exit windows and decay in the air some distance away. Haematite is an antiferromagnet in which the muons see a local field of 1.6 T so the corresponding spectra from those muons landing on the holder's arms do not interfere with the signal from the superconductor. The sample environment on the GPS was a Quantum Technology continuous flow cryostat. Here the sample was mounted on a haematite backing plate.

4.4.2 Results of muon spin rotation experiments

With the field perpendicular to the superconducting planes, detailed μSR measurements were made as a function of temperature at 0.02 T, 0.3 T and 0.6 T. Figure 4.1 shows the temperature dependence of the mean internal field at an applied field of 0.3 T. The onset of diamagnetic behaviour confirms that the transition temperature in this crystal is $\sim$ 93.5 K. Figure 4.2 shows the lineshape taken for the field applied perpendicular to the superconducting planes. This data was taken at 5 K after cooling in an applied field of 0.6 T. This lineshape clearly

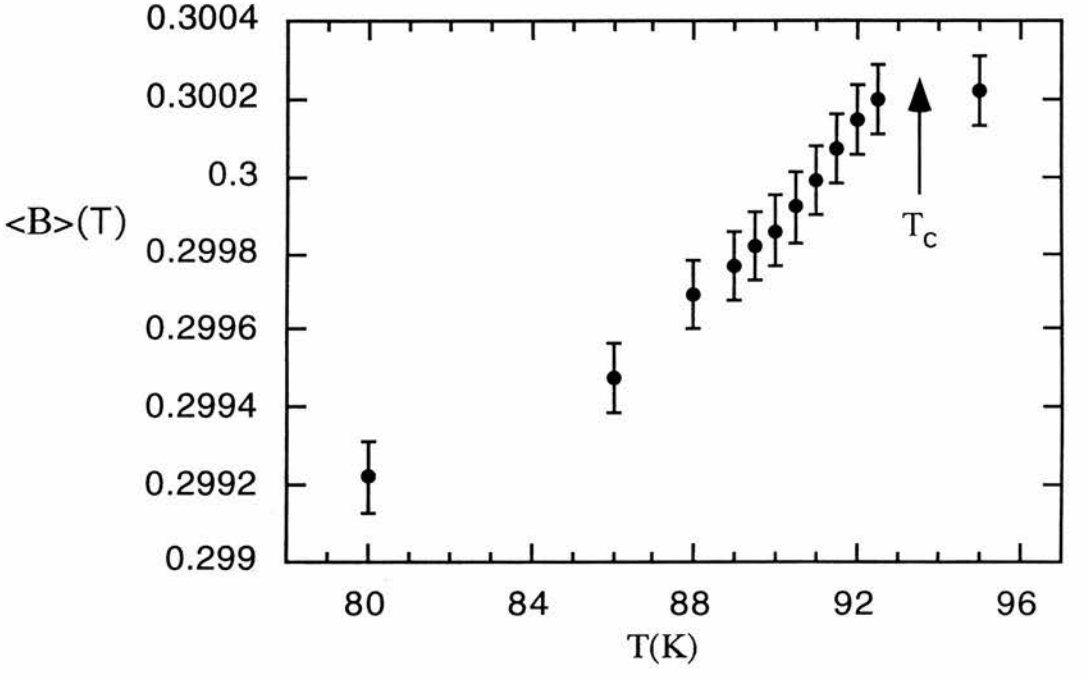

Figure 4.1: The temperature dependence of the mean internal field <B> at 0.3 T. The transition into the superconducting state is determined by the onset of diamagnetic behaviour indicated in this figure.

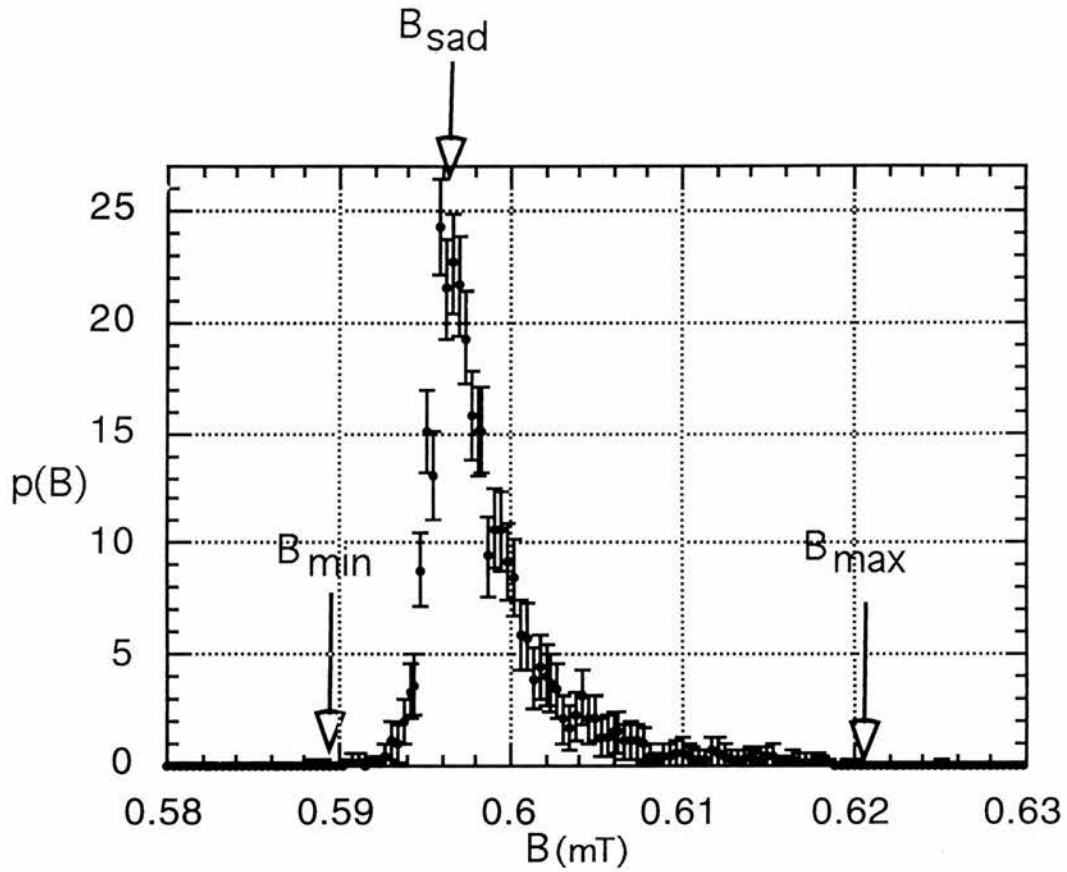

Figure 4.2: The probability field distribution, p(B), for the field applied parallel to the c-axis. This data was taken at 5 K after cooling in an applied field of 0.6 T on the GPS (PSI). It clearly reflects the intrinsic structure of a flux vortex lattice. A cut-off at low fields corresponding to the minimum between flux-lines, B_{min}, a peak corresponding to the most common field at the saddle point between flux lines, B_{sad} and a long high field tail terminating at a high field cut-off, B_{max} (see section 3.2.3) [101]

reflects the intrinsic structure of a flux vortex lattice [101]. A cut-off at low fields, B_{min} corresponding to the minimum between flux-lines, a peak B_{sad} corresponding to the most common field at the saddle point between flux lines and a long tail corresponding to the fields at the flux-line cores [101]. As was seen in section 3.2.2 the lineshape can be used to calculate the penetration depth via the expression

$$\langle \Delta B^2 \rangle = \frac{0.003706 \Phi_o^2}{\lambda^4} \tag{4.1}$$

which was shown to be valid for fields $H_{c1} \ll H \ll H_{c2}$ [64]. Using the value of the rms width of 3.68(18) mT at 5 K gives a value for $\lambda_{ab}(5)$ of 1849(33) Å. If the two fluid model is assumed then, using T_c=93 K gives a similar value for $\lambda_{ab}(0)$ of 1849(33) Å. A simulation program developed by F Ogrin at St. Andrews University incorporating the exact solution for the field profile for a flux line (cf Eq. 4.2) in the London limit ($\lambda \gg \xi$ & $H \ll H_{c2}$) evaluated by *Tinkham (1996)* [10] was used to estimate the penetration depth from Fig. 4.2. This simulation allowed for instrumental broadening of 1 mT. The resultant fit can be seen in Fig. 4.3 and yields a value for the penetration depth of 1400 Å. This value represents an average of the penetration depths λ_a and λ_b which are different in this compound because of a-b anisotropy.

$$h(r) = \frac{\phi_o}{2\pi\lambda^2} K_o(\frac{r}{\lambda}) \tag{4.2}$$

As has been seen from Fig. 4.2 and Fig. 4.3 the field distribution for a 3D lattice has a long high field tail which is under-sampled . For these experiments 5 million events were taken for each spectra and a significant increase in statistics does not improve this situation markedly as the rms is not increased significantly. It can be concluded that with finite statistics the field distribution of the 3D lattice remains undersampled. In addition to this, at finite temperatures, thermal fluctuations may smear out the high fields in the vortex cores and reduce the measured width.

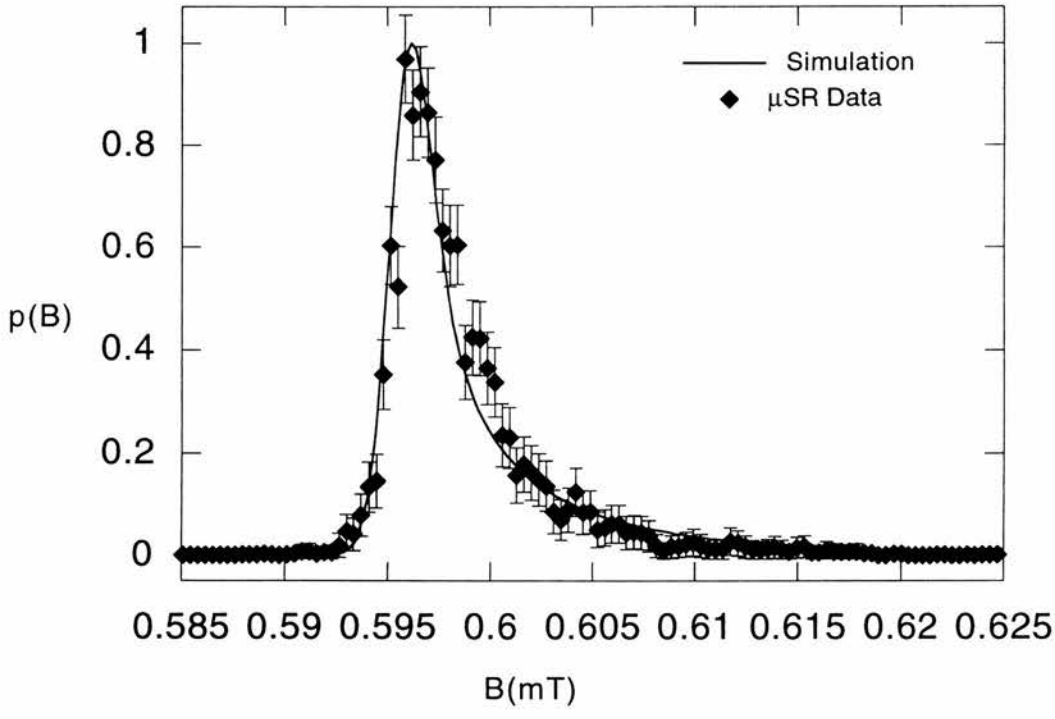

Figure 4.3: The normalised lineshape of Fig. 4.2. The simulation allowing the penetration depth to be extracted is also shown.

The values estimated here however, are not unreasonable when compared to other techniques (see Table 4.2). Figure 4.4 is a graph of the rms variation with angle θ of the field to the c-axis in the ac-plane taken at 10 K and 50 K after cooling in an applied field of 20 mT. The angular variation of the rms of the internal field distribution was indicated in section 3.2.2 to be given by [66]

$$\langle \Delta B^2 \rangle^{1/2}(T)(\vartheta) = \langle \Delta B^2 \rangle^{1/2}(0)(cos^2\vartheta + 1/\gamma_{ij}^2 sin^2\vartheta)^{1/2} \tag{4.3}$$

where $\gamma_{ij} = \sqrt{\frac{M_i}{M_j}} = \frac{\lambda_j}{\lambda_i}$, and θ is the angle between the applied field and the ith axis, for rotations about the kth axis. In previous experiments on *twinned* YBCO crystals Eq. 4.3 was found to be a good description of the angular dependence of the muon depolarisation rate [102, 66, 85]. Fits with Eq. 4.3 to Fig. 4.4 yields values of γ_{ca}=3.9(6) and 3.6(4) for the angular scans at 10 K and 50 K respectively. After consultation with Table 4.1 this estimate of the out-of-plane anisotropy can be seen to differ from the majority of measurements taken previously on YBCO123. These previous studies, however, may have been influenced by the presence of twin-planes. Figure 4.5 shows a graph of the rms field variation against the angle between the a-axis and the field in the ab-plane. Similarly to above, this data was taken at 10 K and 50 K after cooling in an applied field of 20 mT. Fits with Eq. 4.3 yield an in-plane anisotropy, γ_{ab} of 1.16(2) and 1.15(2) at temperatures 10K and 50K respectively. These values are in excellent agreement with SANS measurements on this crystal of 1.18(2) [38, 103]. They are also in good agreement with other methods documented in Table 4.1. Figure 4.6 shows the temperature dependence of the alpha parameter at 0.3 T. As can be seen from the graph a sharp melting transition is evident by the change in sign of α at $\sim$ 91.5 K. A similar transition is observed at $\sim$ 90.5 K in a field of 0.6 T, but is not evident at 20 mT where the α parameter does not show evidence of this melting transition.

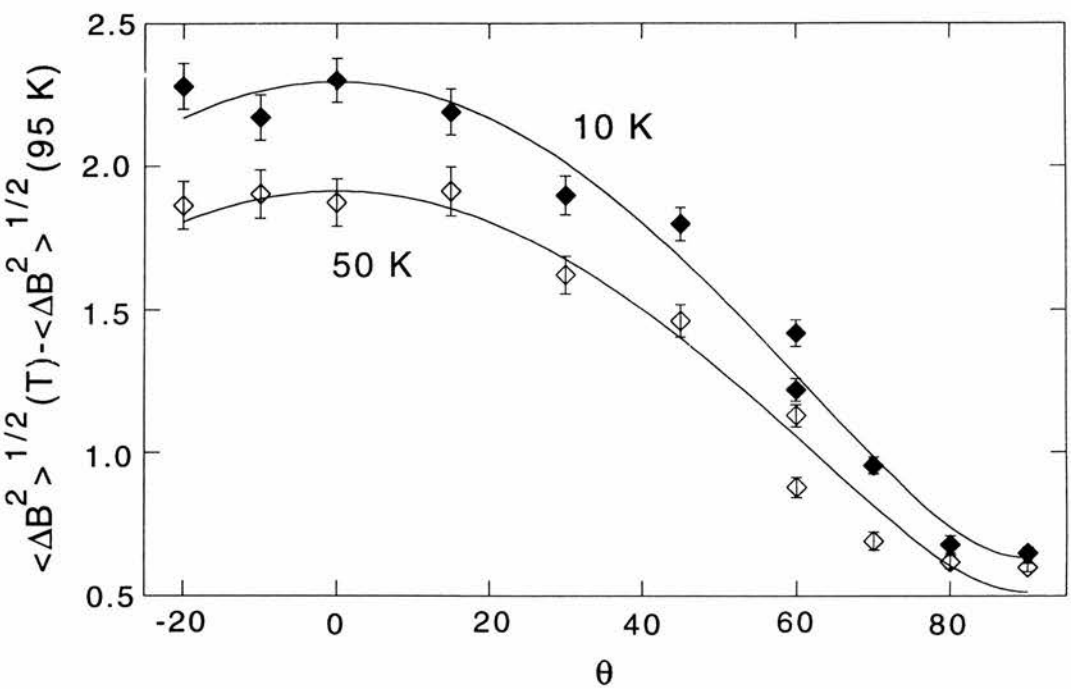

Figure 4.4: The variation of $\langle \Delta B^2 \rangle^{1/2}$ with the angle θ of the trapped field to the c-axis, for rotation within the ac-plane. The curves show the expected theoretical dependences for measurements taken at 10 K and 50 K, yielding values of the anisotropy parameter γ_{ca}=3.9(6) and 3.6(4) respectively. All measurements were made after cooling the sample from above T_c in an applied field of 20 mT.

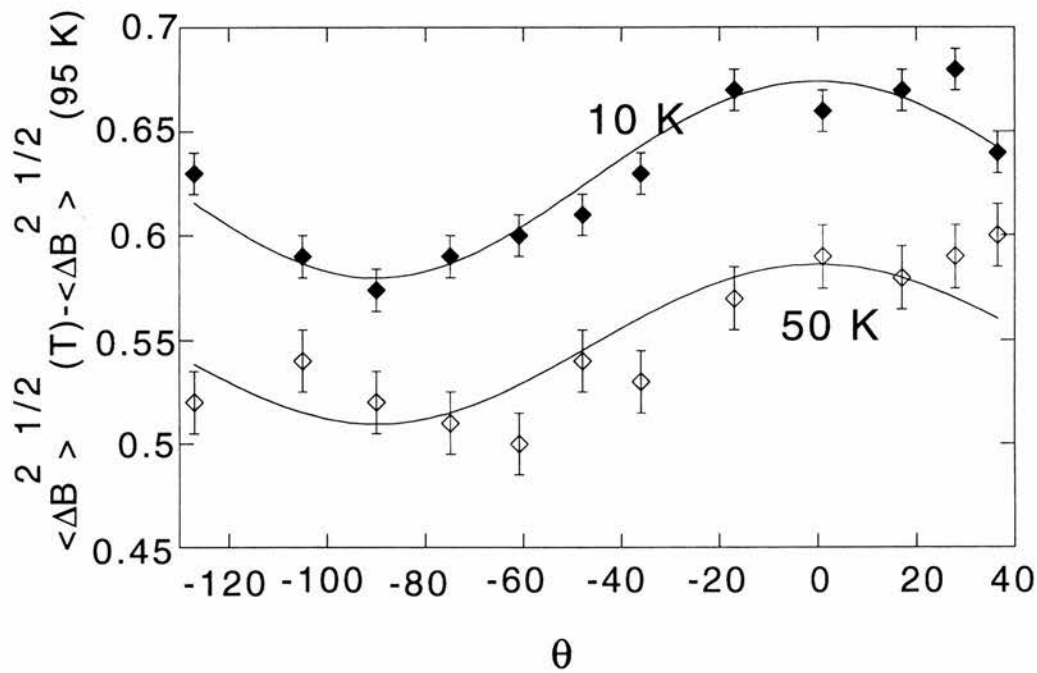

Figure 4.5: Variation of $\langle \Delta B^2 \rangle^{1/2}$ with the angle θ of the field to the a-axis, for a rotation within the ab-plane. The curves show that YBCO follows the theoretical dependences for a well-ordered vortex-line lattice at 20 mT($H > H_{c_1}$) yielding values of γ_{ab}=1.16(2) at 10 K and 1.15(2) at 50 K. All measurements were made after cooling the sample from above T_c in an applied field of 20 mT.

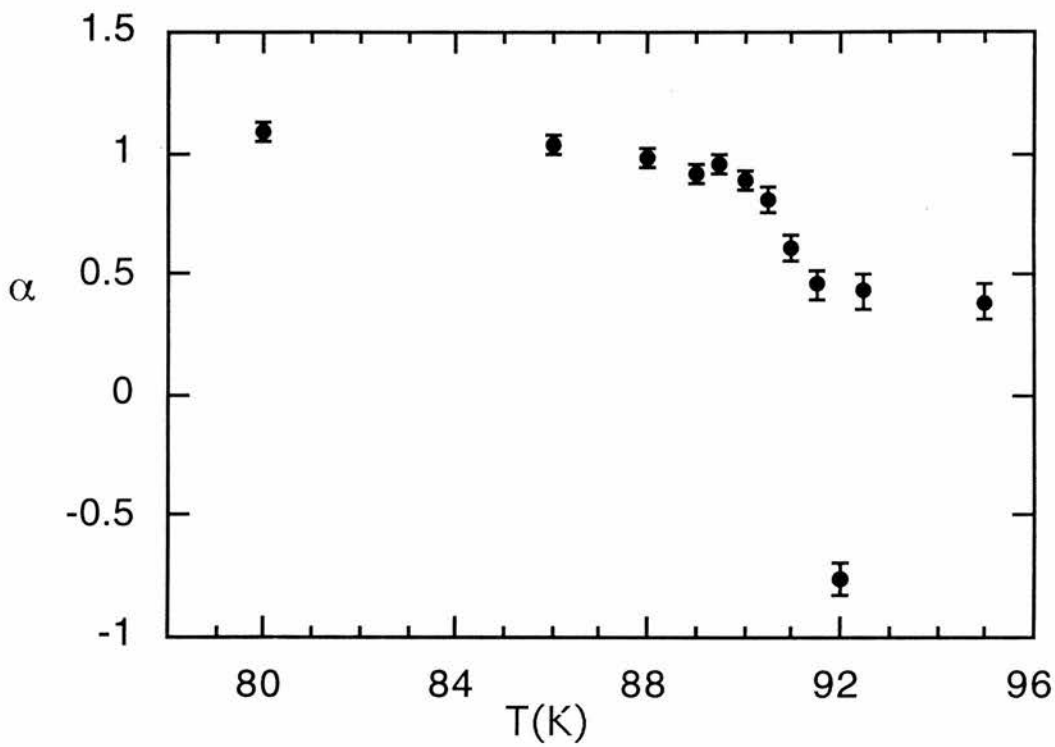

Figure 4.6: Temperature dependence of the lineshape parameter α at a field of 0.3 T. A sharp transition is evident by the change in sign of α. This change in α (see section3.2.3) corresponds to a truncation of the high field tail of the μSR lineshapes. This is due to a loss of c-axis correlation of the pancake vortices.

4.5 Torque Magnetometry

4.5.1 Experimental Setup

The torque sensor that was used on this large single crystal of YBCO123 was a large phosphor bronze cantilever (see section 3.4.2). The single crystal was attached to the cantilever via a mixture of Bostik glue and acetone. The crystal was glued at an orientation in order to rotate the a axis around the fixed field. A similar experiment was carried out rotating the b axis around the fixed field. Measurements were carried out at a field of 0.66 T and 93 K.

4.5.2 Results

Torque measurements were taken in the ca and cb planes in a field of 0.66 T, just below T_c at 93 K. This point in the phase diagram, as was mentioned before, was chosen to make the torque reversible with negligibly small hysteresis. Figure 4.7 shows the torque upon rotation around the a axis in the cb plane, as a function of the angle θ_{cb} between the field and the c axis in the cb plane. In Fig. 4.7 the line represents the fitting curve using a normalised form of Eq. 3.35. This gives the anisotropy parameter as $\gamma_{cb} = \lambda_b/\lambda_c$ =7.3(5). The anisotropy parameter $\gamma_{ca} = \lambda_a/\lambda_c$ was measured by a similar torque measurement around the b axis in the ca plane, which yielded a value of γ_{ca}=6.6(5). The ab anisotropy parameter can then be obtained as γ_{ab}=1.1(1).

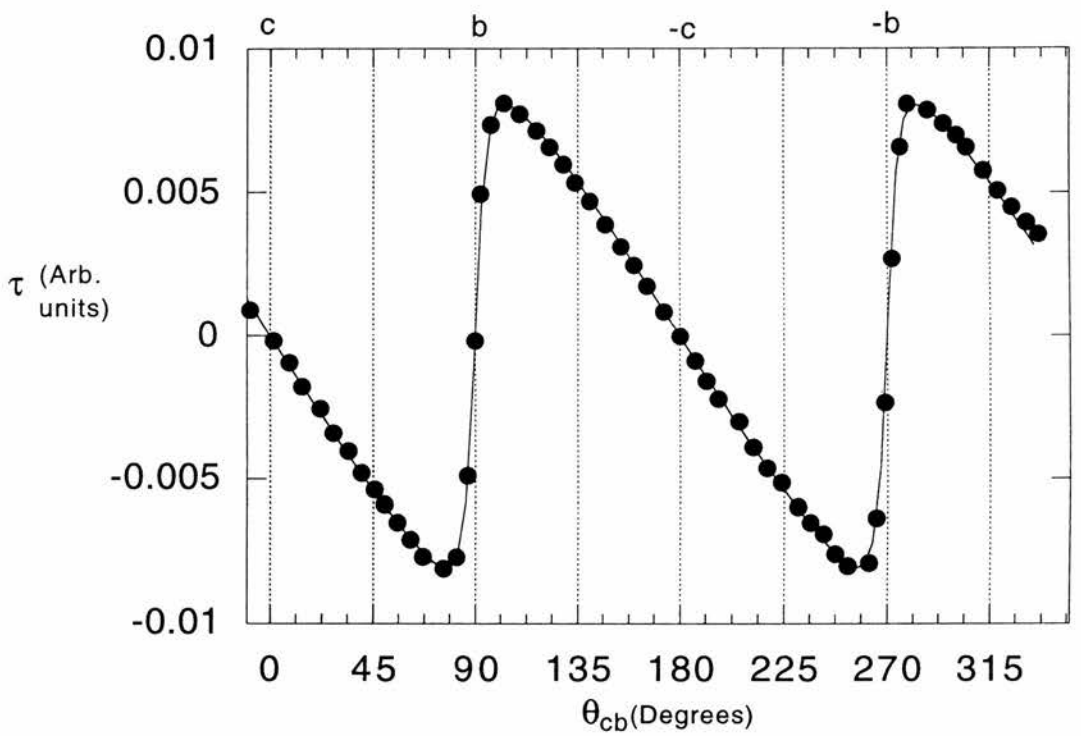

Figure 4.7: The torque of untwinned YBCO upon rotating the field of 0.66 T about the a axis at 93 K, just below T_c. The line represents a fitting curve using a normalised form of Eq. 3.35, yielding an anisotropy γ_{cb}=7.3(5).

4.6 Discussion

To begin with, the anisotropy constants obtained here using μSR will be compared with those obtained by other microscopic techniques. A recent study on the *same* YBCO crystal has recently been performed by *Johnson et al(1999)* [38] using small-angle neutron scattering, entry SANS(USC), Table 4.1. The in-plane anisotropy γ_{ab} could be deduced in that work from the distortion of the diffraction pattern from the vortex lattice observed with the field parallel to the c-direction. The resulting value $\gamma_{ab} = 1.18(2)$ is in good agreement with our value of $\gamma_{ab} = 1.16(2)$ from μSR and $\gamma = 1.1(1)$ from torque measurements. In ref. [38] it was not possible to determine the out of plane anisotropies γ_{ca} or γ_{cb} since at those angles of the field to the c-direction studied, the distortions are not sensitive to these values of the anisotropy. An earlier SANS (entry SANS(SC)) study on *twinned* YBCO crystals performed over a wider range of angles [97] estimated the effective mass ratio $M_{ab}/M_c = 20(2)$, leading to $\gamma_{c-ab} = 4.5(6)$, which is not inconsistent with our estimates of $\gamma_{ca} = 3.9(6)$ ($\gamma_{cb} = 4.5(7)$). It should be noted here, however, that the anisotropy is a function of oxygen doping in YBCO, particularly when comparing the present measurements with earlier μSR studies on a mosaic of twinned crystals which estimated $\gamma_{c-ab} \sim 5$ [102, 85]. Caution should also be exercised when comparing measurements on twinned and untwinned crystals, since in the former the anisotropic pinning present could lead to subtle aberrations of the apparent anisotropy, since the disorder induced in the lattice could lead to a broadening of the μSR lineshapes [104]. These effects, however, are most pronounced for the field close to the c-axis [105, 97], where the contribution to the estimates of the out-of-plane anisotropy are almost negligibly small (cf Eq. 4.3). A recent study on the same crystal used in these experiments has been performed us-

ing polarised neutrons, where the out-of-plane anisotropy may be estimated from the angular dependence of the components of internal field of the vortex lattice both longitudinal and *transverse* to the applied field direction [106, 103]. Preliminary estimates from that experiment are in good agreement with those presented here [103]. The estimates of the in-plane anisotropy γ_{ab} are in good agreement with those obtained by other methods documented in Table 4.1 which probe the bulk properties. Examples of these are Josephson tunnel junctions [41], polarized reflectivity [107], both of which encompassed our estimates in their lower range of values, and Bitter decoration $\gamma_{ab} = 1.13$ [40, 88]. It has been pointed out by separate authors[40, 38, 108, 97] that any disparity in the the above estimates of γ_{ab} for different techniques is primarily a consequence of subtle differences in the oxygen stochiometry of the different samples. Indeed, it has been suggested that the in-plane anisotropy may be completely dependent upon contributions from the CuO chains due to induced superconductivity from their proximity to the CuO_2 planes [109, 110]. It is thus likely that any significant discrepancy between measurements reported here and elsewhere in the literature reflect the dramatic suppression of the chain's condensate by oxygen depletion and disorder [109, 111].

The out-of-plane anisotropy was also measured using torque magnetometry. The values for γ_{cb} and γ_{ca} where estimated to be 7.3(5) and 6.6(5) respectively. These values were extracted using the London model (cf Eq. 3.35) [82], which has been used previously to interpret the torque measurements of the high-T_c superconductors [112, 113, 84, 89]. The average value of the out-of-plane anisotropy, $\gamma_{c-ab} \sim 7$, is significantly larger than the microscopic measurements of μSR and SANS [97, 103] on the same crystal. It should be noted however that the values which are obtained via torque measurements are in reasonable agreement

with those recently obtained by *Ishida et al (1997)* [90] using a similar technique. On their untwinned single crystal, fits using Eq. 3.35 yielded $\gamma_{ca} = 7.6(6)$ and $\gamma_{cb} = 9.0(8)$, implying $\gamma_{ab} = \gamma_{cb}/\gamma_{ca} = 1.18(14)$. While bearing in mind that the values of anisotropy between different crystals can vary due to oxygen doping, it is still noteworthy that torque magnetometry tends to lead to somewhat larger values of the out of plane anisotropy than microscopic techniques such as SANS and μSR. There are several factors which might be influential in this respect. The equation used to fit the torque data does not take into account the discrete nature of the superconducting planes in high-T_c systems [114]. This would not, however, be expected to be significant in YBCO close to optimal doping, since this system is in other respects very well described by an anisotropic London model. Indeed, the same approach is taken when analysing the neutron and muon data [115, 102, 66, 97, 38], and the data can be well described in this way. Additional geometric contributions to the anisotropy can arise in torque magnetometry due to the anisotropic 'demagnetising' factors, but these can be neglected in the region of the phase diagram which has been of interest in these torque measurements (see section 3.4.1). It cannot be discounted however that the differences between the microscopic and macroscopic approaches might hint at some more subtle consequence of the different way each method probes the anisotropy. SANS and μSR, for instance, both probe the penetration depths and resulting anisotropy by observation of the vortex lattice, and not via bulk transport currents. In addition, torque data is generally taken at high temperature in the reversible regime to remove the influence of pinning, and it is effectively a dynamic (non-equilibrium) measurement. μSR and SANS measurements tend to be made at lower temperatures where the shorter penetration depth leads to wider lineshapes and stronger scat-

tering respectively. Thus even though performed in the equilibrium field-cooled state, the experiments still probe the irreversible region of the magnetic phase diagram. At present it is not clear, however, how these differences could lead to the observed discrepancy.

Observations were also made of the flux lattice melting transition in YBCO. This was observed as a sharp change of sign of the alpha parameter. A similar feature in the α parameter in previous measurements of BSSCO has been associated with flux lattice melting [61, 51]. Although thermal measurements are not sensitive enough to resolve a first order transition at such low fields, recent SANS measurements on this crystal have indicated that this sharp melting transition observed here, is consistent with a first order transition [116]. Recent torque magnetometry measurements have also resolved a step in the magnetisation and hence a first order transition at similarly low fields [117].

4.7 Conclusions and Further Work

The results presented in this chapter provide excellent evidence for the anisotropic flux lattice in YBCO. The in-plane anisotropy measured here is of particular interest because of the relatively low out-of-plane anisotropy of YBCO, especially in comparison to BSCCO for example. μSR measurements have also indicated that the flux-lattice in *untwinned* YBCO undergoes an extremely sharp melting transition and SANS measurements on this crystal have indicated that this is a first order transition [116, 100]. An estimate of the magnetic penetration depth by μSR has also been presented here. Although this is in reasonable agreement with other techniques in the literature, it is worth noting here, however, that while μSR is an invaluable and unique method for making *comparative* measurements of the

parameters of the superconducting state, the absolute determination of the penetration depth may contain several possible sources of error, as these are always extracted by making assumptions about the vortex-lattice structure.

Another interesting point of contention that has been raised by this work is the obvious disparity of the out-of-plane anisotropy between measurements using μSR and torque magnetometry. Several reasons for this were explored in the previous section, but, as yet, a satisfactory explanation for this discrepancy has not been reached.

Chapter 5

Observation of novel vortex structure in the organic superconductors κ-(BEDT-TTF)$_2$Cu(NCS)$_2$ and α-(BEDT-TTF)$_2$NH$_4$Hg(SCN)$_4$

5.1 Introduction

In this chapter an extensive study of the flux lattice in κ-(BEDT-TTF)$_2$Cu(SCN)$_2$ [ET-Cu] and α-(BEDT)$_2$NH$_4$Hg(SCN)$_4$ [ET-NH4] is presented. Recent work on the phase diagram in the low-field regime of the HTSC BSCCO has highlighted that the layered vortex structure of this system may not only be partially controlled by electromagnetic coupling, but is perhaps dominated by this phenomenon

in parts of the low-field phase diagram. Although the layered organic systems have, in general, much lower transition temperatures than HTSC, properties, such as large γ and λ make *exotic* effects easily possible in these systems. The two branches of the layered superconductors (organics and HTSC) have been brought together with the work here, which indicates that the crossover from a 3D phase to a 2D disordered phase occurs at very low fields [69] and that both ET-Cu and ET-NH4 may undergo a melting transition. ET-Cu and ET-NH4 were both characterised via the use of the muon spin rotation technique at the Rutherford Appleton Laboratory(RAL), Oxfordshire and at the Paul Scherrer Institut(PSI) Villigen, Switzerland. Small angle neutron scattering was also been carried out on ET-Cu on D22 at the ILL, Grenoble, France.

5.2 Previous Work

The crossover from a 3D phase to a 2D disordered phase and flux-lattice melting are well established phenomena in the HTSC and were first observed via BSCCO by *Cubitt et al (1993)* [91] using SANS. A similar crossover from 3D to 2D behaviour is also documented in the literature for the ET-Cu system [69]. These intrinsic similarities are particularly interesting as they may indicate that the dominant mechanisms controlling the vortex lattice are of a similar nature. In chapter 2 it was seen that a useful model of the layered systems consists of 2D pancake vortices which interact with pancakes in neighbouring planes via a combination of tunneling Josephson currents and electromagnetic interactions [22, 118]. The relative strengths of these different interlayer coupling mechanisms can radically affect the vortex behaviour. This is evident in the low field phase diagram of BSCCO where the form of the melting line does not follow a form that indicates

the dominance of Josephson coupling ($B_m^J \propto 1/\lambda^4 T^2$), but follows a form which indicates that electromagnetic coupling may play a part, ($B_m^{em,J} \propto 1/\lambda^3 T$), and may even dominate ($B_m^{em} \propto 1/\lambda^4 T$) [59, 51] (see section 2.4). In addition to the melting line the crossover from a 3D to a more 2D phase is also radically affected by the dominant coupling mechanism in these materials. This crossover field originates from the competition between shear and tilt energy [57, 61] and occurs when the energetic cost of tilting a vortex line becomes less than the energetic cost to shear it [60]. In a superconductor dominated by Josephson coupling, such as YBCO, this crossover field is given by

$$B_{2D} = \phi_o/(\gamma s)^2. \tag{5.1}$$

To apply such a model to systems of extremely high anisotropy such as ET-Cu, ET-NH4 and BSCCO is misguided, as a consequence of the large anisotropy in these systems (BSCCO$\sim$150 [42, 43], ET-Cu$\geq$100 [44, 45, 46, 47, 48, 49] and ET-NH4 $\approx$ 1000 [50]) and the extremely low B_{2D} predicted. B_{2D} in these systems marks a point in the phase diagram above which Josephson coupling may become ineffective and electromagnetic coupling may play a more dominant role (see section 2.6). For a system which is electromagnetically coupled the criterion for the crossover field is given by

$$B_\lambda = \frac{\phi_o}{\lambda_{ab}^2} \tag{5.2}$$

as was demonstrated to be the case in BSCCO and other layered HTSC by *Aegerter et al (1996)* [60]. This work, as well as the work of *Blatter et al (1996)* [59] and *Lee et al (1997)* [51] has highlighted the dominance of electromagnetic coupling in the low field phase diagram of the layered compound BSCCO and it is of interest to access the type of coupling mechanism which is dominant for the similarly layered structures like ET-Cu and related compounds. Previously in the literature it has

been assumed that the dominant coupling mechanism for ET-Cu is Josephson coupling (e.g [119, 120, 121]). Recent μSR experiments on ET-Cu by *Lee et al (1997)* [69] have cast doubt on this consensus as they indicate that the crossover from 3D to 2D behaviour may be identified with *both* B_λ and B_{2D}. Further to this, *Clem(1991)* [118] has analysed the behaviour of a *purely electromagnetically coupled* pancake stack in the dilute limit and as a consequence found that the stack would be thermally induced to breakup at a field-independent characteristic temperature given by

$$T_b = \frac{\phi_o^2 s}{k_B \mu_o (4\pi)^2 2\lambda_{||}^2}. \tag{5.3}$$

Lee et al (1997) [51] has carried out μSR experiments on ET-Cu that have indicated a reduction of pancake vortex correlations along the field direction at 2.5 mT and at a temperature $\sim$ 5 K, and this they have identified with $T_b \approx$4.5 K. The *breakup temperature*, T_b, offers only an *approximate* energy scale here, but it is clear that this work highlights that thermal disruption of vortex structure can occur, even at these low temperatures, due to the large γ and λ that are encountered in these systems. Further work must be carried out, therefore, in order to fully characterise the exotic vortex phenomena that is evident in the layered organic superconductors such as ET-Cu. Further to this, this may allow one to identify generic trends amongst the layered superconductors.

5.3 Sample Characterisation

The ET-Cu sample consisted of a 10 $\times$ 20mm^2 mosaic of crystals, grown by an electrochemical oxidation method by *T. Sasaki*, Institute for Material Research, Tohoku University, Sendai 980-77, Japan. Each crystal measures typically 1.0 $\times$

$1.5 \times 0.5\text{mm}^2$ with the largest face parallel to the superconducting planes and the superconducting onset $T_c \approx 10.4$ K. The ET-NH_4 sample also consisted of a $10 \times 20\text{mm}^2$ mosaic of crystals supplied by *K. Kanoda*, Department of Applied Physics, University of Tokyo, Hongo, Bunkyo-ku, Tokyo 113, Japan. Each crystal measures typically $1.0 \times 1.0 \times 0.5\text{mm}^2$ and the onset of superconductivity $T_c \approx$ 1.1 K.

5.4 μSR Measurements on κ-(BEDT-TTF)$_2$Cu(NCS)$_2$

5.4.1 Experimental Apparatus

Muon spin rotation measurements were performed to characterise the sample using the MUSR spectrometer at the Rutherford Appleton Laboratory(RAL) and the GPS on the πM3 beamline at PSI. The crystals were mounted with Apiezon grease on a plate of haematite (Fe_2O_3) to give a total area approximately 10 $\times$20 mm^2. Details of the experimental apparatus used above can be found in section 3.2.4.

5.4.2 Results and discussion

Determination of λ and the dimensional crossover

Figure 5.1 shows the lineshape measured at 2.5 K for ET-Cu cooled in a field of 1.5 mT perpendicular to the superconducting planes on GPS , derived using the maximum entropy technique discussed in section 3.2.4. The field distribution of type II superconductors has been calculated [122] and shows a distinct weighting towards fields higher than the mode. This is due to the extremely large fields

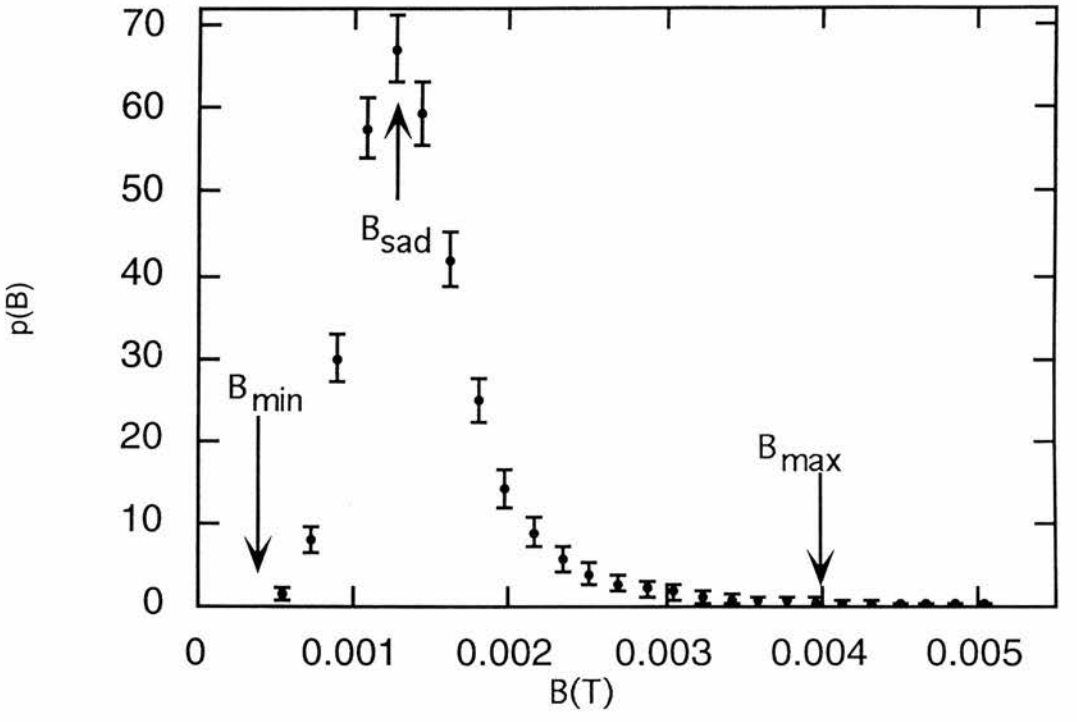

Figure 5.1: The probability field distribution, p(B), for the field applied perpendicular to the superconducting planes. This data was taken at 2.5 K after cooling in an applied field of 1.5 mT on the GPS (PSI) and reflects the intrinsic structure of a flux vortex lattice. Such a lineshape has the following prominent features: a cut-off at low fields corresponding to the minimum between flux-lines, B_{min}, a peak corresponding to the most common field at the saddle point between flux lines, B_{sad} and a long high field tail terminating at a high field cut-off, B_{max} [101]. Such a lineshape, indicative of a well ordered flux-lattice was first observed in ET-Cu by *Lee et al (1997* [69].

present in the vortex cores and is clearly evident in the asymmetric shape of this probability distribution, $p(B)$. The prominent features to be noted for a type II superconductor, evident in this distribution are B_{min}, B_{sad} and B_{max}. The mode of the distribution occurs at B_{sad}, lying below the mean field. Previously published lineshapes in ET-Cu [123, 124, 125] are highly symmetric, with a mode close to the average field. These previous experiments, however, were carried out at much larger fields where it is now evident that the vortex system has undergone a dimensional crossover [69]. The simulation program developed by F. Ogrin at St.Andrews University was used to estimate the penetration depth from Fig. 5.1. The resultant fit can be seen in Fig. 5.2 and yields a value of the penetration depth $\lambda_{||}(2.5\ \mathrm{K})$ of 5200 ± 200 Å. This is in reasonable agreement with reversible magnetisation measurements $\lambda_{||}(0)$=5350 $\pm$ 200 Å [126] and previous μSR experiments on a ET-Cu sample of 5380 ± 200 Å [69] and 7680 ± 700 Å [125]. The latter estimate by μSR, however, was mis-analysed as a consequence of the author's assumption of the presence of a rigid, three-dimensional triangular lattice and the fact that the measurements were taken above the crossover field [69] where the vortex lattice would be extremely disordered.

To expedite a study of the vortex structure by μSR in ET-Cu it is useful to use the dimensionless skewness parameter β, which was first introduced by *Lee et al(1997)* [69] and defined in section 3.2.3 to quantify the symmetry of the lineshapes. As was mentioned earlier a positive value of β indicates a weighting towards higher fields in the field distribution. For a system such as ET-Cu, the relative value of β for a set of measurements is an indicator of the degree of pancake vortex correlations along the field direction.

Figure 5.3 shows the behaviour of the β parameter with field, measured for a

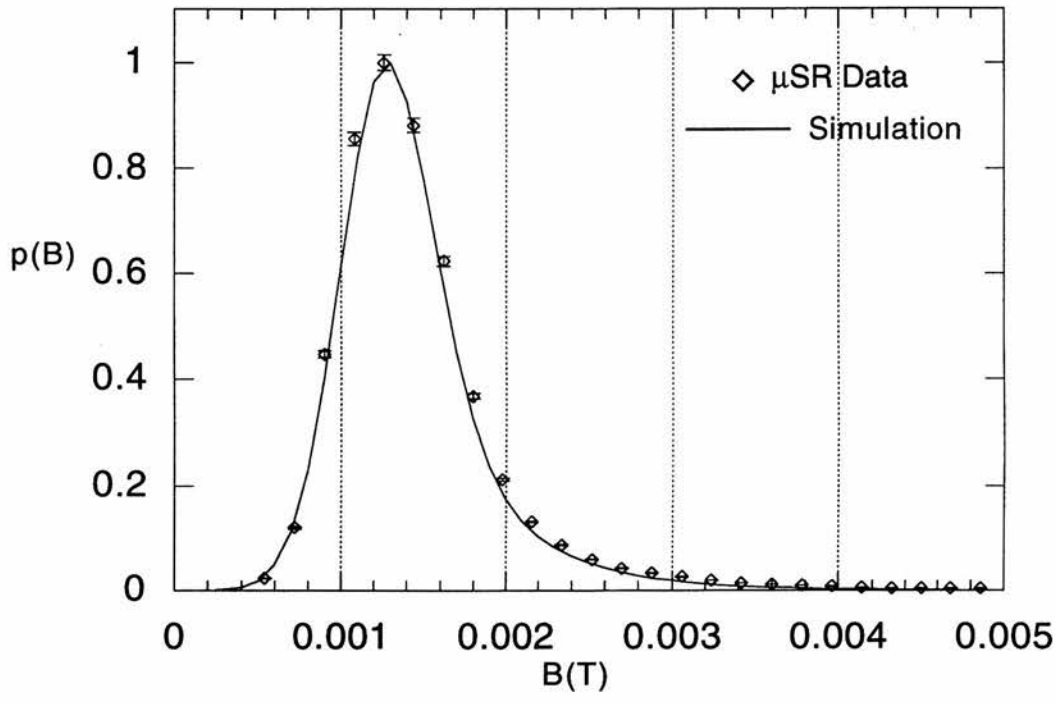

Figure 5.2: The normalised lineshape of Fig. 5.1. The simulation is indicated as a strong black line (see text).

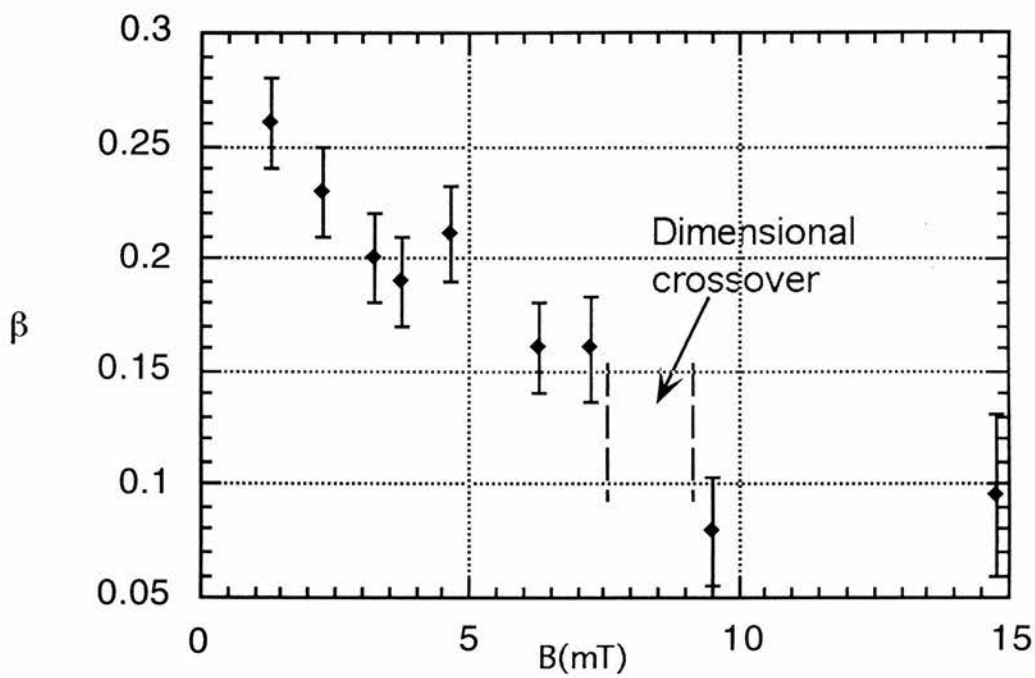

Figure 5.3: The behaviour of the β parameter with field for a deuterated sample of ET-Cu. The β parameter reduces with temperature indicating a reduction of pancake vortex correlations along the field direction. At ~7.5 mT-9 mT the value of the β parameter jumps to a reduced value and plateaus at this value. This jump can be identified as a *dimensional crossover* from 3D to 2D pancake vortex behaviour.

deuterated sample. From section 3.2.2 it can be seen that the contribution to the observed relaxation rate for the superconducting state is $\sigma \propto 1/\lambda^2$. The effect of the long penetration depth in ET-Cu therefore is to reduce the observable contribution to σ due to the superconducting state. This fact makes μSR experiments on ET-Cu extremely challenging as the increased relaxation due to the superconducting state is only just observable above the nuclear depolarisation within the limits of instrumental resolution. Deuterated samples are employed, therefore, to reduce the contribution to the μSR lineshapes from nuclear depolarisation. In Fig. 5.3 the β parameter decreases with field. This reduction in β, reflecting a change in the μSR lineshape, indicates a reduction of pancake vortex correlations along the field direction. The physical significance of this is that the high fields encountered at the core of the fluxlines are increasingly smeared out by this increased disorder of the pancake arrangement along the field direction. At ~7.5 mT-9 mT the value of the β parameter jumps to a much reduced value and plateaus at this value. This jump can be identified as a dimensional crossover from 3D to 2D pancake vortex behaviour (compare Figs. 5.4 and 5.2) where the pancake vortices are no longer well correlated along the field direction as a result the competition between shear and tilt deformation in the fluxline structure (see section 2.6). Both B_λ (~7.7 mT, taking λ ~5200 Å) and B_{2D} (~ 7-30 mT, taking the layer separation for ET-Cu as s~ 1.6 nm and recent estimates of γ ~160-350 [44]) encompass this value, so it is unclear, given this information alone whether to identify this behaviour with a system similar to YBCO or BSSCO (see section 2.6).

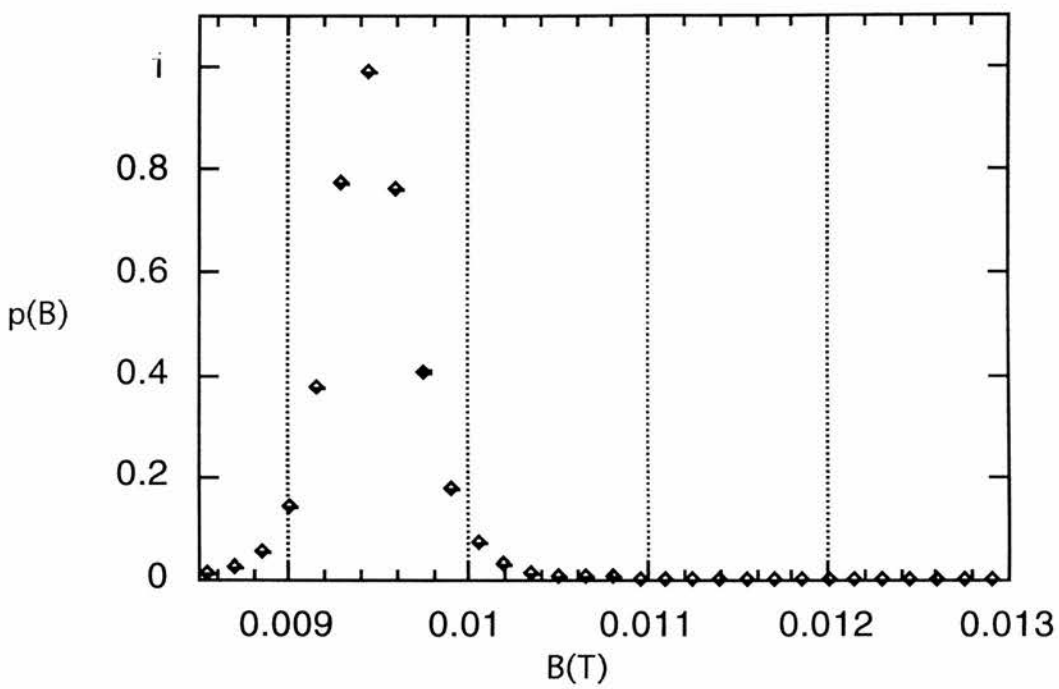

Figure 5.4: The normalised probability field distribution, p(B), for the field applied perpendicular to the superconducting planes. This data was taken at 2.5 K after cooling in an applied field of 9.5 mT on the GPS (PSI). Comparing this figure with Fig. 5.2 a clear reduction in both the *asymmetry* and the *width* is evident. At an applied field of 9.5 mT the vortex structure has undergone a dimensional crossover (see text and Fig. 5.3).

Angular dependence of $\langle \Delta B^2 \rangle^{1/2}$

Figure 5.5 shows the angular dependence of the normalised $\langle \Delta B^2 \rangle^{1/2}$ as a function of angle, for fields of 2 mT, 5 mT and 8 mT at a temperature of 2 K. As was seen earlier, according to the anisotropic $3D$ model the linewidth of the probability distribution as a function of angle follows the form [66]

$$\langle \Delta B^2 \rangle^{1/2}(T)(\vartheta) = \langle \Delta B^2 \rangle^{1/2}(0)(cos^2\vartheta + 1/\gamma_{ij}^2 sin^2\vartheta)^{1/2}. \tag{5.4}$$

In an extremely anisotropic system, $\gamma \gg 1$, such as ET-Cu, this would be expected to reduce to a $\cos(\theta)$ dependence except for values of $\theta \approx 90^o$. A $\cos(\theta)$ dependence has been plotted in Fig. 5.5 for ease of comparison. A clear trend towards a $\cos(\theta)$ dependence is evident for fields of 2 mT and 5 mT. The 8 mT data follows this trend less closely. As a comparison to this data Fig. 5.6, taken from ref. [127], shows a scan of $\langle \Delta B^2 \rangle^{1/2}$ for the μSR lineshape as a function of the field with respect to the c-axis for under doped BSCCO. Here, for fields lower than the crossover field ($B<B_{cr}$=65 mT in under-doped BSSCO) the angular dependence is as expected for a lattice of straight fluxlines, whereas for the high applied field (B=300 mT) it is only weakly dependent on the angle. This may be understood in terms of the pinning-induced disorder of the vortex lattice above B_{cr} where random lateral displacements of vortices in neighbouring layers, due to pinning will induce phase fluctuations in the order parameter. This will lead to the generation of a random array of Josephson vortices, generating fields parallel to the superconducting planes. There is thus a large variation in the local field distribution arising from all components of the internal field. As a result of this, disorder appears to dominate the field distribution, even when the field is tilted away from the c-axis. Ref. [127] also noted that if the component of the B field along the c axis is smaller than the crossover field, $B\cos(\theta)<B_{cr}$, then the pancake

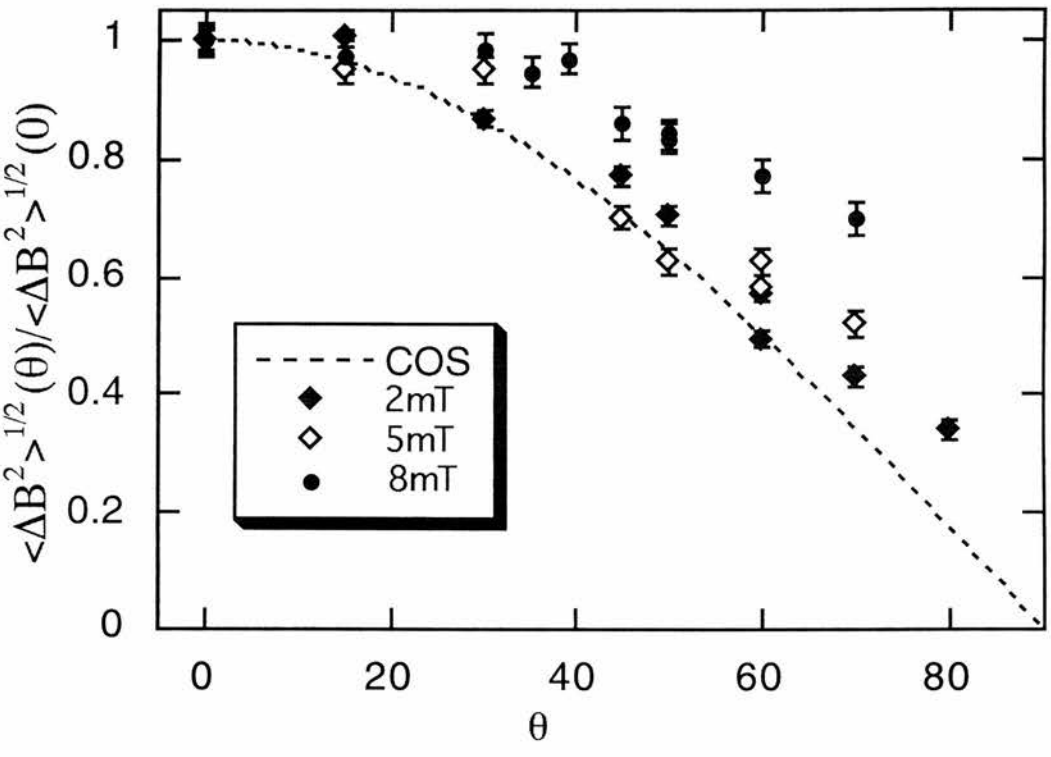

Figure 5.5: The angular dependence of the normalised μSR linewidth as a function of the angle of the field with respect to the c-axis for ET-Cu. The data was taken at a temperature of 2 K. The field values are indicated in the legend and $\cos(\theta)$ is plotted for comparison as the behaviour that would be expected for a lattice of straight vortex lines (cf Eq. 5.4). The fields at 2 mT and 5 mT only roughly follow this behaviour throughout the angular scan and the scan at 8 mT follows this behaviour less closely.

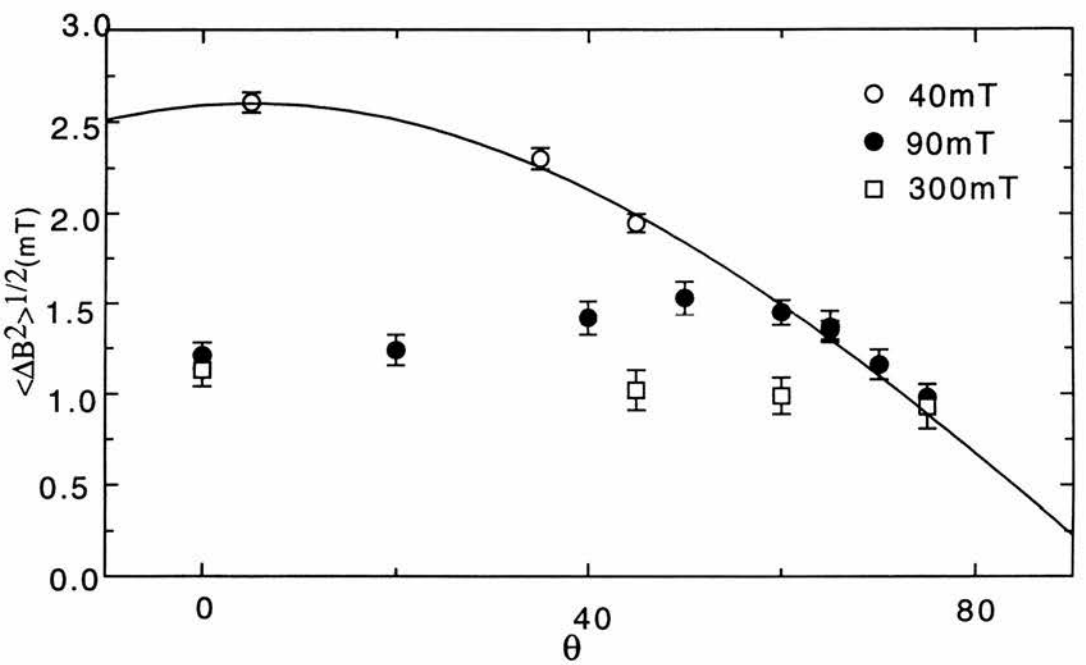

Figure 5.6: The rms as a function of field for over-doped BSSCO, taken from ref. [127]. In this case the angular dependence of the rms clearly separates into that below the dimensional crossover and that above (see text). The data was taken at a temperature of 2 K. For ease of comparison a $\cos(\theta)$ dependence is shown here.

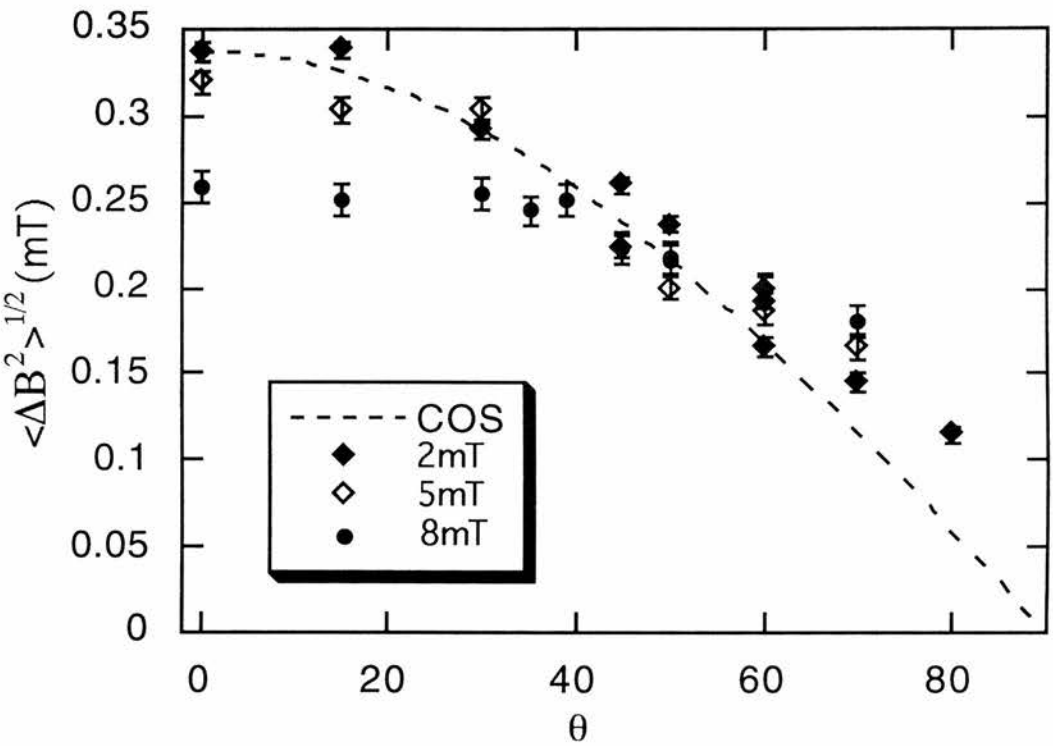

Figure 5.7: A similar graph to that of Fig. 5.6 showing the unnormalised rms values for ET-Cu at fields of 2 mT, 5 mT and 8 mT. It is evident that angular scans at 2 mT and 5 mT weakly follow the expected $\cos(\theta)$ dependence and that the 8 mT angular scan is only weakly dependent upon angle above $\sim 40^{o}$ (see text).

vortices appear to move towards being well aligned along the field direction. This manifests itself in Fig. 5.6 as the rms rejoining the angular dependence (cf Eq.5.4) at the applied field of 90 mT at θ ~60°. Figure 5.7 shows a similar plot for ET-Cu. The behaviour for a lattice of well aligned vortices in this system has been plotted on this graph for ease of comparison. Once again, the angular scans at 2 mT and 5 mT follow a definite trend towards this cos(θ) dependence. The 8 mT data exhibits a plateau until $\sim$ 40° where it begins to be more strongly dependent upon θ. It is clear that, in comparing the previous data taken in the HTSC BSCCO and the present data taken in ET-Cu, that a line-like vortex structure is indicated by the trend towards the cos(θ) dependence at applied fields of 2 mT and 5 mT. The trend towards the cos(θ) dependence and therefore, line-like behaviour, is less evident at an applied field of 8 mT. At this field the vortex structure is in the middle of the dimensional crossover transition detailed in the previous section and would not be expected to be *line*-like. The 8 mT data does, however, become more strongly dependent upon angle above $\theta \sim 40°$ (see Fig. 5.7), similar to the behaviour seen in BSSCO (see Fig. 5.6) when the component of the B field along the c-axis is smaller than the crossover field, B cos(θ)<B_{cr}.

Vortex lattice melting

Figure 5.8 shows the behaviour of the temperature dependence of the average internal field, <B>, and the β parameter, mentioned above, at a field of 3 mT for ET-Cu. The temperature dependence of the average internal field exhibits a decrease to a minimum at $\sim$ 6 K and then an increase to a value which does not quite reach the value for <B> at the lowest temperature point (~1.8 K). This effect has been reported before in BSSCO by *Harshman et al (1991)* [128]. It has

also been observed in YBCO by *Cubitt et al (1993)* [66] and in ET-Cu by *Harshman et al (1994)* [125]. As is evident from the magnetisation curve taken by ref. [123] in ET-Cu (see Fig. 5.10) that this effect is not due to an actual change in the field of the sample and therefore suggests that it represents a change in the weighting with which muons sample the field. Ref. [128] argues that this is plausible in the event of there being a mechanism to produce an enhanced correlation between the stopped muons and the vortex cores, for example, assuming that muons preferentially trap at existing pinning centres. This would explain the apparent disparity between the average field measured in the normal state and the average field measured at the lowest temperatures in the superconducting state. Figure 5.8 also depicts the temperature dependence of the β parameter. As was mentioned earlier, a reduction in the value of the β parameter reflects a change in the lineshape and indicates a reduction of pancake vortex correlations along the field direction. The β parameter also exhibits such a reduction with temperature. It also undergoes a jump at a temperature, T $\sim$5 K, which may be identified with a transition in the flux lattice. A similar jump has previously been identified with the thermally induced break-up of *electromagnetically-coupled pancake stacks* (ECPS) estimated to occur at $T_b = \phi_o^2 s/k_B \mu_o (4\pi)^2 2\lambda_{||}^2 \approx 5.8$ K for ET-Cu [118]. Figure 5.9 shows the behaviour of the average internal field <B>, and the β parameter at a field of 7 mT for ET-Cu. <B> exhibits similar behaviour to that seen in Fig. 5.8. The β parameter also falls with temperature and undergoes a transition at T$\sim$4 K. Similar temperature dependences were taken at fields of 1 mT, 1.5 mT, 2 mT, 4 mT, 5 mT and 9 mT and the temperature at which the β parameter was observed to undergo a transition was noted and plotted in Fig. 5.11. One thing is clear from this graph and this is that the transition is both field and temperature dependent

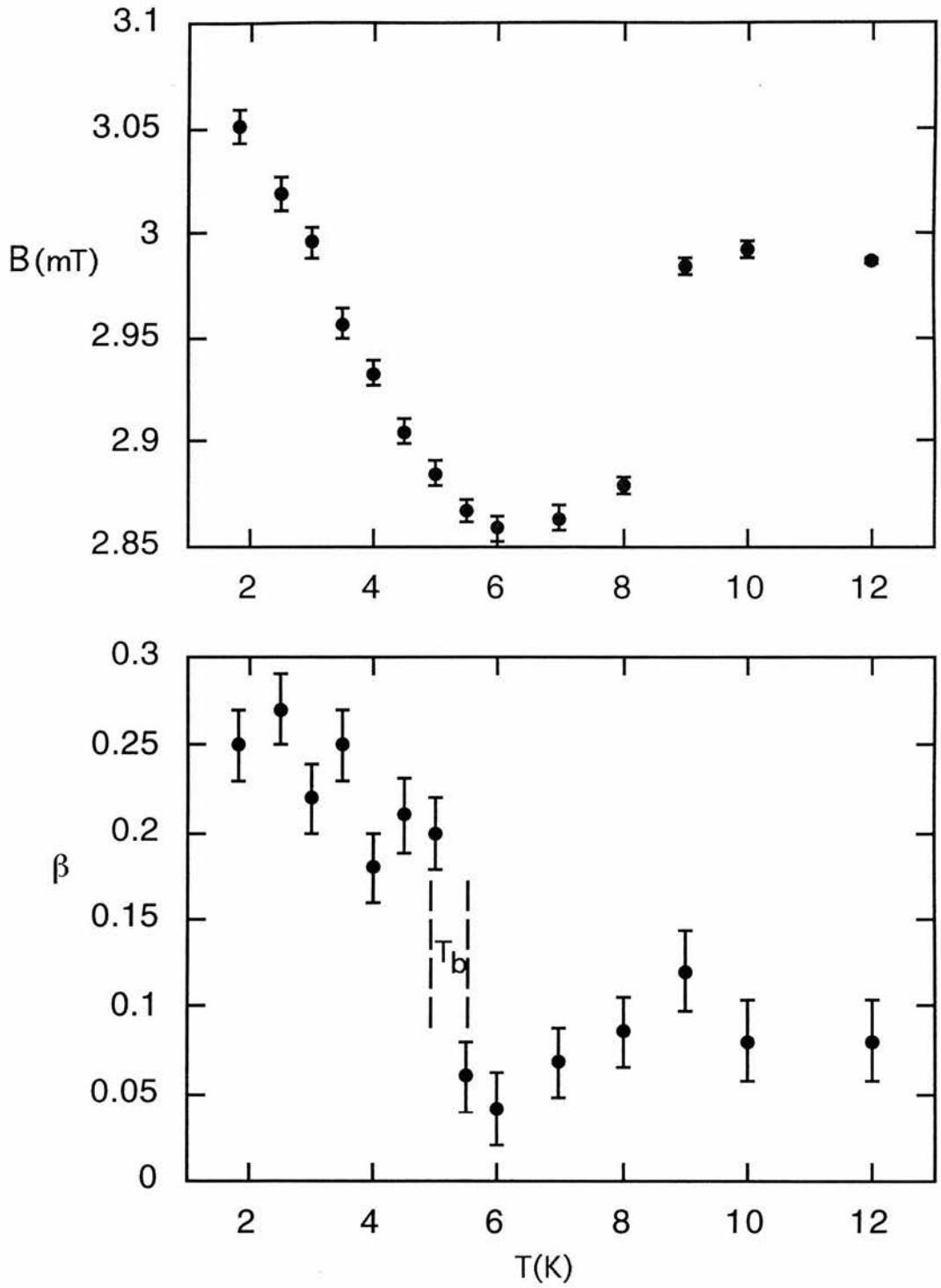

Figure 5.8: The behaviour of the average internal field and the β parameter for ET-Cu in a field of 3 mT. Here a clear jump in β is evident at $\sim$ 5K (see text).

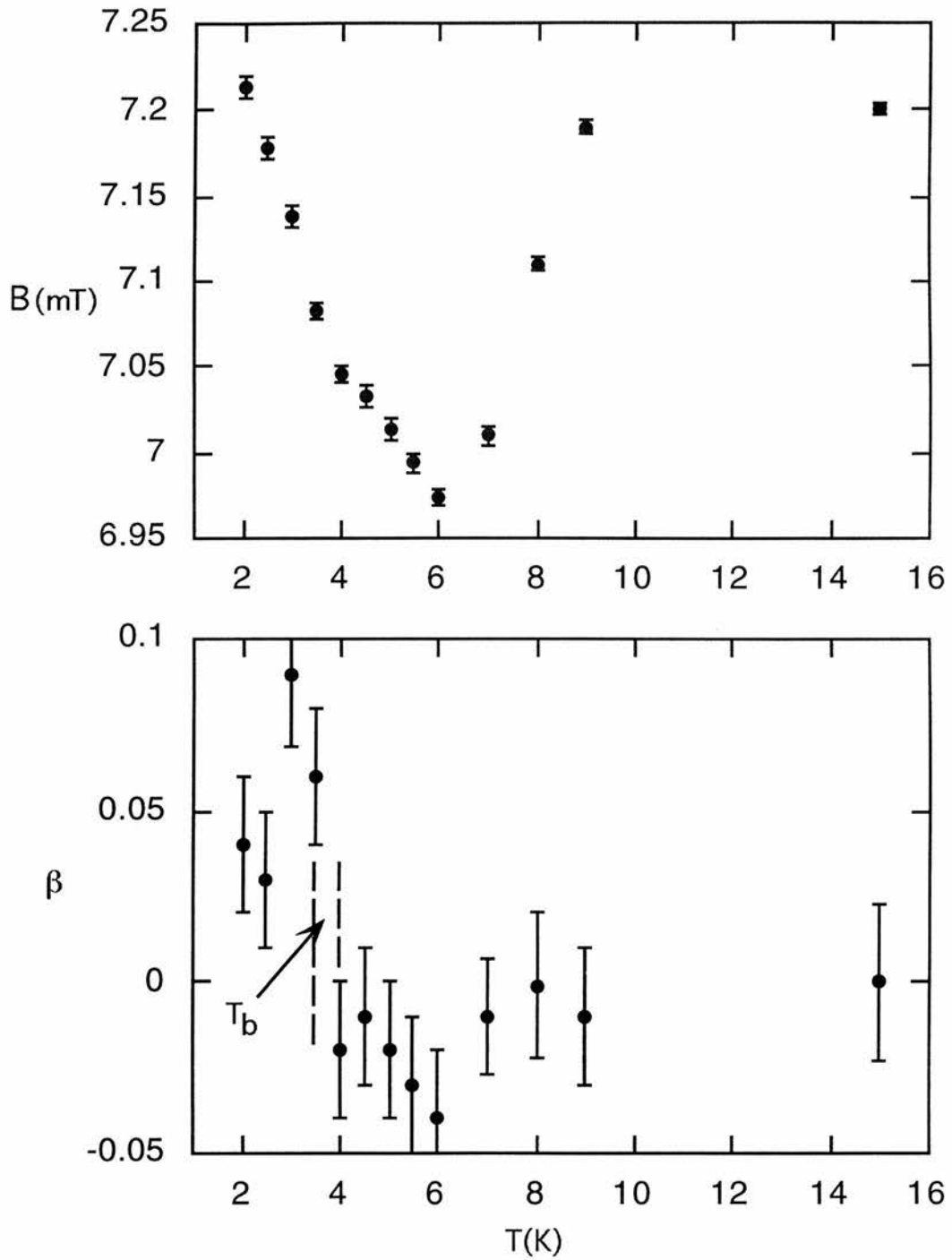

Figure 5.9: The behaviour of the average internal field and the β parameter for ET-Cu in a field of 7 mT. Once again a jump in β is evident at ~3.75 K(see text).

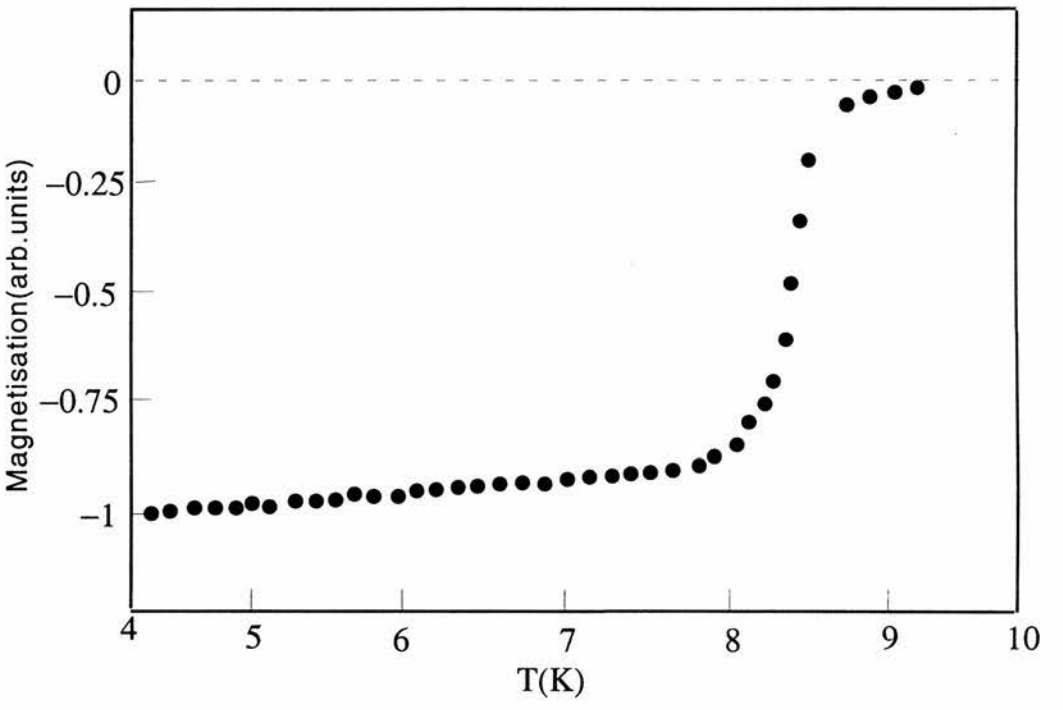

Figure 5.10: Magnetisation curve, taken by field cooling in a field of 0.5 mT for an ET-Cu crystal taken from ref. [123]. This clearly does not exhibit the increase in internal field that is indicated by μSR measurements (cf Figs. 5.8 and 5.9).

and may be identified with a melting line. According to refs. [59, 51] the form of the melting line may be sufficient to identify the dominant coupling mechanism. Following the analysis of ref. [51], a phenomenological curve of the form

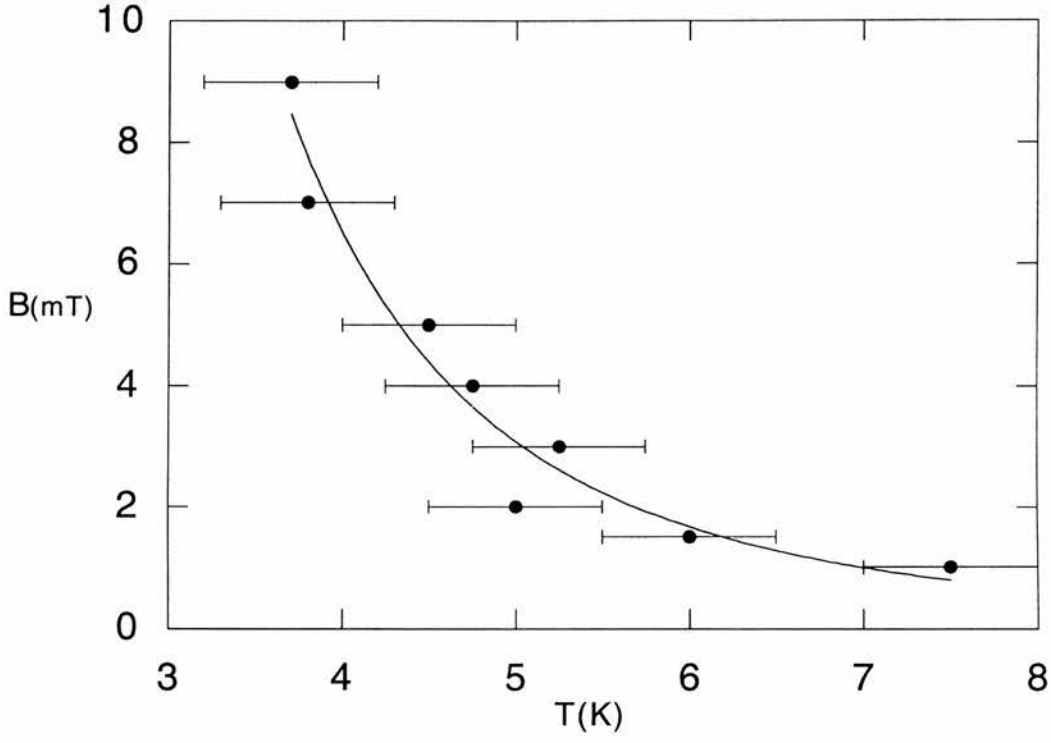

Figure 5.11: The estimated breakup temperature for ET-Cu for a range of applied fields. The fit to Eq. 5.6 is also displayed.

$$B_m^{ph}(T) = \frac{K}{\lambda_{||}^m(T)T} \tag{5.5}$$

where K is a constant and m=4,3 would correspond to Eqs. 2.10 and 2.11 (see section 2.4) was fitted to Fig. 5.11. Equation 5.5 was found to be insufficient in describing Fig. 5.11, so a curve of the form

$$B_m^{ph}(T) = \frac{K}{\lambda_{||}^m(T)T^n} \tag{5.6}$$

was fitted to Fig. 5.11. Here n=2, m=2 correspond to Josephson coupling dominating, and n=1, m=4 corresponds to purely electromagnetic coupling dominating

with n=1, m=3 for the intermediate case where both Josephson coupling and electromagnetic coupling are present. The fit to the melting line in Fig. 5.11 yields values of of n=3.36(10) and m=2.42(12). The value of m here indicates that this melting line is strongly dependent upon temperature and that it cannot be identified with any of the predictions made by ref. [59] for the low field phase diagram of highly anisotropic superconductors from this fit. The observed behaviour, therefore, may be a consequence of the fact that in the fit of this melting line *all* three melting regions identified in Fig. 2.11 (see section 2.6) have been encompassed. By inspection, it is evident from Fig. 5.11 that the melting line below 2 mT has a different form, although there is evidently too little data at present to make any solid predictions. Clearly a more detailed study is required in the low field phase diagram of ET-Cu in order to investigate the different regions that may make up the melting line, as demonstrated to be the case in BSCCO [51] (see section 2.6). Nonetheless, it is clear that, even at these low temperatures there is a $B_m(T)$ as a consequence of γ and λ in these materials.

5.5 μSR Measurements on α-(BEDT-TTF)$_2$NH$_4$Hg(SCN)$_4$

5.5.1 Introduction

Compared to ET-Cu, α-(BEDT-TTF)$_2$NH$_4$Hg(SCN)$_4$ (ET-NH4) is extremely anisotropic ($\gamma \sim$1000 [50]) and exhibits and even longer penetration depth, λ [50]. This system is of particular interest as it may exhibit similar coupling behaviour to the anisotropic ET-Cu system, and also the archetypical anisotropic system, BSSCO. The experimental investigation of such a system by μSR, however, is particularly

challenging as a result of the long penetration depth and the extremely narrow linewidths which result (see section 3.2.2). An investigation such as this is important however, as it may shed light on possible generic trends amongst very anisotropic and extremely anisotropic superconducting systems.

5.5.2 Results and Discussion

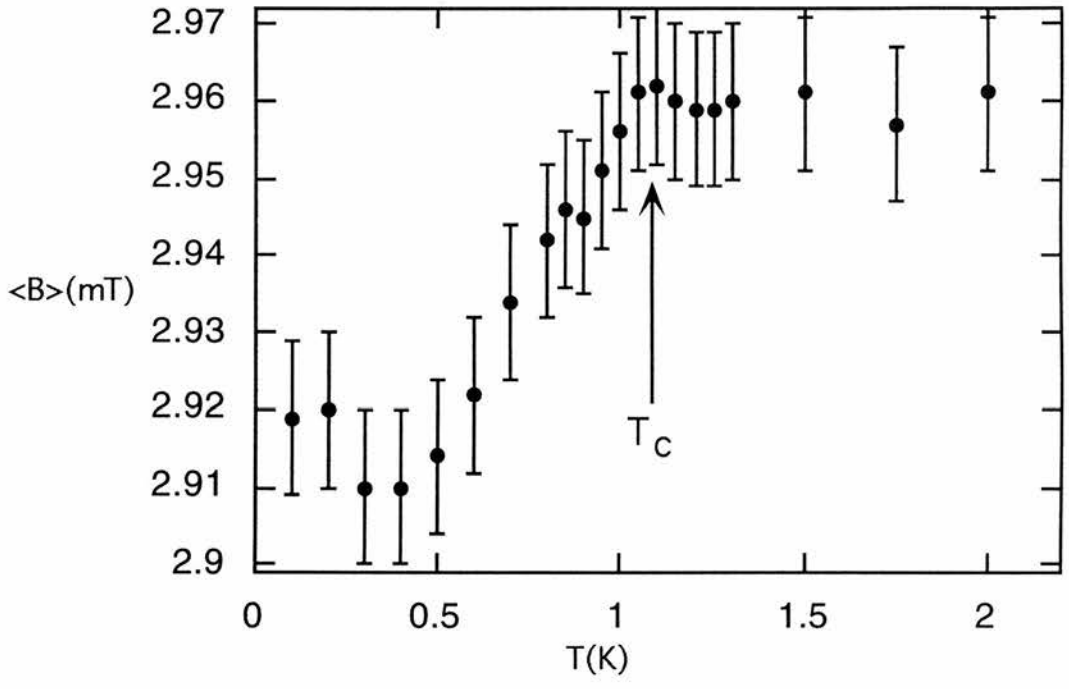

Figure 5.12: The temperature dependence of the mean internal field <B> for α-$(ET)_2NH_4Hg(SCN)_4$) in an applied field of 3 mT. The transition into the superconducting state, T_c, is determined by the onset of diamagnetic behaviour indicated in this figure at $\approx$ 1.1 K. An apparent upturn in <B> similar to that observed in ET-Cu is also observed but this upturn is smaller and may not be significant.

Figure 5.12 shows the temperature dependence of the mean internal field for the organic superconductor α-$(ET)_2NH_4Hg(SCN)_4$ at a field of 3 mT. The onset of diamagnetic behaviour confirms that the transition temperature in this crystal is $\approx$ 1.1 K. Similar to ET-Cu there is an apparent upturn in <B> at the lowest temperatures. In ET-Cu it was suggested that this is due to an increase in the correlations between the stopped muons and the pancake vortex cores, but the upturn here is small and may not be significant.

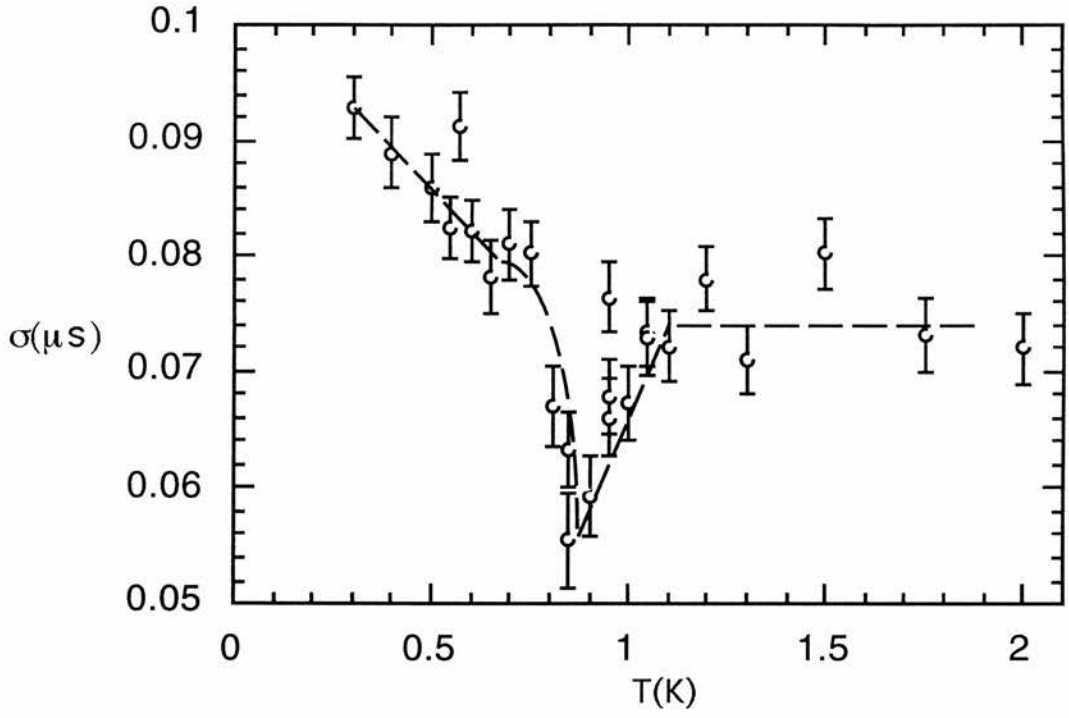

Figure 5.13: A temperature scan for the organic superconductor ET-NH_4 at 1.4 mT. Guides to the eye have been drawn in to indicate the slow decrease in σ from 0.3 K, the rapid change in σ at $\sim$ 0.8 K and the slight increase in σ up to the value attained above T_c.

Figure 5.13 shows a temperature scan at a field of 1.4 mT in ET-NH4 against the μSR damping rate, σ. The β criterion has not been used here as a consequence

of the extremely narrow lineshapes which were measured. As was noted earlier these narrow lineshapes are a result of the extremely long penetration depth in this organic superconductor and the extremely small damping rate which is due to the superconductivity. The μSR damping rate, σ, has been extracted here assuming a Gaussian distribution of internal fields. Figure 5.13 shows a steady decrease in damping rate as a consequence of a reduction in pancake correlations along the field direction as the temperature is increased. There is also a rapid change in σ at $\sim$0.8 K before the damping rate gains in magnitude to plateau in value above T_c. Using Eqs. 3.8 and 3.10 (see section 3.2.2) it has been possible to estimate the in-plane penetration depth to be $\approx$ 12000 Å. If one assumes that the analysis of *Clem et al (1991)* [118] of an ECPS is applicable to this system, then ET-NH4 (with s$\sim$20Å [37]) would be expected to exhibit *thermal breakup* at a temperature $T_b \sim$1 K. As was previously noted, T_b is only an approximate energy scale, but clearly gives a good indication of the relative energy scale at which the vortex structure in ET-NH4 undergoes a transition. Such a transition seems to be observed here, and is made quite possible at such low temperatures in this system as a result of the extremely large anisotropy, γ and penetration depth, λ. However, it is not clear at present why the damping rate falls below that measured in the normal state.

Figure 5.14 shows a field scan of ET-NH4 against the μSR damping rate, σ. It is clear that the damping rate falls as the field increases, indicating a reduction in correlations of the pancake vortices along the direction parallel to the applied field. It then reaches a plateau above 2.2 mT. For B_{2D}, taking $\gamma \sim$1000 [50] and s as 20 Å [37] gives $B_{2D} \sim$ 0.5 mT. From the estimate of the penetration depth, and using Eq. 5.2, it would be expected that $B_\lambda \sim$1.4 mT.

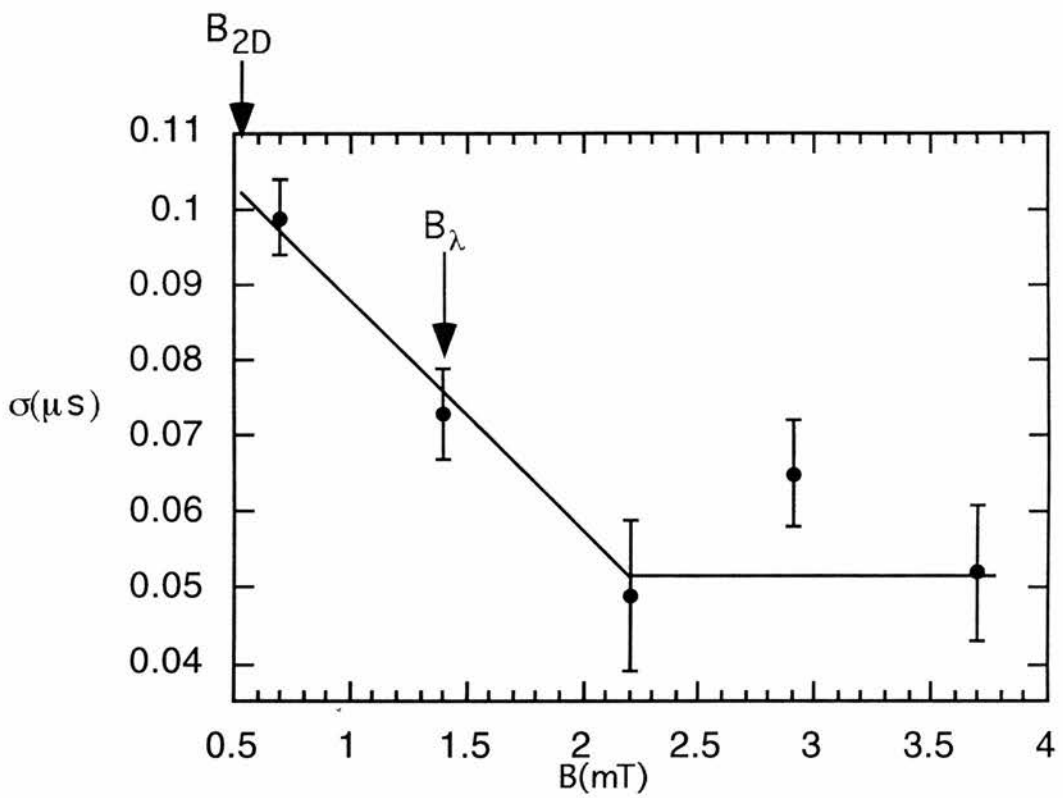

Figure 5.14: A field scan of ET-NH4 against μSR damping rate. There is a reduction in the damping rate until 2.2 mT where the value plateaus. The predictions of the dimensional crossover field for both B_{2D} and B_λ are indicated.

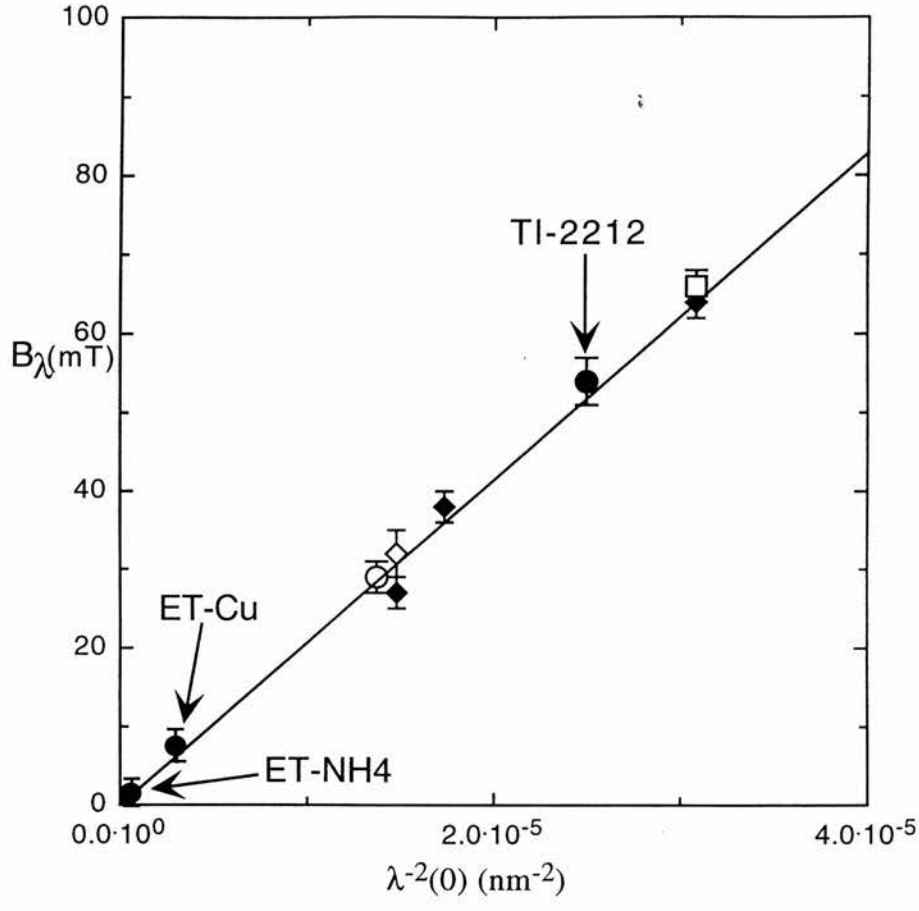

Figure 5.15: The crossover field B_λ as a function of $\lambda_{||}^{-2}$ for different samples taken from ref. [60]. The open symbols correspond to μSR measurements on samples of BSCCO with different stoichiometry. The filled diamonds are taken from ref. [129] and were obtained from magnetization measurements using Hall bar arrays. The filled circle, indicated here, is from a $Tl_2Sr_2CaCu_2O_{8+\delta}$ (Tl-2212) sample taken from ref. [130], where the crossover field was determined by magnetisation measurements. The solid line corresponds to the relation $B_\lambda = \Phi_o/\lambda_{||}^2$. Included in this figure are the measured crossover field and respective penetration depths for the organic systems ET-Cu and ET-NH4 measured here. Although $B_\lambda \sim \Phi_o/\lambda_{||}^2$ is only a rough guide the correlation across many different systems is surprisingly good.

Figure 5.15 shows the experimental values of the measured crossover field plotted as a function of $\lambda_{||}$ taken from ref. [60]. Included in the plot are experimental observations of ET-Cu and ET-NH4 measured in this work. Although $B_{cr} \sim \Phi_o/\lambda_{||}^2$ is only a rough guide for the dimensional crossover for an electromagnetically coupled system the agreement of the organic superconductors with the other systems is surprisingly good.

5.6 Small angle neutron scattering(SANS) on κ-(BEDT-TTF)$_2$Cu(NCS)$_2$

5.6.1 Introduction and Experimental Apparatus

Neutron scattering measurements were carried out on a mosaic of well aligned ET-Cu crystals (200 mg). The mosaic was mounted on a custom built sample holder and was oriented with the a-axes of the crystal parallel to the incident neutron beam. The sample environment was a narrow tailed AS Scientific "Orange" cryostat. The magnetic field was produced by a custom built electromagnet and was aligned with the neutron beam by means of preliminary measurements on a single crystal of niobium. The diffracted intensity was investigated at the lowest attainable temperature of 1.5 K and in fields between 2 mT and 10 mT. The experiments were performed on D22 using a neutron wavelength of 19 Å . It was calculated that this wavelength would increase the angle of diffraction sufficiently in order for a diffraction pattern to be seen, but also offered the best *trade-off* with the incident intensity (see section 3.3). The sample detector distance and the collimation distance for the incident beam were both 17.6 m. This detector distance was chosen to allow good angular resolution.

5.6.2 Results and Discussion

Experiments were carried out above and below the predicted crossover field, B_{cr}, at fields of 10.2 mT, 8.13 mT and 6.1 mT, 4.5 mT, 3.1 mT and 2 mT respectively. Figure 5.16 shows a picture of a tangential average of the diffracted intensity for ET-Cu in a field of 2 mT at a temperature of 1.5 K. The tangential average is defined as the average scattered intensity at radial distances (associated with different scattering vectors, $\mathbf{q}$) from the centre of the detector and was used here as it was evident that the six-fold symmetry expected for a hexagonal lattice was not observed for ET-Cu as mosaic spread of the already *weak* diffracted intensity would be spread thoughout reciprocal space. The expected $\mathbf{q}$ value for the applied field is indicated with an arrow in this figure, and it is evident that a peak at the expected $\mathbf{q}$ is not observed for ET-Cu in a field of 2 mT. The graphs for 10.2 mT, 8.13 mT and 6.1 mT, 4.5 mT, 3.1 mT are equally as unconvincing. There are several factors which may account for the difficulties that where encountered in detecting a flux-lattice in ET-Cu. Firstly, as a consequence of the low fields that have to be applied in order to see the 3D lattice indicated by μSR, the expected Bragg spots are very close to the through beam, even though the detector was at maximal extent. As was mentioned above, the spread of the mosaic would also ensure that the diffracted intensity would be spread throughout reciprocal space. Finally, and most importantly, the diffracted intensity from the flux-lattice in ET-Cu is extremely difficult to measure as a consequence of the relationship between the integrated intensity and the penetration depth through the structure factor, F_{hk} (see Eq. 3.32). The penetration depth ($\sim$ 5400 Å) is significantly larger than that found in BSCCO ($\sim$ 1800 Å) [60] and YBCO ($\sim$ 1400 Å), so it comes as no surprise that in the experiments carried out here, the long range

order associated with a flux-lattice in neutron experiments is extremely difficult to measure. Figure 5.17 indicates the result for the tangential average for a similar experiment on $BSCCO_{opt}$(λ ~2600 Å), cooled to 5 K in a field of 20 mT. Here, the diffracted intensity is evident as a peak spread about the expected **q** value of 1.82×10^{-3}.

5.7 Summary and Conclusions

The work presented in this chapter has concentrated upon the flux lattice structure in the organic superconductors κ-(BEDT-TTF)$_2$Cu(NCS)$_2$ (ET-Cu) and α-(BEDT-TTF)$_2$NH$_4$Hg(SCN)$_4$ (ET-NH$_4$). The observations made here indicate that the penetration depth of these superconductors are 5200 Å and 12000 Å respectively. The dimensional crossover fields were also estimated . These were plotted on a figure from ref. [60] which indicates a *generic* trend between the measured crossover field, B_λ, and the measured penetration depth for systems in which electromagnetic interactions play a dominant role. Measurements of the angular dependence of $\langle\Delta B^2\rangle^{1/2}(T)(\vartheta)$ were also made for ET-Cu in three fields (2 mT, 5 mT and 8 mT). It was found that for applied fields of 2 mT and 5 mT the behaviour of ET-Cu tended towards a $cos(\theta)$ dependence, but never quite gave the perfect agreement that is evident in the BSSCO system. Additionally, the 8 mT data in ET-Cu was found to exhibit no angular dependence until the field was applied at θ >40° where a *weak* angular dependence was evident. This angular dependence at higher angles is similar to the behaviour exhibited in BSSCO at fields where the c-axis component falls below B_{cr} as the sample is rotated and the data regains a $cos(\theta)$ dependence.

Measurements were also made of a melting line in ET-Cu and attempts were

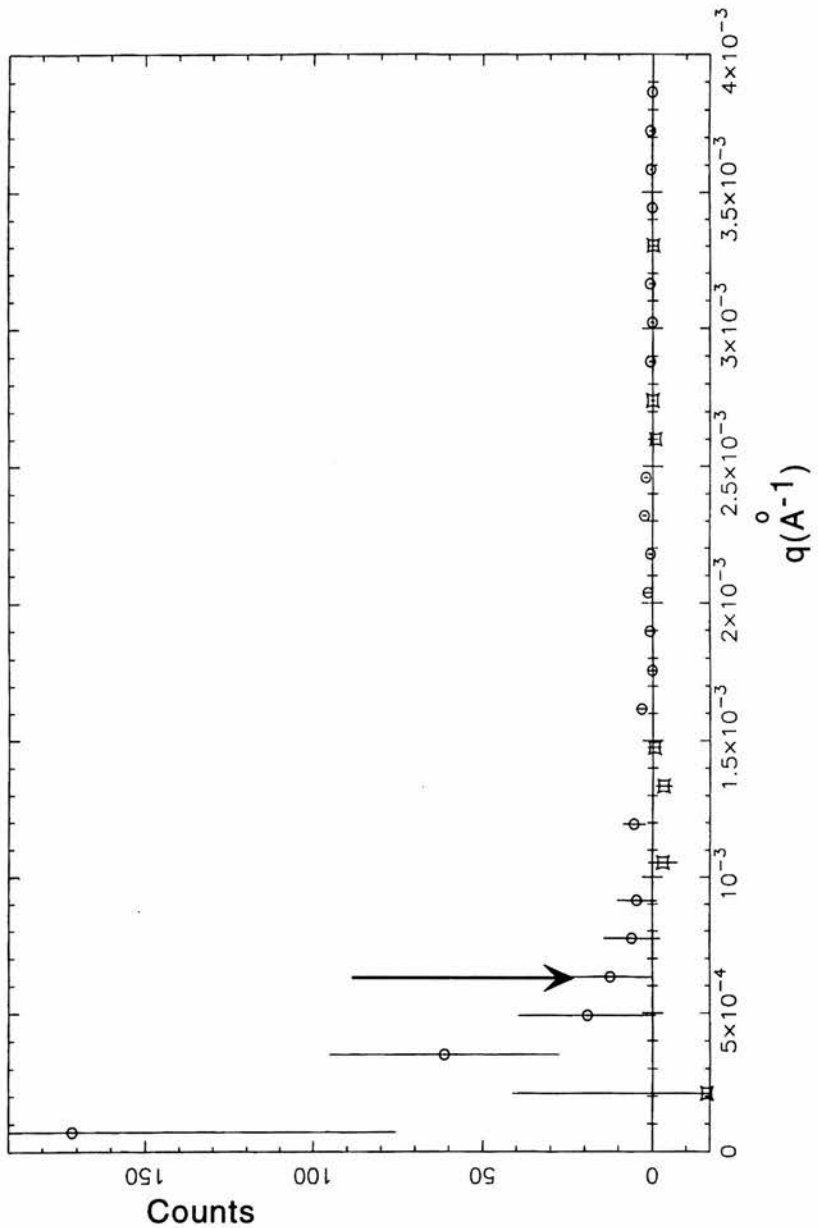

Figure 5.16: The result of a SANS measurement carried out on ET-Cu, cooled to 5 K in a field of 2 mT. The plot indicates the total counts of a tangential average against **q** after the background was subtracted.

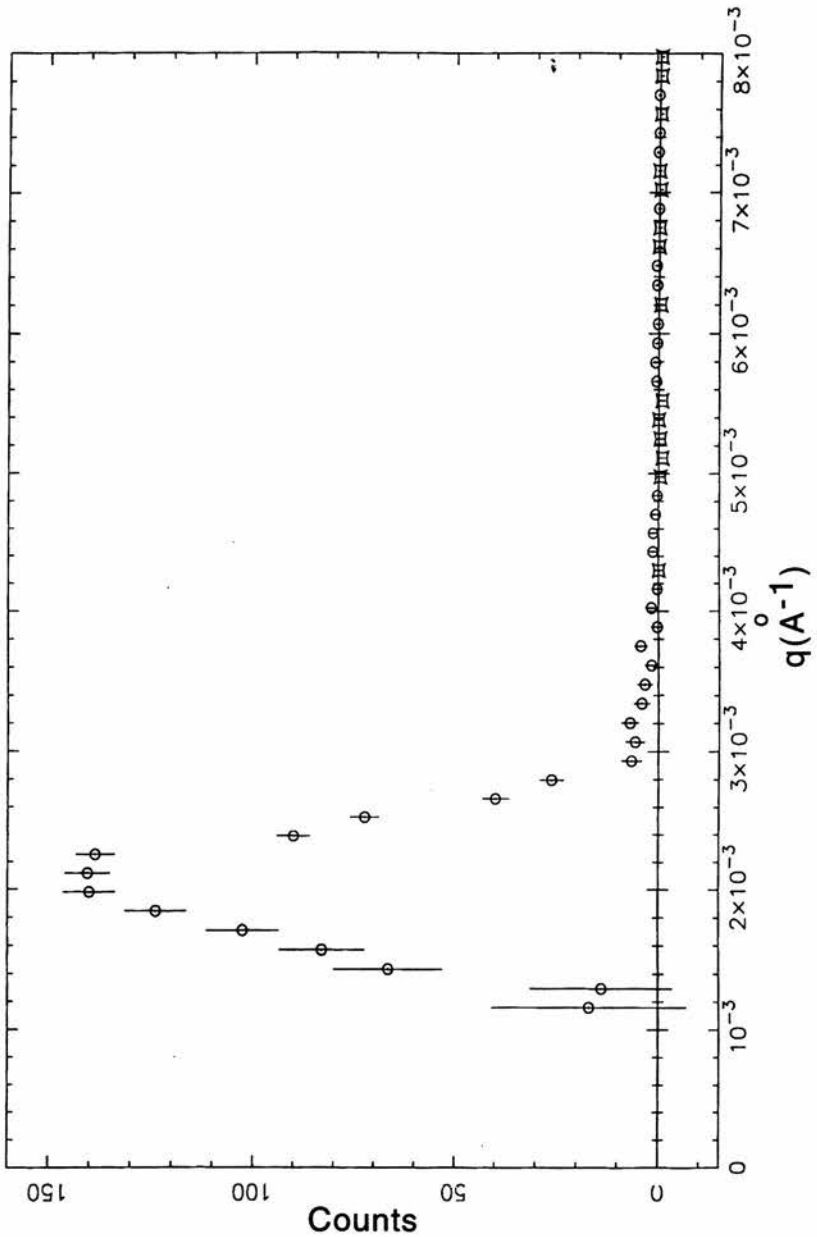

Figure 5.17: The tangential average for a similar experiment as ET-Cu (cf Fig. 5.16) carried out on $BSCCO_{opt}(\lambda \sim 2600$ Å), cooled to 5 K in a field of 20 mT. A peak in the counts spread about the expected **q** value of 1.82×10^{-3} indicates the presence of a flux-line lattice.

made to fit this melting line to the forms of melting line encountered in section 2.4. It was evident from this work that a more detailed investigation of the melting line in ET-Cu must be carried out in order for further information to be brought to fruition, as it can only be concluded that measurements made here possibly span the different melting regimes encountered for BSSCO in section 2.6. Further measurements were also carried out on ET-NH_4. Although these experiments were *extremely* challenging, important information can be extracted from the results. The ET-NH_4 system was seen to undergo a transition in a field of 1.4 mT and at a temperature of 0.8 K. This was found to occur at the correct energy-scale predicted for the melt of an ECPS. However, as the investigation into ET-Cu has demonstrated, further measurements are required in order to investigate the possibility that ET-NH_4 exhibits a melting line. This latter measurement is particularly impressive, as, not only does it indicate the the presence of a flux-pancake lattice in a system with an extremely long penetration depth, ($\lambda_{||}$=12000 Å), and consequently at the edge of detectability, but this flux-pancake-lattice undergoes abrupt changes (cf Fig. 5.13).

5.7.1 Generic conclusions

It is instructive to reiterate the key issues raised by this work. The large values of γ and λ encountered in the organic systems make thermal disruption possible, even at the low temperatures involved. These parameters also indicate that $\lambda \sim \gamma$s, and electromagnetic coupling must play a role in the dynamics of the vortex system, indeed, both organic systems undergo a dimensional crossover which is not inconsistent with $B_\lambda \sim \phi_o/\lambda_{||}^2$. Finally, this work highlights many similarities between the vortex dynamics in layered organic systems and the layered HTSC,

BSSCO (i.e. melting, dimensional crossover, electromagnetic coupling and the angular variation of $\langle \Delta B^2 \rangle^{1/2}(T)(\vartheta))$ and in this sense indicates that much of the vortex behaviour in highly layered superconductors is *generic.*

Chapter 6

Neutron Scattering and μSR studies of optimally doped $Bi_{2.15}Sr_{1.85}Ca_1Cu_2O_{8+\delta}$ (BSCCO)

6.1 Introduction

The high temperature superconductor BSCCO is the archetypal example of an extremely anisotropic superconductor. This leads to a flux lattice with an extremely rich and complex phase diagram. Unlike the flux-lines that are exhibited by YBCO, flux-lines in BSCCO are better described as a stack of 2 dimensional *pancake* vortices. This leads, in the first instance, to regions of the phase diagram where the system exhibits 3D behaviour and regions of the phase diagram where it exhibits more 2D behaviour (see section 2.6). The studies carried out in this chapter focus on an optimally-doped mosaic of high quality $BSCCO_{opt}$ crystals (T_c ~92 K). Measurements on this sample allow recent generic trends presented for highly anisotropic superconductors to be tested [59, 51].

6.2 Previous Work

BSCCO has been the subject of immense theoretical and experimental attention. The large anisotropy of this system results in vortex lines that are highly flexible. Combined with the high transition temperatures this results in large thermal fluctuations and at sufficiently high temperatures the vortex lattice can actually melt. This melting transition has been observed by many different techniques in the literature, such as resistivity [131, 132], magnetisation [133, 92], specific heat [134], latent heat [93], SANS [91] and μSR [61, 51]. As was seen in section 2.6 for over-doped $BSSCO_{over}$ (T_c ~85 K) a dimensional crossover was shown to occur. The appropriate lengthscale for this crossover for this BSCCO system was given by λ_{ab} viz.

$$B_\lambda \approx \frac{\phi_o}{\lambda_{ab}^2}. \tag{6.1}$$

As was seen in section 5.5, *Aegerter et al (1996)* [60] carried out a systematic study of several samples of BSSCO with different oxygen doping and found, together with different samples from other works (see Fig. 5.15), that the dimensional crossover for these was in accord with Eq. 6.1. Measurements presented in chapter 5 of this thesis on the organic systems κ-(BEDT-TTF)$_2$Cu(NCS)$_2$ and α-(BEDT-TTF)$_2$NH$_4$Hg(SCN)$_4$ are also in accord with Eq. 6.1. In this sense these systems may be best understood as conforming to a generic trend in which electromagnetic coupling rather than Josephson coupling predominantly control the behaviour of the vortices. This is, however, a rather contentious point in the literature and many authors (e.g. refs. [120, 119, 121]) still use B_{2D} (cf Eq. 6.2) which predicts the dimensional crossover that would be expected for a system in

which Josephson coupling dominates the vortex behaviour.

$$B_{2D} \approx \frac{\Phi_o}{s^2\gamma^2} \tag{6.2}$$

As was seen in section 2.6, B_{2D} is an appropriate expression for the prediction of the crossover in systems of low anisotropy such as YBCO. In a system of high anisotropy such as BSSCO, using this equation to predict the dimensional crossover is inappropriate as it has been shown that electromagnetic coupling may play an important role [51, 60].

It has been shown previously by *Y.-Q.Song et al (1993,1995)* [135, 136] and demonstrated by *Lee et al (1995)* [137] that thermal fluctuations of the pancake vortices in a superconducting system such as BSCCO lead to a reduction in the width of the field distribution measured for an ideal lattice by μSR (cf Eq. 6.3),

$$\langle \Delta B^2 \rangle(T) = B^2 \sum_{q \neq 0} \frac{1}{[1 + \lambda^2(T) q^2]^2} \tag{6.3}$$

according to the addition of a Debye-Waller factor (cf Eq. 6.4),

$$\langle \Delta B^2 \rangle(T) = B^2 \sum_{q \neq 0} \frac{e^{-q^2 \langle u^2 \rangle / 2}}{[1 + \lambda^2(T) q^2]^2} \tag{6.4}$$

where $< u^2 >$(B,T) is the amplitude of thermal fluctuations. From section 3.3.2 it was seen that the scattered neutron intensity $I(q) \propto |F_{hk}|^2$, where $|F_{hk}|^2$ can be modified by a similar Debye-Waller type correction to account for thermal fluctuations of the vortices. The integrated intensity, I, will therefore vary in a similar manner to the second moment, $< \Delta B^2 >$. The crucial point about $< u^2 >$(B,T) is that in a regime below the dimensional crossover field, B_{cr}, and below the melting line, B_m, it has been argued theoretically [59, 57] that this factor changes according to the type of coupling which is dominant. In ref. [57]

for a system in which Josephson coupling dominates this is given by

$$< u^2 > (B,T) = \frac{16\pi^{3/2} k_B T \lambda_{ab}^2 \gamma}{B^{1/2} \phi_o^{3/2}} \frac{1}{\sqrt{log(k_{max} a_o)}} \tag{6.5}$$

where the approximation k_{max} $\sim 2\pi/a_o$ has been used in this work and a_o is the average intervortex spacing. For a purely electromagnetic coupled system ref. [59] indicates that

$$< u^2 > (B,T) = \frac{8 k_B T \lambda_{ab}^2 a_o^2 \sqrt{3}\pi}{B \phi_o s} log(1 + 4\pi\delta\beta) \tag{6.6}$$

where

$$\beta = \frac{1}{log(1 + \frac{4\lambda_{ab}^2}{c_L^2 a_o^2})} \tag{6.7}$$

and

$$\delta = \frac{32\pi^2 \lambda_{ab}^2 c_{66}}{\phi_o^2} \tag{6.8}$$

where c_{66} is the shear modulus and is $c_{66} = \phi_o^2/64\pi^2\lambda_{ab}^2 a_o^2$ in the region of interest [59]. Finally for a system where both electromagnetic coupling and Josephson coupling are present ref. [59] indicates that

$$< u^2 > (B,T) = 32 k_B T \lambda_{ab}^3 \gamma \sqrt{\beta} \frac{log(1 + 4\pi\delta\beta)}{1 + 4\pi\delta\beta}. \tag{6.9}$$

where β and δ are as indicated in Eqs. 6.7 and 6.8 respectively. It is evident from the above that the dependence of the amplitude for thermal fluctuations is dependent on the penetration depth, field and γ for Eq. 6.5, the penetration depth and field for Eq. 6.6 and on the penetration depth and γ for Eq. 6.9. It also clear, assuming that the same description of the vortex fluctuation applies in both cases, that a relatively modest increase in the value of λ_{ab} will have an increased and more notable effect on the temperature dependence of the μSR linewidth through Eq. 6.4 and on the Integrated intensity, I of a SANS experiment through the Debye-Waller factor than for $BSCCO_{over}$(λ $\sim$1800Å). The primary aim of this chapter

was to investigate, using both μSR and SANS, an optimally doped $BSCCO_{opt}$ sample in which the penetration depth is significantly larger than under-doped BSSCO samples (λ=2600Å >1800Å) [60]. This small difference in penetration depth should have a dramatic effect on $< \Delta B^2 >$ and $I(q)$ depending upon which of Eqs. 6.5, 6.6 and 6.9 is most appropriate in the description of $BSSCO_{opt}$ [51].

6.3 Sample Characterisation

The $BSSCO_{opt}$ sample consisted of a $10\times20mm^2$ mosaic, made from four large crystals supplied by *T. W. Li*, Kamerlingh Onnes Laboratorium, Leiden University, 2300 RA Leiden, The Netherlands. Each of these crystals measured $\sim$ $10\times5\times1.0mm^2$ with the largest face parallel to the superconducting planes and a superconducting onset at 92 K measured by SQUID. These samples were grown using a floating zone technique [138] and then oxygen treated. μSR experiments on this sample were carried out on the GPS (PSI) and MUSR (RAL). SANS experiments were carried out on D22 (ILL).

6.4 Results

Figure 6.1 shows the μSR lineshape for $BSSCO_{opt}$ cooled in a field of 20 mT to 1.5 K taken at PSI with the field applied perpendicular to the superconducting planes. Shown in the figure is the simulation according to F.Ogrin (see section 4.4.2) which allows a penetration depth of 2400 Å to be estimated.

Figure 6.2 shows a neutron diffraction pattern taken on D22 (ILL) for $BSCCO_{opt}$ cooled in an applied field of 20 mT to 5 K. The six-fold symmetry expected for a hexagonal lattice is clearly seen.

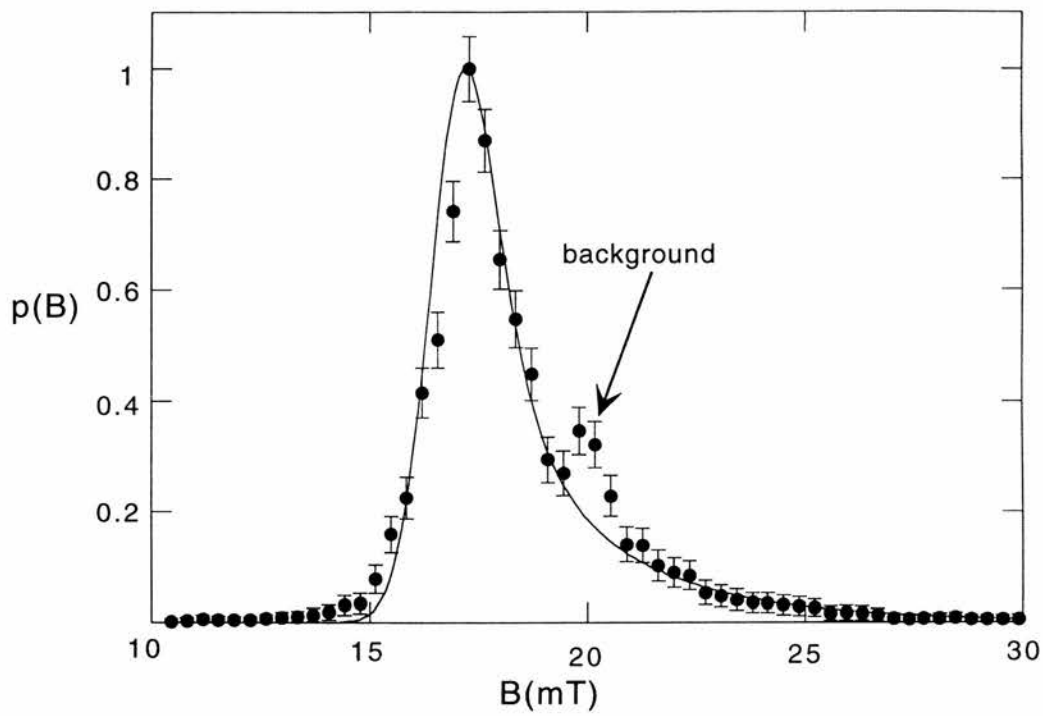

Figure 6.1: This figure shows a μSR lineshape for $BSSCO_{opt}$ cooled in a field of 20 mT to a temperature of 1.5 K with the field perpendicular to the superconducting planes. The simulation by F.Ogrin allowing a rough estimate of the penetration depth is also shown (see 4.4.2). This yields a value of λ=2400 Å. In this figure background is also evident at the applied field. This may be due to muons landing in parts of the metal sample holder which are not covered by haematite.

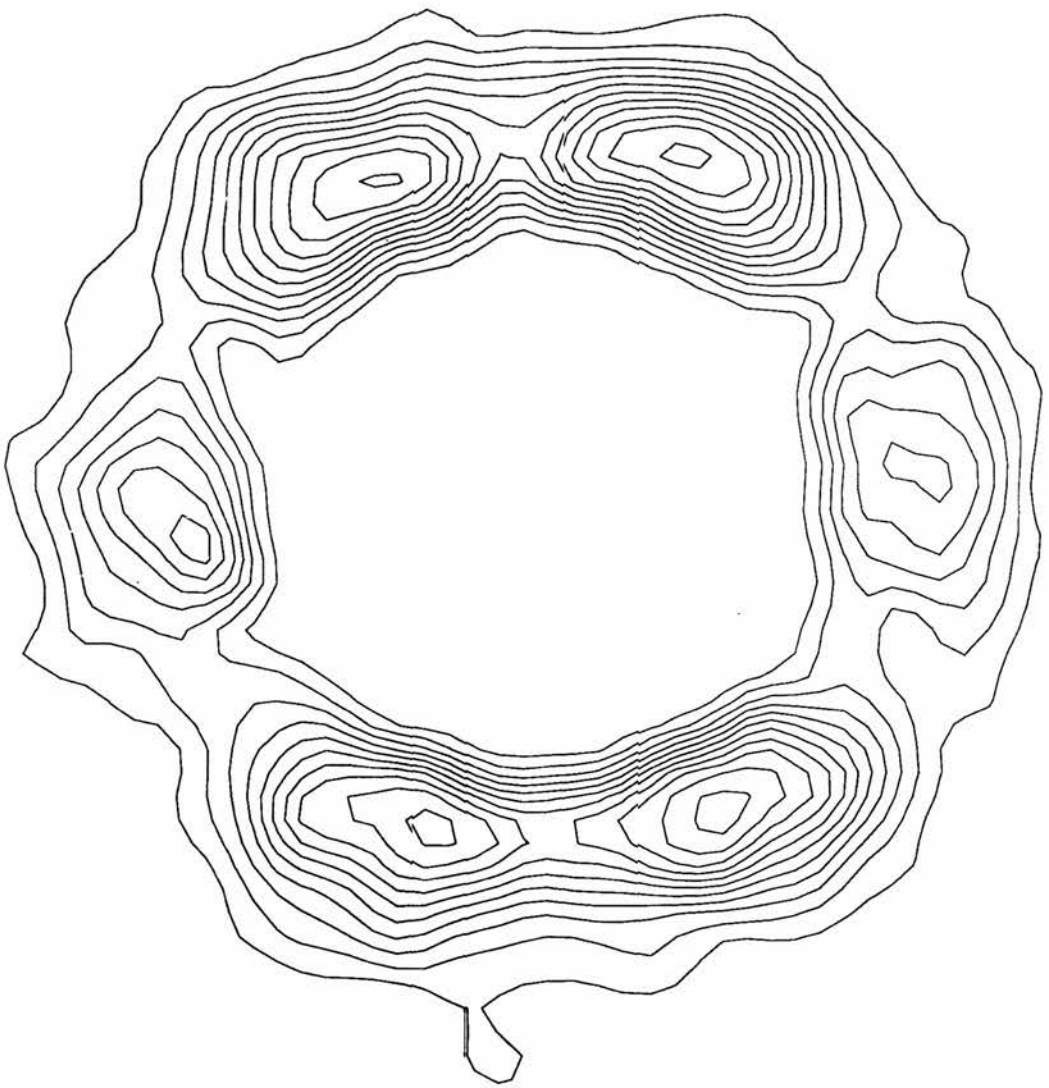

Figure 6.2: The neutron diffraction pattern for $BSSCO_{opt}$ cooled in a field of 20 mT to 5 K. The data was taken with sample-detector and collimator distances of 17.6 m and with a neutron wavelength of 19 Å. The six-fold symmetry expected for a hexagonal lattice is clearly seen. The data has been smoothed to enable clearer visualisation of the structure.

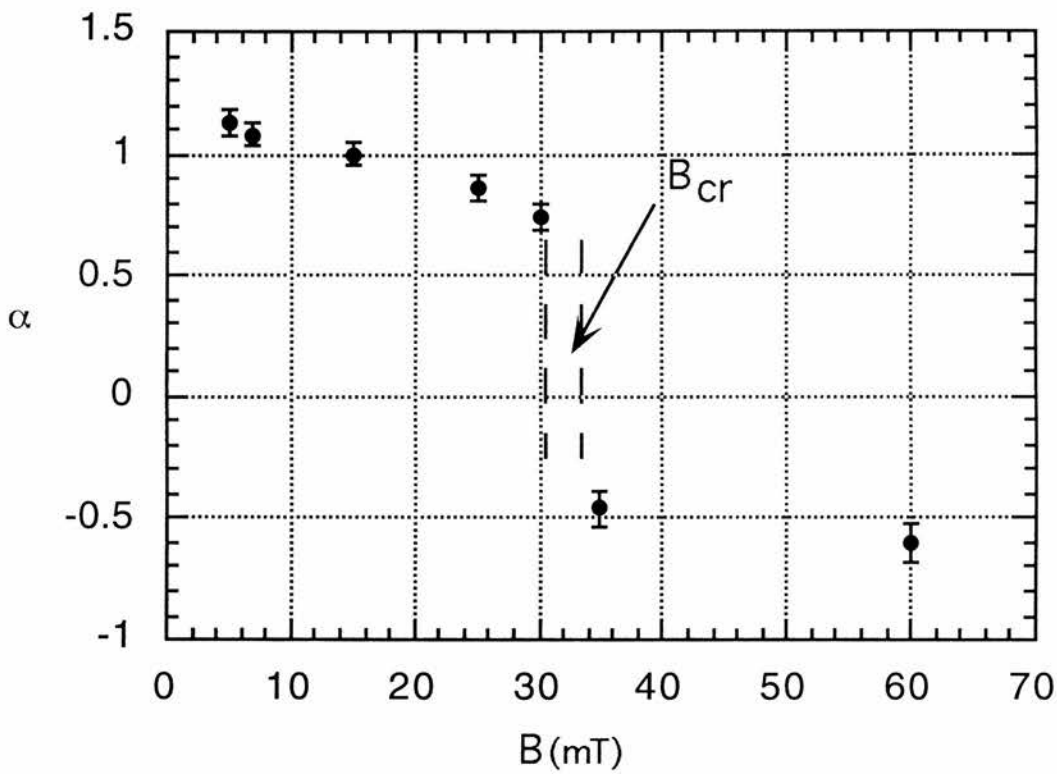

Figure 6.3: A field scan of the α parameter for $BSSCO_{opt}$ taken at PSI at a base temperature of 2 K. The area of the graph at which the dimensional crossover occurs, B_{cr}, is indicated and clearly occurs between 30 mT and 35 mT.

Figure 6.3 shows a field scan of the α parameter for $BSSCO_{opt}$ taken at PSI. The dimensional crossover is clearly observed here as lying between 30 and 35 mT. This is in reasonable agreement with the estimate of B_{cr}, using Eq. 6.1 and $\lambda \approx 2400$ Å, of 36 mT.

Figure 6.4 shows a field scan of I/**q** for a SANS experiment carried out on D22. The intensity clearly begins to reduce at 20 mT and has virtualy reduced to zero at 40 mT. Figure 6.5 and 6.6 show the effect of this reduction in intensity on the clarity of the diffraction pattern going from 30 mT to 35 mT. Figure 6.7 shows the temperature dependence of the α parameter at 20 mT, taken on the GPS (PSI) with the field applied perpendicular to the superconducting planes. A clear transition in the vortex structure is noted as a marked change in the α parameter at $T_m \sim 55$ K. This transition has previously been indicated as being due to vortex lattice melting and was first observed by μSR in BSCCO by *Lee et al (1993)* [61].

Figure 6.8 shows a plot of the normalised SANS intensity and the normalised second moment for the μSR lineshapes at a field of 20 mT. It also shows the normalised second moment for the μSR lineshape at fields of 10 mT and 5 mT. From this graph it is clear that thermal fluctuations that result in a reduction of the rms and the squareroot of the SANS intensity are field dependent. This was first noted by *Lee et al (1995)* [137]. In understanding this behaviour it has proved necessary to simulate the behaviour of Eqs. 6.5, 6.6 and 6.9 at different fields and with different values of γ. Figures 6.9, 6.10 and 6.11 show fluctuation spectra calculated using Eq. 6.4 and Eqs. 6.5, 6.6 and 6.9 respectively, for the fields measured for Fig. 6.8. Figures 6.9 and 6.11 show simulations with a penetration depth of 2400 Å and with a γ of 160, previously estimated for this system in ref. [60] and

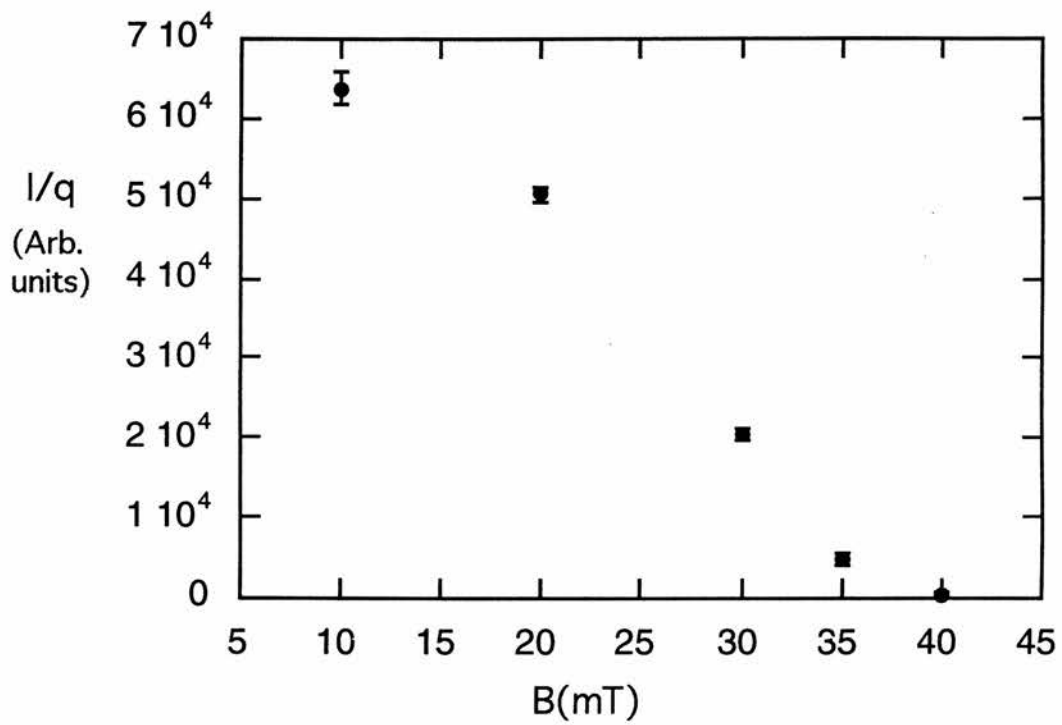

Figure 6.4: A field scan of a boxsum for $BSSCO_{opt}$ taken on D22 at a temperature of 5 K. For each field it was ensured that the same slice of the rocking curve was being measured. The intensity has also been divided by **q** for a direct comparison with the muon data. The dimensional crossover is seen here as a roll-off of the intensity, starting at 20 mT.

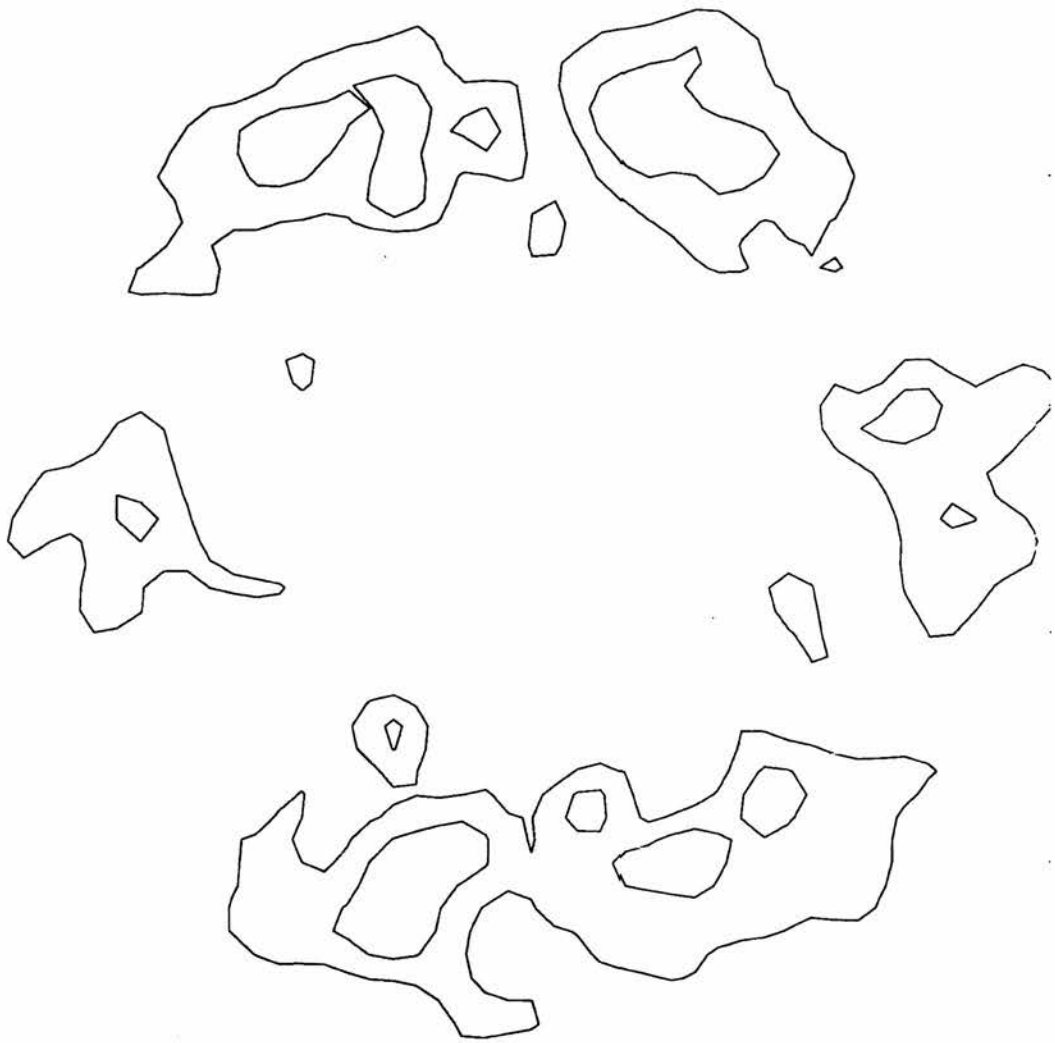

Figure 6.5: A diffraction pattern of $BSSCO_{opt}$ taken at a field of 30 mT at a temperature of 5 K on D22. Evidence for the six-fold symmetry expected for a hexagonal lattice can be seen. Once again, the data has been smoothed to aide visualisation.

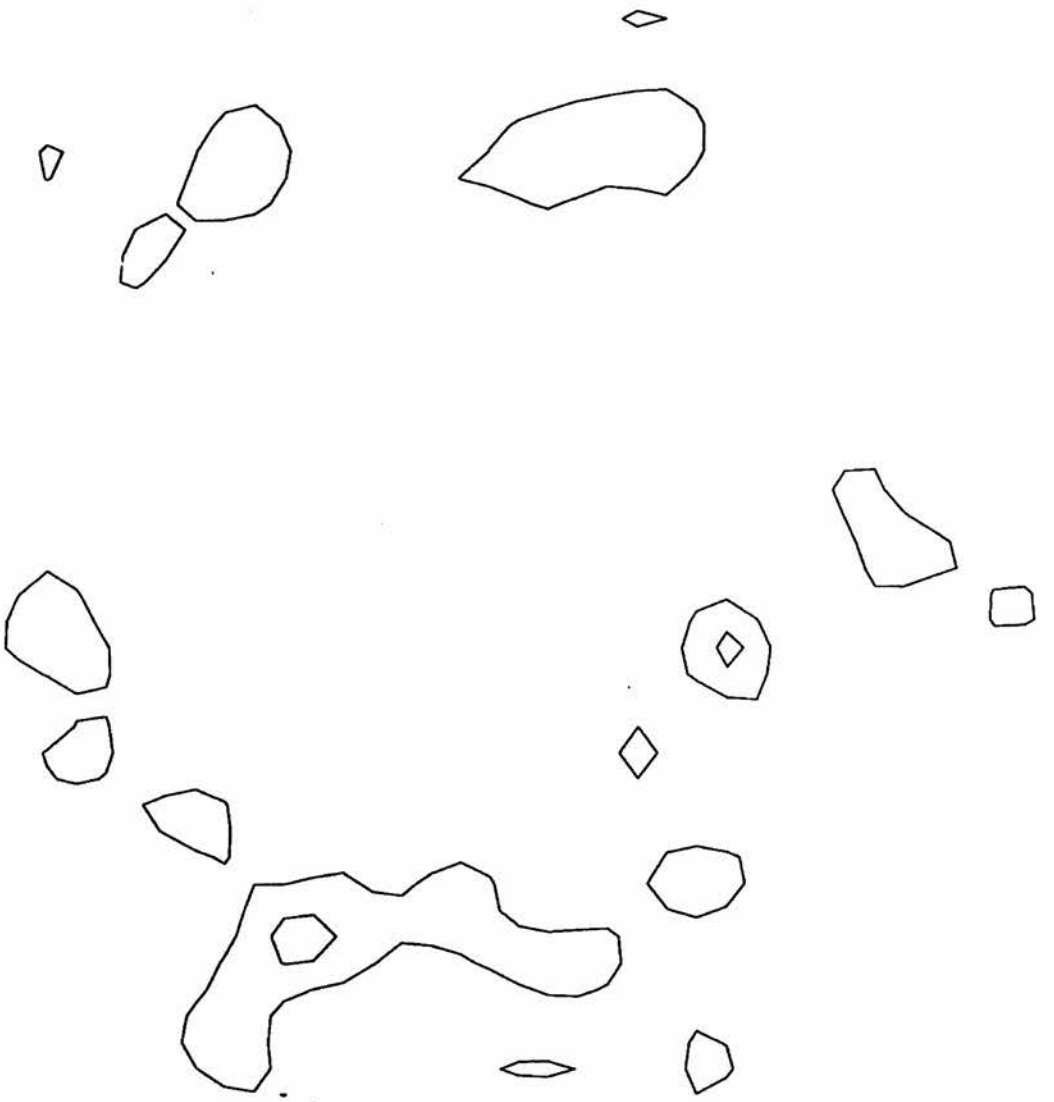

Figure 6.6: A diffraction pattern of $BSSCO_{opt}$ taken at a field of 35 mT at a temperature of 5 K on D22. The six-fold symmetry is not as clearly seen as in Fig. 6.5. The reduction in diffracted intensity is a consequence of the vortex system undergoing a dimensional crossover in which the long range order associated with c-axis correlations is reduced.

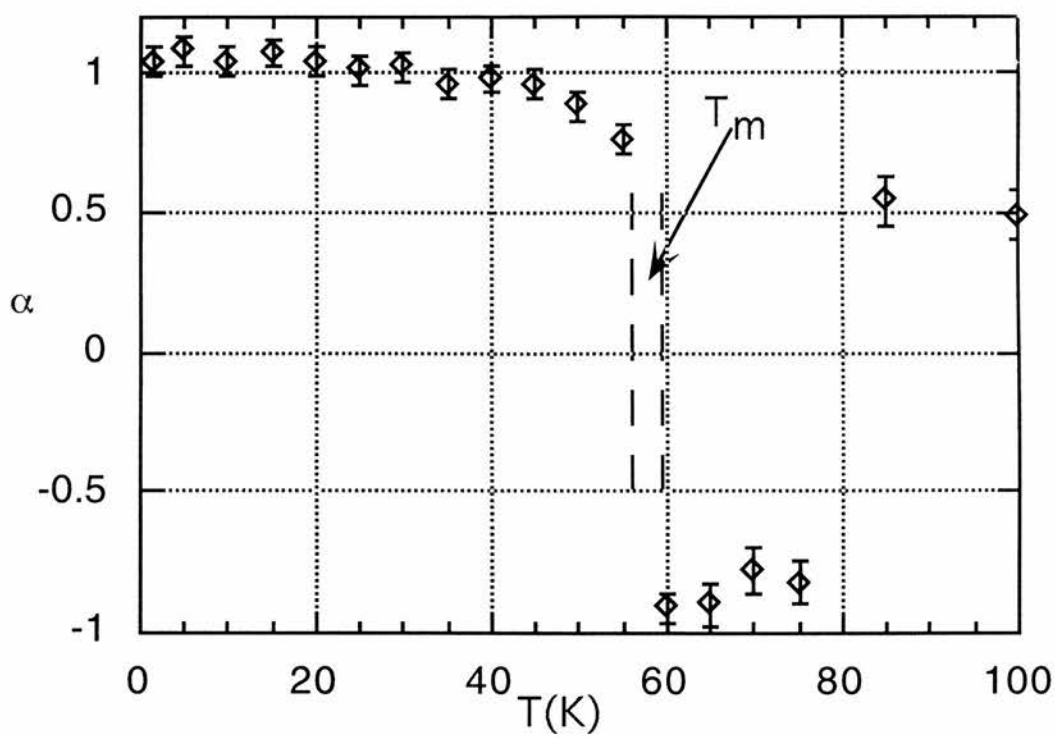

Figure 6.7: A graph of the temperature dependence of the α parameter at 20 mT, taken with the field applied perpendicular to the superconducting planes on the GPS (PSI) for $BSSCO_{opt}$. There is a clear transition in the vortex structure evident at T_m.

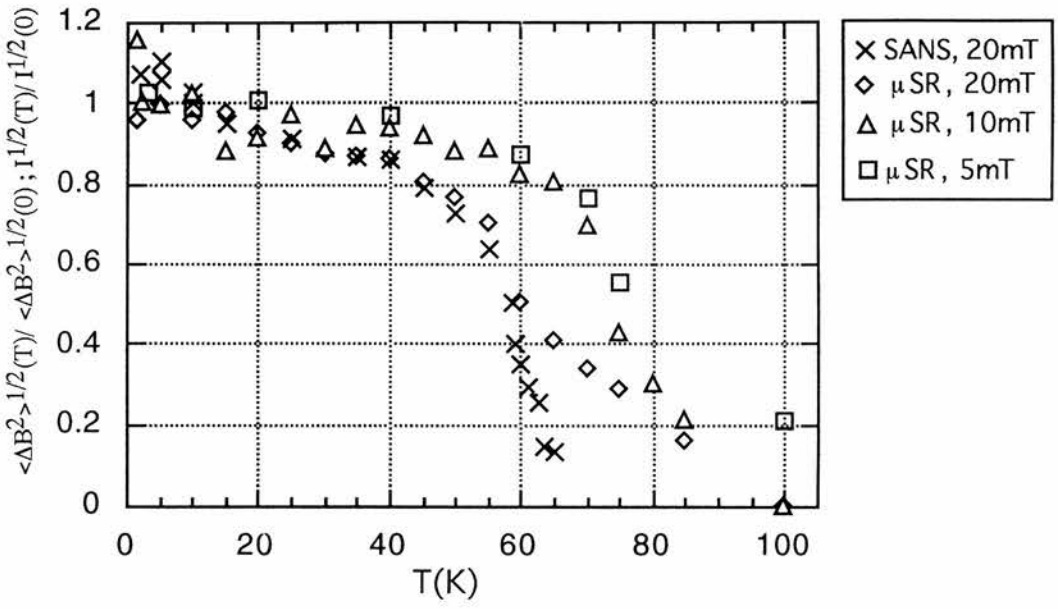

Figure 6.8: A temperature scan of the normalised rms for fields of 20 mT, 10 mT and 5 mT taken with the field applied perpendicular to the superconducting planes. Also shown in the graph is the normalised squareroot of the SANS intensity, taken on D22 (ILL), once again with the field applied perpendicular to the superconducting planes. Data taken here clearly exhibits a field dependence.

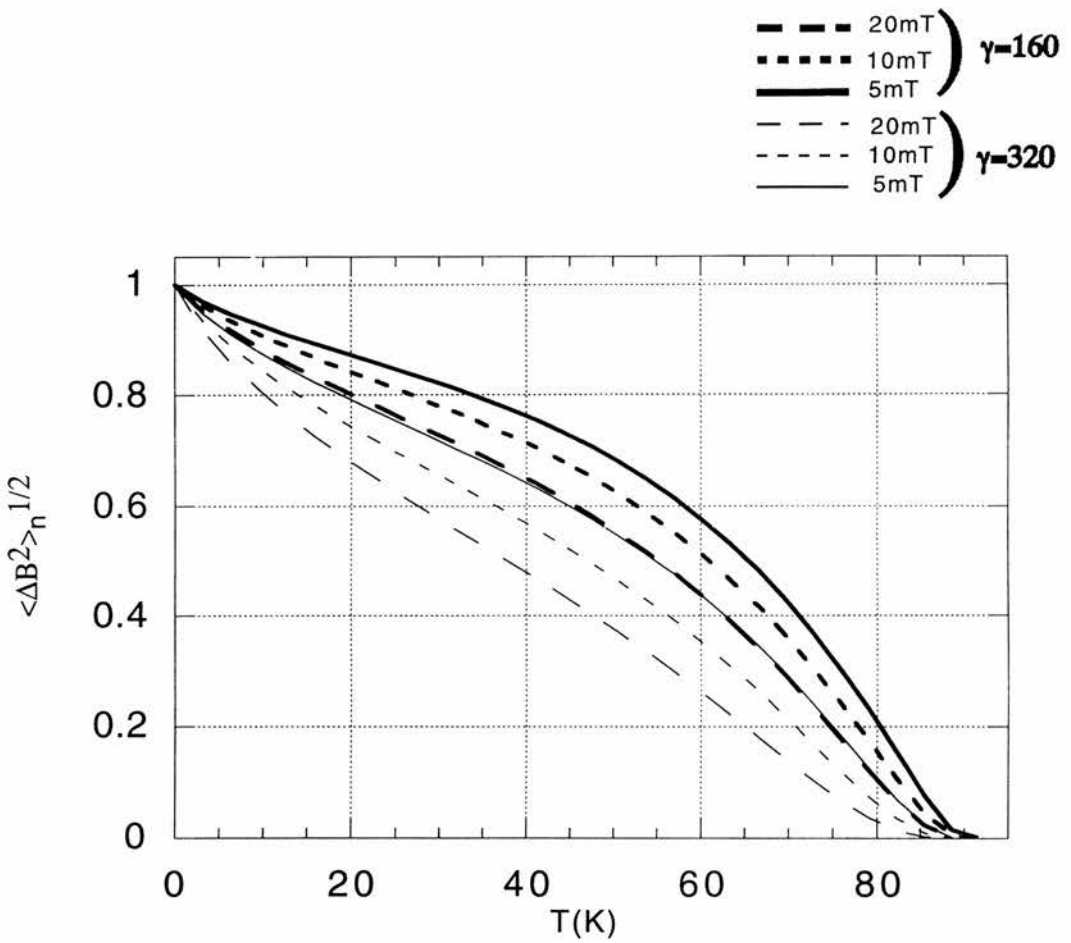

Figure 6.9: The field dependence when the fluctuations are dictated by Josephson coupling alone using Eq. 6.5. Shown in the graph are the expected fluctuation spectra for fields of 5 mT, 10 mT and 20 mT, simulated with a penetration depth of 2400 Å and with two values of γ. The γ used was that previously estimated for this system (γ=160 [60]) and twice this value (γ=320). It is clear from this graph that when γ is doubled the effect on the fluctuation spectra is significant and has a very subtle stronger dependence with field.

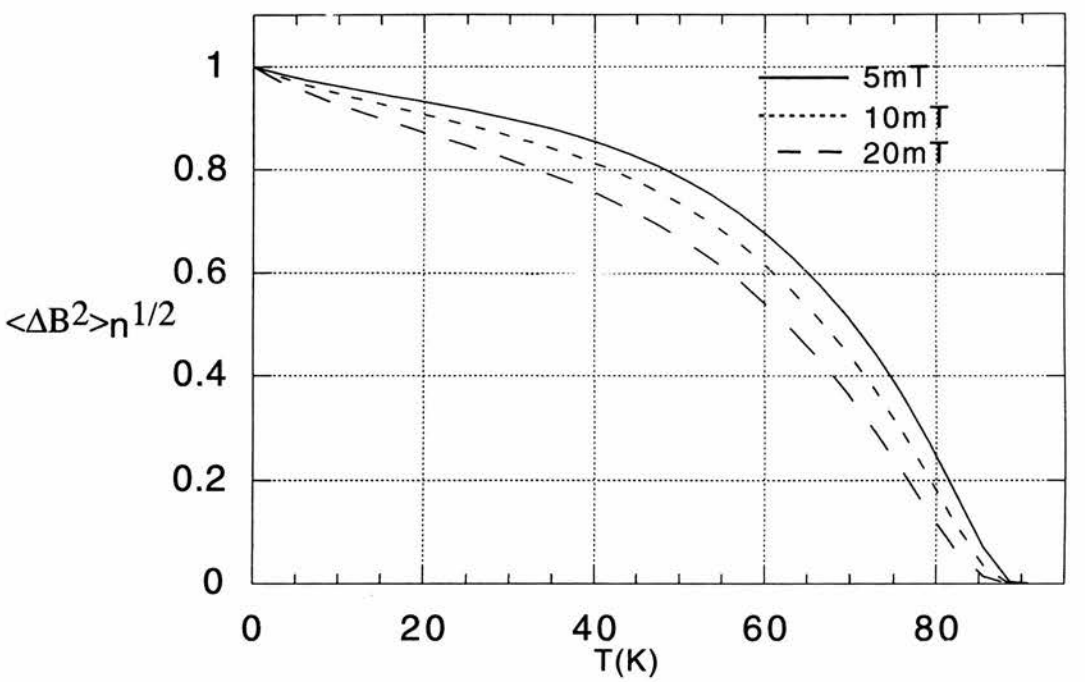

Figure 6.10: The field dependence when the fluctuations are dictated by electromagnetic coupling alone, using Eq. 6.6. A penetration depth of 2400 Å was used in these simulations.

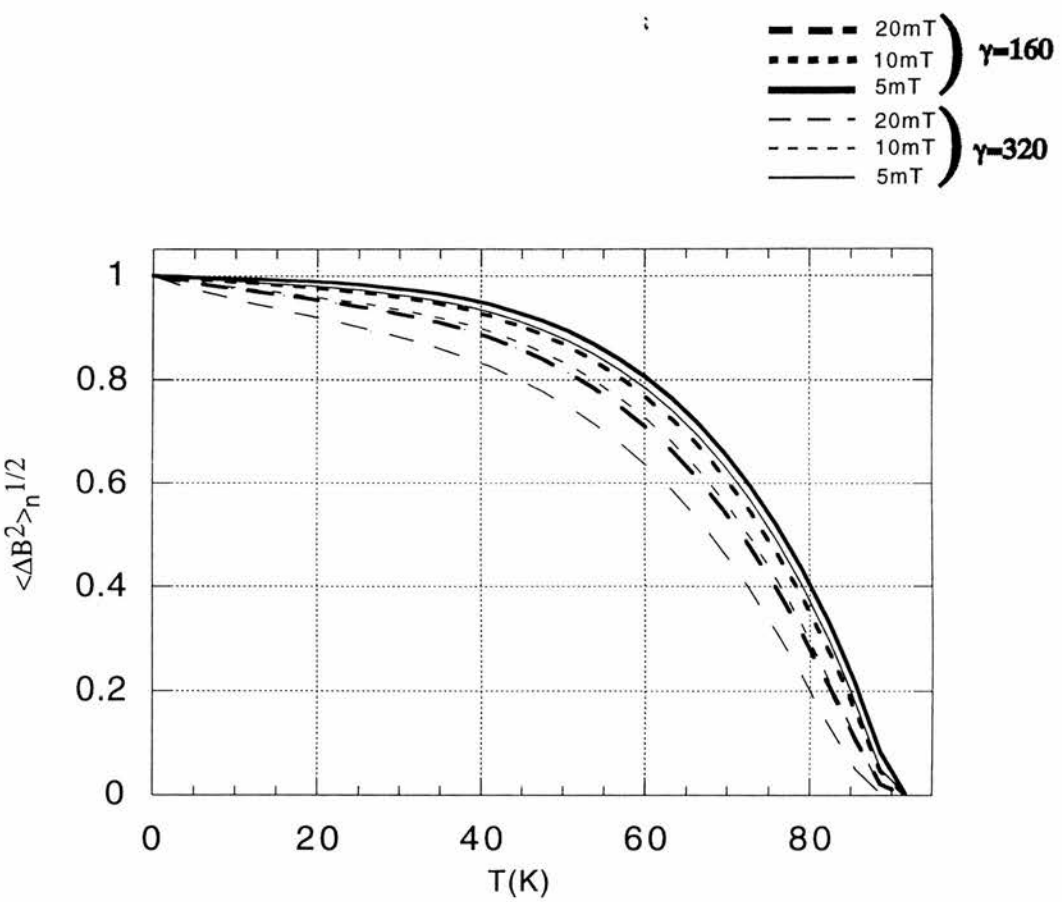

Figure 6.11: The field dependence when the fluctuations are controlled by both Josephson and electromagnetic coupling using Eq. 6.9. Shown in the graph are the expected fluctuation spectra for fields of 5 mT, 10 mT and 20 mT, simulated with a penetration depth of 2400 Å and with two values of γ. The γ used was that previously estimated for this system (γ=160[60]) and twice this value (γ=320). It is a very subtle effect, but it is evident that the field dependence on the fluctuation spectra is stronger with the larger value of γ.

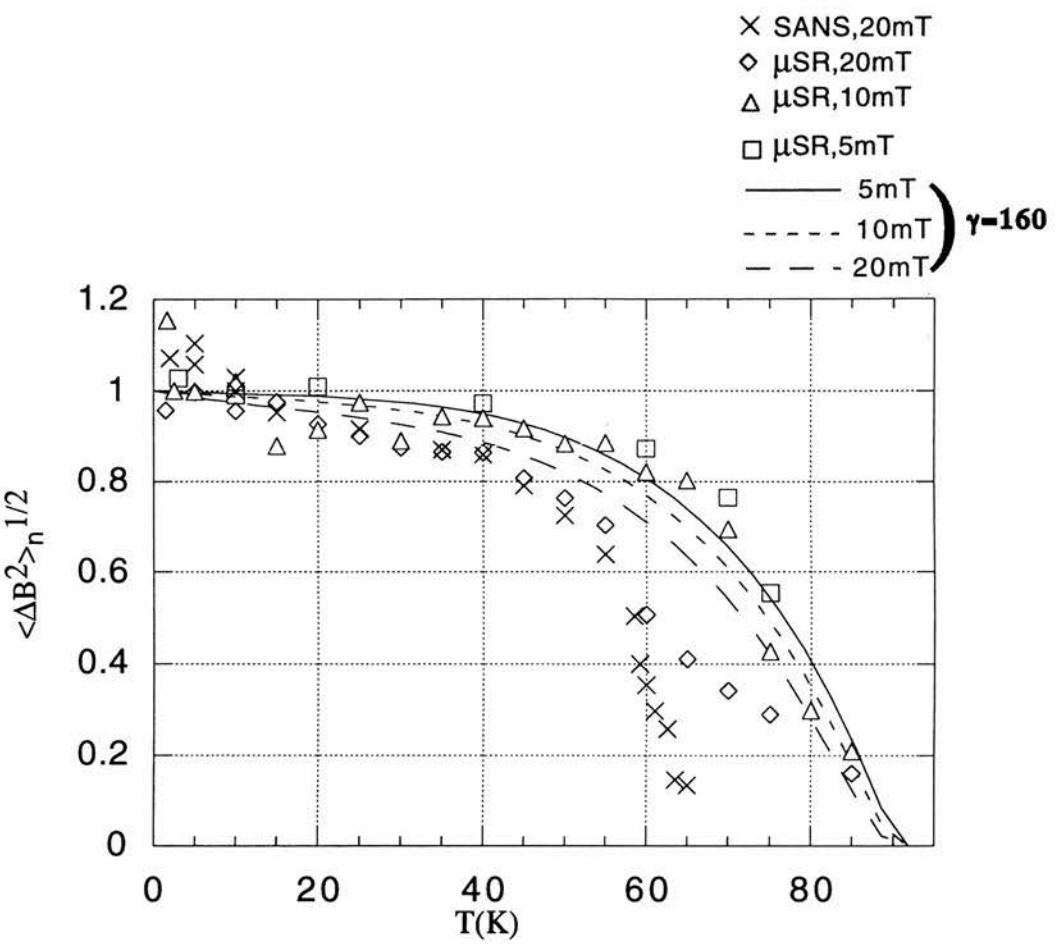

Figure 6.12: A figure containing all of the experimental data from Fig. 6.8 comparing $\langle \Delta B^2 \rangle_n^{1/2}$ against the temperature. Superimposed upon this graph are the simulations for all of the fields for Eq. 6.9 with a penetration depth of 2400 Å and γ=160.

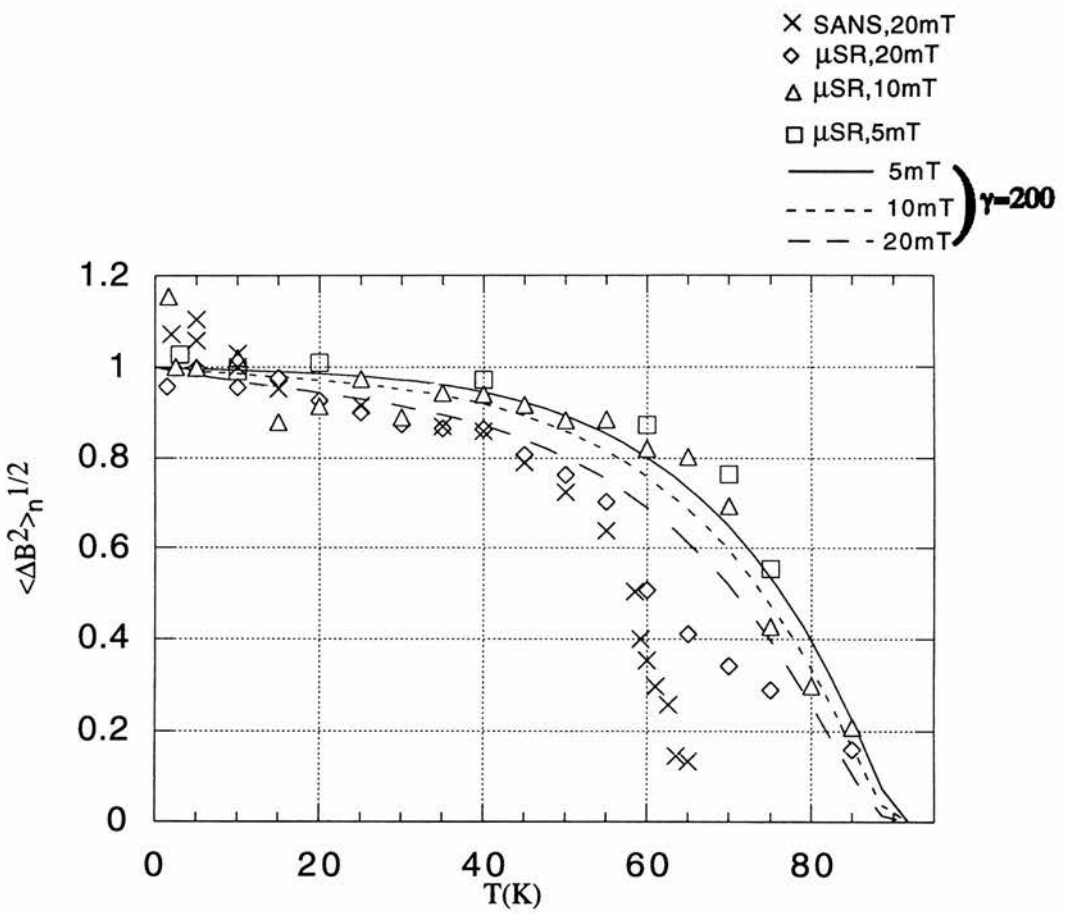

Figure 6.13: Once again a figure containing all of the experimental data from Fig. 6.8 comparing $\langle \Delta B^2 \rangle_n^{1/2}$ against the temperature. The simulations were carried out here with γ=200.

twice this value, γ=320. Figure 6.10 shows simulations with a penetration depth of 2400 Å and a γ of 160. It was evident that the type of coupling which best describes the field dependence of the data shown in Fig. 6.8 was using Eq. 6.9. Figure 6.12 shows a comparison of the data from Fig. 6.8 and the simulations with γ=160 from Fig. 6.11. It was noted earlier that the vortex structure undergoes a transition at $T_m \sim 55$ K in an applied field of 20 mT. A similar transition was evident at fields of 10 mT and 5 mT at $T_m \sim 65$ K and $T_m \sim 85$ K respectively. One would therefore expect the relevant fluctuation spectra to match the data up to these particular temperatures. It is evident that the 5 mT data is in reasonable agreement, but does seem on average to have a smaller dependence upon the fluctuations than theory would suggest. The data taken at 10 mT is in very good agreement with theory up to about 50 K and that data taken at 20 mT exhibits stronger fluctuations than theory would suggest. Figure 6.13 shows a similar graph to Fig. 6.12 with γ=200. It is evident that the theory predicts that fluctuations increase with increasing γ, so the relevant fluctuation spectra in this case migrate away from the 5mT data and towards the 20 mT data. In carrying out further simulations with different values of γ it was evident that a γ of 200 offered the best description of the data.

6.5 Discussion, Conclusions and Further work.

Optimally doped BSSCO crystals were investigated. These crystals were estimated to have a penetration depth of $\sim$ 2400 Å and exhibited a dimensional crossover field of B_{cr} $\sim$35 mT. This concurs with measurements made by ref.[60] in which the dimensional crossover is estimated according to Eq. 6.1. The flux-lattice structure was also observed to undergo a sharp transition in the α parameter which

can be attributed to flux-lattice melting. Finally, measurements were made of the temperature dependence of the rms of the μSR linewidth at three fields below the dimensional crossover field. The integrated SANS intensity was also measured for one of these fields. Simulations of the expected fluctuation spectra were undertaken. It was noted that the best description of the data was afforded in a regime in which both Josephson and electromagnetic coupling control the behaviour of the flux-pancakes. This also indicated that, taking the penetration depth to be 2400Å , the best description of the data was afforded with a value of γ >160. As was seen in section 2.6, *Lee et al (1997)* [51] demonstrated that the melting line of $BSSCO_{over}$ indicated that the flux-structure underwent a gradual transition from electromagnetic dominance to the case were both coupling mechanisms controlled the vortex behaviour at a temperature T^{em} which was indicated to occur at [59, 51]

$$T^{em} \approx T_c \left[1 - \left(\frac{\lambda_{ab}(0)}{\gamma s}\right)^2\right]^{1/4} \tag{6.10}$$

where s is the interlayer separation (s≈15Å). Using λ_{ab}=2400Å and γ=160 [60] Eq. 6.10 indicates that in this system T^{em} ~0 K. This indicates further that the correct regime for $BSSCO_{opt}$ for the data taken in this work is one where both electromagnetic and Josephson coupling control flux-pancake behaviour. This should be contrasted with $BSCCO_{over}$ where Josephson coupling only played a role over a small fraction of the phase diagram [51]. This work thus illustrates a further distinct case in the family of highly anisotropic systems for which electromagnetic coupling plays a significant role.

Chapter 7

μSR studies of irradiated BSCCO

7.1 Introduction

In order for the high temperature superconductors to be technically useful it is essential for the flux lattice to be pinned under the application of an external current, J. The irreversibility line (IL) is a good indication of this in HTSC (see section 1.9). Unfortunately, in these materials , this lies well below $H_{c2}(T)$. In order to improve this situation it has proved fruitful to irradiate samples with heavy ions. If heavy ions of sufficient energy are used, parallel tracks of damage are created called *columnar defects* (CD). CD suppress the superconducting order parameter in their vicinity and act as excellent pinning centres for flux lines due to their extended nature. In particular, the heavy ion irradiation is expected to enhance the apparent tilt modulus, c_{44} in the mixed state of HTSC BSCCO.

The physics of vortices under these conditions has been studied theoretically by *Nelson and Vinokur (1992/1993)* [139, 140], where the physics of the fluxlines has been mapped onto the problem of the localisation of quantum-mechanical bosons in two dimensions. Many interesting properties have been predicted, including

a Bose glass phase and a Mott insulator phase. The effect of several aspects of CD have been studied here in what is continuing research into an area of vortex physics which offers the most interesting and exotic vortex phenomena.

7.2 Previous Work

Heavy ion irradiation was first demonstrated to push the IL to higher fields and temperatures in single crystals of the high temperature superconductor YBCO by *Civale et al (1991)* [141] and *Konczykowski et al (1991)* [142]. Even more striking results were reported on thallium-based compounds by *Budhani, Suenaga* and *Liou (1992)* [143]. This increase results from the extremely strong pinning sites that CD present to the flux lines. CD are cylindrical in shape and typically of a diameter, d_{co}=5-7 nm. The influence of CD is most pronounced when the external field is applied parallel to the defects and fluxlines may be pinned along their entire length. The *matching field*, B_Φ, for a particular sample is the field at which

$$B_\Phi = n\Phi_o \tag{7.1}$$

where n indicates the density of tracks and Φ_o is the flux quantum. It is essentially the applied field at which the density of flux lines would equal that of the defects. In simple terms there are three obvious regimes for an irradiated sample and these are shown in a schematic plan-view in Fig. 7.1. For $B<B_\phi$ the number of defects exceeds the number of vortices and each fluxline occupies a defect. For $B=B_\phi$ the number of defects equals the number of fluxons and for $B>B_\phi$ the number of fluxons exceeds the number of defects resulting in fluxlines which are unpinned. For $B<B_\Phi$, each fluxline will be localised onto a single columnar

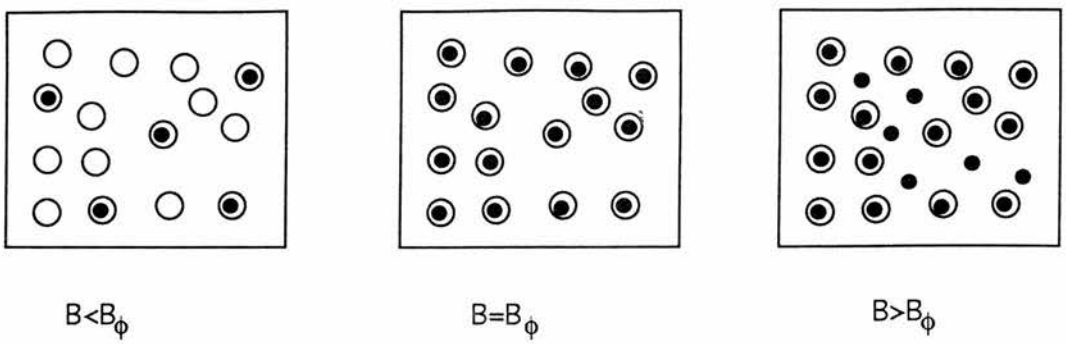

Figure 7.1: A schematic diagram indicating a plan-view of the different regimes that are exhibited in an irradiated sample. The open circles indicate CD and the black circles indicate vortices (see text).

defect. As the temperature is increased from T$\sim$0 K the fluxline may delocalise away from the defect [144]. This is as a result of the increased thermal energy available for the fluxline to breakfree from the pinning potential of the CD and the fact that the pinning tube may be less effective as it becomes energetically less favourable to the superconducting condensate for the normal core of the fluxline to sit directly on the defect when $\xi > d_{co}$. This has been observed in BSCCO as a sharp drop in the IL at temperatures above 78 K [144]. For fields $B=B_\phi$, the number of defects will equal the number of fluxlines. As the temperature is increased from T$\sim$0 K the fluxlines will undergo behaviour similar to that indicated above. *Zech et al (1995)* [144] noted that in this case the IL of a CD sample at the matching field exhibits a crossover from an exponential to a linear behaviour. For $B>B_\phi$ the number of fluxlines will exceed the number of defects, and, together with fluxons pinned on CD, there will be interstitial fluxlines which are not pinned. *Zech et al (1995)* [144] has noted that for $B \gg B_\phi$ the IL of a CD sample approaches the exponential behaviour exhibited by a pristine sample. As was previously mentioned, the effect of CD has been theoretically studied

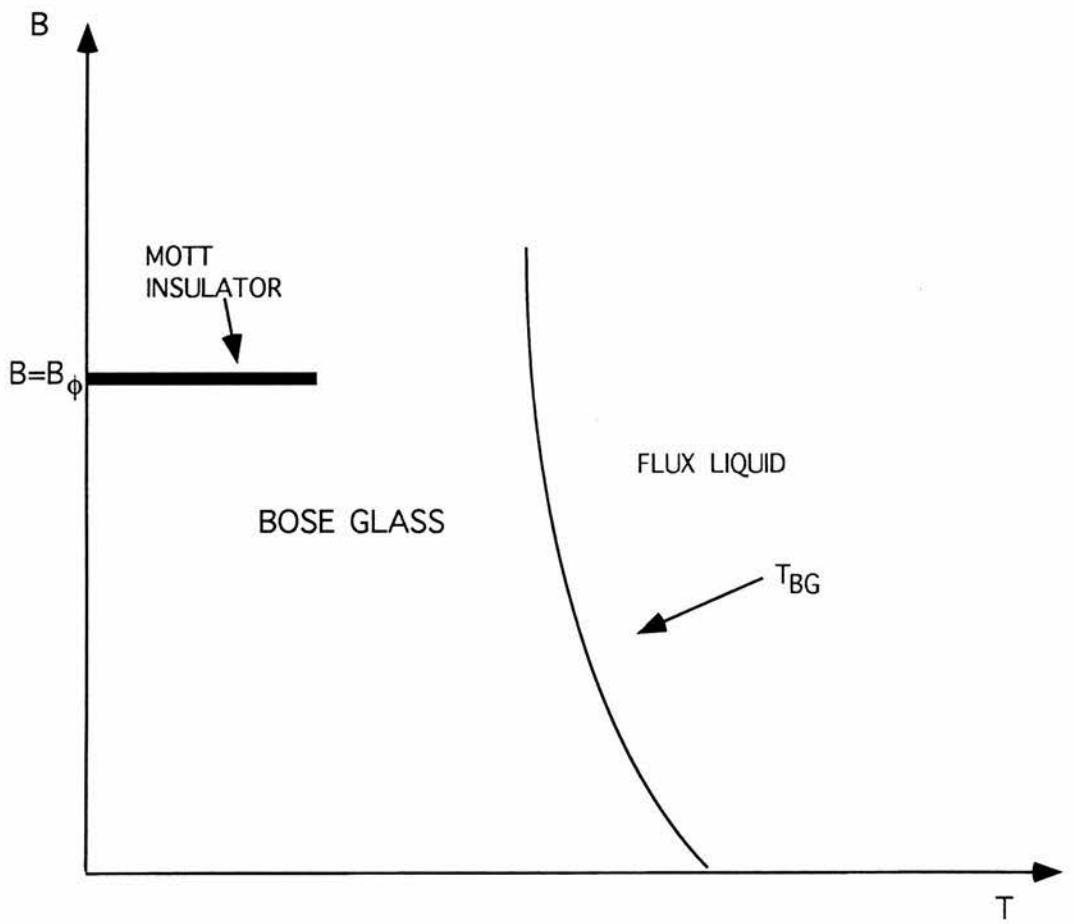

Figure 7.2: A schematic diagram indicating the position of the predictions of *Nelson and Vinokur (1992/1993)* [139, 140] with the Mott Insulator at B=B$_\Phi$, the Bose-Glass(BG) and the transition into the entangled vortex phase through T_{BG}. The Mott Insulator phase is predicted to occur deep in the BG phase.

[139, 140, 145]. Figure 7.2 is based on predictions made by *Nelson & Vinokur (1992,1993)* [139, 140]. Among the predictions of this study is that of a Bose Glass(BG) phase in the presence of CD. The BG phase has an infinite tilt modulus, c_{44}, and is stable over a finite range of field tipping angles [140]. This BG phase is predicted to melt via a second order transition into an entangled vortex phase and a number of authors have observed scaling rules at the melting transition that are consistent with the BG model [146, 147, 148]. A Mott Insulator phase has also been predicted to exist for $B=B_\Phi$. In this phase, both the tilt moduli, c_{44}, and the compression moduli, c_{11}, are infinite and the magnetic field is locked at the matching field for a range of external magnetic inductions, as well as being stable over a finite range of field tipping angles. Experimentally, a great deal of data has been interpreted within the BG theory. However, one can question whether the existence of a true BG phase is realistic in a CD sample as several of the assumptions in the BG model are difficult to realise experimentally. In particular *Täuber and Nelson (1995)* [149] have demonstrated in numerical simulations that, even below B_Φ the positions of the vortices may not be random, but there may exist spatial correlations in a plane perpendicular to the field. These correlations are believed to originate from two sources: firstly, a random distribution of defects will naturally contain some areas where they are closely spaced, such that vortex-vortex interactions will make it energetically unfavourable for all of them to be occupied, even at the matching field. Secondly, for a sample cooled in an applied field at which vortex-vortex interactions are significant (strongly overlapping vortices) at the depinning temperature, the vortices will already be correlated as they enter the irreversible region. As they become localised onto tracks, significant vortex-vortex correlations are thus frozen in [150].

Further to the above, several authors have demonstrated the effect of CD on the anisotropic structures encountered in BSCCO in that they have observed a *line* like fluxline structure in irradiated samples [148, 151] up to much higher fields than in the pristine case when the field is applied parallel to the defects. Additionally, recent Josephson plasma resonance (JPR) measurements have also indicated the presence of two phases with different c-axis correlations in the liquid state [152, 153] in BSCCO in the presence of CD. Clearly a variety of phenomena are exibited by irradiated samples, and this is just the tip of the iceberg. "Interesting physics" also results when the the field is applied at an angle to the correlated disorder, or when CD is produced at an inclination to the *c*-axis in BSSCO. An example of an investigation carried out with CD at an angle to the c-axis was carried out by *Hébert et al (1998)* [154]. They carried out an investigation of three samples, all irradiated with the same fluence of heavy ion beam, comparing the effect of 1) irradiating parallel to the c-direction, 2)irradiation in two coplanar directions and 3)irradiation in three directions symmetrically distributed around the c-axis. The results from this investigation indicate a low-T regime where the pinning efficiency does not depend upon the configuration of irradiation and a high-T regime where the pinning efficiency essentially increases towards the latter CD configuration. It is evident, therefore, that CD have been shown, to offer a very stable framework for the quasi-2D structure that is the flux-lattice in very anisotropic HTSC, BSSCO. The muon studies presented here throw light on some of these issues.

7.3 Sample preparation

A number of high quality single crystals of BSCCO, grown using a floating zone technique [138] were chosen for irradiation. These crystals were supplied by

T. W. Li, Kamerlingh Onnes Laboratorium, Leiden University, 2300 RA Leiden, The Netherlands. Each crystal was cleaved into flat platelets with a thickness of $\sim$ 0.5 mm and arranged in order to ensure that the ions would be able to travel through the extent of the crystals, producing defects traversing the entire sample thickness. The penetration was checked by placing a monitor behind the thickest crystal to record the transmitted flux. The irradiation was performed at GSI in Berlin and at Darmstadt, Germany using 17.7GeV uranium ions at 90° to the superconducting planes. The matching field for sample 1 (CD100) was 100mT at 90°. Sample 2 (CD4) was irradiated 90° to the superconducting planes with a matching field of 4 mT and sample 3 was irradiated in the same manner with a matching field of 200 mT (CD200). These samples were assembled in a manner suitable for muon spin rotation experiments. The T_c for sample 1 is 88.5 K(25) from Squid measurements [100]. Sample 2 has a T_c of 84 K [155] and sample 3 has a T_c of 83 K [155].

7.4 Sample measurements

As before, μSR measurements were performed to characterise the samples using the MUSR spectrometer at the Rutherford Appleton Laboratory (RAL) and the 'GPS' on the πM3 beamline at PSI. The crystals were mounted with Apiezon grease on a plate of haematite (Fe_2O_3) in order to minimise background signal. Further details of the μSR experiments are given in section 3.2.4.

7.4.1 Sample 1

Sample 1 (CD100) has been irradiated to a matching field of 100 mT and has been characterised extensively before by *Wylie (1996)* [156]. In this work a peak at the applied field in the μSR lineshape was noted and this is evident in the work carried out here. This peak is due to regions of the crystal which behave *normally* at all temperatures. These normal regions may be a result of the irradiation, but this can be mainly discounted as the ions were of sufficient energy to pass directly through the crystals. The samples may also have been of lower quality than expected. However, the samples were not investigated prior to irradiation, so the quality of the crystals pre-irradiation cannot be confirmed. In the analysis carried out in the remainder of this chapter these background peaks were subtracted by the removal of a fitted Gaussian. Experiments were carried out at PSI with the applied field parallel to CD on CD100 to gauge the effect of a change in field on the actual pinning potential. This was achieved by first cooling the sample to a field of 5 K in a field $\mu_o H_{ext}^{(1)}$. If the field is then changed to $\mu_o H_{ext}^{(2)}$, the pinned fluxlines are effectively frozen in and will not change their average positions. On raising the temperature, thermal activation of the vortices will cause them to move, leading to a redistribution of the vortex lattice according to the new field. This transition is evident in Fig. 7.3, where CD100 was cooled in a field of 40 mT and then altered to 20 mT. At T=65 K the fluxlines have started to creep out of their equilibrium pinned positions and at T=70 K where there is only one peak evident, centred around the new applied field $\mu_o H_{ext}^{(2)}$. Fig. 7.4 shows the first and second moment, the asymmetry factor and the alpha parameter for a μSR experiment probing pinning with an initial field of 110 mT which was then moved to 90 mT before measurements at different temperatures were taken.

All of the above quantities change dramatically in the same temperature range corresponding to the observation of two peaks in p(B) (see, e.g. T=65 K, Fig. 7.3). Due to a sufficiently large thermal activation, the vortices can move freely and rearrange themselves, producing a "new" lattice of spacing $a^{(2)} \approx \sqrt{\phi_o / B^{(2)}}$. At this point the field gradient, evident at 65 K in Fig. 7.3 may produce strong muon depolarisation which is too fast to be included in the observed time window. This leads to reduced asymmetry. This reduction in asymmetry may also be due to the fact that a_o is spread thinly over a large B-range. The maximum entropy program used to extract the μSR lineshapes would therefore cut the vast majority of the asymmetry out. At even higher temperatures all of the pinned fluxons break-free and this results in one maximum in p(B) (with full asymmetry) being observed (see T=70 K in Fig. 7.3). From Fig. 7.4 it can be seen that the point at which the fluxlines depin from CD around the matching field for CD100 is $T_{dp} \sim 60$ K. This experiment was repeated in all of the regimes displayed in figure 7.1 ($\mu_o H_{ext}^{(1)}$ equal to 40 mT and 170 mT, and reduced to 20 mT and 150 mT respectively) to gauge the effect of this change on the depinning temperature, T_{dp}. These indicated that $T_{dp}^{40mT} \sim 65$ K and $T_{dp}^{170mT} \sim 35$ K. It is evident that the temperature at which the lattice depins decreases as the density of fluxlines increases, particularly at applied fields larger than B_Φ. This particularly low depinning temperature may be as a result of the plastic flow of fluxlines which are not localised on columnar defects (interstitials) when they start to enter/exit the sample. A distinction must be made here between the depinning crossover and the melting line. The depinning crossover is not a melting line as it takes place at a lower temperature (see Fig. 7.5). In Fig. 7.5 it is evident that melting occurs at T $\sim$ 75 K which concurs with *Zech et al(1995)* [144] who noted a decrease

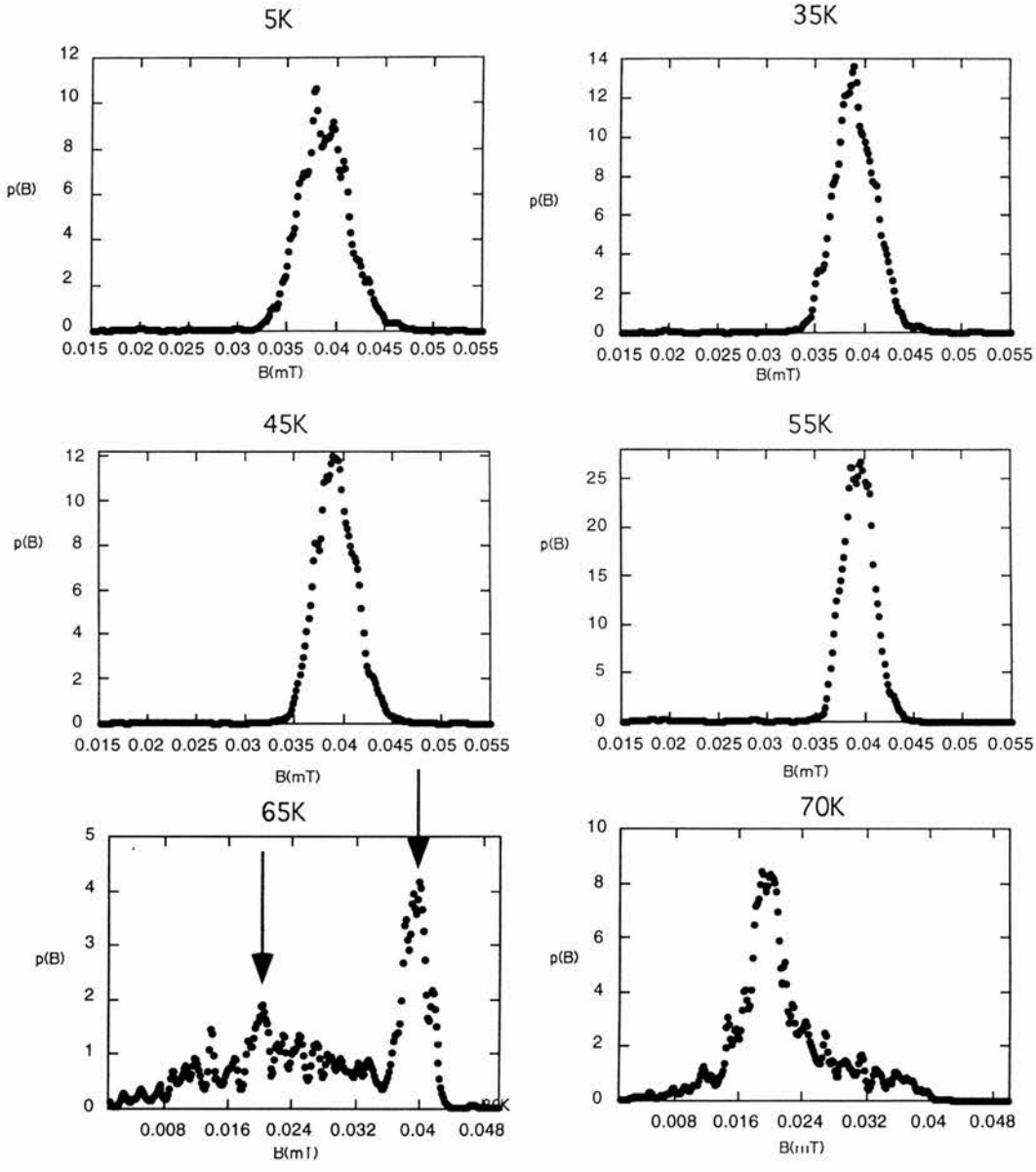

Figure 7.3: The probability distribution at increasing temperatures for CD100 cooled in a field of 40 mT and then altered at base temperature to 20 mT. Indicated in the p(B) at 65 K are the peaks discussed in the text.

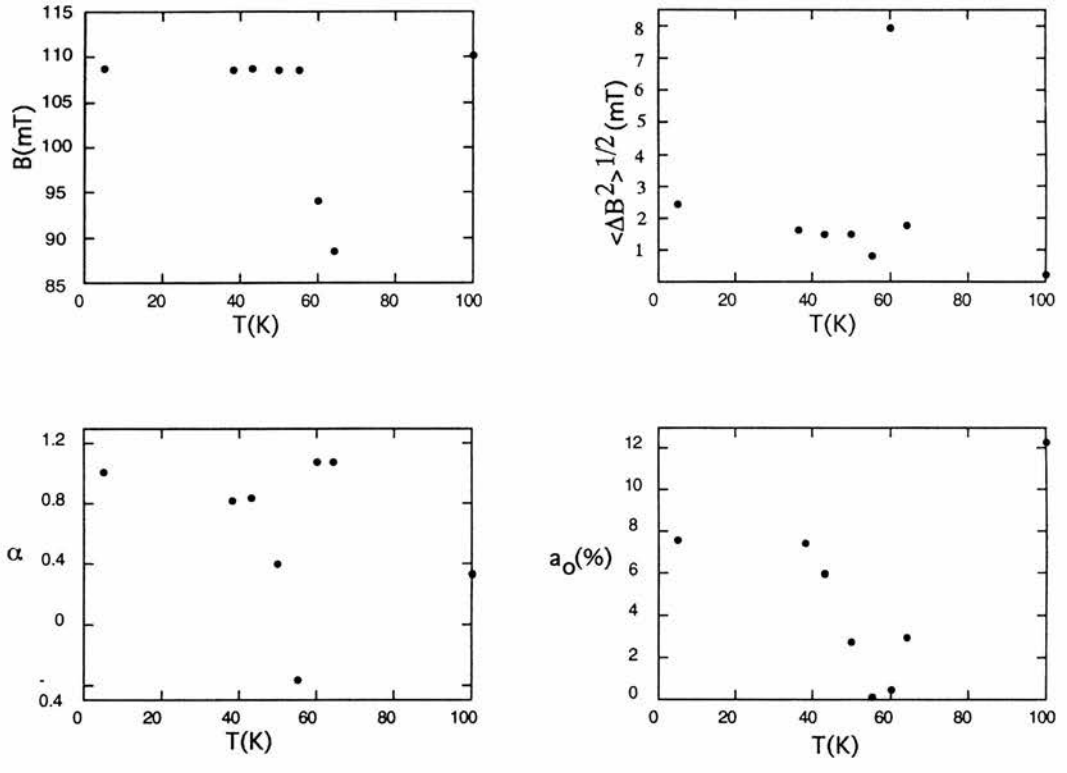

Figure 7.4: A temperature scan of the first and second moment, the α parameter and the asymmetry factor for CD100, cooled in a field of 110 mT and then shifted at base temperature to 90 mT. It can be clearly seen that there is a dramatic change in all of the quantities at $\sim$ 60 K. This has been identified as the point at which the fluxlines depin from CD at $\mu_o H_{ext} \sim B_\phi$.

in the effective anisotropic pinning above T $\sim$ 78 K. The depinning temperature is lower than this. From this work it can be concluded that there is a marked dependence of the depinning temperature on the applied magnetic field as the reduced influence of CD as the density of vortices exceeds that of columnar defects. Figure 7.6 shows the field dependence of the α parameter taken at 5 K for CD100

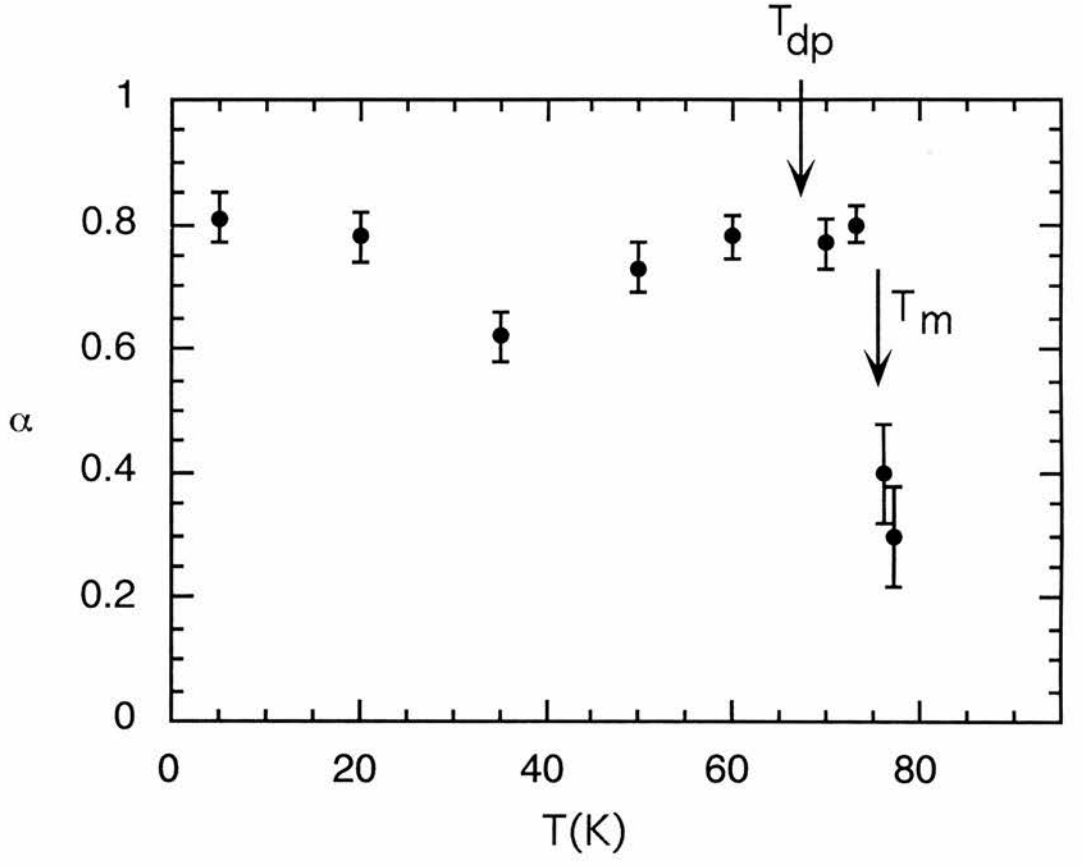

Figure 7.5: A temperature scan of the α parameter for CD100 cooled with the field of 50 mT applied parallel to th CD. The transition in the α parameter, T_m has previously associated in BSCCO with flux lattice melting [61]. The point at which fluxlines depin from CD, T_{dp} is also indicated.

and for a *pristine* sample, both with the field directed along the c-direction. The

data for the pristine sample has been taken from *Aegerter et al(1996)* [60]. It is evident here that up to more than twice B_ϕ(200 mT), the measured value of $\alpha \approx 1$ in the irradiated case. This reflects the existence of the high field tail in the probability distribution which is symptomatic of a high degree of order along the field direction. In contrast to this, the α parameter drops to a value of 0.5 in the pristine case at the crossover field $B_{cr} \sim \Phi_o/\lambda_{ab}^2$=65 mT [61, 60]. It is obvious that in the irradiated sample there is a suppression of the onset of quasi-2D behaviour by the presence of the CD which forces the lattice to maintain a 3D dimensionality. Even at fields greater than B_ϕ where the density of fluxlines exceeds that of CD, those interstitial vortices which are not pinned on tracks are prevented from moving by a linear potential "cage" created by vortices that are pinned on CD [157]. This has the effect of sustaining the high degree of c-axis correlations that are evident in the irradiated case along the track direction. Earlier work carried out here on this sample do indicate, however, that the lattice is less stable in this regime due to strong vortex-vortex interactions (cf $T_{dp}^{170mT} \sim$ 35 K). The field above which the disorder of the lattice is no longer suppressed is estimated to be as $B \geq B_\Phi^2/B_{cr}$ [150]. For CD100 this yields $\sim$ 150 mT. This is in reasonable agreement with the broad crossover observed in Fig. 7.6, but it should be noted that the analysis of ref. [150] was carried out assuming strong Josephson coupling, which may not be appropriate for BSCCO [51, 59, 158]. Figure 7.7 shows measurements of $< \Delta B^2 >^{1/2}$(T) for a range of fields applied parallel to the c-direction. It was seen in section 6.2 that it had been shown by *Y.-Q.Song et al (1993,1995)* [135, 136] and demonstrated by *Lee et al (1995)* [137] that fluctuations of the pancake vortices in a superconducting system such as BSCCO leads to a reduction in the width of the field distribution measured by μSR according to a

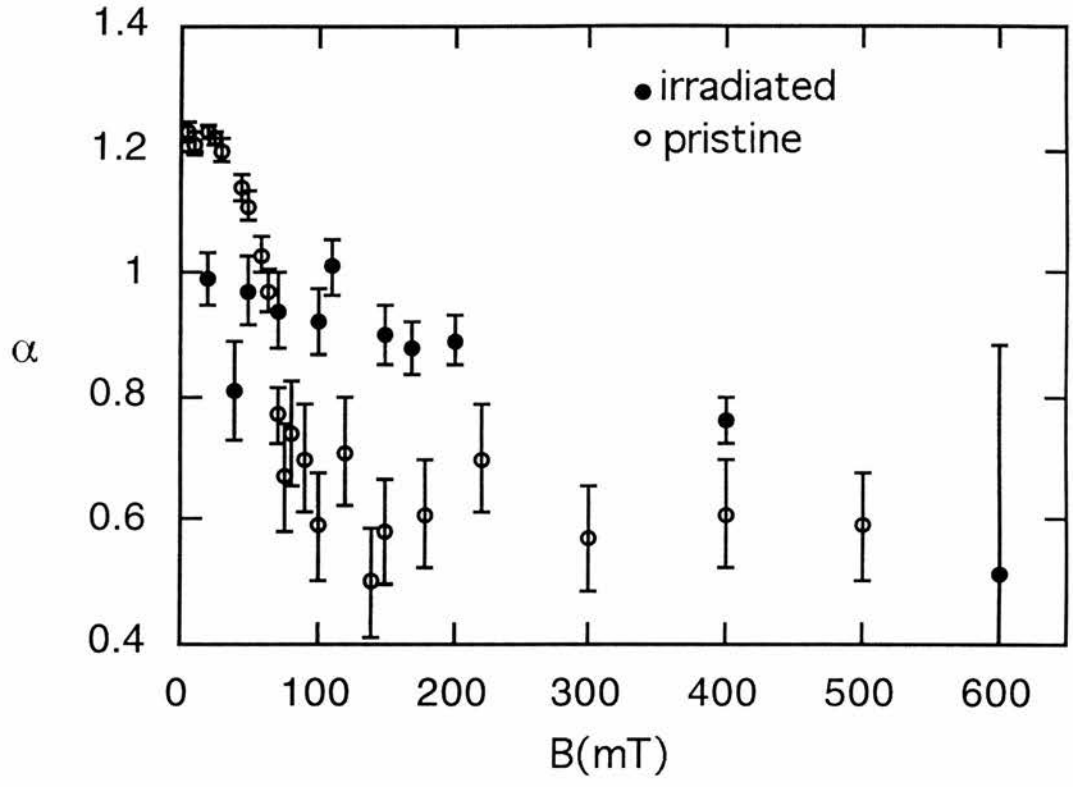

Figure 7.6: A field dependence taken at a temperature of 5 K for the asymmetry parameter, α, for CD100 and for a pristine sample taken from ref. [60]. A reduction in α suggests that the vortices are less straight. In the pristine case this occurs above the crossover field $B_{cr} \sim 65$ mT, whereas for CD100 this change is shifted to much higher fields.

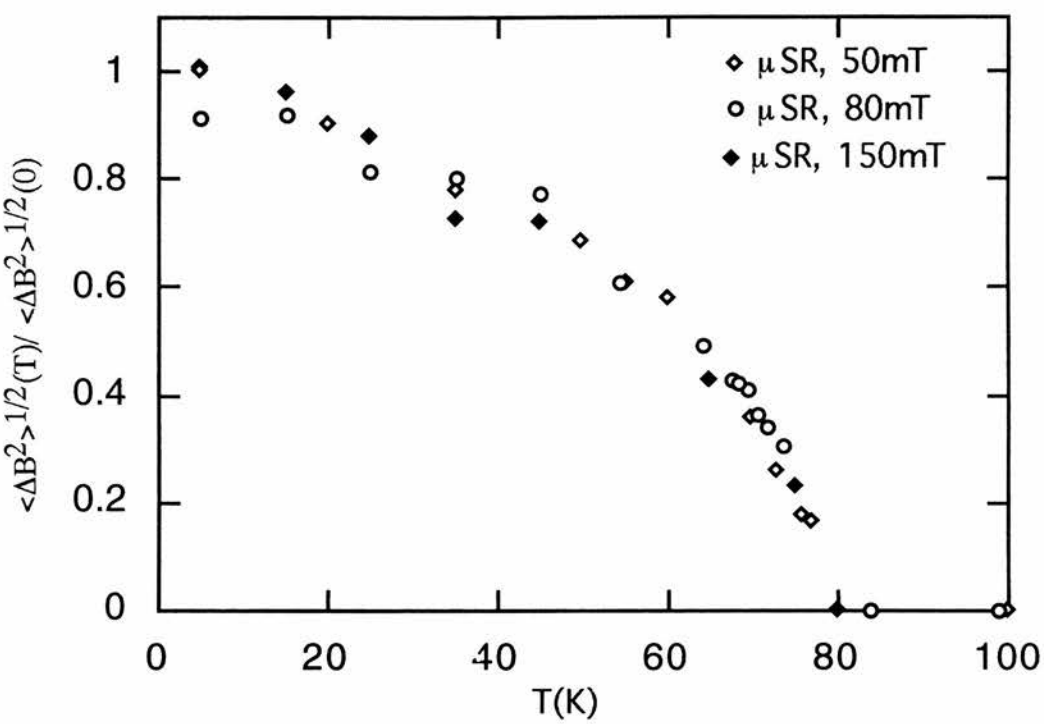

Figure 7.7: The normalised temperature dependence of the μSR linewidth for three applied fields for CD100. This clearly exhibits a temperature dependence which is field *independent*.

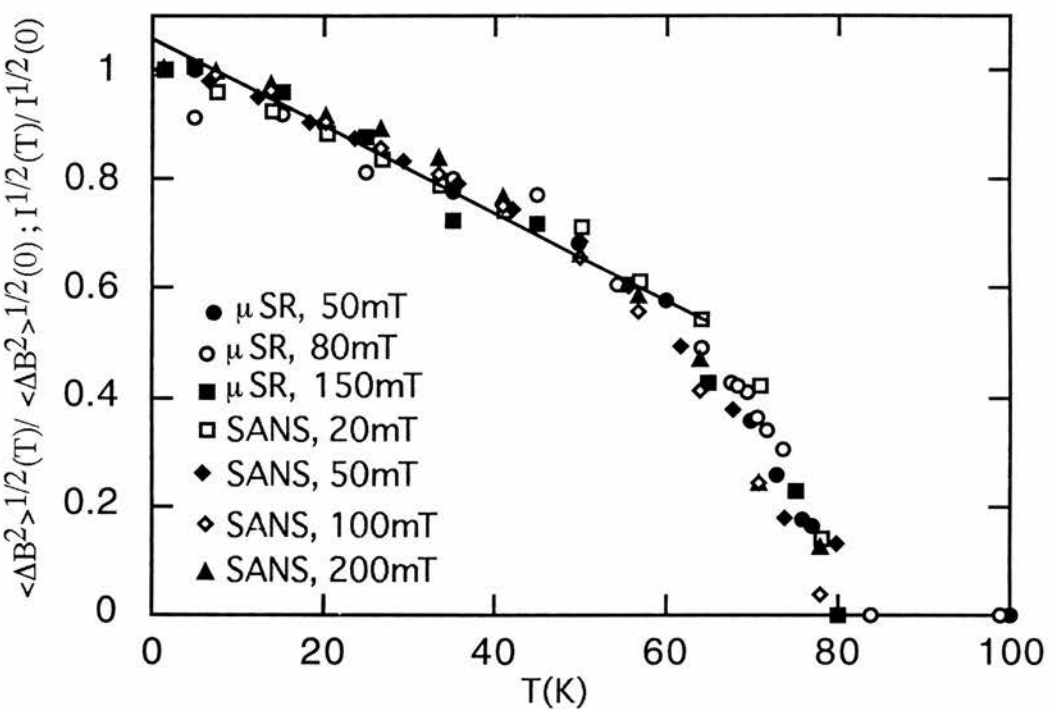

Figure 7.8: The normalised temperature dependence of the μSR linewidth for three applied fields and several applied fields showing the normalised square root of the SANS integrated intensity, see text.

Debye-Waller factor (cf Eq. 7.2).

$$\langle \Delta B^2 \rangle(T) = B^2 \sum_{q \neq 0} \frac{e^{-q^2\langle u^2 \rangle/2}}{[1 + \lambda^2(T)q^2]^2} \tag{7.2}$$

where $\langle u^2 \rangle$ is the mean square displacement of vortices from their average position. For a system with rigid flux lines ($\langle u^2 \rangle$=0) Eq. 7.2 yields a temperature dependence which is field independent for $B_{c2} >> B > B_{c1}$. A field dependence was demonstrated in section 6.4 in pristine BSCCO and by *Lee et al(1995)* [137]. This is as a consequence of the increased effects of vortex fluctuations which become more pronounced as $\langle u^2 \rangle$ increases relative to the inter-vortex distance. Figure 7.7 shows a temperature dependence for CD100 which exhibits field *independence* [158]. This contrasts with the case for the pristine material [51, 137] and implies the strong suppression of the dynamic vortex fluctuations as a consequence of the strong pinning offered to the vortices by CD [145, 139, 140]. This behaviour is mirrored by SANS experiments [158]. Figure 7.8 shows a reproduction from *Lee et al(1998)* [158] which includes SANS measurements on this crystal. In Fig. 7.8 the normalised square root of the SANS signal intensity $I^{1/2}(T)/I^{1/2}(0)$ is shown, where $I(T)$ has been integrated over the full wave vector range of the experiment $\mathbf{q} \sim 10^{-3}$-1.2×10^{-2}Å^{-1} [158]. SANS experiments on pristine BSCCO, as have been seen, (see section 6.4) give rise to a Bragg diffraction pattern as first demonstrated by *Cubitt et al (1993)* [91]. For a system with CD it would be expected that fluxline positions would be highly uncorrelated [139, 140] and the scattered neutron intensity will be given by a convolution of the pair correlation function, $S(q)$, of the vortex positions and the square of the form factor of a single flux line, $f(q) = B[1 + \lambda^2(T)q^2]^{-1}$ [70]. For a truly random configuration of vortices the scattered neutron intensity $I(q) \propto f^2(q)$ and will not contain any structure. According to *E.M.Forgan et al(1998)* [159] and *F.Y.Ogrin et al(1999)* [160] residual

vortex-vortex correlations give a small contribution to $I(q)$, although the data are effectively dominated by $f(q)$. Thus, theoretically the neutron scattered intensity integrated over all wave vectors q depends on $f^2(q)$, which can be modified by a Debye-Waller type correction to account for thermal fluctuations of the vortices (cf Eq. 6.4). The square root of the integrated intensity will therefore vary in a similar manner to $\langle \Delta B^2 \rangle^{1/2}$.

The second moment for a truly *random* flux-lattice measured by μSR has been theoretically studied by *Gorbunov & Smilga(1990)* [161]. It has been predicted that

$$\langle \Delta B^2 \rangle = \frac{\phi_o B_{ext}}{4\pi\lambda^2}. \tag{7.3}$$

For comparison, taking λ as 1800 Å, this model function is plotted in Fig. 7.9. It is clear that the fluxline lattice indicated by these measurements is not random and it is obvious that spatial correlations are present in the system in the presence of CD. The system is not, therefore, entering the true BG phase that has been predicted in the literature [139, 140]. The $\langle \Delta B^2 \rangle^{1/2}$ is reduced in μSR experiments because of under-sampling of the high field in the vortex cores, but in this case this effect cannot account for the deviation that is observed.

7.4.2 Sample 2

Sample 2 (CD4) has a particularly low matching field. The reason for choosing such a low matching field is primarily that, as was mentioned before, one never really attains anything approaching a true BG phase as there still exists a reasonable degree of spatial order in the system (see section 7.2) [162]. This spatial order was evident for measurements on CD100. In the case of CD4, vortex correlations arising as the sample is cooled may be reduced as a result of the low

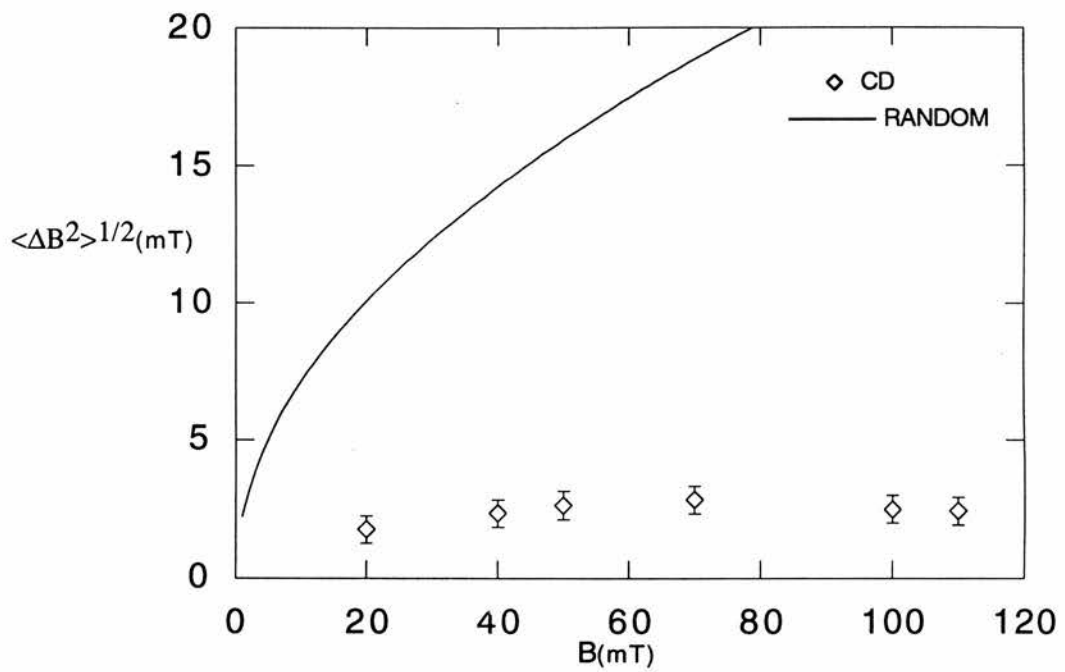

Figure 7.9: The field-scan of $\langle \Delta B^2 \rangle^{1/2}$, taken with the field applied parallel to the defects on GPS (PSI) and at a temperature of 5 K. Here, $\langle \Delta B^2 \rangle^{1/2}$ expected for a completely random arrangement is also plotted. The rms for CD100 clearly does not follow that expected for a random arrangement at any point in this graph.

matching field. When the sample is cooled in fields close to B_Φ the separation of vortices will be larger than the penetration depth, so mutual vortex interactions and hence correlations will be much reduced on freezing. Figure 7.10 shows the field dependence of the μSR linewidth $< \Delta B^2 >^{1/2}$ for CD4. The figure contains the expected dependence for a random arrangement of vortices (Eq. 7.3) and that for an ideal vortex lattice, which at these low fields ($H \leq H_{c1}$) must be calculated from the expression

$$\langle \Delta B^2 \rangle(T) = B^2 \sum_{q \neq 0} \frac{1}{[1 + \lambda^2(T) q^2]^2} \tag{7.4}$$

where q are the reciprocal lattice vectors. It can be seen that even in this sample the behaviour of the fluxlines follow that of the *ideal triangular lattice* more closely than the random case. There is, however, an interesting peak at around 7 mT which is not observed in the pristine material. This may reflect an enhancement of the disorder [163] in the lattice at fields of the order of the matching field. It is clear from these measurements that significant spatial correlations exist in CD4. This comes as no surprise as *Menon et al (1999)* [164] have shown that even a small degree of correlations reduce the expected *random* $< \Delta B^2 >^{1/2}$ considerably and this is further indicated in simulations by *F. Ogrin et al (1999)* [160].

Figure 7.11 displays the full field dependence of $< \Delta B^2 >^{1/2}$ in CD4 up to a field of 170 mT. The effect of CD is not as pronounced as for CD100 (cf Fig. 7.6) and the crossover field is very similar to that measured in the pristine case. The slight difference measured here may be due to a small change in the penetration depth in comparison to the pristine case or may be due to a some pertubative influence of CD. Figure 7.12 and 7.13 show temperature scans at the matching field, B_ϕ, of the α parameter and $< \Delta B^2 >^{1/2}$ for CD4 with the external field applied parallel to the defects. At this field one would expect that the density of

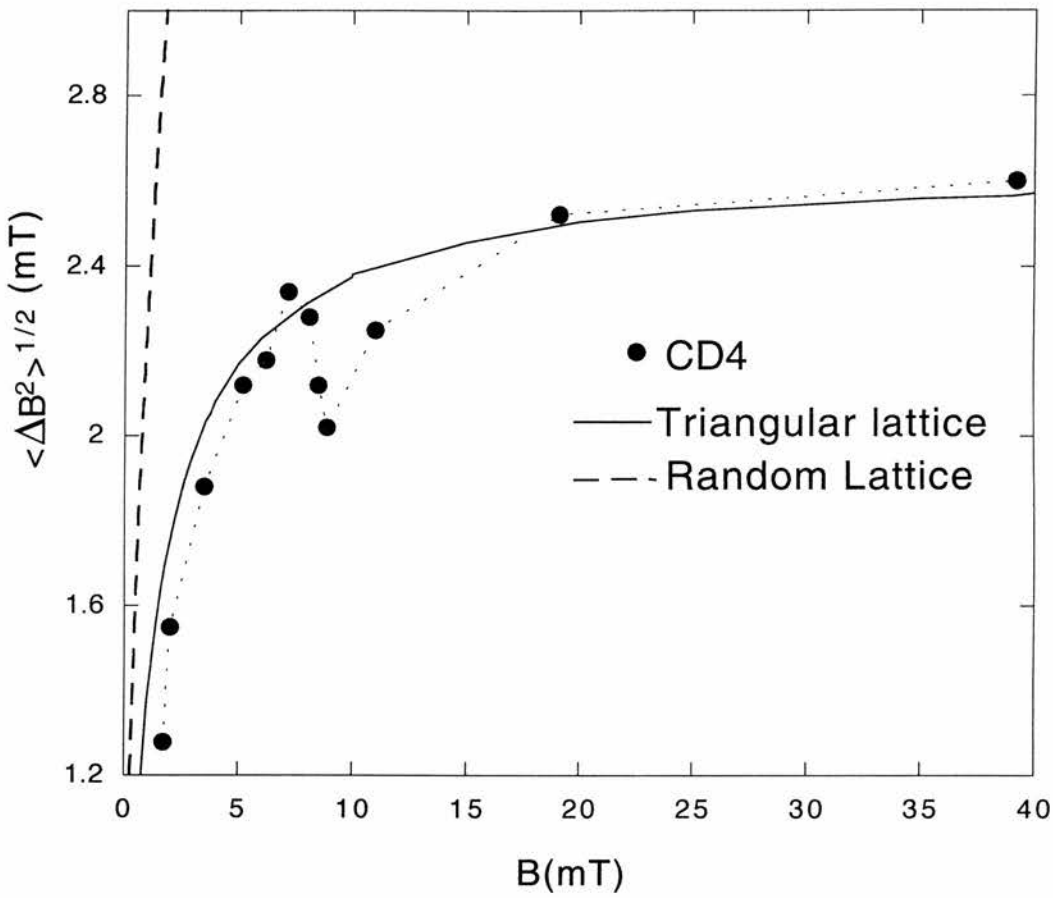

Figure 7.10: The field-scan of the rms field taken with the field applied parallel to CD on GPS (PSI), taken at a temperature of 5 K. Here, the rms field expected for a completely random arrangement is also plotted together with the rms expected for an ideal triangular lattice. The rms for CD4 clearly follows that expected for an ideal triangular lattice more closely than that expected on a completely ideal case.

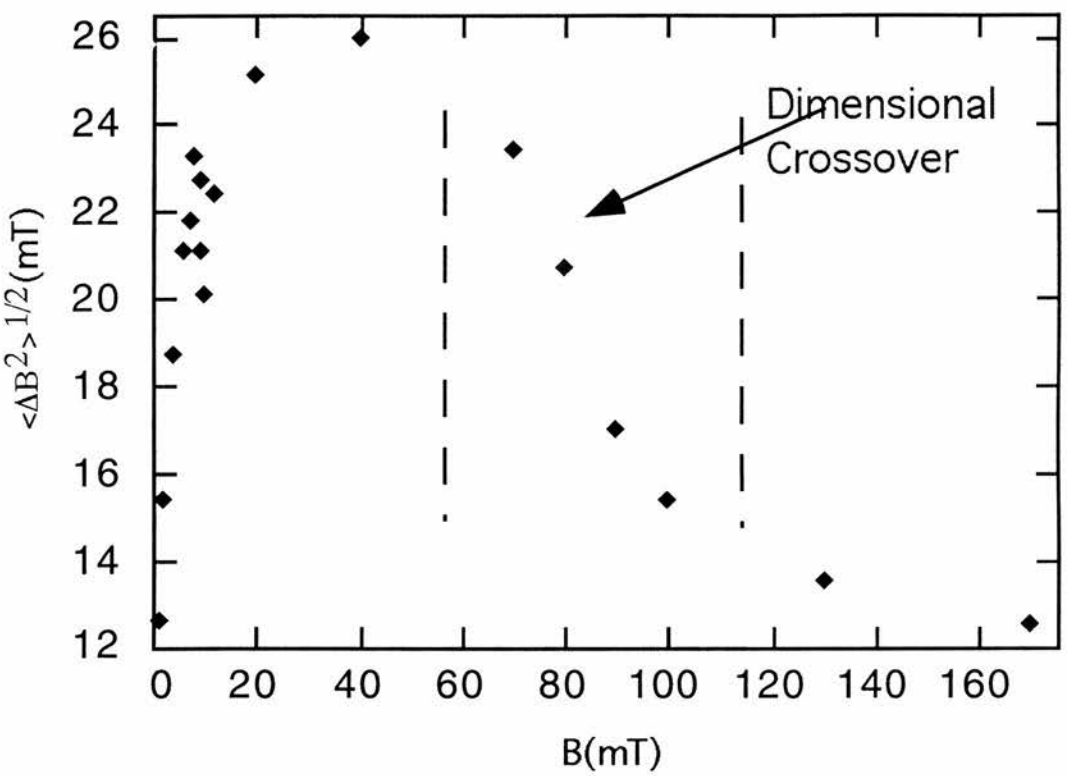

Figure 7.11: This figure shows the rms of CD4, with the applied field parallel to CD up to a field of 170 mT taken on GPS (PSI) at a temperature of 5 K. The area of the graph at which the dimensional crossover occurs has been roughly indicated. This is very similar to the pristine case, see Fig. 7.6.

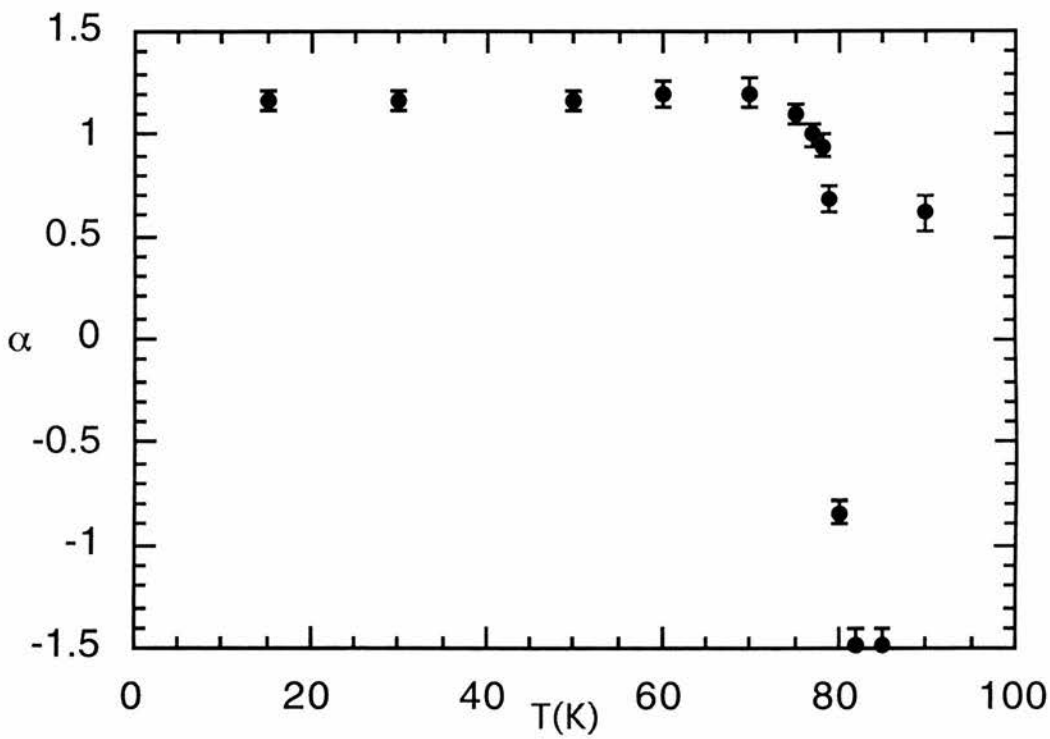

Figure 7.12: A temperature scan at the matching field, 4 mT, of the α parameter in CD4. The field has been applied parallel to the defects. There is a clear transition in α at T$\sim$78 K.

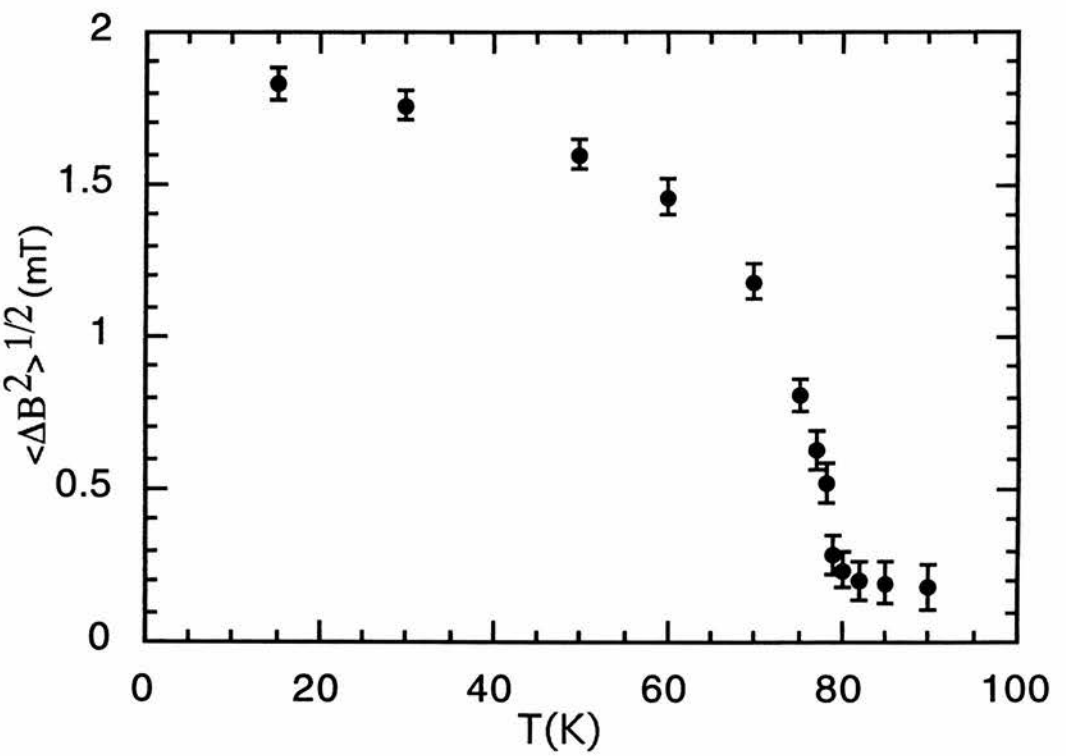

Figure 7.13: A temperature scan at the matching field, 4 mT, of the rms in CD4 with the field applied parallel to the defects.

fluxlines is equivalent to that of the CD. In Fig. 7.12 the α parameter maintains a value ~1.2 until ~78 K. This indicates that the fluxlines are effectively straight up until ~78 K, where, as noted by ref. [144], the CD pinning tube becomes less effective as a result of the increased thermal energy of the vibrating pancakes and the reduction in the effectiveness of the pinning tube as $\xi > d_{co}$ (see section 7.2). This is a conclusion which is mirrored by the behaviour of the rms value in Fig. 7.13. This slowly decreases until ~ 70 K, after which it rapidly decreases indicating that the fluxlines become less straight above ~ 70 K. Figure 7.14, 7.15 and 7.16 show the full field dependence of the α parameter at 5 K, the lowest points of the field

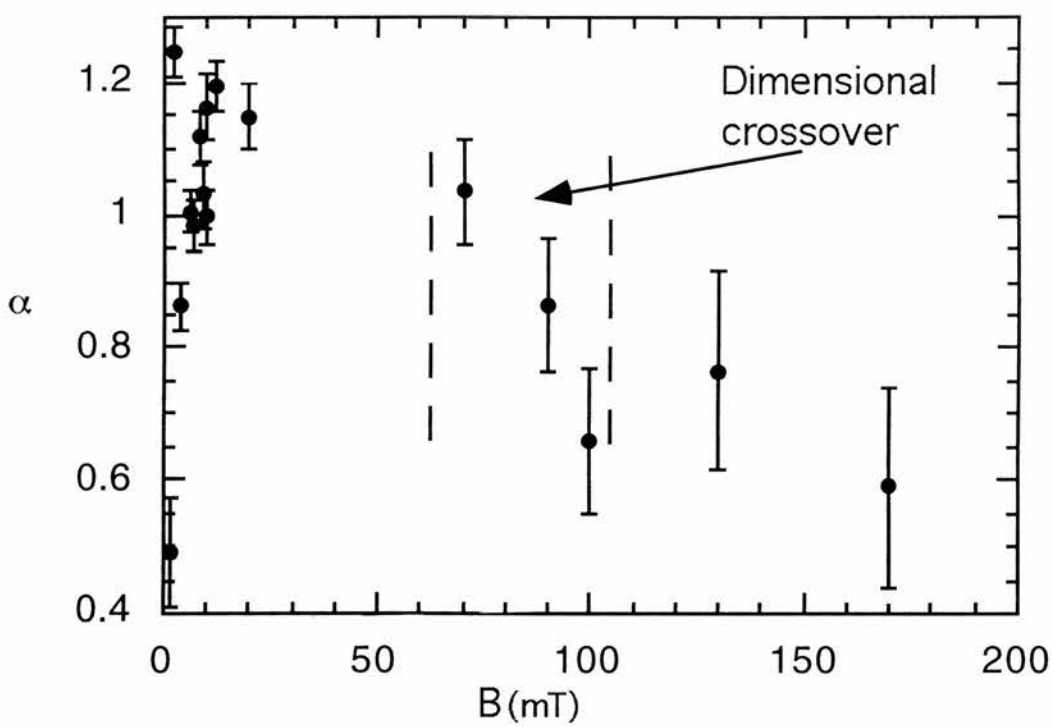

Figure 7.14: A field scan of the α parameter in CD4 up to a field of 170 mT, taken at a temperature of 5 K and with the applied field parallel to the defects on GPS. There is a broad crossover starting at B~50 mT in which the fluxlines become less straight.

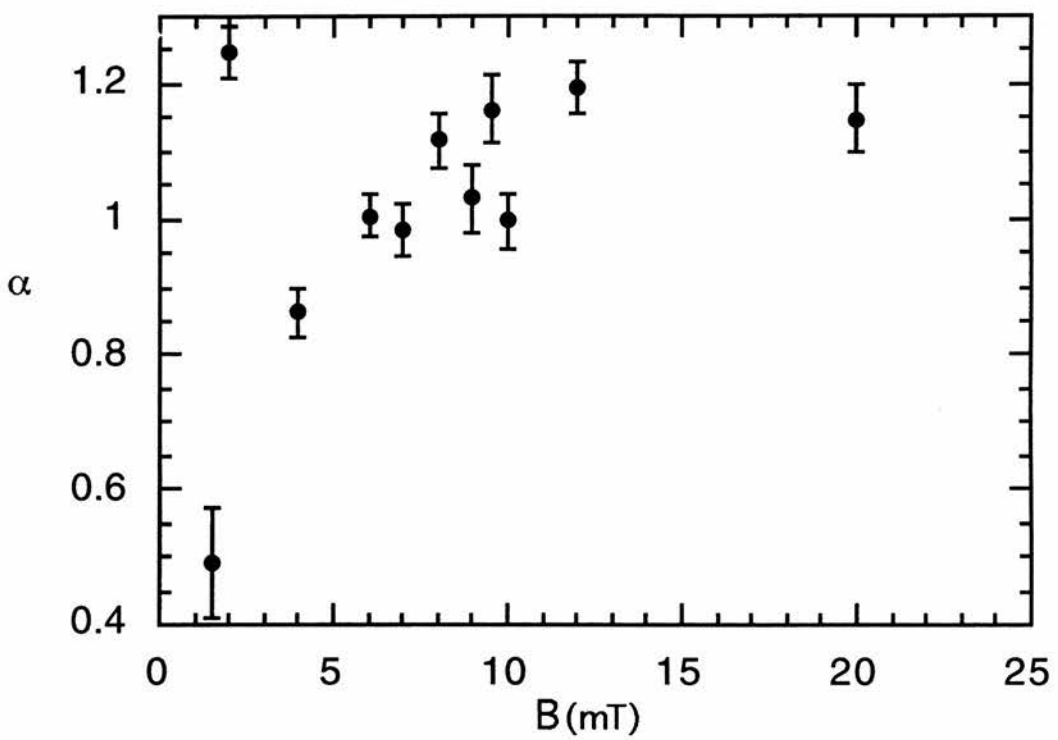

Figure 7.15: A field scan of the α parameter in CD4 showing the data around the matching field from Fig. 7.14. This data was taken at a temperature of 5 K with the applied field parallel to the defects.

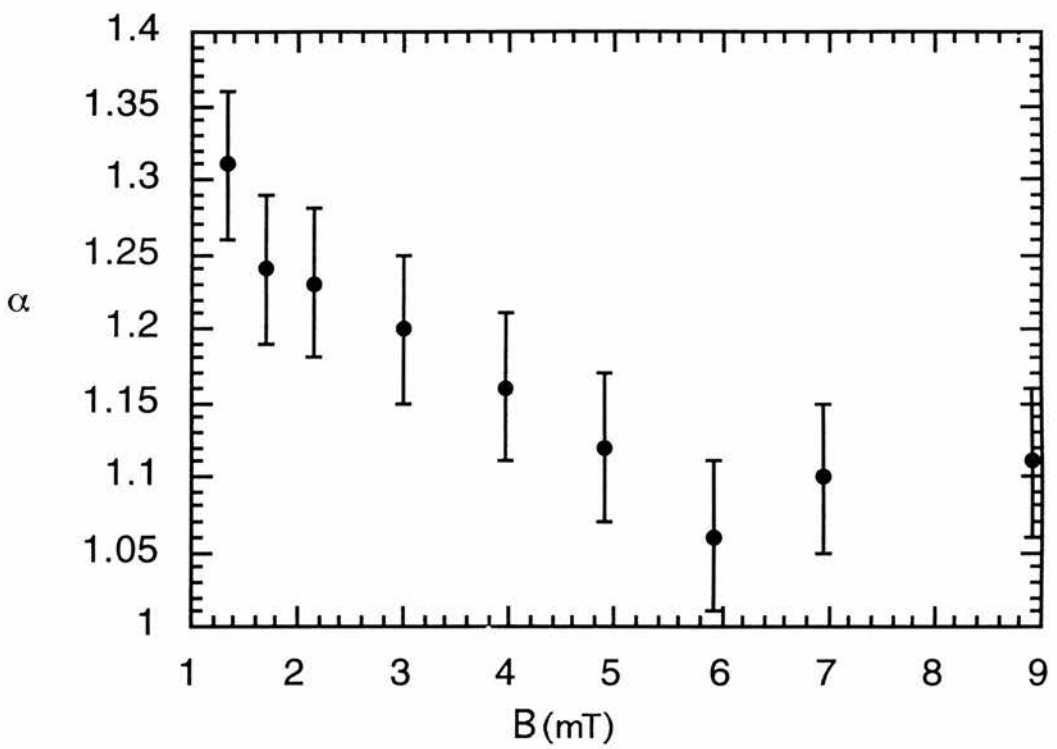

Figure 7.16: The field dependence of the α parameter at 70 K in CD4 with the field applied parallel to the defects. A gradual decrease in α and consequently the straightness of the fluxlines is observed here.

dependence of the α parameter at 5 K and a field scan of the α parameter at an elevated temperature of 70 K. From Fig. 7.14 it is clear that at applied fields $B \gg B_\phi$ and $\sim B_{cr}$ in the pristine case the α parameter is much reduced from that when the fluxlines are essentially straight ($\alpha \sim 1$). Figure 7.15 shows an enhanced view of the α parameter for applied fields around the matching field (B_ϕ=4 mT) taken from Fig. 7.14. *Straight* line vortices are indicated for most of the field range, with deviations occurring at the lowest fields, near to the matching field. For Fig. 7.16, taken at an elevated temperature of 70 K, it is evident that the fluxlines are particularly straight at the lowest applied field here, with a reduction in straightness for higher applied fields. This increased straightness or enhancement in c-axis correlations in comparison to the results at low temperature and low field may be a result of the increased thermal energy that allows the flux-pancakes greater mobility to breakfree from the configuration that they may have been frozen into when the sample was cooled to 5 K.

Figure 7.17 shows a plot of the rms against field at the elevated temperature of 70 K. It is evident from this that the peak at 7 mT(5 K) (see Fig. 7.10) is lost at this elevated temperature. This peak was indicated to be as a result of an enhancement of the disorder in the lattice at fields of the order of the matching field. Plotted in Fig. 7.17 is the rms expected for an ideal triangular lattice. The data follows this quite closely and may indicate that at 70 K the fluxlines will form a more hexagonal-like flux-lattice as the penetration depth increases with temperature and the flux-pancakes interact more strongly, being less restricted at these higher temperatures by the CD framework.

Measurements were also undertaken with the field applied at 45° to CD4 on MUSR, RAL. Figures 7.18 and 7.19 show a temperature scan of the rms and the

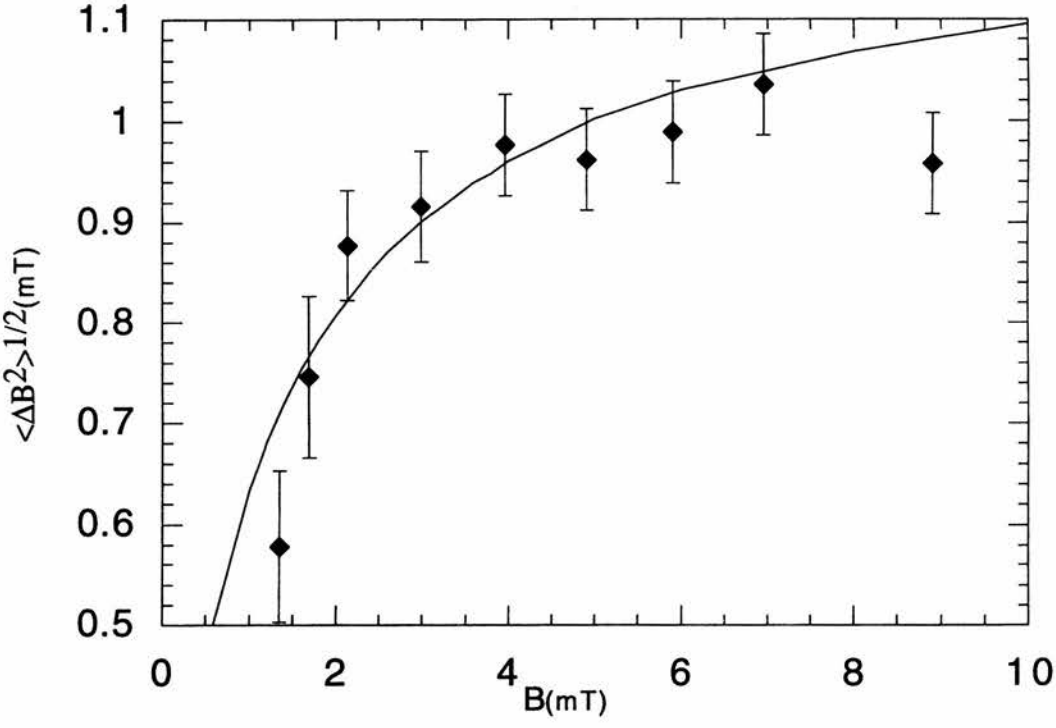

Figure 7.17: The field dependence of $< \Delta B^2 >^{1/2}$ for CD4 at a temperature of 70 K. Shown in the graph is the expected rms for an ideal triangular lattice.

α parameter, respectively, at an applied field of half the matching field, 2 mT. As is expected in the presence of CD the vortex lattice does not melt until T$\approx$78 K [144]. In the temperature range T>65 K both the value of the rms and the asymmetry parameter undergo an enhancement. An enhancement in the α parameter indicates increased c-axis correlations or *straighter* fluxlines. This enhancement is similar to the behaviour of the α parameter at an elevated temperature of 70 K with the field applied parallel to CD (see Fig. 7.16). The effect of CD in this experimental geometry is more difficult to interpret, since with the field applied at 45°, the CDs may not behave as correlated disorder, but as point pins in the *ab* planes. It was however noted that at $\sim B_\phi/2$ in CD100 the depinning temperature was T_{dp} ~65 K. The behaviour exhibited above may therefore be interpreted as the flux-pancakes depinning from CD and forming more line-like fluxlines. The possible behaviour exhibited by the flux-pancakes in CD4 at 2 mT is shown in Fig. 7.20. The arrangement may also be similar to variations of the "totally adjusted" arrangement of *Hardy et al (1996)* [165] (see Fig. 7.21), but it is difficult to say as the α parameter is still quite high (cf CD100). It should also be noted here that this enhancement is also similar to that seen in pristine BSCCO at B $\sim$ 80-90 mT [70, 100] with the field applied perpendicular to the superconducting planes. In pristine BSCCO this is well above the dimensional crossover field (B_{cr}=65 mT). A temperature scan at an applied field of 4 mT (see Fig. 7.22) of the α parameter does not show such a prominent enhancement above $\sim$ 60 K. From plots of the rms at these two fields (see Figs.7.18 and 7.23) it is also evident that the rms at 2 mT also undergoes an enhancement above $\sim$ 60 K, where there is no enhancement at 4 mT. The absence of this behaviour at 4 mT may be due to the fact that as the density of fluxons equals that of CD (point-pins), there may be

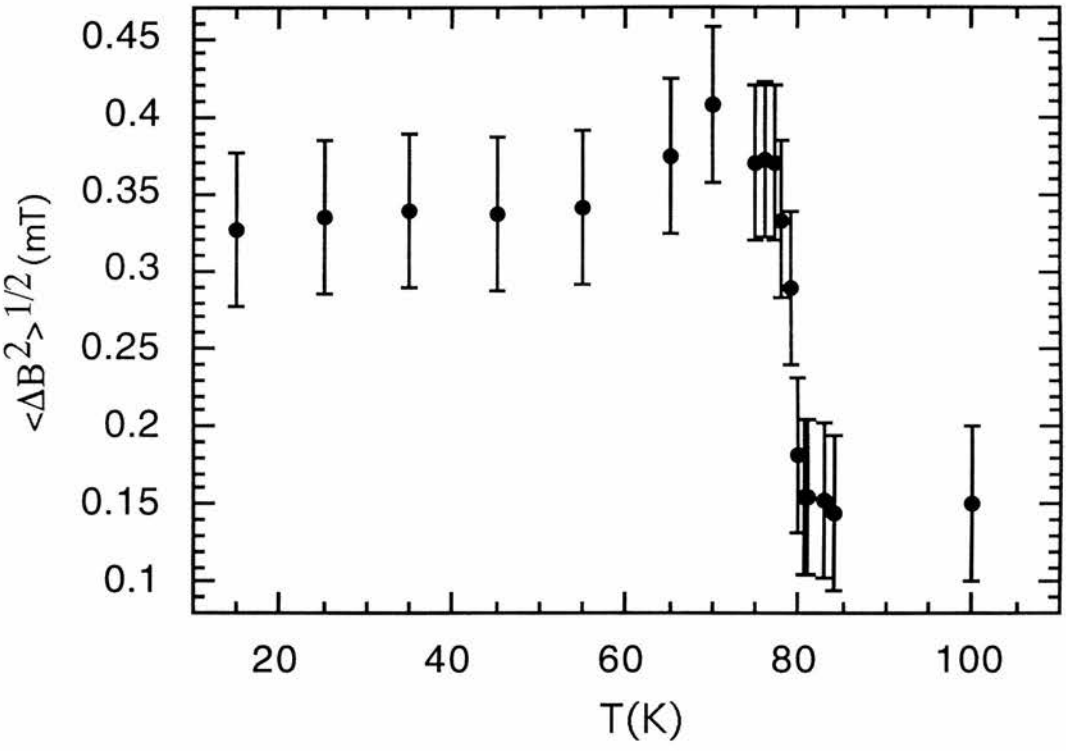

Figure 7.18: A temperature scan of $< \Delta B^2 >^{1/2}$ at an applied field of 2 mT and at 45° to CD for CD4. A clear enhancement is seen in $< \Delta B^2 >^{1/2}$ above T~60 K. This data was taken on MUSR using the CCR.

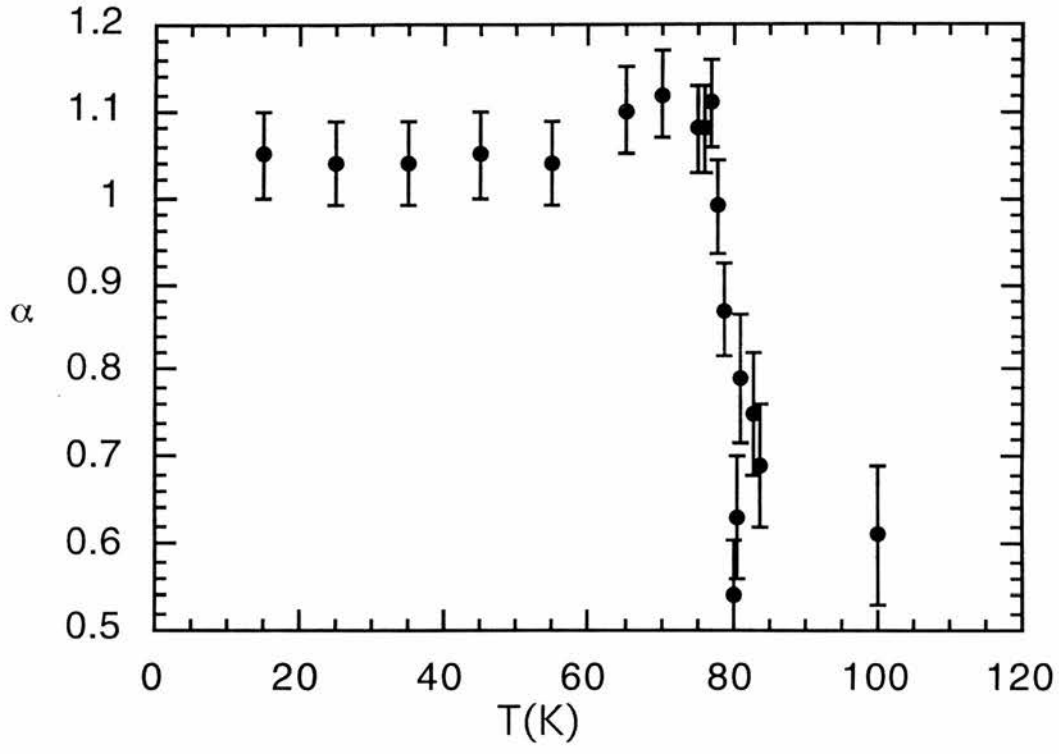

Figure 7.19: A temperature scan of the α parameter at an applied field of 2 mT and at 45° to the superconducting planes for CD4. An enhancement is seen here above T~60 K indicating an enhancement in the straightness of the fluxlines. This enhancement is similar to that seen in Fig. 7.16 where measurements were taken with the field applied parallel to CD. Again, this data was taken on MUSR using the CCR.

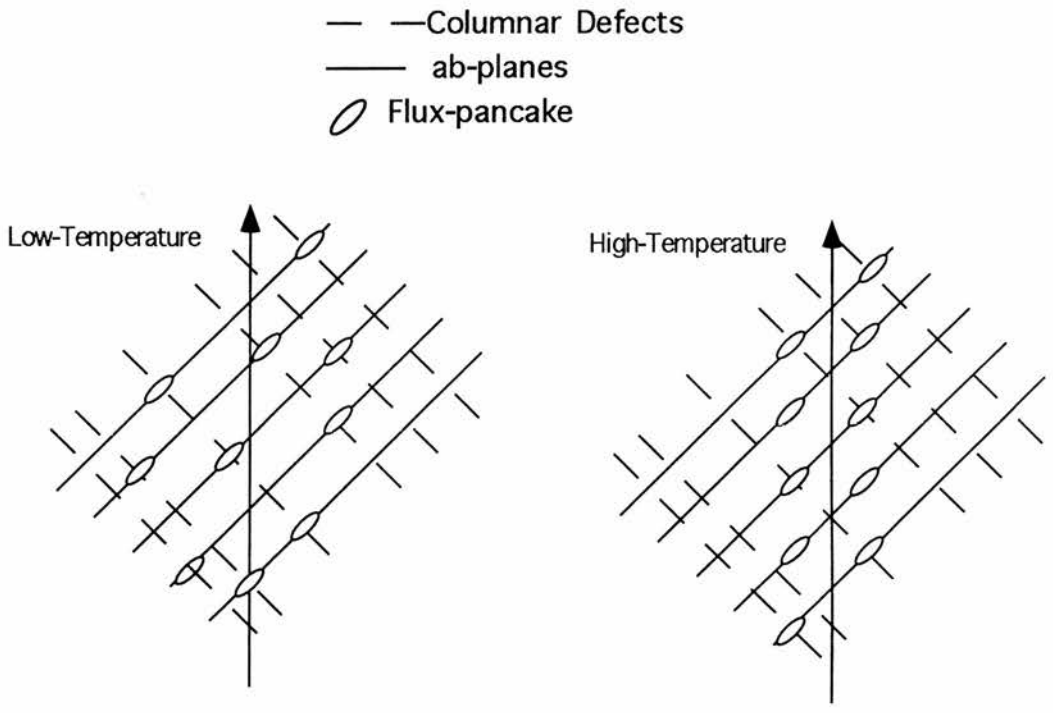

Figure 7.20: A schematic of the possible effect of columnar defects (CD) when the external field is applied at an angle to the CD. At low temperatures the CD act as point-pins. This would result in fluxlines which are disordered along their length. At higher temperatures the flux pancakes depin from the point-pins and form more *line-like* fluxlines. The effect of this is a possible reason for the enhancement in α seen above 60 K in Fig. 7.19, although the value of α below 60 K is still relatively high, indicating that in this region the fluxlines are also relatively straight.

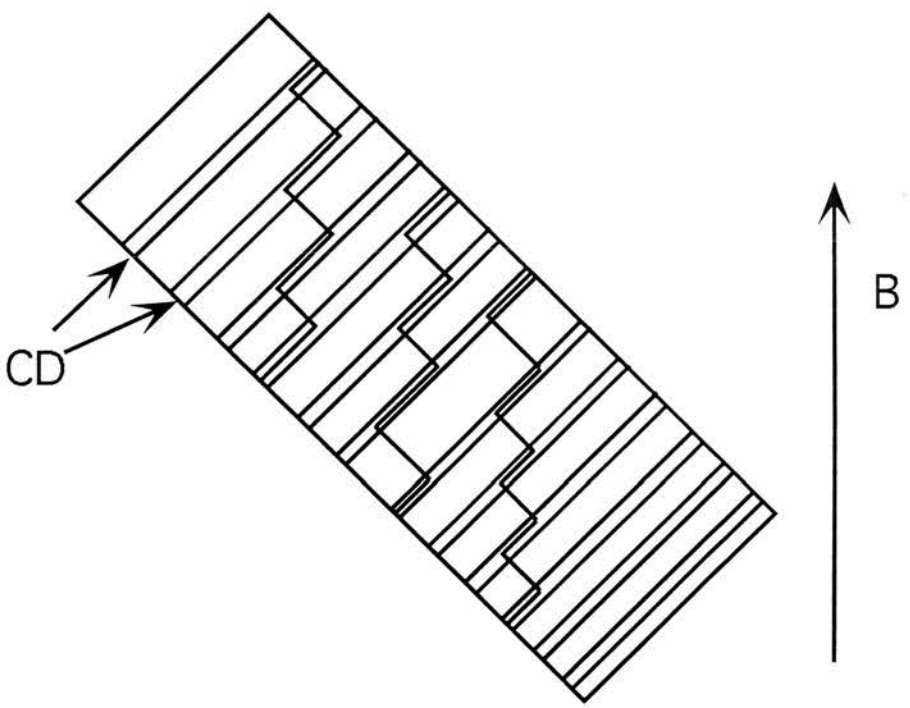

Figure 7.21: A schematic of a variation of the "totally adjusted" arrangement of ref. [165] for a sample with the field applied 45^o to the CD. Flux lines are depicted as forming a zig-zag pattern through the CD.

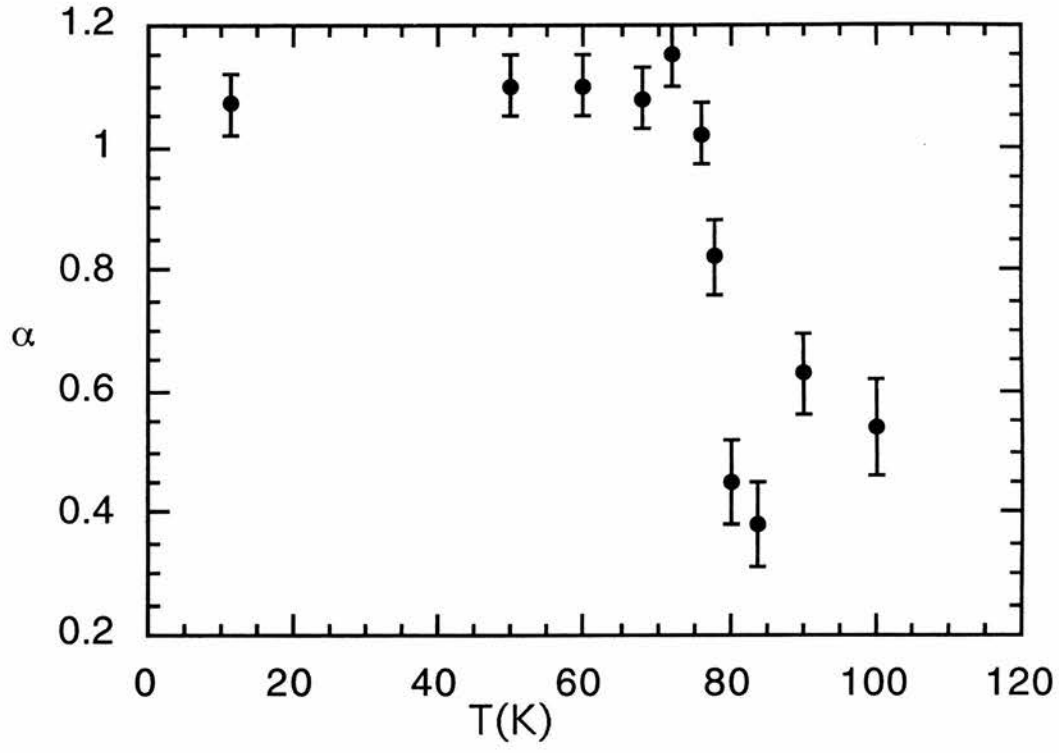

Figure 7.22: A temperature scan of the α parameter at an applied field of 4 mT at 45° to the CD in CD4, taken on the MUSR instrument using the CCR.

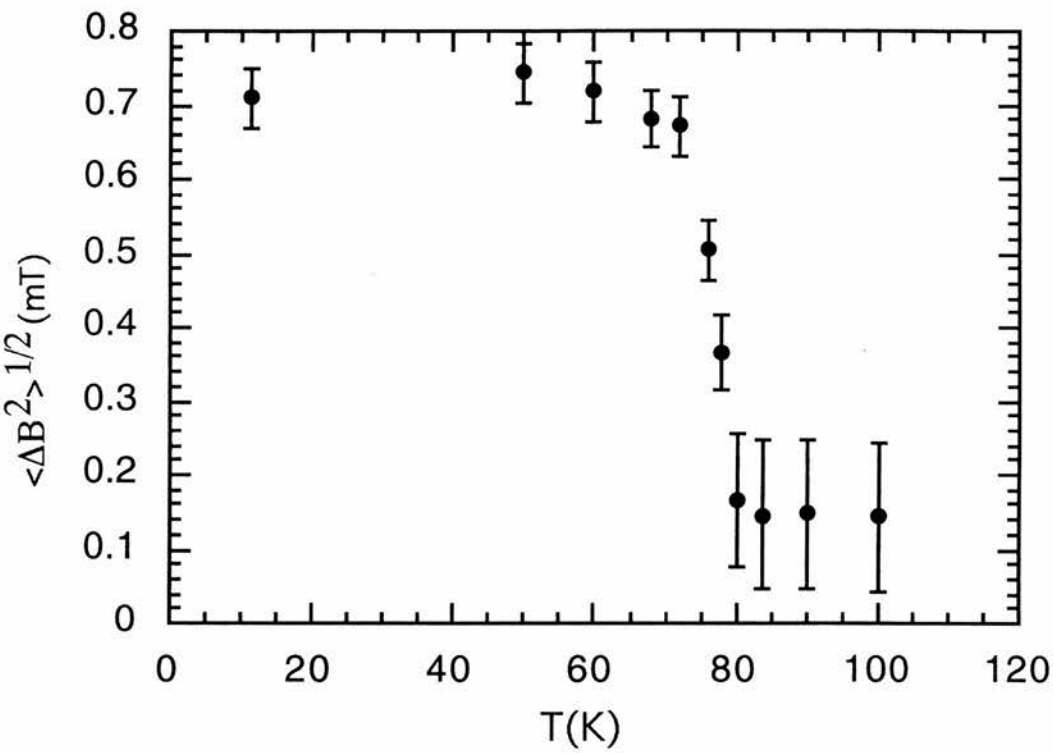

Figure 7.23: A temperature scan of the rms at an applied field of 4 mT at 45° to the CD in CD4.

no free point pins for an enhancement to occur as suggested by Fig. 7.20. Figures 7.24 and 7.25 show a field-scan of the rms and the α parameter taken at RAL with the applied field at 45° at a temperature of 12 K. From Fig. 7.25 there appears to be a gradual decrease in α with field indicating a reduction in the straightness of the fluxlines. This behaviour is not as apparent when the field-scan was taken with the applied field parallel to CD (cf Figs. 7.14 and 7.15). In this case there does not appear to be the gradual decrease in α. It is difficult to compare these two cases however, as the latter was measured at 5 K parallel to CD and the former was measured at 12 K and 45° to CD. The rms, Fig. 7.24, does not exhibit such startling behaviour as the rms with the field applied parallel to CD (cf Fig. 7.10), but without wishing to overinterpret the data there is a slight enhancement in $< \Delta B^2 >^{1/2} \sim$ 8 mT. This may be indicative of similar enhancement in disorder to that indicated at 7 mT in Fig. 7.10 but, it should be noted here, however, that an enhancement in the value of $< \Delta B^2 >^{1/2}$ is due to an increase in the disorder of stiff fluxlines which may not be realised with the applied field at an angle to the CD.

7.4.3 Sample 3

CD200 is a sample that has been irradiated to a matching field of 200 mT. It has already been seen that the out-of-plane correlation of pancake vortices is enhanced by the presence of CD and the extent of their effect on the dynamic and static response of the flux lattice. Although the measurements published here do not provide convincing experimental evidence for the completely random distribution of fluxlines that are required for the ideal BG model, it has been noted that the ideal BG model is difficult to realise experimentally. Apart from this, a pinning

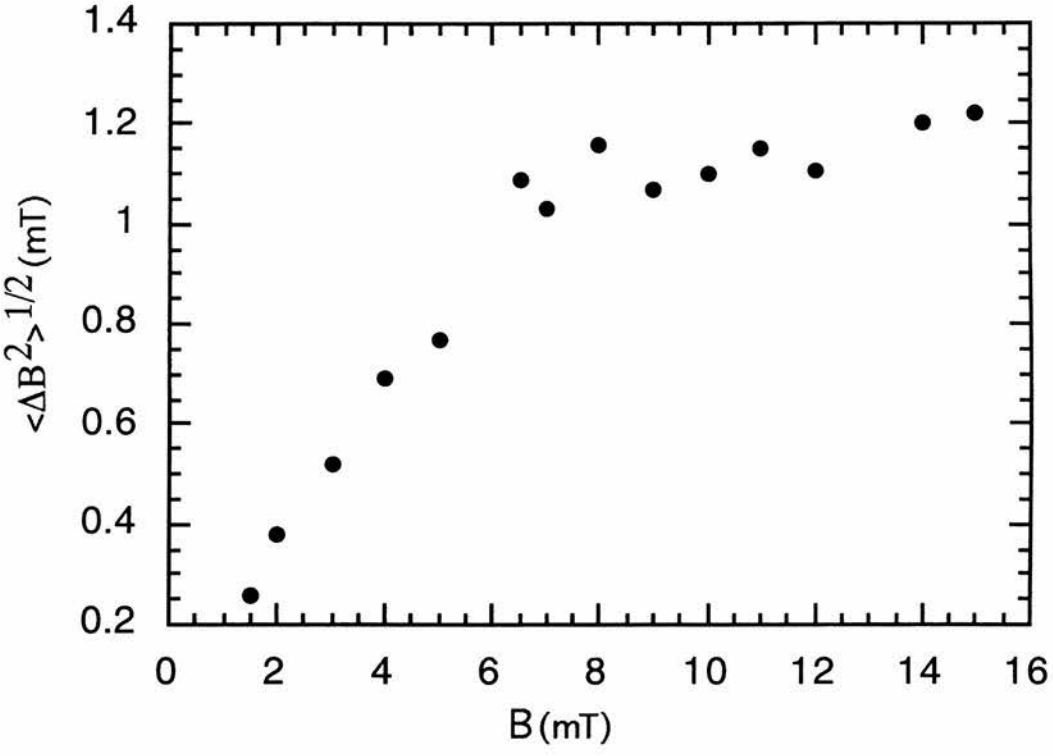

Figure 7.24: A field scan of the rms for CD4 with the applied field at 45° to CD, taken on MUSR, RAL at a temperature of 12 K.

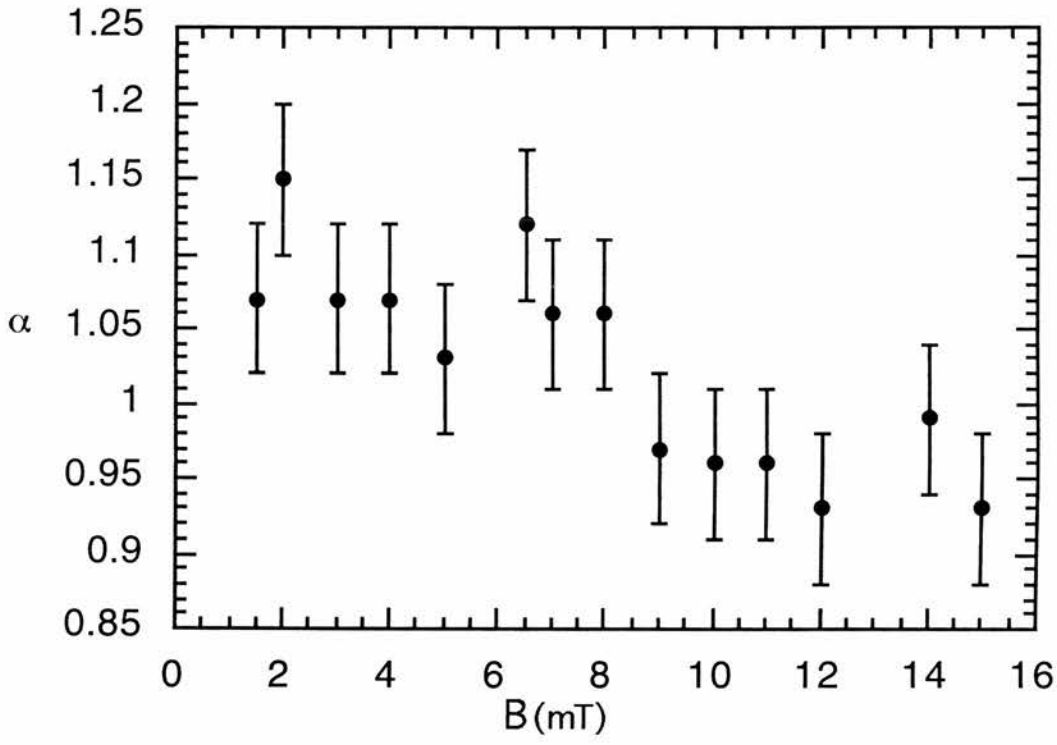

Figure 7.25: A field scan of the α parameter for CD4 with the applied field at 45° to CD, taken on MUSR, RAL at a temperature of 12 K.

mediated, or BG melt has been observed in CD4 (cf Fig. 7.19), but the nature of the flux-lattice above this melting transition, however, is still in doubt. Recent Josephson plasma resonance (JPR) measurements, which enable one to quantitatively determine the magnitude of interlayer phase coherence [166, 167, 168] have indicated that there are two liquid phases in irradiated samples [152, 153]. This is the *coupled* and the *decoupled* liquid. (Decoupling of vortices occurs when there is a loss of interlayer coherence, mainly due to strong thermal fluctuations of the pancakes within the individual layers). Further, these experiments have indicated that the vortices tend to *recouple* with increasing magnetic field [152, 153] and work by *Bulaevskii et al (1996)* [169] has indicated that this may be an entropy-driven process. This re-alignment of the pancake-vortices is in stark contrast to measurements on the pristine material, indeed, neutron and muon measurements indicated that pancakes are highly disordered along the c-axis at all temperatures above 65 mT [91, 60]. However, as was noted earlier, more recent neutron experiments on BSSCO have indicated that in the pristine material the flux-pancake configurations become more *line-like* at high temperature and fields ($\sim$ 80-90 mT) [70, 100].

Quantitatively, JPR measurements on a BSSCO sample with a T_c of 85.7 K and a matching field of 1 Tesla confirm the existence of the different phases in a limited temperature range ($\approx$ 62-68 K) and separated by a a *recoupling* line at $B \sim B_\phi/4$ [152]. In the absence of a sample with a matching field of 1 Tesla to further test these predictions, a sample with a matching field of 200 mT was investigated (CD200), presuming that the areas of interest for CD200 would be present at roughly the same equivalent region of the phase diagram. Experiments were carried out on CD200 at PSI and RAL. Figure 7.26 is a plot of the α parame-

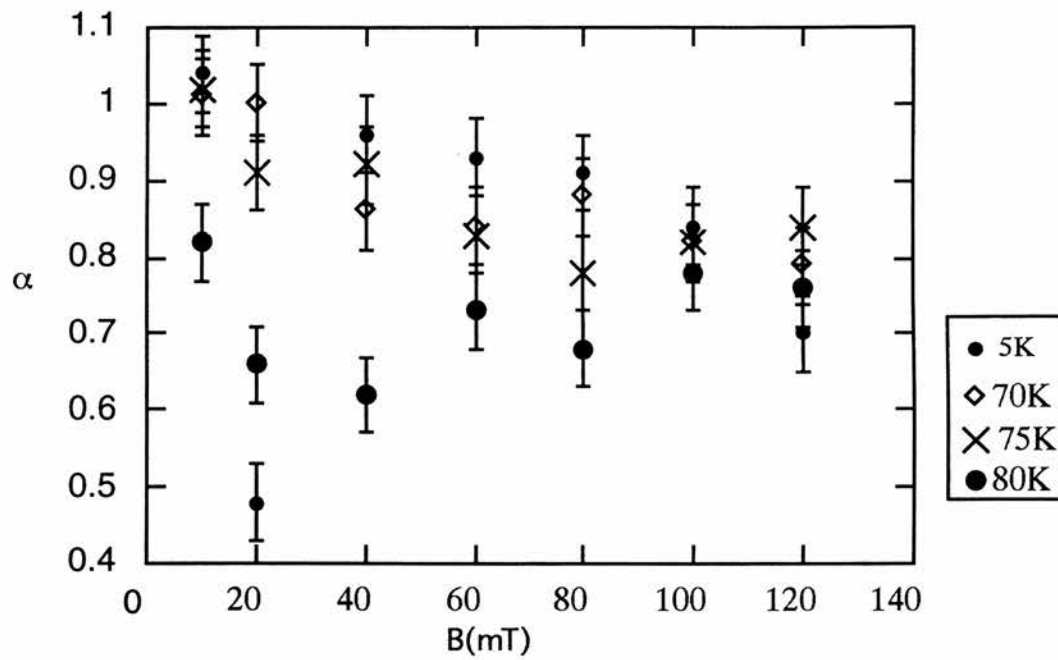

Figure 7.26: The variation of the α parameter with field for various temperatures, measured with the field applied parallel to the defects at PSI for CD200.

ter at different fields and temperatures taken with the field applied parallel to the defects at PSI. As was discussed earlier, the α parameter was introduced by *Lee et al (1993)* [61], and characterises the shape or skewness of the μSR lineshape. Coming under this definition the α parameter is ideal as an indication of c-axis correlations between pancakes in the bulk of a superconductor.

The expected behaviour of α for a system going through the *recoupling* line is indicated in Fig. 7.28. This figure indicates that as the system goes through the irreversibility line at point A (see Fig. 7.27) the value of the α parameter would decrease in accord with a reduction of c-axis correlations of the pancakes. As the system passes through the *recoupling* line at point B (see Fig. 7.27) there is an increase in α and at a point higher in the phase diagram the system *decouples* once again. It is difficult to pick out any obvious trends from Fig. 7.26. To give a clearer picture and highlight any obvious changes in the α parameter, Fig. 7.29 shows graphs of the normalised α parameter for differences between 70 K, 75 K, 80 K and the base temperature for these measurements (5 K). In this figure all of the α values have been normalised to the value of that at an applied field of 10 mT and 5 K. This indicates that any deviation in c-axis correlations from the straightline vortex case encountered in the vortex solid phase will be indicated by a reduction in α_n from α_n=0. In Fig. 7.29 there is a definite decrease in α_n at 10 mT and 80 K. This indicates the decoupling of the pancakes. The pancakes then progressively recouple as the field is increased above 50 mT. The evidence for the decoupling of the pancakes at 70 K and 75 K is less convincing, but α_n does decrease with increasing field indicating that the pancakes decouple. As the field is increased further α_n tends towards 0, perhaps as the pancakes recouple after marginally decoupling.

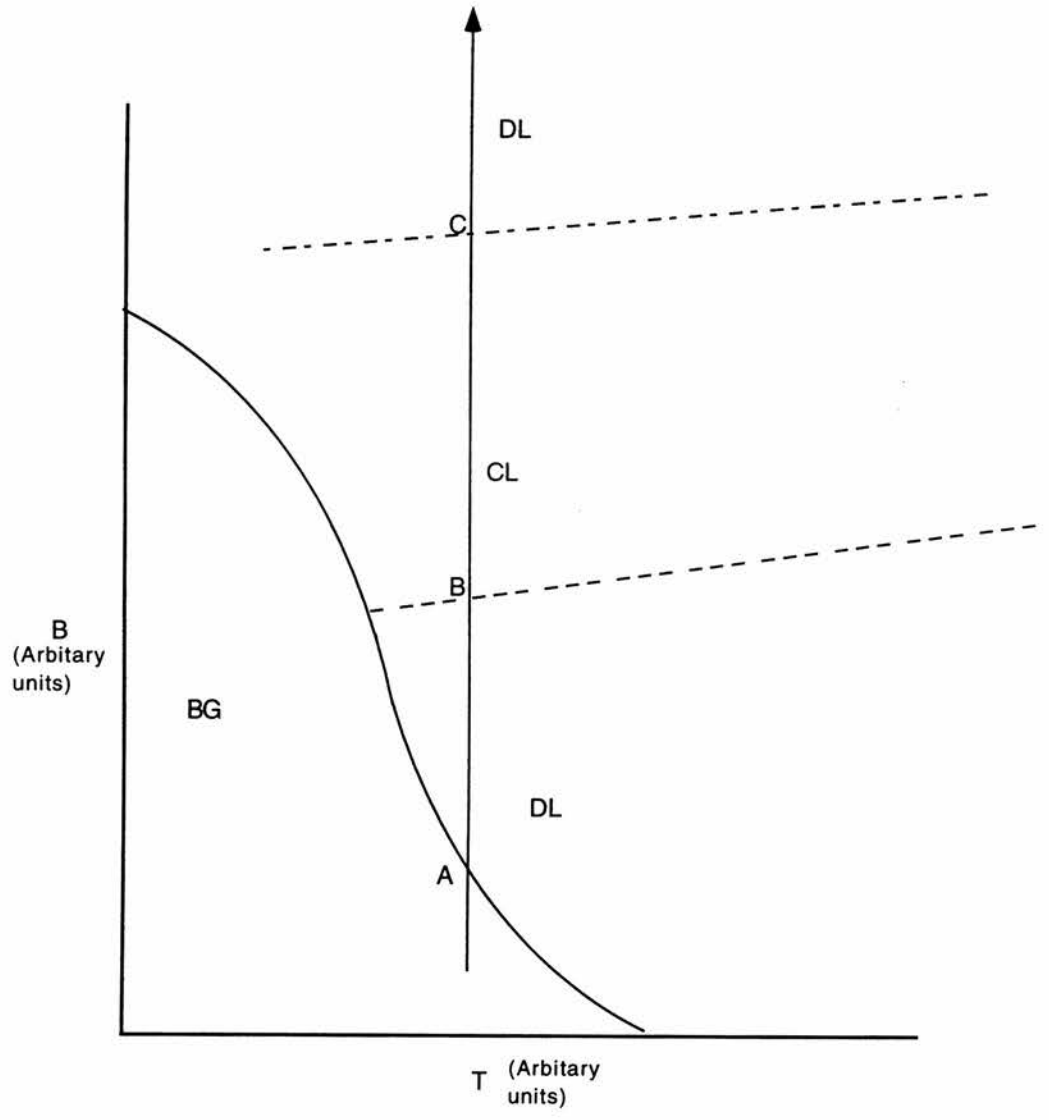

Figure 7.27: A schematic of the phase diagram expected for BSCCO with a set of columnar defects. Shown in the diagram is the expected positions of the decoupled liquid (DL) and the coupled liquid (CL). The path shown by arrow ABC is explained in the text.

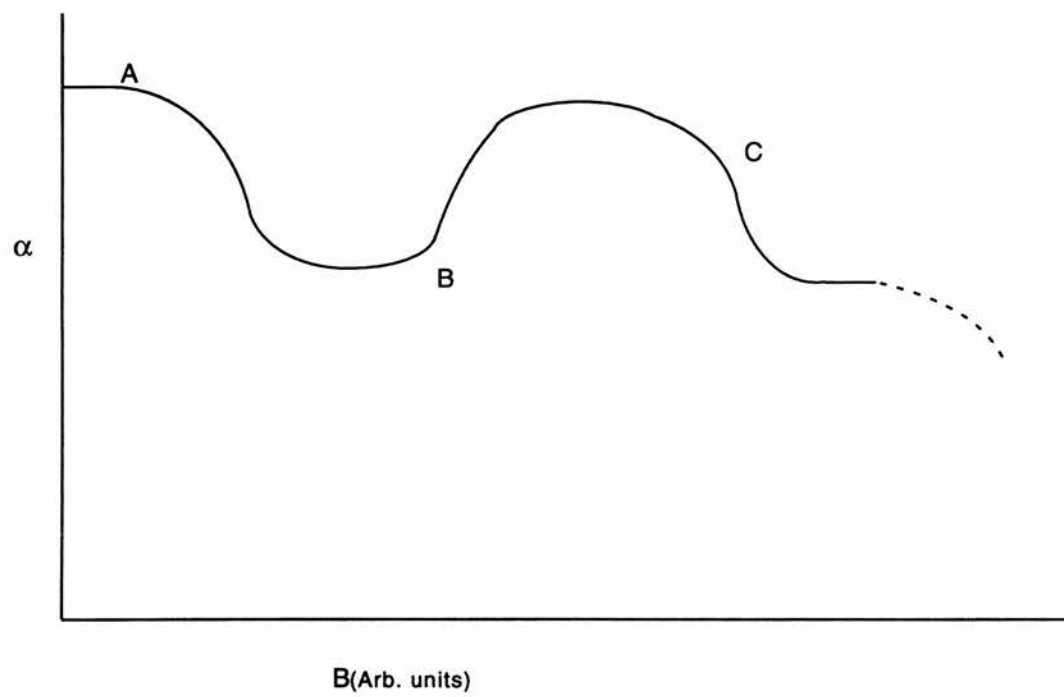

Figure 7.28: A schematic of the expected variation of the α parameter with temperature for arrow ABC in Fig. 7.27 (see text).

These experiments were repeated on MUSR (RAL). Fig. 7.30 shows a plot of the α parameter at different temperatures and fields measured with the field applied at 45° to the CD. Again, as the applied field is at an angle to the CD the results are slightly more difficult to interpret. Without wishing to overinterpreting the data it is evident that at 35 mT and 70 K, 76 K and 80 K there is a rapid decrease in α which is recovered at 40 mT. This may be indicative of a decoupling transition followed by a recoupling transition. In this case the decoupling/recoupling transition occurs over a very small field range. At 40 mT and at a temperature of 60 K the α parameter is also markedly reduced which may be indicative of a decoupling transition.

7.5 Conclusions

Three different samples with differing matching fields have been studied. Although all three samples have been shown to exhibit different phenomena, in general all of the samples that have been irradiated exhibit an enhancement of the elastic moduli in comparison to the pristine case. This is evident by the increase in temperature at which the mixed state enters the entangled liquid phase that is predicted by BG theory (see e.g Figs. 7.5 and 7.12). It was demonstrated by measurements on a sample with a matching field of 100 mT that CD suppress both *static* disorder and may also suppress *dynamic* disorder. It was also demonstrated that this sample did not display a completely random distribution of fluxlines as required by an ideal BG model. It was noted here, however, that a small correlation between fluxlines has been demonstrated to produce a μSR lineshape which is significantly different from that expected for the *random* case [164, 160]. A sample with a matching field of 4 mT (CD4) was specifically investigated in order to explore the

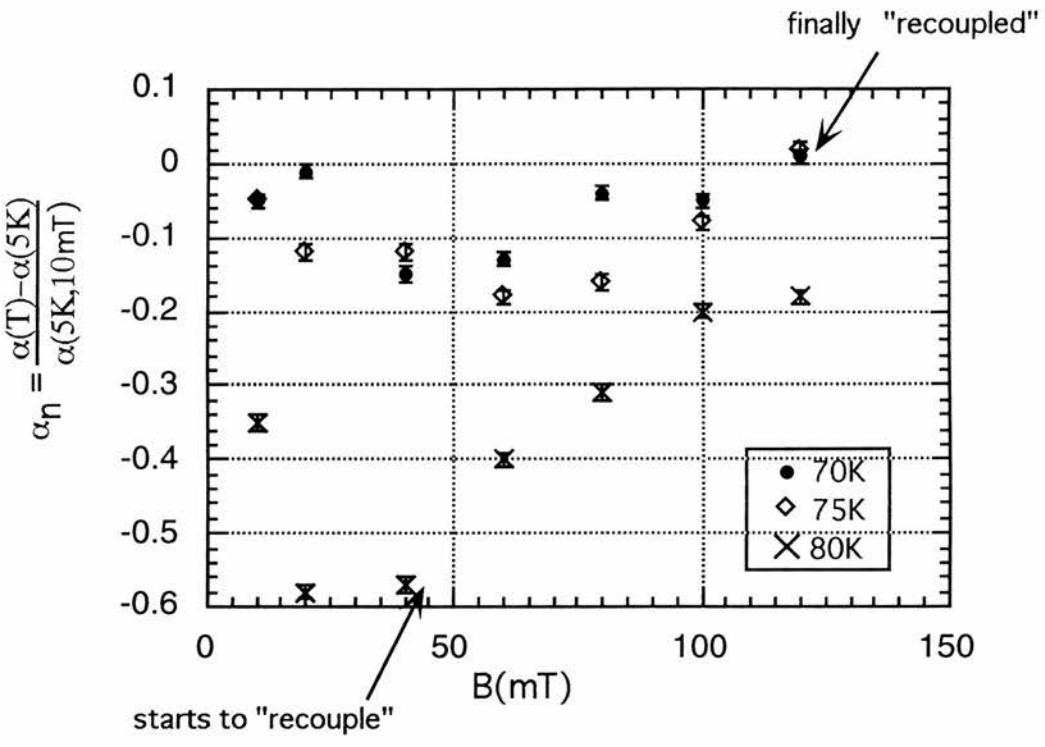

Figure 7.29: The normalised α parameter for differences between 70 K, 75 K,80 K and the base temperature (5 K). All the α values in this figure have been normalised to that value attained at 10 mT and 5 K.

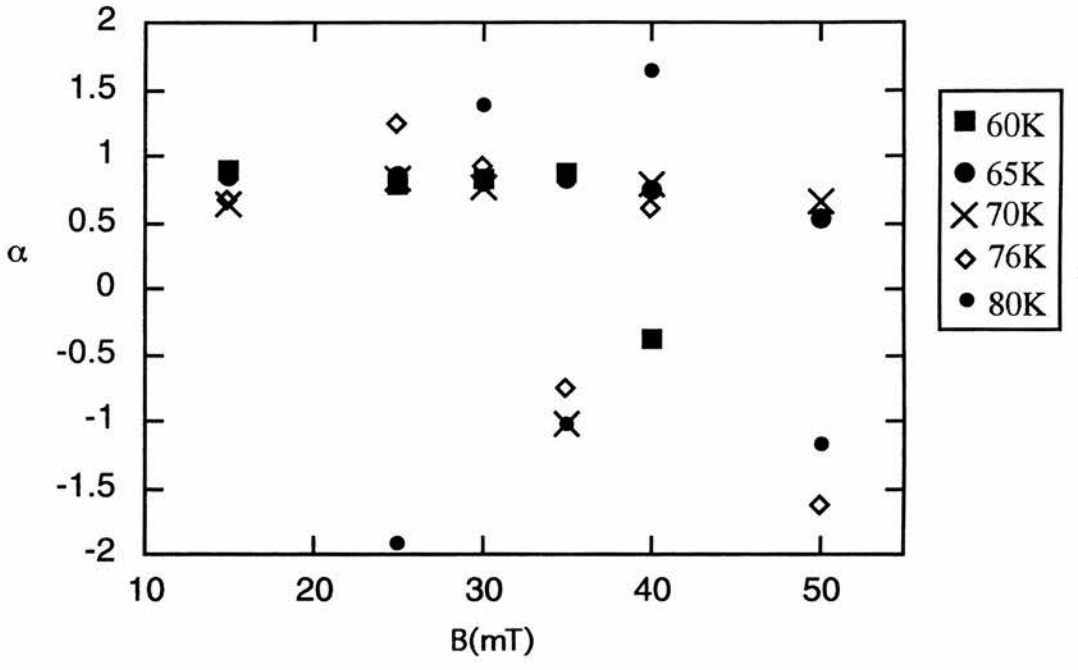

Figure 7.30: The α parameter for CD200 at different temperatures and fields taken at RAL with the CD at 45° to the applied field.

Bose-Glass phase, but this too exhibited μSR lineshapes with rms values which differed markedly from that required for an *ideal* BG model and it was shown here that in this case the distribution actually observed followed that of an ideal lattice more closely. CD4 was also noted to exhibit behaviour which was indicative of an enhancement of the disorder (for stiff fluxlines) in the lattice at fields of the order of B_ϕ. Finally, experiments were carried out in order to attempt to identify evidence for *recoupling* and a *decoupling* in the liquid state for a sample with a matching field of 200mT (CD200). Strong evidence for the *recoupling* line is evident from JPR measurements [152, 153], and, although there is some evidence for the decoupling and recoupling of pancakes at different temperatures in CD200 it is apparent that a more extensive investigation is required before any strong conclusions can be made.

Chapter 8

Summary, Conclusions and Future Work

8.1 Summary and Conclusions

Following on from work that was done on over doped $Bi_{2.15}Sr_{1.85}Ca_1Cu_2O_{8+\delta}$ ($BSCCO_{over}$) [51] the primary aim of this thesis was to investigate the coupling mechanisms that exist between the flux-pancakes in the superconducting layers in systems of different superconducting anisotropy, γ. This previous work indicates that in the low field phase diagram of $BSCCO_{over}$ that electromagnetic coupling plays a more dominant role, where, in the past, it has been assumed that Josephson coupling alone controls the pancake behaviour.

Firstly, an *untwinned* $YBa_2Cu_3O_{7-\delta}$ ($YBCO_{untwinned}$) crystal was studied. The absence of twin-planes permitted a complete investigation of the in and out-of-plane anisotropy to be carried out. Microscopic measurements of these anisotropies were in good agreement and these indicated that, further to previous measurements on $YBCO_{twinned}$, the out-of-plane anisotropy was indicated to be even lower.

However, a large discrepancy was noted here between the out-of-plane anisotropy measured by microscopic techniques and that measured by torque magnetometry.

Secondly, two organic superconductors were studied. κ-(BEDT-TTF)$_2$Cu(SCN)$_2$ [ET-Cu] is reported to have a very high anisotropy ($\gamma \geq 300$) and α-(BEDT-TTF)$_2$NH$_4$Hg(SCN)$_4$ [ET-NH4] has an extremely large anisotropy ($\gamma \geq 1000$). The large values of γ and λ make thermal disruption possible in these systems, even at the low temperatures involved. These parameters also indicate that in these systems $\lambda \sim \gamma$s and *clearly* electromagnetic coupling must play a role, indeed, this is mirrored by the similarities in vortex dynamics that these systems share with the layered HTSC, BSSCO (i.e melting, dimensional crossover, electromagnetic coupling and the angular variation of $\langle \Delta B^2 \rangle^{1/2}(T)(\vartheta)$).

Next, an optimally doped BSCCO crystal was investigated (BSSCO$_{opt}$). The nature of this study was based upon the presence and influence of thermal disorder on the vortex-pancake system and consequent measurements of lineshapes from μSR. Previously, similar measurements upon BSCCO$_{over}$, had once again indicated that electromagnetic coupling could not be ignored as a dominant coupling mechanism. Since the magnitude of thermal displacements of the pancakes for electromagnetic coupling are predicted to depend strongly on the value of the penetration depth of the material involved, BSSCO$_{opt}$ was chosen as a suitable candidate for study. As this system exhibits a significantly larger λ than BSCCO$_{over}$, the presence and dominance of electromagnetic coupling would therefore be expected to have a significant and noticeable change on measurements of the μSR lineshapes. Measurements indicated that, as a consequence of the material properties of BSSCO$_{opt}$ (i.e. γ, λ) this system had actually entered a regime in which *both* Josephson and electromagnetic coupling play a role. This fact can be con-

trasted with measurements on $BSCCO_{over}$ in which it was evident that the role of Josephson coupling was limited to a small region of the phase diagram [51].

Finally, measurements on three samples of irradiated BSSCO were carried out. These measurements indicated primarily that, in the presence of columnar defects, the elastic moduli of the vortex system were enhanced, allowing the *dynamic* and *static* disorder of the pancake-vortices in these systems to be significantly suppressed. Further, other properties such as the Bose-Glass phase and the presence of a *recoupling* line in the liquid state were investigated with interesting results.

In final summary, it is clear from the experimental work carried out in this thesis that electromagnetic coupling cannot be ignored as an important coupling mechanism in the very layered superconducting systems. In the past, it has been assumed that Josephson coupling dominates, but, as this work has highlighted, electromagnetic coupling plays a more significant role and may even dominate pancake-vortex behaviour. From these facts alone, it is clear that much of the vortex behaviour exhibited in the very layered superconductors can be viewed as *generic*.

8.2 Future Work

The main thrust of the future work that has been highlighted by the research carried out in this thesis is in the area of organic superconductors. The pioneering work that has been carried out here on these systems has indicated that, although the penetration depths exhibited by these systems are in general very long, properties of the flux-lattice can still be measured by μSR. As the degree of superconducting anisotropy is controlled to a great extent by the anion layer X, it is possible to study a range of ET materials with differing properties by varying X.

In carrying out such an investigation all aspects of vortex matter physics may be studied. The promise of such studies has been improved further by the implementation of a muon-on-request' facility at PSI, Switzerland (Indeed, measurements have already been carried out (October 1999) on a new batch of high quality ET-Cu and these have offered further insight into the phase diagram of this organic superconductor [170]). Additionally, SANS experiments on ET-Cu carried out in this thesis, although offering a null result here, have indicated that it is possible to observe neutron scattering at extremely low **q**-values and, as has been indicated above, have paved the way for experiments into systems which exhibit flux-lattices and flux-lattice transitions at very low fields. The most notable investigation to date is that of the square flux-lattice in Strontium Ruthenate (Sr_2RuO_4) [74].

References

[1] H. K. Onnes, Comm. Leiden 120b (1911).

[2] W. Meissner, R. Ochsenfeld Naturwissenschaften **21** 787(1933).

[3] F. London, H. London, Z. Phys. **96** 359 (1935).

[4] V. L. Ginzburg, L. D. Landau, Zh. Eksp. Teor. Fiz. (In Russian) **20** 1044 (1950).

[5] L. D. Landau, Phys. Z. Sowjet. **11** 545 (1937).

[6] J. Bardeen, L. N. Cooper, J. R. Schrieffer, Phys. Rev. **108** 1175 (1957).

[7] J. G. Bednorz, K. A. Miller, Z. Phys. B **64** 189 (1986).

[8] M. K. Wu, J. R. Ashburn, C. J. Torng, P. H. Hor, R. L. Meng, L. Gao, Z. J. Huang, Y. Q. Wang, C. W. Chu, Phys. Rev. Lett. **58** 908 (1987).

[9] A. Schilling, M. Cantoni, J. D. Guo, H. R. Ott, Nature **363** 56 (1993).

[10] Michael Tinkham, *Introduction to superconductivity*, 2nd Ed., McGraw Hill (1996).

[11] D. R. Tilley & J. Tilley, *Superfluidity and Superconductivity*, 3rd Ed., Adam Hilger (1990).

[12] J. R. Waldram, *Superconductivity of Metals and Cuprates*, IOP (1996).

[13] C. J. Gorter, H. B. G. Casimir, Physica **1** 306 (1934).

[14] R. F. Gasparovic, W. L. McLean, Phys. Rev. B **2** 2519 (1970).

[15] L. N. Cooper, Phys.Rev. **104** 1189 (1956).

[16] H. Fröhlich, Phys.Rev. **79** 845 (1950).

[17] P. Townsend, J. Sutton, Phys.Rev. **28** 591 (1962).

[18] W. L. Mcmillan, Phys.Rev. **167** 331 (1968).

[19] C. E. Gough, M. S. Colclough, E. M. Forgan, R. G. Jordan, M. Keene, C. M. Muirhead , A. I. M. Rae, N. Thomas, J. S. Abell, Nature **326** 855 (1987).

[20] A. A. Abrikosov, Sov. Phys. JETP **5** 1174 (1957).

[21] A. B. Pippard, Proc. Camb. Phil. Soc. **47** 617 (1951).

[22] W. E. Lawrence, S. Doniach, in *Proceedings of the XIIth International Conference on Low-Temperature Physics, Kyoto 1970*, edited by E. Kanda (Keigaku, Tokyo, 1970), p. 361.

[23] J. T. McDevitt, Department of Chemistry and Biochemistry WWW server, University of Texas at Austin (1997).

[24] P. Schleger, W. N. Hardy, B. X. Yang, Physica C **176** 261 (1991).

[25] J. M. Bell, Phys.Rev.B **37** 541 (1988).

[26] S. Romer, Private communication.

[27] C. W. Chu, J. Betchtold, L. Gao, P. H. Hor, Z. J. Huang, R. L. Meng, Y. Y. Sun, Y. Q. Wang, Y. Y. Xue, Phys. Rev. Lett. **60** 941 (1988).

[28] H. Akamatu, H. Inokuchi, Y. Matsunaga, Nature (London) **173** 168 (1954).

[29] W. A. Little, Phys. Rev. A **134** 1416 (1964).

[30] W. A. Little, Sci. Am. **212** 21 (1965).

[31] D. Jerome, A. Mazaud, M. Ribault, K. Bechgaard, J. Phys. Lett. **41** L95 (1980).

[32] M. Mizuno, A. F. Garito, M. P. Cava, J. Chem. Soc. Chem. Commun **1978** 18.

[33] G. Saito, T. Enoki, K. Torimuri, H.Inokuchi, Solid State Commun. **42** 557 (1982).

[34] H. Urayama, H. Yamochi, G. Saito, K. Nozawa, T. Sugano, M. Kinoshita, S. Sato, K. Oshima, A. Kawamoto, J. Tanaka, Chem. Lett. **1988** 55.

[35] A. M. Kini, U. Geiser, H. H. Wang, K. D. Carlson, J. M. Williams, W. K. Kwok, K. D. Vandervoort, J. E. Thompson, D. l. Stupka, D. Jung, M. H. Whangbo Inorg. Chem. **29** 2555 (1990).

[36] J. M. Williams, A. M. Kini, H. H. Wang, K. D. Carlson, U. Geiser, L. K. Montgomery, G. J. Pyrka, D. M. Watkins, J. M. Kommers, S. J. Boryschuk, A. V.Strieby Crouch, W. K.Kwok, J. E. Schirber, D. L. Overmyer, D. Jung, M. H. Whangbo, Inorg. Chem. **29** 3272 (1990).

[37] Micheal Lang, *Superconductivity Review* **2** pp.1-115 (Gordon and Breach Science Publishers, 1996).

[38] S. T. Johnson, E. .M. Forgan, S. H. Lloyd, C. M. Aegerter, S. L. Lee, R. Cubitt, P. G. Kealey, C. Ager, S. Tajima, A. Rykov, D. McK. Paul, Phys. Rev. Lett. **82** 2792 (1999).

[39] G. J. Dolan, F. Holtzberg, C. Field and T. R. Dinger, Phys. Rev. Lett. **62** 2184 (1989).

[40] D. N. Basov *et al.*, Phys. Rev. Lett **74** 598 (1995).

[41] A. G. Sun *et al.*, Phys. Rev. B **52** R15731 (1995).

[42] D. E. Farrell, S. Bonham, J. Foster, Y. C. Chang, P. Z. Jiang, K. G. Vandervoort, D. J. Lam, V. G. Kogan, Phys. Rev. Lett. **63** 782 (1989).

[43] J. C. Martinez, S. H. Brongersma, A. Koshelev, B. Ivlev, P. H. Kes, R. P. Griessen, D. G. de Groot, Z. Tarnawski and A. A. Menovsky, Phys. Rev. Lett. **69** 2276 (1992).

[44] P. A. Mansky, P. M. Chaikin, R. C.Haddon, Phys. Rev. B bf 50 15929 (1994).

[45] S. Friemel, C. Pasquier, Physica C **265** 121 (1996).

[46] S. Friemel, C. Pasquier, D. Jérome, J. Phys. I (France) **6** 2043 (1996).

[47] S. Friemel, C. Pasquier, D. Jérome, J. Low-Temp. Phys. **105** 1727 (1996).

[48] D. E. Farrell, C. J. Allen, R. C.Haddon, S. V. Chichester, Phys. Rev. B **42** 8694 (1990).

[49] S. Kawamata, K. Okuda, T. Sasaki, N. Toyota, Solid State Commun. **89** 955 (1994).

[50] H. Taniguchi, Y. Nakazawa, K. Kanoda, Phys. Rev. B. **57** 3623 (1998).

[51] S. L. Lee, C. M. Aegerter, B. Stauble-Pumpin, E. M. Forgan, J. Blatter, R. Cubitt, H. Keller, M. Willemin, S. H. Lloyd, T. W. Li, P. Kes, Phys. Rev. B **55** 5666 (1997).

[52] A. I. Larkin, Y. N. Ovchinnikov, J. Low. Temp. Phys. **34** 409 (1979).

[53] D. S. Fisher, M. P. A. Fisher, D. A. Huse, Phys. Rev. B **43** 130 (1991).

[54] E. H. Brandt, J. Low-Temp. Phys. **26** 709 (1977).

[55] A. Houghton, R. A. Pelcovits, A. Sudbo, Phys. Rev. B **40** 6763 (1989).

[56] A. Sudbø, E. H. Brandt, Phys. Rev. Lett. **66** 1781 (1991).

[57] L. I. Glazman, A. E. Koshelev, Phys. Rev. B **43** 2835 (1991).

[58] G. Blatter, M. V. Feigel'man, V. B. Geshkenbein, A. I. Larkin, V. M. Vinokur, Rev. Mod. Phys. **66** 1125 (1994).

[59] G. Blatter, V. Geshkenbein, A. Larkin, H. Nordborg, Phys. Rev. B **54** 72 (1996).

[60] C. M. Aegerter, S. L. Lee, H. Keller, E. M. Forgan, S. H. Lloyd, Phys. Rev. B **54** 15661 (1996).

[61] S. L. Lee, P. Zimmermann, H. Keller, M. Warden, I. M.Savić, R. Schauwecker, D. Zech, R. Cubitt, E. M. Forgan, P. H. Kes, T. W. Li, A. A. Menovsky, Z. Tarnawski, Phys. Rev. Lett. **71** 3862 (1993).

[62] J. H. Brewer *et al.*, Hyper. Inter **63** 41 (1990).

[63] H. Keller, IBM Journal of research and development **33** 314 (1989).

[64] W. Barford, J. M. F. Gunn, Physica C **156** 515 (1988).

[65] S. L. Thiemann, Z. Radovic, V. G. Kogan, Phys. Rev B **39** 11406 (1989).

[66] R. Cubitt, E. M. Forgan, M. Warden, S. L. Lee, P. Zimmermann, H. Keller, I. M.Savić, P. Wenk, D. Zech, P. H. Kes, T. W. Li, A. A. Menovsky, Z. Tarnawski, Physica C **213** 126 (1993).

[67] B. D. Rainford, G. J. Daniell, Hyper. Inter **87** 1129 (1994).

[68] R. Cubitt, Ph.D Thesis, University of Birmingham (1994).

[69] S. L. Lee, F. L. Pratt, S. J. Blundell, C. M. Aegerter, P. A. Pattenden, K. H. Chow, E. M. Forgan, T. Sasaki, W. Hayes, H. Keller, Phys. Rev. Lett **79** 1563 (1997).

[70] E. M. Forgan, in *Neutron Scattering in Layered Copper-Oxide Superconductors*, edited by A. Furrer, Physics and Chemistry of Materials with Low-Dimensional Structures (Kluwer Academic, Boston, 1998).

[71] S. L. Lee, E. M. Forgan, C.1.7.3 *Neutron techniques: Flux-line lattice*, edited by D. Caplin, Handbook of superconducting materials (IOP, to be published).

[72] C. Dewhurst, Private communication.

[73] Neil W. Ashcroft, David. N. Mermin, *Solid State Physics* (Saunders College, Philadelphia, 1975).

[74] T. M. Riseman, P. G. Kealey, E. M. Forgan, A. P. Mackenzie, L. M. Galvin, A. W. Tyler, S. L. Lee, C. Ager, D. McK.Paul, C. M. Aegerter, R. Cubitt, Z. Q. Mao, T. Akima, Y. Maeno, Nature **396** 242 (1998).

[75] C. M. Aegerter, S. H. Lloyd, C. Ager, S. L. Lee, S. Romer, H. Keller, E. M. Forgan, J. Phys.: Condens. Matter **10** 7445-7451 (1998).

[76] D. McK.Paul, C. V. Tomy, C. M. Aegerter, R. Cubitt, S. H. Lloyd, E. M. Forgan, S. L. Lee, M. Yethiraj, Phys. Rev. Lett. **80** 1517 (1998).

[77] D. K. Christen, F. Tasset, S. Spooner, H. A. Mook, Phys. Rev. B. **15** 4506 (1977).

[78] R. Cubitt, E. M. Forgan, D. McK Paul, S. L. Lee, J. S. Abell, H. Mook, P. A. Timmins, Physica B **180-1** 377 (1992).

[79] The ILL web pages (1999).

[80] Charles Kittel, *Introduction to Solid State Physics*, 7th Ed. (John Wiley & Sons, 1996).

[81] V. G. Kogan, Phys. Rev. B **24** 1572 (1981).

[82] V. G. Kogan, Phys. Rev. B **38** 7049 (1988).

[83] D. E. Farrell, C. M. Williams, S. A. Wolf, N. P. Bansal, V. G. Kogan, Phys. Rev. Lett. **61** 2805 (1988).

[84] D. Zech *et al.*, Phys. Rev. B **53** R6026 (1996).

[85] B. Pümpin, H. Keller, W. Kündig, I. M. Savić, J. W. Schneider, H. Simmler, P. Zimmermann, E. Kaldis, S. Rusiecki, C. Rossel, E. M. Forgan, J. of the Less. Comm. Metals. **164-165** 994 (1990).

[86] D. R. Harshman, L. F. Schneemeyer, J. V. Waszczak, G. Aeppli, R. J. Cava, B. Batlogg, L. W. Rupp, E. J. Ansaldo, D. Ll Williams, Phys. Rev. B **39** 851 (1989).

[87] G. J. Dolan, G. V. Chandrashekar, T. R. Dinger, C. Field, F. Holtzberg, Phys. Rev. Lett. **62** 827 (1989).

[88] N. L. Wang *et al.*, Phys. Rev. B **57** 1 (1998).

[89] D. Zech *et al.*, Phys. Rev. B **54** 12535 (1996).

[90] Takekazu. Ishida *et al.*, Phys. Rev. B **56** 11897 (1997).

[91] R. Cubitt, E. M. Forgan, G. Yang, S. L. Lee, Paul D. McK, H. A. Mook, M. Yethiraj, P. H. Kes, T. W. Li, A. A. Menovsky, Z. Tarnawski, K. Mortensen, Nature **365** 407 (1993).

[92] E. Zeldov, D. Majer, M. Konczykowski, A. I. Larkin, V. M. Vinokur, V. B. Shtrikman, Nature **375** 373 (1995).

[93] A. Schilling, R. A. Fisher, N. E. Phillips, U. Welp, D. Dasgupta, W. K. Kwok, G. W. Crabtree, Nature **382** 791 (1996).

[94] A. Schilling, R. A. Fisher, N. E. Phillips, U. Welp, W. K. Kwok, G. W. Crabtree, Phys. Rev. Lett. **78** 4833 (1997).

[95] A. Junod, M. Roulin, J. -Y. Genoud, B. Revaz, A. Erb, E. Walker, Physica C **275** 245 (1997).

[96] G. Blatter, V. B. Geshkenbein, A. I. Larkin, Phys. Rev. Lett. **68** 875 (1992).

[97] M. Yethiraj *et al.*, Phys. Rev. Lett. **71** 3019 (1993).

[98] C. M. Aegerter, S. T. Johnson, W. J. Nuttall, S. H. Lloyd, M. T. Wylie, M. P. Nutley, E. M. Forgan, R. Cubitt, S. L. Lee, D. McK.Paul, M. Yethiraj, H. A. Mook Vortex lattice melting in twinned YBCO.

[99] A. I. Rykov *et al.*, in Advances in Superconductivity VIII (Proc. ISS'95), Eds: H. Hayakawa and Y. Enomoto (Springer, Tokyo, 1996) p. 341.

[100] S. H. Lloyd, Ph.D thesis, University of Birmingham, (1999).

[101] C. M. Aegerter, S. L. Lee, Appl. Magn. Reson. **13** 75-93 (1997).

[102] E. M. Forgan, S. L. Lee, S. Sutton, J. S. Abell, S. F. J. Cox, C. A. Scott, H. Keller, B. Pumpin, J. W. Schneider, H. Simmler, P. Zimmerman,I. M.Savić, Hyper. Int. **63** 71-72 (1990).

[103] P. G. Kealey *et al.*, In preparation.

[104] E. H. Brandt, Phys. Rev. B **37** 2349 (1988).

[105] M. Yethiraj *et al.* Phys. Rev. Lett. **70** 857 (1993).

[106] E. M. Forgan, P. G. Kealey, T. M. Riseman, S. L. Lee, D. McK. Paul, C. M. Aegerter, R. Cubitt, P. Schleger, A. Pautrat, Ch. Simon, S. T. Johnson, Physica B **267-268** 115 (1999).

[107] M. Ichioka *et al.*, Phys. Rev. B **53** 15316 (1996).

[108] B. Janossy, D. Prost, S. Pekker, L. Fruchter, Physica. (Amsterdam) **181C** 51 (1991).

[109] J. L. Tallon *et al.*, Phys. Rev. Lett. **74** 1008 (1995).

[110] V. Z. Kresin, S. A. Wolf, Phys. Rev. B **46** 6458 (1992).

[111] C. Bernhard, Ch. Niedermayer, U. Binninger, A. Hofer, Ch. Wenger, J. L. Tallon, G. V. M. Williams, E. J. Ansaldo, J. I. Budnik, C. E. Stronach, D. R. Noakes, M. A. Blankson-Mills, Phys. Rev. Lett. **52** 10488 (1995).

[112] D. E. Farrell *et al.*, Phys. Rev. Lett. **67** 1165 (1991).

[113] K. Okuda *et al.*, J. Phys. Soc. Jpn. **60** 3226 (1991).

[114] L. N. Bulaevskii., Phys. Rev. B **44** 910 (1991).

[115] S. L. .Thiemann, Z. Radovic, V. G. Kogan, Phys. Rev. B **39** 11406 (1989).

[116] C. M. Aegerter *et al.*, Vortex lattice melting in untwinned YBCO, to be published.

[117] M. Willemin, A. Schilling, H. Keller, C. Rossel, J. Hofer, U. Welp, W. K. Kwok, R. J. Olsson, G. W. Crabtree, Phys. Rev. Lett **81** 4236 (1998).

[118] J. R. Clem *et al*, Phys. Rev. B **43**, 7837 (1991).

[119] C. Pasquier, S. Friemel, D. Jerome, J. Low-Temp. Phys. **105** 1681 (1996).

[120] C. Bernhard, Ch. Wenger, Ch. Niedermayer, D. M. Pooke, J. L. Tallon, Y. Kotaka, J. Shimoyama, K. Kishio, D. R. Noakes, C. E. Stronach, T. Sembiring, Phys. Rev. B **52** R7050 (1995).

[121] T. Nishizaki, T. Sasaki, T. Fukase, N. Kobayashi, **54** R3760 (1996).

[122] A. D. Sidorenko*et al*, Hyper.Inter **63** 49 (1990).

[123] D. R. Harshman *et al.*, Phys. Rev. Lett. **64** 1293 (1990).

[124] L. P. Le *et al* Phys. Rev. Lett. **68** 1923 (1992).

[125] D. R. Harshman *et al.*, Phys. Rev. B. **49** 12990 (1994).

[126] M. Lang, N. Toyota, T. Sasaki, H. Sato, Phys. Rev. Lett. **69** 1443 (1992).

[127] C. M. Aegerter, J. Hofer, I. M.Savić, H. Keller, S. L. Lee, C. Ager, S. H. Lloyd, E. M. Forgan, Phys. Rev. B **57** 1253 (1998).

[128] D. R. Harshman, R. N. Kleiman, M. Inui, G. P. Espinosa, D. B. Mitzi, A. Kapitulnik, T. Pfiz, D. Ll. Williams, Phys. Rev. Lett. **67** 3152 (1991).

[129] B. Khaykovich, E. Zeldov, D. Majer, T. W. Li, P. H. Kes, M. Konczykowski, Phys. Rev. Lett. **76** 2555 (1996).

[130] V. N. Kopylov *et al.*, Physica C **170** 291 (1990).

[131] W. K. Kwok, J. Fendrich, U. Welp, S. Fleshler, J. Downey, G. W. Crabtree, Phys. Rev. Lett **72** 1088 (1994).

[132] D. T. Fuchs, E. Zeldov, D. Majer, R. A. Doyle, T. Tamegai, S. Ooi, M. Konczykowski, Phys. Rev. B **54**, R796 (1996).

[133] H. Pastoriza, M. F. Goffman, A. Arribere, F. de la Cruz, Phys. Rev. Lett. **72** 2951 (1994).

[134] M. Roulin, A. Junod, E. Walker, Science **273** 1210 (1996).

[135] Y. -Q. Song, W. P. Halperin, L. Tonge, T. J. Marks, Phys. Rev. Lett. **70** 3127 (1993).

[136] Y. -Q. Song *et al.*, Physica (Amsterdam) **241C** 187 (1995).

[137] S. L. Lee, M. Warden, H. Keller, J. W. Schneider, D. Zech, P. Zimmermann, R. Cubitt, E. M. Forgan, M. T. Wylie, P. H. Kes, T. W. Li, A. A. Menovsky anf Z. Tarnawski, Phys. Rev. Lett. **75** 922 (1995).

[138] T. W. Li *et al.*, J. Crystal Growth **135** 481 (1994).

[139] D. R. Nelson, V. M.Vinokur, Phys. Rev. Lett. **68** 2398 (1992).

[140] D. R. Nelson, V. M.Vinokur, Phys. Rev. B **48** 13060 (1993).

[141] L. Civale, A. D. Marwick, T. K. Worthington, M. A. Kirk., J. R. Thompson, L. Krusin-Elbaum, Y. Sun, J. R. Clem, F. Holtzberg, Phys. Rev. Lett **67** 648 (1991).

[142] M. Konczykowski, F. Rullier-Albenque,E. R. Yacoby, A. Shaulov, Y. Yeshurun, P. Lejay, Phys. Rev. B **44** 7167 (1991).

[143] R. C. Budhani, M. Suenaga and S. H. Liou, Phys. Rev. Lett. **69** 3816 (1992).

[144] D. Zech, S. L. Lee, H. Keller, G. Blatter, B. Janossy, P. H. Kes, T. W. Li, A. A. Menovsky, Phys. Rev. B **52** 6913 (1995).

[145] G. Blatter, M. V. Feigel'man, V. B.Geshkenbein, A. I. Larkin, V. M. Vinokur, Rev. Mod. Phys. **66** 1125 (1994).

[146] W. Jiang, N. C. Yeh, D. S. Reed, U. Kriplani, D. A. Beam, M. Konczykowski, T. A. Tombrello, F. Holtzberg, Phys. Rev. Lett. **74** 1438 (1994).

[147] L. Krusin-Elbaum, L. Civale, G. Blatter, A. D. Marwick, F. Holtzberg C. Field, Phys. Rev. Lett. **72** 1914 (1994).

[148] C. J. van der Beek, M. Konczykowski, V. M. Vinokur, T. W. Li, P. H. Kes, G. W. Crabtree, Phys. Rev. Lett. **74** 1214 (1995).

[149] U. C. Tauber, D. R. Nelson, Phys. Rev. B **52** 16106 (1995).

[150] A. E. Koshelev *et al.*, Phys. Rev. B **53** R8855 (1996).

[151] R. Doyle, W. S. Seow, Y. Yan, A. M. Campbell, T. Mochiku, K. Kadowaki, G. Wirth, Phys. Rev. Lett. **77** 1155 (1996).

[152] M. Kosugi, Y. Matsuda, M. B. Gaifullin, L. N. Bulaeskii, N. Chikumoto, M. Konczykowski, J. Shimoyama, K. Kishio, K. Hirata, K. Kumagai, Phys. Rev. Lett. **79** 3763 (1997).

[153] M. Sato *et al.*, Phys. Rev. Lett. **79**, 3759 (1997).

[154] S. Hébert, V. Hardy, G. Villard, M. Hervieu, Ch. Simon, J. Provost, Phys. Rev. B **57** 649 (1998).

[155] C. M. Aegerter, Privatc communication.

[156] M. Wylie, Ph.D thesis, University of Birmingham, (1996).

[157] B. Radzihovsky, Phys. Rev. Lett. **74** 4923 (1995).

[158] S. L. Lee, C. M. Aegerter, S. H. Lloyd, E. M. Forgan, C. Ager, M. B. Hunt, H. Keller, I. M.Savić, R. Cubitt, G. Wirth, K. Kadowaki, N. Koshizuka, Phys. Rev .Lett. **81** 5209 (1998).

[159] E. M. Forgan, in *Neutron Scattering in Layered Copper-Oxide Superconductors*, edited by A. Furrer, Physics and Chemistry of Materials with Low-Dimensional Structures (Kluwer Academic, Boston, 1998).

[160] F. Y. Ogrin, S. L. Lee, C. Ager, C. M. Aegerter, E. M. Forgan, S. H. Lloyd, P. G. Kealey, T. Riseman, R. Cubitt, G. Wirth, *in proceedings of ECNS, Budapest, 1999*, to be published in Physica B.

[161] V. N. Gorbunov, V. P. Smilga, Hyperfine Interactions **63** 109-116 (1990).

[162] S. L. Lee, C. Ager, C. M. Aegerter, T. M. Riseman, ISIS experimental report, RB Number 9829 (1998).

[163] E. H. Brandt, Phys. Rev. Lett. **66** 3213 (1991).

[164] G. I. Menon *et al.*, submitted to PRL (1999).

[165] V. Hardy, A. Wahl, S. Hébert, R. Ruyter, J. Provost, D. Groult, Ch. Simon, Phys. Rev. B **54** 656 (1996).

[166] Y. Matsuda, M. B. Gaifullin, K. Kumagai, M. Kosugi K. Hirata, Phys. Rev. Lett. **78** 1972 (1997).

[167] O. K. C. Tsui *et al.*, Phys. Rev. Lett. **76** 819 (1996).

[168] Y. Matsuda *et al.*, Phys. Rev. Lett. **75** 4512 (1995).

[169] L. N. Bulaevskii *et al.* Phys. Rev. Lett. **77** 936 (1996).

[170] F. Y. Ogrin, C. Ager, S. L. Lee, F. L. Pratt, S. J. Blundell, T. Sasaki, N. Toyota, K. Kanoda, K. Nagamine H. Keller, to be published.